Emerging patterns from the collective dynamics of microswimmers in an external field

Dissertation

zur Erlangung des Grades
„Doktor der Naturwissenschaft“

am Fachbereich Physik, Mathematik und Informatik
der Johannes Gutenberg-Universität in Mainz

Fabian Rouven Kössel
geboren in Saarbrücken

Mainz, den 29. November 2019

Teile der Dissertation wurden bereits veröffentlicht:

»Controlling stability and transport of magnetic microswimmers by an external field«
Fabian R. Koessel and Sara Jabbari-Farouji
2019 EPL **125** 28001

Abstract

In recent years, the focus in soft matter physics has shifted gradually from equilibrium towards non-equilibrium systems. In particular, active particles that transform ambient energy into directed motion, have become a popular testbed for out-of-equilibrium statistical physics. From the collective dynamics of active particles fascinating phenomena emerge, such as pattern formation, unusual rheological properties, and transitions between ordered and disordered states. Some envisioned future applications of active particles, such as micro-scale targeted drug delivery, require some form of external control to influence the particles' dynamics and behaviour. Such a control could possibly be provided by an external (magnetic) field. Furthermore, experiments on active magnetotactic bacteria (MTB) in an external magnetic field have demonstrated intriguing pattern formation. Although not well understood, they have indicated the importance of hydrodynamic interactions for the dynamics of MTB.

In this thesis, we develop 3D kinetic theories of a dilute suspension of active magnetic microswimmers to study their collective dynamics and pattern formation in an external field. To solve the arising non-linear equations numerically, we develop a novel hybrid simulation method that, using a stochastic sampling technique, integrates a Brownian dynamics solver on the particle level with a continuum pseudo-spectral method to calculate interactions between particles. We show that, for weakly magnetized microswimmers, the interplay between long-ranged hydrodynamic interactions and the external field can lead to distinct patterns for pusher- and puller-type microswimmers. A linear stability analysis of the homogeneous steady state not only predicts accurately the regime in which pattern formation occurs, but reveals that the mechanism of the pattern formation is driven by bend and splay instabilities. These instabilities lead to a partial depolarization and reduce the average speed of the swimmers. In particular, pullers undergoing a splay instability collectively create a flow against their average direction of motion parallel to the external field, resulting in a self-inflicted and significant reduction of their effective speed.

For active particles that are strongly magnetized, magnetic dipole-dipole interactions have to be considered. Even in the absence of an external magnetic field, they can cause a spontaneous magnetization — similar to passive magnetic systems. Moreover, the dipole-dipole interactions can lead to instabilities of the polarized homogeneous steady state that, after a transient, highly ordered pattern formation, result in a condensation of the particles into polarized travelling clusters.

Zusammenfassung

In den letzten Jahren hat sich der Schwerpunkt der Physik der weichen Materie allmählich vom Gleichgewicht zu Nicht-Gleichgewichtssystemen verlagert. Insbesondere aktive Teilchen, die Umgebungsenergie in gerichtete Bewegung umwandeln, sind zu einem beliebten Versuchsfeld für die statistische Physik abseits des Gleichgewichts geworden. Aus der kollektiven Dynamik aktiver Teilchen ergeben sich faszinierende Phänomene wie Musterbildung, ungewöhnliche rheologische Eigenschaften und Übergänge zwischen geordneten und ungeordneten Zuständen. Einige der angestrebten Anwendungen aktiver Teilchen, wie z.B. die gezielte Wirkstoffabgabe auf mikroskopischen Skalen, erfordern eine externe Kontrolle, um die Dynamik und das Verhalten der Teilchen zu beeinflussen. Eine solche Kontrolle könnte möglicherweise durch ein externes (Magnet-)Feld erfolgen. Darüber hinaus haben Experimente mit aktiven magnetotaktischen Bakterien (MTB) in einem externen Magnetfeld eine faszinierende Musterbildung offenbart. Obwohl nicht ausreichend verstanden, haben sie auf die Bedeutung hydrodynamischer Wechselwirkungen für die Dynamik der MTB hingewiesen.

Im Rahmen dieser Arbeit werden dreidimensionale kinetische Theorien einer verdünnten Suspension aktiver magnetischer Mikroschwimmern erarbeitet, um ihre kollektive Dynamik und Musterbildung in einem externen Feld zu untersuchen. Um die auftretenden nichtlinearen Gleichungen numerisch zu lösen, wurde ein neuartiges hybrides Simulationsverfahren entwickelt, das unter Verwendung einer stochastischen Abtasttechnik einen Brownschen Dynamiklöser auf Teilchenebene mit einem Kontinuums-Pseudospektralverfahren integriert, um Wechselwirkungen zwischen den Teilchen zu berechnen. Es wird gezeigt, dass bei schwach magnetisierten Mikroschwimmern das Zusammenspiel von langreichweitigen hydrodynamischen Wechselwirkungen und dem externen Feld zu unterschiedlichen Mustern für Pusher- und Puller-Mikroschwimmer führen kann. Eine lineare Stabilitätsanalyse des homogenen stationären Zustandes sagt nicht nur das Regime, in dem die Musterbildung stattfindet, genau voraus, sondern zeigt auch, dass der Mechanismus der Musterbildung durch Biege- und Spreizinstabilitäten (*bend and splay instabilites*) angetrieben wird. Diese Instabilitäten führen zu einer teilweisen Depolarisierung und reduzieren die Durchschnittsgeschwindigkeit der Schwimmer. Insbesondere Puller, die einer Spreizinstabilität ausgesetzt sind, erzeugen gemeinsam eine Strömung entgegen ihrer mittleren Bewegungsrichtung parallel zum externen Feld, was zu einer selbst verursachten und signifikanten Reduktion ihrer Effektivgeschwindigkeit führt.

Für stark magnetisierte aktive Teilchen sind magnetische Dipol-Dipol-Wechselwirkungen zu berücksichtigen. Selbst wenn kein äußeres Magnetfeld vorhanden ist, können die Wechselwirkungen, ähnlich zu passiven Systemen, zu einer spontanen Magnetisierung führen. Darüber hinaus können die Dipol-Dipol-Wechselwirkungen zu Instabilitäten des polarisierten homogenen stationären Zustandes führen, die nach einem vorübergehenden, hochgeordneten Musterbildung zu einer Kondensation der Teilchen zu polarisierten wandernden Clustern führen.

Contents

List of Symbols

Symbol	Definition	Meaning
$\mathbf{x}, x_i, \mathbf{v}(\mathbf{x})$	$\mathbf{x} \in \mathbb{R}^n, x_i \in \mathbb{R}, \mathbf{v} : \mathbb{R}^n \to \mathbb{R}^n$	a vector quantity $\mathbf{x}$ with components x_i and a vector field $\mathbf{v}$, usually $n = 3$; capital bold Latin letters denote tensors/tensor fields
$\mathbf{f} * \mathbf{g}$	$(\mathbf{f} * \mathbf{g})(\mathbf{x}) = \int \mathrm{d}\mathbf{y}\, \mathbf{f}(\mathbf{x} - \mathbf{y}) \cdot \mathbf{g}(\mathbf{y})$	convolution of vector fields $\mathbf{f}$ and $\mathbf{g}$
$\check{\mathbf{x}}$	$\check{\mathbf{x}} = \|\mathbf{x}\|^{-1}\mathbf{x}$	a normalized vector
$\widehat{\mathbf{v}}$	$\widehat{\mathbf{v}}(\mathbf{k}) = \frac{1}{(2\pi)^{n/2}} \int \mathrm{d}\mathbf{x}\, e^{-\mathrm{i}\mathbf{k}\cdot\mathbf{x}}\, \mathbf{v}(\mathbf{x})$	the n-dimensional Fourier-transform of a field $\mathbf{v}$
$\langle f(\mathbf{x}) \rangle$	$\langle f(\mathbf{x}) \rangle = \int \mathrm{d}\mathbf{x}\, \Psi(\mathbf{x})\, f(\mathbf{x})$	expectation value of f under the probability density Ψ, the integral is to be taken over *all* degrees of freedom, if not specified otherwise
∇, Δ	$\nabla f = \partial_{x_i} f = \frac{\partial}{\partial_{x_i}} \check{\mathbf{e}}_i$ and $\Delta = \nabla \cdot \nabla$	the Nabla and Lapalce operators, using the partial derivative ∂_{x_i} with respect to x_i and an orthonormal basis $\check{\mathbf{e}}_i$
$\mathbf{ab} = \mathbf{a} \otimes \mathbf{b}$	$(\mathbf{ab})_{ij} = a_i b_j$	dyadic product of vectors (or tensors) $\mathbf{a}, \mathbf{b}$, sometimes the $\otimes$ notation is used for clarity
$\mathbf{A} : \mathbf{B}$	$\mathbf{A} : \mathbf{B} = A_{ij} B_{ij}$	double dot product/contraction of two (2nd rank) tensors $\mathbf{A}, \mathbf{B}$, generalizes to higher rank

1 Introduction

1.1 Preface

The dynamics and behaviour of large groups of various animals or insects have fascinated scientists for a long time. The complex collective dynamics of a flock of birds, a colony of ants, a school of fish, a herd of sheep, or even a group of people[1] is an emergent property of interactions between individuals and is often very distinct from the dynamics of an individual (see Figure 1.1 for a few examples). What all these systems have in common is that their participants move around autonomously and actively, and they are therefore often referred to as active systems [2, 3]. Active systems and their properties have also inspired diverse studies, ranging from the improvement of optimization algorithms [4] to the study of traffic jams in agent based systems [5]. A famous example of the former is an optimization algorithm based on the self-organization mechanisms observed in a colony of ants, which solves the travelling-salesman problem more efficiently than previous solutions [6].

Recently, physicists have taken interest in active matter, in particular in microscopic self-propelled particles in both artificial and microbiotic systems. Not only do these systems exhibit novel properties distinct from their passive counterparts [7–14], but due to their non-equilibrium nature and reduced complexity (as compared with multi-cellular organisms), they also serve as a testbed for the statistical physics of systems out of equilibrium [15]. A distinct, if not defining, feature of active systems is a local input of energy into the system, as opposed to a global input of energy at the boundaries (for example, external shear) that drives the system constantly out of equilibrium. More precisely, biological and artificial self-propelled particles transform ambient energy into mechanical work or directed motion while possibly interacting with each other and their environment. Possible interaction mechanisms include chemotaxis [16–18], hydrodynamic [19–21] or magnetic [22–26] interactions, as well as phototaxis [27, 28], magnetotaxis [29], and gravitaxis [30–34]. These interactions give rise to novel properties not found in equilibrium systems, such as pattern formation, unusual mechanical and rheological properties, and non-equilibrium transitions between ordered and disordered states [8].

[1] for instance, the moshpit dynamics at a metal concert [1]

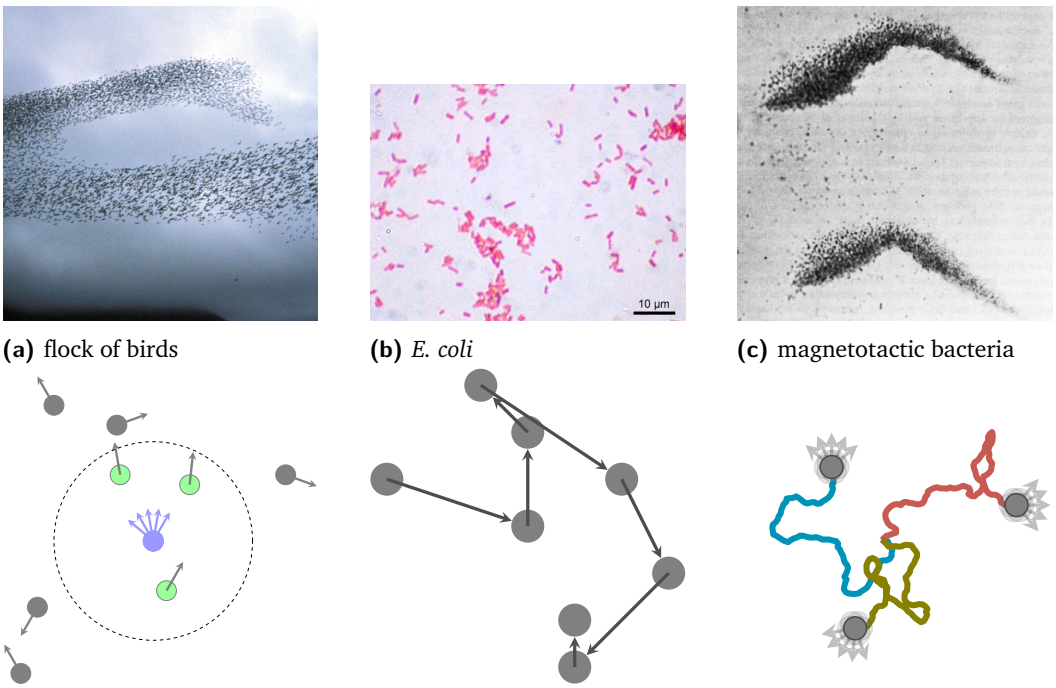

(a) flock of birds **(b)** *E. coli* **(c)** magnetotactic bacteria

(d) Vicsek model **(e)** run-and-tumble particle **(f)** active Brownian particles

Fig. 1.1.: Some examples of active systems (a-c) and illustrations of common models describing such systems (d-f). (a) Pattern formation in a flock of birds (source: D. Dibenski, U.S. Fish and Wildlife Service); (b) Microscopic image of gram stained Escherichia coli bacteria (source:Wikimedia; copyright: Y_tambe, Creative Commons, CC-BY-SA 3.0, 2005); (c) Band formation observed in magnetotactic bacteria in an external magnetic field (source: [23]; used with kind permissions of Elsevier, 1988); (d) Schematic representation of the cooperative movement of particles that align and adapt their velocity to the average orientation of their neighbour in the Vicsek model; (e) Illustration of a particle trajectory of a run-and-tumble particle — straight run phases are interrupted by a random reorientation (tumble); (f) Schematic trajectories of active Brownian particles that are self-propelled along their intrinsic orientation and are exposed to environmental noise affecting both their position and orientation.

Active systems can be broadly classified as wet or dry. Dry active systems either lack long-ranged hydrodynamic interactions altogether or their dynamics is dominated by more localized effects, such as steric interactions. Examples of dry active matter are grains jumping on a vibrating plate [35], dense swarming bacterial suspensions [36], and molecular motors transporting filaments [37]. On the other hand, in wet active systems, long-ranged hydrodynamic interactions play an important role in dictacting the dynamics of the system. Examples of wet systems are microswimmers in thin films [38], dense suspensions of driven nano-filaments [39], and the system described in this thesis.

This work focuses on one example of a wet active system, a suspension of magnetic microswimmers, and aims to explore the hydrodynamically induced pattern formations observed in an external field analogous in experiments on magnetotactic bacteria (MTB). Figure 1.1c shows a snapshot from an experiment on MTB in band formation [23]. Although hydrodynamic interactions are often neglected in studies of passive and active colloidal systems [40–43], this work demonstrates the importance of hydrodynamic interactions especially for polarized and dilute active suspensions. Furthermore, this work examines the interplay between these long ranged (hydrodynamic or magnetic) interactions and a magnetic external alignment torque, as discussed in Chapters 4 and 5[2]. In this system, anisotropic interactions combined with a forced alignment offer an exciting playground to study collective phenomena. Furthermore, the prospects for using active suspensions in applications such as micro-scale *cargo transport*, *targeted drug delivery*, and *microfluidic devices* [44–47], incentivize applying an external control mechanism. A promising approach for such a control mechanism is given by a magnetic field interacting with magnetic colloids, which describes the system discussed in this work.

To study active systems, like the one presented in this work, a suitable description of the system is necessary. However, even in seemingly simple artificial microscopic active systems, such as a system of Janus particles [48, 49], the particles' dynamics is influenced by a multitude of signals and other interactions, making a complete description of their dynamics currently infeasible. Instead, active systems are often approached in an idealized and simplified fashion, typically by a coarse graining procedure. In such a procedure, the art is to include the relevant mechanisms that give rise to the studied properties and neglect or approximate the irrelevant mechanisms. By exploiting symmetries and length- and time-scale separations in a system, a description of its dynamics can not only be simplified, rendering the system more tractable, but a more universal description of the system can be obtained. One systematic approach to such a description is using the methods of non-equilibrium statistical mechanics. For example, in the presence of time-scale separation (various processes happening at different rates), processes with a fast relaxation time can often be included effectively in the form of damping and noise.

Considerations along these lines have led to a variety of minimal models of active matter. Commonly employed models are the Vicsek model [50], run-and-tumble particles [51], and active Brownian particles as shown in Figure 1.1f. All these models approximate the detailed self-propulsion mechanism of a particle by an imposed self-propulsion velocity along the particle's orientation. However, they differ

[2]Although, the formalism concerning the external control field is not intrinsically restricted to the magnetic case and remains valid for any external torque.

in the treatment of the inter-particle interaction. The Vicsek model, illustrated in Figure 1.1d, describes cooperative movement emerging from simple alignment rules between neighbouring participants, and has been used to model the dynamics of a flock of birds as the one depicted in Figure 1.1a [50]. Run-and-tumble particles on the other hand have been employed to describe, among others, the dynamics of *E. coli*-bacteria, depicted in Figure 1.1b [51, 52]. In this model, the dynamics of a particle is approximated by periods of movement along an almost straight line (run), alternated with sudden and rapid randomizations of the orientation (tumble), as illustrated in Figure 1.1e. Finally, one of the most successful models, is the active Brownian particle (ABP) model, which has been studied extensively in recent years [53–56]. ABP model microscopic self-propelled particles that are exposed to a noisy environment. Countless collisions of the immersed particles with fluid molecules are approximated by frictional and stochastic forces and torques (see Figure 1.1f). ABPs self-propel with a prescribed velocity along their intrinsic orientation, while their orientation changes gradually due to noise. This approximation assumes an aforementioned time-scale separation between the fluid collisions occurring at a high rate and the long-time dynamics of the colloids that are of interest. In both run-and-tumble particles and ABP, inter-particle interactions are often modelled with a pair-potential.

These models of active particles can be studied on different levels of description. In particle based methods, such as molecular dynamics (MD), in the special case of Brownian Dynamics, or Stokesian dynamics simulations, the colloids and their interactions are described explicitly. These simulation methods evolve the system's dynamics by numerically integrating Newton's or Langevin's equations. Stokesian dynamics extends the MD/BD-method by additionally taking the surrounding fluid in a continuum approximation into account. Particle based methods are especially suited to study the detailed microscopic dynamics of — possibly dense — suspensions of active particles [13]. However, when studying the collective dynamics of a large number of particles, a description on that level is not necessarily required. For these systems, the particle description itself can be coarse grained into distributions of properties, i.e. probabilistic continuum models, and thus, shifting the scale into a mesoscopic regime. The dynamics of these distributions can then be formulated by making use of conservation laws, such as the conservation of particle number (for examples, see Ref. [8, 20, 57–59]). In this approach, symmetries of the system can become more apparent or are explicitly incorporated into the structure of the

model[3]. The review paper [8] gives an overview of various systems described in this fashion.

In the present work, the focus lies on the collective dynamics and the formation of patterns on the mesoscopic scale in relatively dilute suspensions of magnetic microswimmers. Therefore, 3D kinetic theories[4] of a wet system of active, magnetic particles in an external field is developed. Based on the model of ABP, the collective dynamics of point-like microswimmers is described by the dynamics of a probability distribution function governed by a conservation equation, the so called Smoluchwoski equation. Chapter 2 provides the theoretical background needed to develop these models and demonstrates, how long-ranged hydrodynamic and magnetic dipole-dipole interactions can be incorporated within the framework of a kinetic theory. In Chapter 3, a novel numerical method to solve the non-linear Smoluchowksi equation coupled to interaction fields is presented, accompanied by a brief introduction to the method of linear stability analysis — a valuable tool to study the dynamics near steady states of the system. In Chapter 4, the dynamics and pattern formation of hydrodynamically interacting microswimmers with a weak magnetic dipole moment is studied using both numerical and analytical methods. Using similar methods, in Chapter 5, a suspension of magnetically interacting microswimmers is analysed, pushing the model to its limits. However, before diving into this specific class of systems, the next section gives a brief general introduction to the fascinating and surprising world of microswimmers.

1.2 Swimming at low Reynold's number

Life in highly viscous environments is very different from what we are used to. When we build up momentum on a bicycle or glide in the water after a sturdy breast stroke, we rely on our inertia to carry us onward. In contrast, due to its small size and speed, a swimming microbe (and comparable artificial microswimmers) inhabits a regime in which it cannot rely on inertia to propel itself. In this regime, viscous forces dominate and inertia is quickly lost because it is transformed into thermal energy due to friction with and inside the surrounding medium. As a consequence, a microswimmer needs to apply a constant force in order to move and inertia becomes negligible: as soon as the force ceases, the swimmer comes to rest instantaneously.

[3] For example, a system of axially symmetric particles might be accurately described by just their density and polarization distribution.

[4] Hydrodynamics require a three-dimensional treatment because two-dimensional hydrodynamics are fundamentally different from the 3D case. In 3D the Green's function (Oseen tensor) scales with r^{-1}, whereas in 2D it scales with $\ln r$.

A less obvious consequence of dominant viscous forces is that the notion of time duration is lost. In fact, the self-propulsion dynamics becomes time-independent: whether, for example, a flagellum beats fast or slowly does not matter. Hence, a directed propulsion is only possible for a beating motion (or mechanical deformation) that breaks time-reversal symmetry. Otherwise, a swimmer would end up where it started after it completes a swimming cycle. This insight is attributed to Edward Mills Purcel and is today known as the scallop theorem [60]. Summarizing this paragraph, it states:

> In order to archive self-propulsion at low Reynolds number in a Newtonian fluid, a swimmer's motion must not be invariant under time-reversal.

Therefore, microbes have developed a multitude of propulsion mechanisms that are not reciprocal. For example, *E. coli* rotate a bundle of flagella in spiral configuration [9], and Clamydomonas has two flexible flagella which beat differently for the fore and back motion [9]. On the other hand, artificial swimmers, like Janus particles, circumvent the Scallop theorem by making use of chemical reactions on their asymmetrically functionalized surface. They generate a local gradient field that imposes a flow along their surface and thus self-propel [14, 48, 49].

To quantify the importance of inertia in a fluid or for immersed microswimmers, the Reynolds number is commonly used. It relates the inertial forces to the viscous forces and is defined as

$$\mathrm{Re} = \frac{\text{inertial force}}{\text{viscous force}} = \frac{\rho u L}{\eta},$$

in which ρ is the density of the fluid or the microswimmer, u is the typical velocity of the fluid flowing around the immersed body, L is a characteristic length scale of the swimmer, and η the dynamic viscosity of the fluid.

For example, a fish swimming in water, from a Goby to a Sailfish, has a Reynolds number in the approximate range of 10^3 and 10^7 [61]. In this regime, inertia dominates and the dynamics persists long after the driving force has ceased. However, imagine the same fish swimming in a substance like honey instead of water. The Reynolds number will be in the order of 10^{-5} or smaller. In this regime, every movement is nearly instantaneously stopped once the drive stops. A swimming microbe finds itself in such a situation. Because of its tiny mass and dimensions, the Reynold's number of a microbe swimming in water is of the range of 10^{-5} to 10^{-3}. Being in a low Reynolds number regime leads to overdamped dynamics, which as will be discussed in Section 2.1. In this regime, the microswimmer has to constantly invest energy to maintain its speed, as described in Section 2.2. This motion of the microswimmer simultaneously exerts stresses on the fluid in which it is immersed, resulting in a

flow that influences the motion of other swimmers. The minimal model of swimming used in this work and the consequences for the flow are described in Section 2.8.

The following chapter provides the theoretical background to develop and discuss a kinetic theory of an active, magnetic suspension of microswimmers.

2 Theoretical background

The aim of this chapter is to provide the theoretical background needed to model and understand the collective dynamics of interacting microswimmers under the influence of external magnetic fields. In theory, the system could be described on a very detailed level. For instance, the solvent could be treated explicitly on the particle level or the self-propulsion mechanism could involve the modelling of individual flagella for a biological swimmer. However, in practice, such a detail-oriented approach is often analytically intractable and numerically complex. Luckily, on a meso- and macroscopic scale, microscopic degrees of freedom often average out and produce stable and well-defined mean values that can be used to describe the system.

Typical self-propelled colloids extend microns in size. For example, water molecules are approximately 10^4 to 10^5 times smaller than the immersed particles. This scale separation allows to approximate the fluid by a continuous field instead of distinct and discrete particles. By making use of symmetries and invariants of the system, the fluid field dynamics can be described by a system of conservation equation called the Navier-Stokes equations.

Additionally, there exists a time scale separation between the movement of the colloids and the momentum transfer in a fluid. Perturbations in the fluid travel much faster than the colloids translate. Therefore, in good approximation, the fluid reacts nearly instantaneously to a particle's movement. Moreover, as briefly discussed in the introduction, viscous forces dominate inertial forces at these scales [62]. In combination, this leads to a quasi-static description of the fluid formulated in the time-independent Stokes equation. However, thermal fluctuations in the fluid and their impact on immersed particles are not captured by a continuous field approach. Numerous collisions between the fluid molecules and the colloid give rise to a jittering motion of the colloid, the so-called Brownian motion. On a mesoscopic level the deterministic tracking of all those collisions is of no direct interest and therefore is modelled by a stochastic process instead. Deterministic equations of motion are replaced by a stochastic differential equation called the Langevin's equation with a stochastic force and torque modelling the collisions with the fluid molecules.

Integration of the stochastic Langevin equations leads to just one possible realization of the stochastic process. An equivalent approach is to describe the dynamics of the

whole ensemble, a set of all possible realizations, by means of the time evolution of a probability density function (PDF). This leads to Fokker-Planck equations — sometimes also referred to as Smoluchowski equations in the case of overdamped dynamics relevant for dynamics of colloidal suspensions. A Fokker-Planck equation describes the time evolution of a statistical ensemble under the assumption of Gaussian Brownian noise and Markovian (no memory) dynamics. Given the PDF of the ensemble, expectation values of various quantities can be determined.

When describing the dynamics of multiple (overdamped) colloids the PDF and therefore the Smoluchowski equation generally depends on the configuration (position and orientation) of all particles. However, in this work, the main focus is to study the *collective* dynamics emerging from the individual dynamics of interacting particles. For long- and mid-ranged interactions, a particle will interact with many other particles at any given time. Therefore, it is often justified to approximate the combined effect on a particle by a mean-field averaging over the other particle's degrees of freedom.

In summary, in this chapter, a probabilistic model for dynamics of active colloids is developed, where the inter-particle interactions are incorporated in the mean-field approximation. In particular, hydrodynamic and magnetic interactions are studied. At the end of the chapter, a powerful tool to analyse the dynamics near a steady state of the system is briefly introduced: the linear stability analysis.

The chapter is organized as follows: First, Brownian particles are discussed and how their dynamics is represented by a stochastic differential equation called the Langevin equation. The statistical ensemble of the particles can be equivalently described by a probability density function (PDF) that evolves according to a Fokker-Planck equation, or in the case of overdamped dynamics by a Smoluchowski equation. Then, inter-particle interactions are introduced and a mean-field approach is developed to incorporate both magnetic and hydrodynamic interactions into the model. Magnetic dipole-dipole interactions are derived from Maxwell's equations. The hydrodynamic interactions are a result of perturbations in the solvent caused by the self-propulsion of the particles. The self-propulsion and its interaction with the solvent is modelled in a force-dipole approximation used in the Stokes equation describing the solvent.

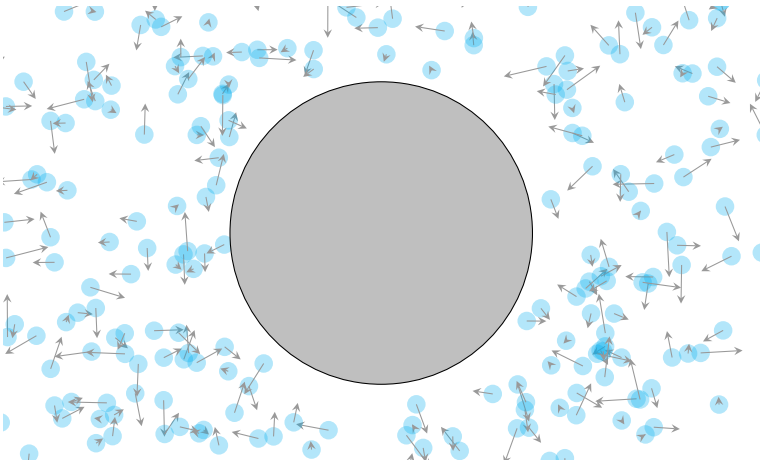

Fig. 2.1.: A cartoon of a Brownian particle in a solvent (not at real scale). Numerous solvent particles constantly collide with the colloid, transferring momentum.

2.1 Brownian motion & Langevin equation

A fluid consists of countless molecules that are in constant motion. A suspended colloid therefore collides incessantly with numerous fluid particles at any given moment, exchanging momentum with the fluid. This is illustrated in Figure 2.1. For a small but massive colloid the dominant effect is friction: An initial momentum of the colloid is transferred gradually to the fluid until nearly all its kinetic energy is thermalized. If the fluid is in thermal equilibrium and assuming a small Reynolds number, friction can be formulated by Stokes' Law[1],

$$m\ddot{\mathbf{x}} = \mathbf{F} - \xi_{\mathrm{t}}\dot{\mathbf{x}}, \tag{2.1}$$

with the velocity $\dot{\mathbf{x}}$, the acceleration $\ddot{\mathbf{x}}$, the mass m of a colloid, and the frictional force $\mathbf{F}_{\mathrm{fric}} = -\xi_{\mathrm{t}}\dot{\mathbf{x}}$. The force $\mathbf{F}$ on the colloid, also referred to as the drift force, can be considered to be zero for the following discussion. According to Stokes' law, the translational friction coefficient is given by $\xi_{\mathrm{t}} = 6\pi\eta R$, with the radius of the particle R, and the dynamic viscosity of the fluid η. Given an initial value problem of a particle with an initial velocity $\dot{\mathbf{x}}(0) = \mathbf{v}_0$, the equation of motion (2.1) (with a vanishing external force, $\mathbf{F} = 0$) has the solution

$$\dot{\mathbf{x}}(t) = \mathbf{v}_0\, e^{-\frac{t}{\tau}}. \tag{2.2}$$

[1]The assumption of a quiescent fluid in the derivation of the friction coefficient has been criticized (for example [63]), because the time scales $\tau = m/\xi$ on which the frictional dynamics occur are comparable to the time scales perturbations travel in the fluid $\propto \rho L^2/\eta$ for particles with densities comparable to the fluid [64, 65]. A more precise derivation of the unsteady translation of spheres can be found in [64].

Thus, an initial velocity decays exponentially to zero with a relaxation time of $\tau = m/\xi_\mathrm{t}$.

2.1.1 Langevin equation

In the case that the colloid has a small mass m, collisions with the fluid particles have a more immediate effect and result in a visible fluctuating velocity of the colloid: The Brownian motion. A deterministic description of the colloid's dynamics would have to include the fluid particles explicitly. However, if the dynamics at time scales larger than the inter-collision time are of interest, a deterministic description is not necessary. Instead, it can be approximated by a stochastic process retaining the same properties on average. To this end, equation (2.1) is modified to include an additional stochastic force term representing thermal fluctuations,

$$m\ddot{\mathbf{x}} = \mathbf{F} - \xi_\mathrm{t}\dot{\mathbf{x}} + g\mathbf{\Gamma}, \tag{2.3}$$

with some coefficient g determining the strength of the (thermal) noise. Equation (2.3) is called the Langevin equation with a stochastic Langevin force $\mathbf{\Gamma}$ with zero mean, $\langle \mathbf{\Gamma}(t) \rangle = 0, \forall t \in \mathbb{R}$. The Langevin force is a stochastic process parametrized by time. Furthermore, it is assumed that the collisions happen independently of one another. Thus, the Langevin force is temporally uncorrelated, $\langle \Gamma_i(t)\Gamma_j(t') \rangle = \delta_{ij}\delta(t-t')$. From the central limit theorem and the high collision rate it follows that $\mathbf{\Gamma}(t)$ is normally distributed for every t [66]. A complete uncorrelated noise is also referred to as white noise. Its power spectrum does not depend on the frequency[2], which indicates an idealized »memoryless« process [68].

The velocity auto-correlation resulting from equation (2.3) is given by[3]

$$\langle \dot{x}_i(t_1)\dot{x}_j(t_2) \rangle = v(0)^2\, e^{-\frac{\xi_\mathrm{t}}{m}(t_1+t_2)} + \frac{g^2}{2\xi_\mathrm{t} m}\left(e^{-\frac{\xi_\mathrm{t}}{m}|t_1-t_2|} - e^{-\frac{\xi_\mathrm{t}}{m}(t_1+t_2)} \right).$$

For long times t_1 and t_2, i.e. $t_{1,2} \gg \frac{m}{\xi_\mathrm{t}}$, the velocity auto-correlation is approximately given by

$$\langle \dot{x}_i(t_1)\dot{x}_j(t_2) \rangle \approx \frac{g^2}{2\xi_\mathrm{t} m}\delta_{i,j}\, e^{-\frac{\xi_\mathrm{t}}{m}|t_1-t_2|}. \tag{2.4}$$

[2] This can be seen with the help of the Wiener-Khintchine theorem, which states that the power spectrum is the Fourier transform of the correlation function of a stochastic process [67, 68].

[3] For a derivation, see Ref. [67].

It follows that the translational diffusion in terms of the mean-square displacement is given by

$$\begin{aligned}\left\langle \left(\mathbf{x}(t)-\mathbf{x}(0)\right)^2 \right\rangle &= \sum_{i=1}^{3} \int_0^t \mathrm{d}t_1 \int_0^t \mathrm{d}t_2 \, \langle \dot{x}_i(t_1)\dot{x}_i(t_2)\rangle \\ &= 3\frac{g^2 m}{\xi_\mathrm{t}^3}\left(\frac{\xi_\mathrm{t}}{m}t - 1 + e^{-\frac{\xi_\mathrm{t}}{m}t}\right),\end{aligned}$$

where equation (2.4) was used. In the long-time limit ($\frac{\xi_\mathrm{t}}{m}t \gg 1$), the leading term is given by

$$\left\langle \left(\mathbf{x}(t)-\mathbf{x}(0)\right)^2 \right\rangle \approx 3\frac{g^2 m}{\xi_\mathrm{t}^3}\left(\frac{\xi_\mathrm{t}}{m}t\right) = \frac{3g^2}{\xi_\mathrm{t}^2}t \equiv 6D_\mathrm{t}^\mathrm{eq}\, t, \tag{2.5}$$

defining the equilibrium translational diffusion coefficient D_t^eq. Therefore, the coefficient g can be expressed by $g = \xi_\mathrm{t}\sqrt{2D_\mathrm{t}^\mathrm{eq}}$.

In addition, with the help of the equipartition theorem, a relation between the diffusion coefficient and the temperature can be derived. In the stationary state, the average kinetic energy is given by

$$\langle E\rangle = \frac{1}{2}m\sum_{i=1}^{3}\left\langle \dot{x}_i^2 \right\rangle = \frac{3}{4\xi_\mathrm{t}}g^2 = \frac{3}{2}k_B T,$$

with the temperature T and the Boltzmann-constant k_B. The last equation is derived from the equipartition theorem of a system in thermal equilibrium that assigns an energy of $\frac{1}{2}k_B T$ to every degree of freedom. In three dimensions, the energy in the translational degrees of freedom adds up to $\langle E\rangle = \frac{3}{2}k_B T$. Hence, the coefficient g can be expressed by the temperature of the system, $g^2 = 2\xi_\mathrm{t}k_B T$. Using equation (2.5) the equilibrium diffusion coefficient is given by $D_\mathrm{t}^\mathrm{eq} = k_B T/\xi_\mathrm{t}$, which is known as the Einstein(-Smoluchowski) relation. This is a special case of the fluctuation-dissipation theorem.

An analogous chain of arguments can be made for rotational diffusion [69, 70]. Here, the stochastic Langevin force is replaced by a Langevin torque $\mathbf{\Lambda}$, so that for the angular velocity $\boldsymbol{\omega}$ of a colloid the Langevin equation reads

$$\mathbb{I}\,\dot{\boldsymbol{\omega}} = \mathbf{M} - \xi_\mathrm{r}\boldsymbol{\omega} + \xi_\mathrm{r}\sqrt{2D_\mathrm{r}^\mathrm{eq}}\mathbf{\Lambda}, \tag{2.6}$$

with the inertia tensor $\mathbb{I}$, the rotational friction coefficient $\xi_\mathrm{r} = 8\pi\eta R^3$, a torque $\mathbf{M}$ on the colloid, and the rotational diffusion coefficient $D_\mathrm{r}^\mathrm{eq} = k_B T/\xi_\mathrm{r}$.

Translational diffusion corresponds to a random walk in (flat) space, whereas rotational diffusion can be represented as a random walk of a unit orientation vector $\mathbf{n}$

Fig. 2.2.: Example of a random walk on the surface of the unit sphere, representing rotational diffusion. The plotted line traces the tip of the orientation vector $\mathbf{n}$ of a particle.

on the (curved) surface of the unit sphere. An example of such a random walk is shown in Figure 2.2.

For active colloidal systems (microswimmers) the assumption of thermal equilibrium is invalid as energy is constantly transferred into the system. However, the general ideas remain true for the systems studied in this work. For active systems, here the diffusion coefficients are replaced by effective coefficients and in simulations their values are approximated by those of the equilibrium.

2.1.2 Overdamped limit

In the case that viscous forces on a colloid dominate its inertial forces, the relaxation time τ in equation (2.2) becomes very small. An initially given kinetic energy is quickly dissipated and an unforced particle comes to rest immediately. Therefore, this scenario is also called the »overdamped limit«. As discussed in the introduction in Chapter 1, microscopic colloids often fall into the realm of this scenario.

In the overdamped limit, equations (2.3) and (2.6) reduce to a balance of forces and can be written as

$$\dot{\mathbf{x}} = \frac{1}{\xi_\mathrm{t}}\mathbf{F} + \sqrt{2D_\mathrm{t}}\boldsymbol{\Gamma} \tag{2.7}$$

$$\boldsymbol{\omega} = \frac{1}{\xi_\mathrm{r}}\mathbf{M} + \sqrt{2D_\mathrm{r}}\boldsymbol{\Lambda}. \tag{2.8}$$

The Langevin equation for a normalized orientation vector $\mathbf{n}$, with $\mathbf{n}^2 = 1$, is given by the relation $\dot{\mathbf{n}} = \boldsymbol{\omega} \times \mathbf{n}$ and results in the Langevin equation for the orientation,

$$\dot{\mathbf{n}} = \frac{1}{\xi_\mathrm{r}} \mathbf{M} \times \mathbf{n} + \sqrt{2D_\mathrm{r}} \boldsymbol{\Lambda} \times \mathbf{n}. \tag{2.9}$$

The force $\mathbf{F}$ and torque $\mathbf{M}$ on a colloid can have multiple origins. For self-propelled particles, a part of the force $\mathbf{F}$ is the self-propulsion force $\mathbf{F}_\mathrm{sp}$, as described in the following section.

2.2 Self-propelled particles

An active particle is defined by its ability to transform ambient energy into directed motion. The energy is often supplied in the form of chemical energy. It is either metabolized by microorganisms and drives body deformations or the energy is released by catalytic reactions on the surface of asymmetric, artificial swimmers (diffusiophoresis). Popular artificial swimmers are Janus particles that are coated with two different materials at each semi-sphere [71]. Laser light, creating a thermal gradient across the swimmer (self-thermophoresis), can be another possible energy source [72]. In any case, energy is pumped into the system and drives it far from equilibrium.

Many publications study these different propulsion mechanisms in detail. For a review see Ref. [9, 14]. In this work, the focus are not the intricate details of the propulsion mechanism and the self-propulsion is rather incorporated phenomenologically into the model by adding a self-propulsion velocity $\mathbf{F}_\mathrm{sp}/\xi_\mathrm{t} = \mathbf{v}_\mathrm{sp} = U_0 \mathbf{n}$ along the orientation vector $\mathbf{n}$ to the Langevin equation (2.8):

$$\dot{\mathbf{x}} = U_0 \mathbf{n} + \frac{1}{\xi_\mathrm{t}} \mathbf{F} + \sqrt{2D_\mathrm{t}} \boldsymbol{\Gamma}. \tag{2.10}$$

As discussed in the introduction in Chapter 1, microswimmers in water have a Reynolds number in the range of 10^{-5} to 10^{-4} leading to relaxation times smaller than $100\,\mathrm{ns}$ in which the microswimmer hardly moves at all compared to its body length. Therefore, it remains justified to completely ignore inertial terms in the Langevin equation (2.10) and to use the overdamped limit as above.

Some organic microswimmers additionally change their orientation actively. In many cases, the result is a *run and tumble* motion [69]. The running phase is a (mostly) straight swimming phase due to self-propulsion, as discussed above. It is

interrupted by a short tumbling phase where the microswimmer randomly reorients itself. The tumbling rate $1/t_{\text{tumble}}$ however can depend on the local environment, for example, giving certain microswimmer the ability to follow a chemical gradient on average[73]. In the case that the tumbling rate is constant, the effective long time translation of a run and tumble-microswimmer can be modelled by an effective rotational diffusion $D_{\text{r}}^{\text{tumble}} \propto 1/t_{\text{tumble}}$, leading to an effective rotational diffusion coefficient $D_{\text{r}}^{\text{eff}} = D_{\text{r}}^{\text{Brown}} + D_{\text{r}}^{\text{tumble}}$.

In the Langevin equation for the time evolution of orientation $\mathbf{n}$, the rotational diffusion parameter would be adapted accordingly,

$$\dot{\mathbf{n}} = \frac{1}{\xi_{\text{r}}}\mathbf{M} \times \mathbf{n} + \sqrt{2D_{\text{r}}^{\text{eff}}}\boldsymbol{\Lambda} \times \mathbf{n}. \tag{2.11}$$

The self-propelled particles described phenomenologically by equations (2.10) and (2.11) is known as the active Brownian particle model. In the following, the rotational diffusion coefficient is simply denoted by D_{r} that may include an effective tumbling behaviour in addition to the Brownian rotation.

The addition of self-propulsion changes the dynamics of the system drastically. Together with rotational diffusion the result of the modified Langevin equation (2.10) for an active Brownian particle is a persistent random walk with a persistence length given by $l = U_0 D_{\text{r}}$. The Brownian motion of a self-propelled particle has been studied extensively by Ref. [74].

In general, the self-propulsion velocity of a particle can depend on its environment (for example on a chemical gradient [75]). However, here we assume a constant self-propulsion speed U_0.

Equations (2.7) and (2.8) describe a stochastic process that encompasses many possible concrete trajectories/realizations. Stochastic differential equations are challenging to approach analytically. An alternative, equivalent approach of the stochastic process is the description of the whole statistical ensemble by means of a probability distribution function (PDF). The time evolution of the PDF is given by a Fokker-Planck equation or in the case of overdamped dynamics by a Smoluchowski equation. The description in form of a PDF has the advantage of being easier to manipulate and explore with common tools of mathematical analysis.

2.3 Smoluchowski equation

A Smoluchowski equation for a probability density function (PDF) $\Psi(y_1, \ldots, y_M, t)$ in M variables, $y_i, i = 1, \ldots, M$, is a time-dependent probability conservation equation of the form

$$\begin{aligned} & \partial_t \Psi = -\nabla \cdot \left[\mathbf{D}^{\text{drift}} \Psi - \nabla \cdot \mathbf{D}^{\text{diff}} \Psi \right] \\ \Leftrightarrow \qquad & \partial_t \Psi = \left[-\sum_{i=1}^{M} \partial_{y_i} D_i^{\text{drift}} \Psi + \sum_{i,j=1}^{M} \partial_{y_i} \partial_{y_j} D_{ij}^{\text{diff}} \Psi \right], \end{aligned} \tag{2.12}$$

with the drift and diffusion coefficients $D_i^{\text{drift}}(y_1, \ldots, y_N, t)$, also called flux velocities or drift velocities, and $D_{ij}^{\text{diff}}(y_1, \ldots, y_N, t)$. The PDF $\Psi(y_1, \ldots, y_N, t)$ encodes the probability for the system being in the state given by y_i at a time t. Equation (2.12) states that the change of the probability density in a volume is given by the flux $\left[\mathbf{D}^{\text{drift}} \Psi - \nabla \cdot \mathbf{D}^{\text{diff}} \Psi \right]$ from and into the volume and the total probability is therefore conserved.

Generally, the diffusion coefficient can be a matrix $D_{ij}^{\text{diff}}(y_1, \ldots, y_N, t)$ that can formalize interactions between particles labelled with i and j [70]. However, for this work, in the mean-field approximation as discussed in the following, it is sufficient to assume the diffusion parameter to be a scalar function — possibly depending on the variables y_i, i.e. $D_{ij}^{\text{diff}} = D^{\text{diff}}(y_1, \ldots, y_N, t)$.

In the case of Brownian particles in the overdamped limit, the dependent variables are given by the positions $\mathbf{x}_i$ and orientations $\mathbf{n}_i$ of a particle labelled with i and the Smoluchowski equation is referred to as the Smoluchowski equation. Hence, the PDF $\Psi(\{\mathbf{x}\}, \{\mathbf{n}\}, t)$ gives the probability density for N particles being at the positions $\{\mathbf{x}\} \equiv (\mathbf{x}_1, \ldots, \mathbf{x}_N)$ with orientations $\{\mathbf{n}\} \equiv (\mathbf{n}_1, \ldots, \mathbf{n}_N)$ at a time t.

As stated in the previous section, given a Langevin equation, a corresponding Smoluchowski equation can be found. For the sake of simplicity, the procedure is presented for the one-dimensional case. However, it readily generalizes for higher dimensions. Let a one-dimensional overdamped Langevin-equation be given by

$$\dot{x}(t) = h(x, t) + g(x, t)\Gamma(t), \tag{2.13}$$

with a drift h and a noise strength g. Before a link between the coefficients of the Langevin and Smoluchowski equation can be established, a brief discussion about stochastic differential equations is necessary (also see the Ref. [68, 76–78]).

The general solution of the stochastic Langevin-equation (2.13) is given by the expression

$$x(t) - x(0) = \int_0^t \mathrm{d}t'\; h\left(x(t'), t'\right) + \int_0^t \mathrm{d}W(t')\; g\left(x(t'), t'\right), \tag{2.14}$$

with the Wiener process[4] $W(t)$ corresponding to the stochastic force $\Gamma(t)$ [67, 68][5]. Because a stochastic process can be quite erratic and not well-behaved (for example, a Wiener process has almost never a derivative), the second integral is not inherently well-defined. Rather, an axiomatic approach in defining the integral has to be taken. A first approach to define an integral of the form $\int_a^b \mathrm{d}W(t)\, f(W(t), t)$, for a function f and a stochastic (Wiener) processes W, is based on the Riemann-Stieltjes integral

$$\int_a^b \mathrm{d}W(t)\, f\left(W(t), t\right) \equiv \lim_{n\to\infty} \sum_{k=0}^{n} f\left(W(t_k^*), t_k^*\right) \left[W(t_{k+1}) - W(t_k)\right], \tag{2.15}$$

for intervals $[t_k, t_{k+1})$ of a time partition indexed with $k \in \mathbb{N}$, with $t_0 < t_1 < \cdots < t_n$, and a value $t_k \leq t_k^* \leq t_{k+1}$ inside an interval. If the limit exists, the value of the integral generally depends on the choice of the sampling point t_k^*. There are two commonly used conventions, the Itô and the Stratonovich interpretation of the integral [67, 79, 80].

In the Itô interpretation, the sampling point is taken to be the left-most value of the interval, i.e. $t_k^* = t_k$. This interpretation is also called non-anticipative, because the function f is only evaluated for the current time t_k in an interval (before a collision with the solvent's molecules in the case of Brownian motion). In the Stratonovich interpretation, the midpoint of the interval is used, so that $t_k^* = \frac{t_{k+1}+t_k}{2}$. As a consequence, in the evaluation of the integrand the future time t_{k+1} is used (before and after a collision). Therefore, this scheme is called anticipative.

Bearing this in mind, the coefficients of the one-dimensional Smoluchowski equation,

$$\partial_t \Psi(x,t) = -\partial_x D^{\text{drift}}(x,t)\Psi(x,t) + \partial_x^2 D^{\text{diff}}(x,t)\Psi(x,t),$$

corresponding to the Langevin-equation (2.13), can be derived [67]. The diffusion coefficient is given by

$$D^{\text{diff}}(x,t) = \frac{1}{2} g^2(x,t). \tag{2.16}$$

[4] A Wiener process is a special continuous stochastic process, with independent, standard normally distributed increments giving a precise mathematical description of a Brownian process.

[5] In non-strict sense, the stochastic force relates to the Wiener process by differentiating, $\partial_t W(t) = \Gamma(t)$. However, strictly speaking these equations is meaningless without a proper definition, because the derivative of a Wiener process almost never exists. A more suitable relation is given by $W(t) = \int_0^t \mathrm{d}t' \Gamma(t')$ [68].

In case the function g depends on the variable x, the value of the drift coefficient D^{drift} depends on the interpretation of stochastic integrals. In the Itô interpretation the drift coefficient is given by

$$D^{\text{drift}}_{\text{Itô}}(x,t) = h(x,t), \tag{2.17}$$

whereas in the Stratonovich interpretation it is given by

$$D^{\text{drift}}_{\text{Strat}}(x,t) = h(x,t) + \frac{1}{2} g(x,t)\partial_x g(x,t). \tag{2.18}$$

In the latter, the drift coefficient $D^{\text{drift}}_{\text{Strat}}$ includes a spurious drift $\frac{1}{2}g(x,t)\partial_x g(x,t)$ that is also expected to be observed in a realistic experiment of Brownian particles. Physically, it can be derived by assuming finite collision times and finite accelerations of the particles [67, 68]. Therefore, physicists often rely on the Stratonovich interpretation. However, in certain cases, as can be seen in Section 5.2, the Itô interpretation remains relevant. If the noise strength g does not depend on the particle's position or orientation, both interpretations yield the same result in any case.

In the Smoluchowski equation, the stochastic force Γ in the Langevin equation is replaced by a diffusion of the probability density, »penalizing« curvature in the PDF and smoothing it out. This corresponds to an information loss[6]. Perfect information is given by $\Psi(\mathbf{x}) = \delta(\mathbf{x} - \mathbf{y})$ for a particle that can be certainly found at position $\mathbf{y}$. However, due to the (quasi) random nature of the Brownian motion, the position of the particle becomes less and less certain over time. Therefore, the initially sharp peak in the PDF becomes a spread out distribution with a growing variance. In case of a purely Brownian particle, the distribution is Gaussian. The effect and the correspondence of the Langevin and Smoluchowski equation is illustrated in Figure 2.3 for one particle.

2.3.1 Smoluchowski equation

The time evolution of the probability density function $\Psi(\{\mathbf{x}\}, \{\mathbf{n}\}, t)$ describing a system of N interchangeable particles with positions $\mathbf{x}_j$ and orientation vectors $\mathbf{n}_j$,

[6] In case of a discrete probability measure this loss of information is quantifiable by the Shannon entropy, $S = -\sum_i P_i \log P_i$. It is zero for a certain state and increasingly negative with rising uncertainty about the state. Unfortunately, the extension to the continuous case is not trivial [81, 82].

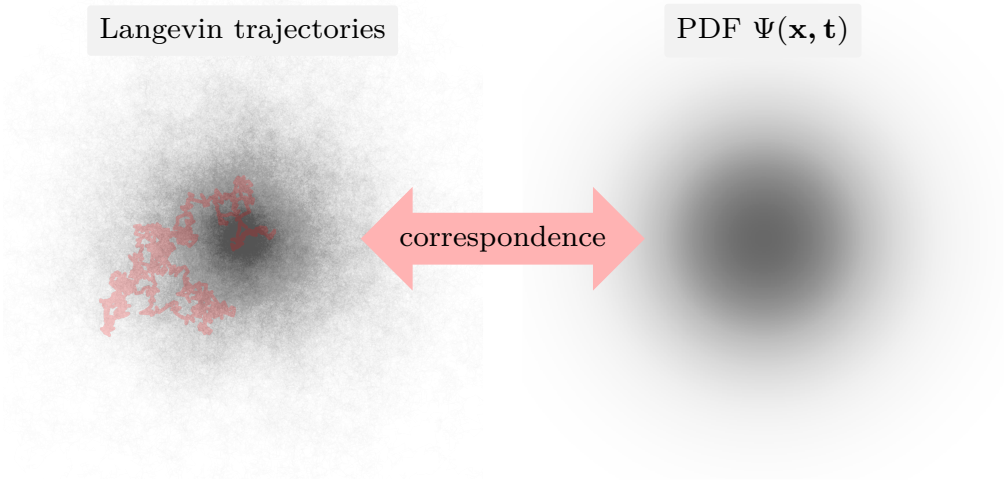

Fig. 2.3.: Illustration of the correspondence of stochastic Langevin equation and the description via probability density function (PDF) using the Smoluchowski equation. On the left, multiple realizations of the path of one Brownian particle starting from one initial position is plotted. One arbitrary possible path is highlighted in red. On the right, a visualization of the corresponding PDF is shown.

each obeying the Langevin equations (2.7) and (2.8), is expressed by a Smoluchowski equation of the form

$$\partial_t \Psi = -\left[\sum_{j=1}^{N} \nabla_j \cdot \mathbf{v}_\mathrm{t}^j + \sum_{j=1}^{N} \nabla_{\mathbf{n}_j}^\circ \cdot \mathbf{v}_\mathrm{r}^j + \sum_{j=1}^{N} \Delta_j D_\mathrm{t} + \sum_{j=1}^{N} \Delta_{\mathbf{n}_j}^\circ D_\mathrm{r}\right] \Psi, \tag{2.19}$$

called the Smoluchowski equation, with the Dirichlet and Neumann boundary conditions for the positions $\{\mathbf{x}\}$, given by

$$\lim_{\|\mathbf{x}_j\| \to \infty} \Psi(\{\mathbf{x}\}, \{\mathbf{n}\}, t) = 0, \quad \forall j \in \{1, \ldots, N\} \tag{2.20}$$

$$\lim_{\|\mathbf{x}_j\| \to \infty} \nabla\Psi(\{\mathbf{x}\}, \{\mathbf{n}\}, t) = 0, \quad \forall j \in \{1, \ldots, N\}, \tag{2.21}$$

and periodic boundary conditions for the orientations $\{\mathbf{n}\}$. The boundary conditions can be justified by assuming a finite information transport speed so that the PDF has finite support. Compared to equation (2.12), the drift coefficients have been split up into translational and rotational flux velocities of the jth particle, $\mathbf{v}_\mathrm{t}^j$ and $\mathbf{v}_\mathrm{r}^j$, and the diffusion coefficients are given by the translational and rotational diffusion coefficients, D_t and D_r. The spatial nabla operator $\nabla_j = \nabla_{\mathbf{x}_j}$ acts on the jth particle's position and the Laplace operator is defined by $\Delta_j = \nabla_j \cdot \nabla_j$. The nabla operator on the surface of a unit sphere is defined by the orthogonal projection of the gradient operator in $\mathbf{n}$, $\nabla_\mathbf{n}^\circ = (\mathbb{1} - \mathbf{nn}) \cdot \nabla_\mathbf{n}$, with the dyadic product of two

vectors $\mathbf{ab} = \mathbf{a} \otimes \mathbf{b}, (\mathbf{ab})_{ij} = a_i b_j$. The Laplace operator on the unit sphere is given by $\Delta^\circ_{\mathbf{n}} \equiv \nabla^\circ_{\mathbf{n}} \cdot \nabla^\circ_{\mathbf{n}}$. All derivatives in equation (2.19) also act on Ψ. In the equations above and in the following, the shorthand $\{\mathbf{x}\} \equiv (\mathbf{x}_1, \ldots, \mathbf{x}_N)$ stands for all spatial variables — $\{\mathbf{n}\}$ analogously — so that

$$\Psi(\{\mathbf{x}\}, \{\mathbf{n}\}, t) \equiv \Psi_N(\mathbf{x}_1, \ldots, \mathbf{x}_N, \mathbf{n}_1, \ldots, \mathbf{n}_N, t).$$

The translational and rotational flux velocities relate to the overdamped Langevin equations (2.7) and (2.8) by

$$\begin{aligned}
\mathbf{v}_{\mathrm{t}}^j(\{\mathbf{x}\}, \{\mathbf{n}\}, t) &= \frac{1}{\xi_{\mathrm{t}}} \mathbf{F}_j(\{\mathbf{x}\}, \{\mathbf{n}\}, t) \\
\mathbf{v}_{\mathrm{r}}^j(\{\mathbf{x}\}, \{\mathbf{n}\}, t) &= \frac{1}{\xi_{\mathrm{r}}} \mathbf{M}_j(\{\mathbf{x}\}, \{\mathbf{n}\}, t) \times \mathbf{n}_j.
\end{aligned}$$

In the case that the diffusion coefficients D_{t} and D_{r} depend on the position or orientation, in the Stratonovich interpretation the spurious drift term has to be added according to equation (2.18).

The PDF Ψ is normalized as

$$\left(\prod_{i=1}^{N} \int \mathrm{d}\mathbf{x}_i \mathrm{d}\mathbf{n}_i \right) \Psi(\{\mathbf{x}\}, \{\mathbf{n}\}, t) = 1, \tag{2.22}$$

with the integral over all possible configurations of particles

$$\left(\prod_{i=1}^{N} \int \mathrm{d}\mathbf{x}_i \mathrm{d}\mathbf{n}_i \right) \bullet = \int_{(\mathbb{R}^3)^N} \mathrm{d}\mathbf{x}_1 \ldots \mathrm{d}\mathbf{x}_N \int_{(\mathbb{S}^2)^N} \mathrm{d}\mathbf{n}_1 \ldots \mathrm{d}\mathbf{n}_N \bullet .$$

For the sake of notational brevity, in the following all integrals are considered to be taken over the whole configuration space if not specified otherwise, so that $\int \mathrm{d}\mathbf{x} \equiv \int_{\mathbb{R}^3} \mathrm{d}\mathbf{x}$ and $\int \mathrm{d}\mathbf{n} \equiv \int_{\mathbb{S}^2} \mathrm{d}\mathbf{n}$. The set $\mathbb{S}^2$ denotes the surface of a unit sphere in three dimensions.

The PDF Ψ encodes the probability to find the particles in a particular configuration at a given time and contains the same information as given by the corresponding Langevin equations, including all correlations and dependencies between the particles. In case not all of that information is needed, a partial probability density can be calculated by integrating over the auxiliary degrees of freedom.

2.3.2 Partial distribution functions

The partial distribution function of $s < N$ particles with coordinates of position $\mathbf{x}_{i\leq s}$ and orientation $\mathbf{n}_{i\leq s}$ can be obtained by integrating over the remaining degrees of freedom of the particles with index $s < i < N$,

$$\Psi_s(\{\mathbf{x}_{i\leq s}\},\{\mathbf{n}_{i\leq s}\},t) = \frac{N!}{(N-s)!}\left(\prod_{i=s+1}^{N}\int \mathrm{d}\mathbf{x}_i\mathrm{d}\mathbf{n}_i\right)\ \Psi(\mathbf{x}_1,\ldots,\mathbf{x}_N,\mathbf{n}_1,\ldots,\mathbf{n}_N,t). \tag{2.23}$$

The shorthand $\{\mathbf{x}_{i\leq s}\} = (\mathbf{x}_1,\ldots,\mathbf{x}_s)$ denotes all variables with index smaller or equal to s. Under the assumption that the particles are interchangeable, the probability density distribution has exchange symmetry

$$\Psi_N(\ldots,\mathbf{y}_i,\ldots,\mathbf{y}_j,\ldots) = \Psi_N(\ldots,\mathbf{y}_j,\ldots,\mathbf{y}_i,\ldots) \quad \forall i,j < N, \mathbf{y}\in\{\mathbf{x},\mathbf{n}\}. \tag{2.24}$$

The combinatorial factor $\frac{N!}{(N-s)!}$ takes the interchangeability of identical particles into account and is equal to the number of ways of choosing an ordered subset of size s. To obtain a probability density function from the distribution Ψ_s, it has to be normalized by dividing by the combinatorial factor above.

In particular the single- and pair-distribution functions Ψ_1 and Ψ_2 are given by

$$\Psi_1(\mathbf{x}_1,\mathbf{n}_1,t) = N\left(\prod_{i=2}^{N}\int \mathrm{d}\mathbf{x}_i\mathrm{d}\mathbf{n}_i\right)\ \Psi(\{\mathbf{x}\},\{\mathbf{n}\},t) \tag{2.25}$$

$$= \frac{1}{N-1}\int \mathrm{d}\mathbf{x}_2\mathrm{d}\mathbf{n}_2\ \Psi_2(\mathbf{x}_1,\mathbf{n}_1,\mathbf{x}_2,\mathbf{n}_2,t) \tag{2.26}$$

$$\Psi_2(\mathbf{x}_1,\mathbf{x}_2,\mathbf{n}_1,\mathbf{n}_2,t) = N(N-1)\left(\prod_{i=3}^{N}\int \mathrm{d}\mathbf{x}_i\mathrm{d}\mathbf{n}_i\right)\ \Psi(\{\mathbf{x}\},\{\mathbf{n}\},t), \tag{2.27}$$

where the indices are interchangeable.

The partial distribution functions are especially useful in the calculations of mean values. As an example, the mean particle density of particles at positions $\mathbf{y}_j$ is given by the expectation value

$$\begin{aligned}\rho(\mathbf{x},t) &= \left\langle \sum_{j=1}^{N}\delta(\mathbf{x}-\mathbf{y}_j)\right\rangle \\ &= \left(\prod_{i=1}^{N}\int \mathrm{d}\mathbf{y}_i\mathrm{d}\mathbf{n}_i\right)\Psi(\{\mathbf{y}\},\{\mathbf{n}\},t)\sum_{j=1}^{N}\delta(\mathbf{x}-\mathbf{y}_j)\end{aligned}$$

$$
\begin{aligned}
&= \sum_{j=1}^{N} \int \mathrm{d}\mathbf{n}_j \left(\prod_{i \neq j} \int \mathrm{d}\mathbf{y}_i \mathrm{d}\mathbf{n}_i \right) \int \mathrm{d}\mathbf{y}_j \Psi(\{\mathbf{y}\}, \{\mathbf{n}\}, t) \delta(\mathbf{x} - \mathbf{y}_j) \\
&= \sum_{j=1}^{N} \int \mathrm{d}\mathbf{n}_j \left(\prod_{i \neq j} \int \mathrm{d}\mathbf{y}_i \mathrm{d}\mathbf{n}_i \right) \Psi(\{\mathbf{y}\}|_{\mathbf{y}_j = \mathbf{x}}, \{\mathbf{n}\}, t) \\
&= \sum_{j=1}^{N} \int \mathrm{d}\mathbf{n}_j \, \frac{1}{N} \Psi_1(\mathbf{x}, \mathbf{n}_j, t) \\
&= \int \mathrm{d}\mathbf{n} \, \Psi_1(\mathbf{x}, \mathbf{n}, t). \qquad (2.28)
\end{aligned}
$$

using the interchangeability, so that the sum is over identical terms, i.e. $\sum \mapsto N$, and the index in the last step can be dropped. The brackets $\langle \bullet \rangle$ denote the ensemble average over the free parameter, in this concrete case over the variables $\{\mathbf{y}\}$ and $\{\mathbf{n}\}$.

Similarly, the polarization field is given by the mean orientation in an infinitesimal volume located at $\mathbf{x}$ and is given by

$$
\begin{aligned}
\mathbf{p}(\mathbf{x}, t) &= \left\langle \sum_{j=1}^{N} \mathbf{n}_j \delta(\mathbf{x} - \mathbf{y}_j) \right\rangle \\
&= \int \mathrm{d}\mathbf{n} \, \Psi_1(\mathbf{x}, \mathbf{n}, t) \, \mathbf{n}. \qquad (2.29)
\end{aligned}
$$

Each partial distribution obeys a Smoluchowski equation that can be derived from equation (2.19) by integration. In general, this is not trivial because of the couplings between particles. However, it is easily possible in a mean-field interaction scheme, where the particles are not coupled directly to each other.

2.4 Smoluchowski equation of the single particle distribution with mean-field interactions

Let a Smoluchowski equation of the PDF be given by

$$\partial_t \Psi = \sum_{j=1}^{N} \left[-\nabla_j \cdot \mathbf{v}_{\mathrm{t}}^j \Psi - \nabla_{\mathbf{n}_j}^{\circ} \cdot \mathbf{v}_{\mathrm{r}}^j \Psi + \Delta_j \, D_{\mathrm{t}} \Psi + \Delta_{\mathbf{n}_j}^{\circ} \, D_{\mathrm{r}} \Psi \right]. \tag{2.30}$$

For particles that only interact indirectly via a mean interaction field, the flux velocities $\mathbf{v}_{\mathrm{t}}^j(\mathbf{x}_j, \mathbf{n}_j)$ and $\mathbf{v}_{\mathrm{r}}^j(\mathbf{x}_j, \mathbf{n}_j)$ of a particle j only depend on the coordinates of the particle itself. Hence, the particles do not interact directly with each other, but their interaction is mediated by a local interaction with an interaction field. Under this assumption, the PDF factorizes into single particle contributions,

$$\Psi(\{\mathbf{x}\}, \{\mathbf{n}\}, t) = \prod_{j=1}^{N} \frac{1}{N} \Psi_1(\mathbf{x}_j, \mathbf{n}_j, t) = N^{-N} \prod_{j=1}^{N} \Psi_1(\mathbf{x}_j, \mathbf{n}_j, t),$$

Then, the scaled (by N) Smoluchowski equation (2.30) for the single-particle distribution Ψ_1 in a system of non-interacting particles for any focus particle simplifies to

$$\partial_t \Psi_1 = -\nabla \cdot [\mathbf{v}_{\mathrm{t}} \Psi_1] - \nabla_{\mathbf{n}}^{\circ} \cdot [\mathbf{v}_{\mathrm{r}} \Psi_1] + \mathbb{D} \Psi_1, \tag{2.31}$$

where the particle label has been dropped and the diffusion operator is given by

$$\mathbb{D} = D_{\mathrm{t}} \, \Delta + D_{\mathrm{r}} \, \Delta_{\mathbf{n}}^{\circ}. \tag{2.32}$$

Strictly speaking, equation (2.31) is not a Smoluchowski equation, because Ψ_1 is not a probability density. However, scaling the equation by $1/N$ makes it a Smoluchowski equation. Therefore, in the following the equation is still referred to as a Smoluchowski equation.

The same result can also be derived without the factorization ansatz by making explicit use of the boundary conditions given by the equations (2.20) ans (2.21). Starting from equation (2.30), the Smoluchowski equation of the single particle distribution Ψ_1 can be derived by integrating over all but one tagged particle with index 1 (without loss of generality).

The flux terms are given by

$$\partial_t \Psi_1(\mathbf{x}_1, \mathbf{n}_1, t) = -N \left(\prod_{i=2}^{N} \int \mathrm{d}\mathbf{x}_i \mathrm{d}\mathbf{n}_i \right) \sum_{j=1}^{N} [\nabla_j \cdot \mathbf{v}_{\mathrm{t}}^j + \nabla_{\mathbf{n}_j}^{\circ} \cdot \mathbf{v}_{\mathrm{r}}^j] \Psi(\{\mathbf{x}\}, \{\mathbf{n}\}, t) + \dots$$

$$
\begin{aligned}
&= -\left[\nabla_1 \cdot \mathbf{v}_\mathrm{t}^1 + \nabla_{\mathbf{n}_1}^\circ \cdot \mathbf{v}_\mathrm{r}^1\right] \Psi_1(\mathbf{x}_1, \mathbf{n}_1, t) \\
&\quad - \frac{1}{N-1} \sum_{j=2}^{N} \int \mathrm{d}\mathbf{n}_j \underbrace{\int \mathrm{d}\mathbf{x}_j \, \nabla_j \cdot \left[\mathbf{v}_\mathrm{t}^j \Psi_2(\mathbf{x}_1, \mathbf{x}_j, \mathbf{n}_1, \mathbf{n}_j, t)\right]}_{=0} \\
&\quad - \frac{1}{N-1} \sum_{j=2}^{N} D_\mathrm{r} \int \mathrm{d}\mathbf{x}_j \underbrace{\int \mathrm{d}\mathbf{n}_j \, \nabla_{\mathbf{n}_j}^\circ \cdot \left[\mathbf{v}_\mathrm{r}^j \Psi_2(\mathbf{x}_1, \mathbf{x}_j, \mathbf{n}_1, \mathbf{n}_j, t)\right]}_{0} \\
&= -\left[\nabla_1 \cdot \mathbf{v}_\mathrm{t}^1 + \nabla_{\mathbf{n}_1}^\circ \cdot \mathbf{v}_\mathrm{r}^1\right] \Psi_1(\mathbf{x}_1, \mathbf{n}_1, t) + \dots
\end{aligned}
$$

In the second step, the assumption was used that the jth flux only depends on the jth particle and in the second to last step Gauß' divergence theorem was used. For the integration over the volume $V(r)$ a sphere of the radius r the Gauß' theorem yields

$$
\int_{V(r)} \mathrm{d}\mathbf{x} \, \nabla \cdot \mathbf{v}_\mathrm{t}^j \Psi_2 = \int_{\partial V(r)} \mathrm{d}\mathbf{A} \cdot \mathbf{v}_\mathrm{t}^j \Psi_2.
$$

By demanding that the pair distribution and its derivatives vanish for $r \to \infty$, thus making use of the boundary conditions (2.20) and (2.21), the integral vanishes as well.

For the orientational part the Gauß' divergence theorem in tangential space of the unit sphere can be applied. For flux velocity with $\mathbf{v}_\mathrm{r}^j$ tangential to the unit sphere's surface it holds.

$$
\int_{\mathbb{S}^2} \mathrm{d}\mathbf{n} \; \nabla_\mathbf{n}^\circ \cdot (\mathbf{v}_\mathrm{r}^j \Psi_2) = 0.
$$

The identity is proved in the Appendix A.3 in Corollary A.3.1.

If the diffusion parameters D_t and D_r are constants, the diffusion of the single probability density Ψ_1/N can be found by integrating the diffusive part of the Fokker-Planck equation (2.19) over all but one focus particle:

$$
\begin{aligned}
\partial_t \Psi_1(\mathbf{x}_1, \mathbf{n}_1, t) &= \dots + N \left(\prod_{i=2}^{N} \int \mathrm{d}\mathbf{x}_i \mathrm{d}\mathbf{n}_i \right) \left[\sum_{j=1}^{N} D_\mathrm{t} \, \Delta_j + \sum_{j=1}^{N} D_\mathrm{r} \Delta_{\mathbf{n}_j}^\circ \right] \Psi(\{\mathbf{x}\}, \{\mathbf{n}\}, t) \\
&= \dots + (D_\mathrm{t} \, \Delta_1 + D_\mathrm{r} \Delta_{\mathbf{n}_1}^\circ) \Psi_1(\mathbf{x}_1, \mathbf{n}_1, t) \\
&\quad + \frac{1}{N-1} \sum_{j=2}^{N} D_\mathrm{t} \int \mathrm{d}\mathbf{n}_j \underbrace{\int \mathrm{d}\mathbf{x}_j \, \nabla_j \cdot \left[\nabla_j \Psi_2(\mathbf{x}_1, \mathbf{x}_j, \mathbf{n}_1, \mathbf{n}_j, t)\right]}_{=0} \\
&\quad + \frac{1}{N-1} \sum_{j=2}^{N} D_\mathrm{r} \int \mathrm{d}\mathbf{x}_j \underbrace{\int \mathrm{d}\mathbf{n}_j \, \nabla_{\mathbf{n}_j}^\circ \cdot \left[\nabla_{\mathbf{n}_j}^\circ \Psi_2(\mathbf{x}_1, \mathbf{x}_j, \mathbf{n}_1, \mathbf{n}_j, t)\right]}_{0} \\
&= \dots + (D_\mathrm{t} \, \Delta_1 + D_\mathrm{r} \Delta_{\mathbf{n}_1}^\circ) \Psi_1(\mathbf{x}_1, \mathbf{n}_1, t).
\end{aligned}
$$

In the second to last step Gauß's divergence theorem is used again, given by

$$\int_{V(r)} \mathrm{d}\mathbf{x} \nabla \cdot \nabla \Psi = \int_{\partial V(r)} \mathrm{d}\mathbf{A} \cdot \nabla \Psi \xrightarrow[r\to\infty]{} 0.$$

The second term vanishes by applying Corollary A.3.1 to the integral

$$\int_{\mathbb{S}^2} \mathrm{d}\mathbf{n}\ \nabla^\circ_{\mathbf{n}} \cdot (\nabla^\circ_{\mathbf{n}}\, \Psi_2) = 0.$$

The Corollary applies, because the surface gradient $\nabla^\circ_{\mathbf{n}}\, \Psi_2$ is tangential to the unit sphere surface by definition.

Together, the same single-particle Smoluchowski equation as in equation (2.31) is obtained.

$$\partial_t \Psi_1 = -\nabla \cdot [\mathbf{v}_\mathrm{t} \Psi_1] - \nabla^\circ_{\mathbf{n}} \cdot [\mathbf{v}_\mathrm{r} \Psi_1] + \mathbb{D} \Psi_1.$$

The single particle Smoluchowski equation derived above is only valid for mean-field interactions mediated by an interaction field. In Sections 2.6 and 2.8 two such fields are presented, based on magnetic dipole-dipole and hydrodynamic interactions respectively. For directly interacting particles, where the interaction can be described by a pair potential $U(\mathbf{x}_i, \mathbf{x}_j)$, the single particle Smoluchowski equation must be adapted. The interactions introduce pair correlations captured by the pair distribution Ψ_2. In a mean-field theory, the pair distribution is not directly available. As a consequence, a pair interaction can only be expressed approximatively in a mean-field theory, as discussed in the next Section.

2.5 Pair interaction in a mean-field theory

Given a translational invariant pair potential $U(\mathbf{x}_i, \mathbf{x}_j) = U(\|\mathbf{x}_i - \mathbf{x}_j\|)$ that is independent of a particle's orientation, the force on any particle labelled with i is given by

$$\mathbf{F}_j(\{\mathbf{x}\}) = -\sum_{i \neq j}^{N} \nabla_{\mathbf{x}_j} U(\mathbf{x}_i, \mathbf{x}_j).$$

The gradient operator $\nabla_{\mathbf{x}_j}$ is the gradient with respect to the particle with index j. The Smoluchowski equation of particles interacting via the pair potential U (ignoring the diffusive terms) is given by

$$\partial_t \Psi = -\sum_{j=1}^{N} \nabla_{\mathbf{x}_j} \cdot \left[\frac{1}{\xi_\mathrm{t}} \mathbf{F}_j \Psi \right]. \tag{2.33}$$

To derive the time evolution of the single particle distribution Ψ_1, as previously defined in (2.25), equation (2.33) is integrated over all but one focus particle. Without loss of generality, the focus particle is labelled with $i = 1$. The integrated equation (2.33) is given by

$$\begin{aligned}\partial_t \Psi_1 &= -N \left(\prod_{i=2}^{N} \int \mathrm{d}\mathbf{x}_i \mathrm{d}\mathbf{n}_i \right) \sum_{j=1}^{N} \nabla_{\mathbf{x}_j} \cdot \left[\frac{1}{\xi_\mathrm{t}} \mathbf{F}_j \Psi \right] \\ &= -N \left(\prod_{i=2}^{N} \int \mathrm{d}\mathbf{x}_i \mathrm{d}\mathbf{n}_i \right) \nabla_{\mathbf{x}_1} \cdot \left[\frac{1}{\xi_\mathrm{t}} \mathbf{F}_1 \Psi \right] \\ &= -\nabla_{\mathbf{x}_1} \cdot \left[\frac{1}{\xi_\mathrm{t}} N \left(\prod_{i=2}^{N} \int \mathrm{d}\mathbf{x}_i \mathrm{d}\mathbf{n}_i \right) \mathbf{F}_1 \Psi \right]. \end{aligned} \tag{2.34}$$

The integrals over all but the focus particle vanish. This follows from Gauß' divergence theorem over a sphere with radius r and volume $V(r)$, yielding

$$\int_{V(r)} \mathrm{d}\mathbf{x}\, \nabla \cdot \mathbf{F}\Psi = \int_{\partial V(r)} \mathrm{d}\mathbf{A} \cdot \mathbf{F}\Psi \xrightarrow[r\to\infty]{} 0.$$

By making use of the boundary conditions given in equation (2.20), it follows that the flux $(\mathbf{F}\Psi)(r \to \infty) = 0$ goes to zero in infinity and therefore the integrals vanish.

The integral in the last term of equation (2.34) can be interpreted as the (partial) expectation value of the force density on *any* particle arbitrarily labelled with $i = 1$. The mean force density is given by

$$\begin{aligned}\overline{\mathbf{f}}(\mathbf{x}_1, \mathbf{n}_1, t) &= N \left(\prod_{i=2}^{N} \int \mathrm{d}\mathbf{x}_i \mathrm{d}\mathbf{n}_i \right) \; \Psi(\{\mathbf{x}\}, \{\mathbf{n}\}, t)\, \mathbf{F}_1(\{\mathbf{x}\}) \\ &= -N \sum_{j=2}^{N} \left(\prod_{i=2}^{N} \int \mathrm{d}\mathbf{x}_i \mathrm{d}\mathbf{n}_i \right) \; \Psi(\{\mathbf{x}\}, \{\mathbf{n}\}, t)\, \nabla_{\mathbf{x}_1} U(\mathbf{x}_1, \mathbf{x}_j). \end{aligned}$$

Because of equation (2.24), the labels in the integrals in every summand can be permuted so that the particle in the argument of the potential is always $j = 2$, leaving $(N - 1)$ identical expressions. Consequently, the mean force density can be written as

$$\begin{aligned}\overline{\mathbf{f}}(\mathbf{x}, \mathbf{n}, t) &= -\int \mathrm{d}\mathbf{x}' \mathrm{d}\mathbf{n}' \left[N(N-1) \left(\prod_{i=3}^{N} \int \mathrm{d}\mathbf{x}_i \mathrm{d}\mathbf{n}_i \right) \; \Psi(\{\mathbf{x}\}, \{\mathbf{n}\}, t) \right] \nabla_{\mathbf{x}} U(\mathbf{x}, \mathbf{x}') \\ &= -\int \mathrm{d}\mathbf{x}' \mathrm{d}\mathbf{n}'\, \Psi_2(\mathbf{x}, \mathbf{x}', \mathbf{n}, \mathbf{n}', t), \nabla_{\mathbf{x}} U(\mathbf{x}, \mathbf{x}') \end{aligned} \tag{2.35}$$

where in the last step the definition of Ψ_2 in equation (2.27) was used and the indices 1 and 2 were dropped and replaced with $(\mathbf{x}_1, \mathbf{x}_2) \mapsto (\mathbf{x}, \mathbf{x}')$ and $(\mathbf{n}_1, \mathbf{n}_2) \mapsto (\mathbf{n}, \mathbf{n}')$ [43, 83].

By plugging the result in equation (2.35) back into the Smoluchowski equation (2.33),

$$\partial_t \Psi_1 = -\nabla \cdot \left[\frac{1}{\xi_\mathrm{t}} \overline{\mathbf{f}}[\Psi_2] \right],$$

it becomes clear that the evolution of the single particle distribution Ψ_1 depends on the pair distribution Ψ_2. In general, the Smoluchowski equation of Ψ_s including a pair interaction depends on Ψ_{s+1}, which can be seen by integrating the Smoluchowski equation (2.33) over the remaining $N - s$ degrees of freedom. This hierarchy of equation is also referred to as the *BBGKY* hierarchy (Bogoliubov–Born–Green–Kirkwood–Yvon hierarchy) [84–87]. It reflects the complex inter-particle relations. In practice, approximations breaking the hierarchy have to be made.

The pair distribution Ψ_2 is related to the pair correlation function (or radial distribution function) $g^{(2)}$ by

$$\Psi_2(\mathbf{x}, \mathbf{x}', \mathbf{n}, \mathbf{n}', t) = \Psi_1(\mathbf{x}, \mathbf{n}, t)\, \Psi_1(\mathbf{x}', \mathbf{n}', t)\, g^{(2)}(\mathbf{x}, \mathbf{x}', \mathbf{n}, \mathbf{n}', t). \tag{2.36}$$

This can be substituted into equation (2.35), yielding

$$\begin{aligned} \overline{\mathbf{f}}_\mathrm{MF}(\mathbf{x}, \mathbf{n}, t) &= -\int \mathrm{d}\mathbf{x}' \mathrm{d}\mathbf{n}'\, \Psi_1(\mathbf{x}, \mathbf{n}, t)\, \Psi_1(\mathbf{x}', \mathbf{n}', t)\, g^{(2)}(\mathbf{x}, \mathbf{x}', \mathbf{n}, \mathbf{n}', t)\, \nabla_\mathbf{x} U(\mathbf{x}, \mathbf{x}') \\ &= -\Psi_1(\mathbf{x}, \mathbf{n}, t) \int \mathrm{d}\mathbf{x}' \mathrm{d}\mathbf{n}'\, \Psi_1(\mathbf{x}', \mathbf{n}', t)\, g^{(2)}(\mathbf{x}, \mathbf{x}', \mathbf{n}, \mathbf{n}', t)\, \nabla_\mathbf{x} U(\|\mathbf{x} - \mathbf{x}\|), \end{aligned}$$

resulting in the mean-field Smoluchowski equation

$$\begin{aligned} \partial_t \Psi_1 &= -\nabla \cdot \left[\Psi_1(\mathbf{x}, \mathbf{n}, t) \frac{-1}{\xi_\mathrm{t}} \int \mathrm{d}\mathbf{x}' \mathrm{d}\mathbf{n}'\, \Psi_1(\mathbf{x}', \mathbf{n}', t)\, g^{(2)}(\mathbf{x}, \mathbf{x}', \mathbf{n}, \mathbf{n}', t)\, \nabla_\mathbf{x} U(\|\mathbf{x} - \mathbf{x}\|) \right] \\ &\equiv -\nabla \cdot \left[\frac{1}{\xi_\mathrm{t}} \overline{\mathbf{F}}_\mathrm{MF}(\mathbf{x}, t) \Psi_1(\mathbf{x}, \mathbf{n}, t) \right], \end{aligned} \tag{2.37}$$

The mean-field interaction force is defined by

$$\overline{\mathbf{F}}_\mathrm{MF}(\mathbf{x}, t) = -\int \mathrm{d}\mathbf{x}' \mathrm{d}\mathbf{n}'\, \Psi_1(\mathbf{x}', \mathbf{n}', t)\, g^{(2)}(\mathbf{x}, \mathbf{x}', \mathbf{n}, \mathbf{n}', t)\, \nabla_\mathbf{x} U(\|\mathbf{x} - \mathbf{x}'\|). \tag{2.38}$$

The derivation is also valid for orientation dependent pair-potentials $U(\mathbf{x}, \mathbf{x}', \mathbf{n}, \mathbf{n}')$, the interaction force will then depend on the orientation $\mathbf{n}$ as well.

One possible approach to break the *BBGKY* hierarchy is to treat the pair correlation function as an input parameter to the model. This approach was taken in *Bialké* et al. [43], where the pair correlation function was obtained from fits to N-particle Brownian dynamics simulations. However, the present work addresses mostly dilute suspensions. In this case, neglecting inter-particle correlations altogether by setting $g^{(2)} = 1$ is a legitimate approach, resulting in a mean-field theory. In many cases, especially for dilute suspensions, it gives qualitatively sound results and reflects the focus on pattern formation and coarse grained collective dynamics. Still, the discussion becomes relevant again in Chapter 5 when discussing volume exclusion effects. Under this assumption, the mean-field interaction force simplifies to

$$\overline{\mathbf{F}}_{\mathrm{MF}}(\mathbf{x}, t) = -\int \mathrm{d}\mathbf{x}' \mathrm{d}\mathbf{n}'\, \Psi_1(\mathbf{x}', \mathbf{n}', t)\, \nabla_{\mathbf{x}} U(\|\mathbf{x} - \mathbf{x}'\|). \tag{2.39}$$

In practice, various different interactions between the particles can be considered. In the next sections, mean-field interactions with an external and internal magnetic field are discussed, as well has Stokesian hydrodynamic interactions.

2.6 Dipolar magnetic interactions

A magnetic swimmer interacts with a surrounding magnetic field. The magnetic field can be of external origin (for example the earth magnetic field or Helmholtz-coils in a laboratory) or it can be generated by other magnetic particles in its environment, leading to an inter-particle interaction. In nature, magnetotactic bacteria were observed growing a ferrimagnetic structure called magnetosome inside their bodies [88–92]. Artificial magnetic swimmers have been, for example, produced and characterized in Refs. [93, 94].

For simplicity, in this work it is assumed that the swimmers carry a fixed magnetic dipole moment $\boldsymbol{\mu} = \mu\mathbf{n}$ along their orientation vector $\mathbf{n}$. Consequently, swimmers in a magnetic field tend to align their orientation along the field lines of an ambient magnetic field due to a magnetic torque acting on the dipole moment. Furthermore, each swimmer produces a dipolar magnetic field on its own other swimmers are exposed and react to. The result is a magnetic interaction between the swimmers.

In a mean-field model, the pair-interaction is replaced by an interaction with a mean magnetic field generated by all swimmers together. Similar to a magnet, the collective alignment of the magnetic moments lead to a magnetization of the suspension, which can be used to calculate the internal magnetic field. The derivation of the internal

magnetic field is the subject of this section, starting with a brief review of the magnetic dipole moment and its reaction to a magnetic field. These results are later used in Chapter 5 to incorporate a magnetic dipole-dipole interaction in a kinetic theory of magnetic microswimmers.

2.6.1 Magnetic dipole moment

The (microscopic) magnetic (dipole) moment is defined by

$$\boldsymbol{\mu} \equiv \frac{1}{2} \int d\mathbf{x}\, \mathbf{x} \times \mathbf{j}(\mathbf{x}), \tag{2.40}$$

given a current density $\mathbf{j}$ — as described for example in »Classical electrodynamics« from J. D. Jackson [95].

The magnetic moment constitutes the leading order term in a multipole expansion (Taylor series in powers of the inverse distance $1/x$) of the vector potential $\mathbf{A}$ of a local current density $\mathbf{j}$ [95]

$$\mathbf{A} = \frac{\mu_0}{4\pi} \frac{\boldsymbol{\mu} \times \mathbf{x}}{x^3} + \dots.$$

Therefore, the magnetic flux density $\mathbf{B}_{\text{dip}} = \nabla \times \mathbf{A}_{\text{dip}}$ of a single magnetic dipole moment is given by

$$\mathbf{B}_{\text{dip}}(\mathbf{x}) = \mu_0 \mathcal{B}_{\text{dip}}(\mathbf{x}) \cdot \boldsymbol{\mu} \equiv \frac{\mu_0}{4\pi} \left(\frac{3\mathbf{x}\mathbf{x}}{x^5} - \frac{\mathbb{1}}{x^3} \right) \cdot \boldsymbol{\mu}, \tag{2.41}$$

defining the dipolar flux density operator $\mathcal{B}_{\text{dip}} = \frac{1}{4\pi} \left(\frac{3\mathbf{x}\mathbf{x}}{x^5} - \frac{\mathbb{1}}{x^3} \right)$.

The potential energy of a magnetic moment in a magnetic flux density $\mathbf{B}$ is given by

$$U_m = -\boldsymbol{\mu} \cdot \mathbf{B}. \tag{2.42}$$

In case the magnetic flux density has a gradient, it gives rise to a force acting on the magnetic moment located at the position $\mathbf{x}$,

$$\mathbf{F}_{\text{m}}(\mathbf{x}) = -\nabla U_m(\mathbf{x}) = \nabla(\boldsymbol{\mu} \cdot \mathbf{B}(\mathbf{x})) = \boldsymbol{\mu} \cdot \nabla \mathbf{B}(\mathbf{x}). \tag{2.43}$$

In any case, a magnetic dipole moment at the position $\mathbf{x}$ experiences a torque

$$\boldsymbol{\tau}_{\text{m}}(\mathbf{x}) = \boldsymbol{\mu} \times \mathbf{B}(\mathbf{x}) \tag{2.44}$$

that strives to align the moment with the local field.

Consequently, two magnetic dipole moments exposed to each other's magnetic fields will interact via both force and torque. In case of a suspended magnetic particle, viscous forces and torques have to be considered as well in order to derive the resulting equations of motion.

2.6.2 Alignment torque of magnetic colloids

Given a freely suspended particle with a moment of inertia tensor $\mathbb{I}$ and a magnetic dipole moment $\boldsymbol{\mu} = \mu\mathbf{n}$ pointing along its orientation $\mathbf{n}$, the torque $\boldsymbol{\tau}$ on the particle in a magnetic flux density $\mathbf{B}$ is given by

$$\boldsymbol{\tau}(t) = \mathbb{I}\frac{\mathrm{d}}{\mathrm{d}t}\boldsymbol{\omega}(t) = \boldsymbol{\tau}_{\mathrm{m}}(t) - \xi_{\mathrm{r}}\boldsymbol{\omega} = \mu\mathbf{n}(t) \times \mathbf{B} - \xi_{\mathrm{r}}\boldsymbol{\omega}. \tag{2.45}$$

The angular velocity of the particle's rotation is denoted by $\boldsymbol{\omega}$. The rotational friction coefficient ξ_{r} reflects the interaction with the solvent.

In the limit of overdamped dynamics (at a low Reynold's number), the moment of inertia is negligible (see Section 2.1.2). In this case, equation (2.45) simplifies to an instantaneous balance of torques,

$$\mu\mathbf{n} \times \mathbf{B} = \xi_{\mathrm{r}}\boldsymbol{\omega}.$$

Using the relation $\dot{\mathbf{n}} = \boldsymbol{\omega} \times \mathbf{n}$, the time evolution of the orientation $\mathbf{n}$ of a magnetic particle in the presence of a magnetic field can be found to be

$$\dot{\mathbf{n}} = (\mathbb{1} - \mathbf{nn}) \cdot \frac{\mu}{\xi_{\mathrm{r}}}\mathbf{B}. \tag{2.46}$$

The operator $(\mathbb{1} - \mathbf{nn})$ performs an orthogonal projection with respect to a unit vector $\mathbf{n}$. The rotation of the particle due to a magnetic field is illustrated in Figure 2.4.

As mentioned earlier, the magnetic flux density can be of external origin or generated internally by the magnetic dipole moment of the particles. The latter mechanism is described in the following.

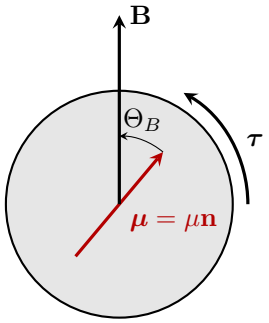

Fig. 2.4.: A particle carrying a magnetic dipole moment $\boldsymbol{\mu} = \mu \mathbf{n}$ along its orientation $\mathbf{n}$ is rotating towards a magnetic flux density $\mathbf{B}$ due to a magnetic torque $\boldsymbol{\tau}$. The torque vector $\boldsymbol{\tau}$ in this configuration points out of the image plane. The angle between $\mathbf{n}$ and $\mathbf{B}$ is denoted by Θ_B.

2.6.3 Magnetization of a magnetic colloidal suspension

The internal magnetic flux density generated by a suspension of colloids carrying magnetic dipole moments $\boldsymbol{\mu}_i$ is a superposition of the microscopic dipolar fields, given in equation (2.41), of each individual magnetic moment. However, on larger scales numerous individual colloids are involved at any time. Hence, an explicit treatment on the microscopic level is not necessary and a coarse grained description (field description) can be used instead. To this end, the magnetization is introduced that approximates the discrete distribution of magnetic moments by a continuous field.

The magnetization $\mathbf{M}$ is defined as the magnetic moment per volume [95]. A non rigorous[7] definition can be provided in terms of sum of microscopic magnetic moments $\boldsymbol{\mu}_i$ contained in a small but finite volume $v(\mathbf{x})$ surrounding the point $\mathbf{x}$:

$$\mathbf{M}(\mathbf{x}) \approx \frac{1}{v(x)} \sum_{i \in v(\mathbf{x})} \boldsymbol{\mu}_i.$$

In case of magnetic colloids with magnetic dipole moment $\boldsymbol{\mu}_i = \mu \mathbf{n}_i$ at positions $\mathbf{y}_i$, the magnetization can be defined by

$$\mathbf{M}(\{\mathbf{x}\}, \{\mathbf{n}\}) = \sum_{i=1}^{N} \boldsymbol{\mu}_i \delta(\mathbf{x} - \mathbf{y_i}). \tag{2.47}$$

For Brownian particles the exact position the particles and their orientation, and therefore their magnetic moments, is known only probabilistically in form of a

[7] A more rigorous definition can be found in [96] that explicitly deals with transition from the discrete sum to a continuous field.

probability density function. Given a PDF $\Psi(\{\mathbf{x}\},\{\mathbf{n}\},t)$, the mean magnetization can be found by the expectation value of the PDF Ψ, denoted by the brackets, of (2.47) and is given by

$$\begin{aligned}\langle \mathbf{M} \rangle_{\{\mathbf{n}\}}(\mathbf{x},t) &= \left\langle \sum_{i=1}^{N} \boldsymbol{\mu}_i(t)\delta(\mathbf{x}(t)-\mathbf{y_i}(t)) \right\rangle \\ &= \mu \mathbf{p}(\mathbf{x},t), \end{aligned} \tag{2.48}$$

using the polarization field defined in equation (2.29)

$$\mathbf{p}(\mathbf{x},t) = \int_{\mathbb{S}^2} \mathrm{d}\mathbf{n}\ \Psi_1(\mathbf{x},\mathbf{n},t)\,\mathbf{n},$$

and the one particle distribution function Ψ_1 given in equation (2.25).

From now on, the mean magnetization $\langle \mathbf{M} \rangle_{\{\mathbf{n}\}}$ is just denoted by $\mathbf{M}$ and the brackets are dropped. Having obtained the mean magnetization field $\mathbf{M}$ of a suspension of magnetic colloids, the resulting internal magnetic flux density $\mathbf{B}_{\text{int}}$ can eventually be derived in the next section.

2.6.4 Internal magnetic field

Given a magnetization field $\mathbf{M}(\mathbf{x},t)$ of a colloidal suspension, equation (2.48), the resulting (internal) magnetic flux density $\mathbf{B}_{\text{int}}$ can be obtained from the Maxwell-equations, in general given by

$$\nabla \times \mathbf{H} = \mathbf{J}_{\text{free}} + \partial_t \mathbf{D} \tag{2.49}$$

$$\nabla \cdot \mathbf{B}_{\text{int}} = 0, \tag{2.50}$$

in which the magnetic field is given by

$$\mathbf{H} = \frac{1}{\mu_0}\mathbf{B}_{\text{int}} - \mathbf{M} \tag{2.51}$$

and the free current density $\mathbf{J}_{\text{free}}$. The free current density is zero for a magnetic suspension, $\mathbf{J}_{\text{free}} = 0$. Furthermore, it is assumed that the suspension has negligible electrical polarization, i.e. the electric displacement field is given by $\mathbf{D} = \epsilon_0 \mathbf{E}$, with the electrical field $\mathbf{E}$.

In order to obtain the magnetic flux density $\mathbf{B}_{\text{int}}$, a solution of the Maxwell-equations above can be formulated in Fourier-space (assuming the Fourier transforms exist). The

Fourier-transformed equations (2.49) and (2.50) in time and space ($(\mathbf{x}, t) \mapsto (\mathbf{k}, \omega)$) read

$$\mathrm{i}\,\mathbf{k} \times \widehat{\mathbf{B}}_{\text{int}}(\mathbf{k}, \omega) = \mathrm{i}\mu_0\,\mathbf{k} \times \widehat{\mathbf{M}}(\mathbf{k}, \omega) + \mathrm{i}\frac{\omega}{c^2}\widehat{\mathbf{E}}(\mathbf{k}, \omega) \tag{2.52}$$

$$\mathrm{i}\,\mathbf{k} \cdot \widehat{\mathbf{B}}_{\text{int}}(\mathbf{k}, \omega) = 0, \tag{2.53}$$

with the wave vector $\mathbf{k}$, the angular frequency ω, the Fourier-transform $\widehat{\bullet}(\mathbf{k}, t)$ of $\bullet$ and $\mu_0\epsilon_0 = c^{-2}$. Note that these equations are only meaningful for $\mathbf{k} \neq 0$.

By applying $\mathbf{k} \times \bullet$ on both sides of equation (2.52) while multiplying by i and by making use of

$$\mathbf{k} \times (\mathbf{k} \times \mathbf{a}) = -k^2 \left(\mathbb{1} - \check{\mathbf{k}}\check{\mathbf{k}}\right) \cdot \mathbf{a},\ \check{\mathbf{k}} = k^{-1}\mathbf{k}$$

for a vector $\mathbf{a}$, the equation (2.52) transforms into

$$k^2 \left(\mathbb{1} - \check{\mathbf{k}}\check{\mathbf{k}}\right) \cdot \widehat{\mathbf{B}}_{\text{int}} = \mu_0 k^2 \left(\mathbb{1} - \check{\mathbf{k}}\check{\mathbf{k}}\right) \cdot \widehat{\mathbf{M}} - \frac{\omega}{c^2}\mathbf{k} \times \widehat{\mathbf{E}}. \tag{2.54}$$

Because of equation (2.53), the left side simplifies to

$$k^2 \left(\mathbb{1} - \check{\mathbf{k}}\check{\mathbf{k}}\right) \cdot \widehat{\mathbf{B}}_{\text{int}} = k^2 \widehat{\mathbf{B}}_{\text{int}}.$$

The curl of the electric field is given by the Maxwell-equation $\nabla \times \mathbf{E} = -\partial_t \mathbf{B}_{\text{int}}$ or $\mathbf{k} \times \widehat{\mathbf{E}} = -\omega \widehat{\mathbf{B}}_{\text{int}}$. Applying these identities to equation (2.54) and solving for $\widehat{\mathbf{B}}_{\text{int}}$ gives

$$\widehat{\mathbf{B}}_{\text{int}}(\mathbf{k}) = \frac{\mu_0 k^2}{k^2 - \frac{\omega^2}{c^2}} \left(\mathbb{1} - \check{\mathbf{k}}\check{\mathbf{k}}\right) \cdot \widehat{\mathbf{M}}(\mathbf{k}), \tag{2.55}$$

assuming $\mathbf{k} \neq 0$. In very good approximation, the time spectrum of every quantity should have a finite support with an upper bound $\omega < \omega_b$ in the order of $1\,\mathrm{kHz}$ (estimated orientational thermal fluctuations), while the wavenumber has a lower bound $k > k_b$ in the order of one over the sample size (order of sub meters), so that $\frac{\omega_b}{k_b} \ll c$. Consequently, the electric field can be neglected in all following considerations leading to a quasi magnetostatic approximation. The pre-factor in equation (2.55) becomes equal to μ_0.

Every possible magnetization can be separated into a homogeneous space dependent heterogeneous part $\mathbf{M} \equiv \mathbf{M}_{\mathrm{c}} + \mathbf{M}_{\mathrm{v}}$ or $\widehat{\mathbf{M}}(\mathbf{k}) = \widehat{\mathbf{M}}_{\mathrm{c}}\delta(\mathbf{k}) + \widehat{\mathbf{M}}_{\mathrm{v}}(\mathbf{k} \neq 0)$ for the Fourier transformed identity. The non-constant part corresponds to $k > 0$ in Fourier space. The Fourier-transform of the magnetic flux density can be expressed as

$$\widehat{\mathbf{B}}_{\text{int}} = \mu_0 \left(\mathbb{1} - \check{\mathbf{k}}\check{\mathbf{k}}\right) \cdot \widehat{\mathbf{M}}_{\mathrm{v}}, \forall k > 0, \tag{2.56}$$

for the non-constant part.

For a constant magnetization $\mathbf{M}_c$ the $k = 0$ mode has to be considered. In this case, equation (2.56) is not meaningful and a different approach is required. By neglecting the electric field and in the absence of a free current density the magnetic field can be expressed as a gradient field of scalar magnetic potential Φ_m:

$$\nabla \times \mathbf{H} = 0 \Rightarrow \mathbf{H} = -\nabla \Phi_m.$$

For an arbitrary magnetization the scalar potential fulfils the Poisson equation

$$\Delta \Phi_m = -\nabla \cdot \mathbf{M}.$$

The term $-\nabla \cdot \mathbf{M}$ acts as an effective magnetic charge density. If there is no boundary surface, as it is the case for an infinite system, the general solution of the Poisson equation can be constructed by using the Green's function of the Laplacian,

$$\begin{aligned} \Delta \mathcal{G}_\Delta(\mathbf{x}) &= \delta(\mathbf{x}) \\ \Rightarrow \mathcal{G}_\Delta(\mathbf{x} - \mathbf{x}') &= \frac{1}{4\pi \|\mathbf{x} - \mathbf{x}'\|}, \end{aligned}$$

$$\Phi_m(\mathbf{x}) = -\frac{1}{4\pi} \int d\mathbf{x}' \frac{\nabla' \cdot \mathbf{M}(\mathbf{x}')}{\|\mathbf{x} - \mathbf{x}'\|}. \tag{2.57}$$

For a constant magnetic field $\nabla \cdot \mathbf{M}_c = 0$ and the magnetic scalar potential is $\Phi_{m,c} = 0$. This means that the magnetic field is $\mathbf{H}_c = -\nabla \Phi_{m,c} = 0$ and the magnetic flux density is given by

$$\mathbf{B}_{\text{int},c} = \mu_0 \mathbf{M}_c. \tag{2.58}$$

Or equivalently,

$$\widehat{\mathbf{B}}_{\text{int}}(\mathbf{k} = 0) = \mu_0 \widehat{\mathbf{M}}(\mathbf{k} = 0). \tag{2.59}$$

In summary, the Fourier transform of the magnetic flux can be given by

$$\widehat{\mathbf{B}}_{\text{int}}(\mathbf{k}) = \mu_0 \widehat{\mathcal{B}}^{\text{dip}}(\mathbf{k}) \cdot \widehat{\mathbf{M}}(\mathbf{k}), \tag{2.60}$$

with the magnetic dipole kernel

$$\widehat{\mathcal{B}}^{\text{dip}}(\mathbf{k}) \equiv \begin{cases} \left(\mathbb{1} - \check{\mathbf{k}} \check{\mathbf{k}} \right), & k > 0 \\ \mathbb{1} & k = 0 \end{cases}. \tag{2.61}$$

The operator in equation (2.61) can be understood to be the fundamental solution of Maxwell's equations for a point magnetization in free-space

$$\nabla \times \mathbf{B}_{\text{int}}(\mathbf{x}) = \delta(\mathbf{x})\, \mu_0 \mathbf{J}_m,$$

with a constant magnetization current $\mathbf{J}_m = \nabla \times \mathbf{M}$. Therefore, the operator $\widehat{\mathcal{B}}^{\text{dip}}$ corresponds to the magnetic dipole flux density of a single magnetic moment $\mathbf{B}_{\text{dip}}$ given in equation (2.41). Strictly speaking, $\mathcal{B}^{\text{dip}} = 1/4\pi \left(3\mathbf{x}\mathbf{x}/x^5 - \mathbb{1}/x^3\right)$, as defined in equation (2.41), and $\widehat{\mathcal{B}}^{\text{dip}}$ are not direct Fourier-transforms of each other, because the integrals do not converge. However, it is in line with the interpretation of the magnetic flux being the superposition of the fields of a configuration of magnetic dipoles $\boldsymbol{\mu}_j = \mu \mathbf{n}_j$. In a colloidal suspension described by the PDF Ψ, the expectation value/ensemble average of this superposition is given by

$$\begin{aligned}
\mathbf{B}_{\text{int}}(\mathbf{x}) &= \left\langle \sum_j \mu_0 \mathcal{B}^{\text{dip}}(\mathbf{x} - \mathbf{y}_j) \cdot \boldsymbol{\mu}_j \right\rangle \\
&= \sum_j \int \mathrm{d}\mathbf{y}_j\, \mu_0 \mathcal{B}^{\text{dip}}(\mathbf{x} - \mathbf{y}_j) \cdot \int \mathrm{d}\mathbf{n}_j\, \frac{1}{N} \Psi_1(\mathbf{y}_j, \mathbf{n}_j)\, \mu \mathbf{n}_j \\
&= \int \mathrm{d}\mathbf{y}\, \mu_0 \mathcal{B}^{\text{dip}}(\mathbf{x} - \mathbf{y}) \cdot \mathbf{M}(\mathbf{y}) \\
&= \left(\mu_0 \mathcal{B}^{\text{dip}} * \mathbf{M}\right)(\mathbf{x}).
\end{aligned} \tag{2.62}$$

Because of the interchangeability of the colloids the sum above is over identical terms, so that $\sum_j \mapsto N$. Furthermore, the definition of the single particle distribution (see equation (2.25)) and the mean magnetization of a magnetic suspension $\mathbf{M} = \mu \mathbf{p}$ (see equation (2.48)) was used. The convolution (denoted by the star operator) on the right-hand side of the equation directly corresponds to equation (2.56), because of the convolution theorem.

It is important to note that in general the magnetic flux density sensitively depends on surface effects of a spatially confined magnetization. A brief discussion of the non-trivial case of finite geometries can be found in box 2.1. In order to compare the presented model quantitatively with an experiment, interfacial corrections have to be considered. A time-independent surface effect can be incorporated into the magnetic dipole kernel by an effective pre-factor.

In conclusion, given a (well-behaved) mean-field magnetization $\mathbf{M} = \mu \mathbf{p}$ the corresponding internal magnetic flux density is given by the convolution of the dipolar flux density operator and the magnetization, which is proportional to the polarization field:

$$\mathbf{B}_{\text{int}} = \mu_0 \mathcal{B}^{\text{dip}} * \mu\, \mathbf{p}. \tag{2.63}$$

Magnetic colloids, especially active ones, not only create and interact with a magnetic field. The solvent influences their dynamics as well. The basis of these hydrodynamic interactions is discussed in the following two sections.

2.1 INFO Finite magnetized geometries

In case of a hard magnetization, in the sense that the magnetization has compact support and drops suddenly to zero outside a volume V, an interface term has to be included in addition to the volume term in equation (2.57). At the border of the volume the discontinuous magnetization acts like an effective magnetic surface charge density

$$\sigma_M = \mathbf{a} \cdot \mathbf{M},$$

with the surface normal vector $\mathbf{a}$ [95]. The solution to the magnetic potential in the volume now can be written as

$$\Phi_m(\mathbf{x}) = -\frac{1}{4\pi}\int_V d\mathbf{x}' \frac{\nabla' \cdot \mathbf{M}(\mathbf{x}')}{\|\mathbf{x}-\mathbf{x}'\|} + -\frac{1}{4\pi}\oint_{\partial V} \frac{d\mathbf{A}' \cdot \mathbf{M}(\mathbf{x}')}{\|\mathbf{x}-\mathbf{x}'\|}.$$

For a uniform magnetization throughout the volume V, so that there is no boundary surface, the first term vanishes and only the surface contributes to the potential.

For example, a magnetized sphere of radius R contains a magnetic field of $\mathbf{H}_{\text{sphere}} = -\mathbf{M}_0/3$ regardless of the size [95]. This still holds for an infinitely large sphere, which is a fundamentally different result as in the case of no boundaries at all!

To illustrate the issue further, consider a cylinder of radius R and length $2L$. The magnetic field inside the volume on the symmetry axis is given by

$$\mathbf{H}_{\text{cylinder}} = -\frac{\mathbf{M}_0}{2}\left(\frac{z-L}{\sqrt{R^2+(z-L)^2}} - \frac{z+L}{\sqrt{R^2+(z+L)^2}} + 2\right).$$

Scaling the cylinder to infinite size while fixing the aspect ratio between L and R to $\gamma = R/L$ leads to a non-vanishing magnetic field

$$\mathbf{H}_{\text{cylinder}} \xrightarrow[R,L\to\infty]{\gamma=const} \left(\frac{1}{\sqrt{1+\gamma^2}} - 1\right)\mathbf{M}_0,$$

Depending on the aspect ratio, an arbitrary magnetic field (and therefore magnetic flux) can be constructed for an infinitely large cylinder.

In both cases energy is »lost« to the stray field outside the volume that is not available any more for the field inside. The example of a cylinder is particularly illustrative, because increasing the aspect ratio γ effectively shifts energy from the inside field to the stray field that escapes the volume at the circular caps of the cylinder. Conceptionally, the $\mathbf{H}$-field is generated by an effective circular current $\propto \nabla \times \mathbf{M}$ at the cylinder's mantle — the volume contributions cancel each other. Consequently, having a very long cylinder, $\gamma \to 0$, pushes the stray field located at the caps arbitrary far away and leaves most energy for the field inside, i.e. $H \to 0$. It is the same result as in the case of absent boundaries. On the other hand, an infinitely wide cylinder, $\gamma \to \infty$, has almost all energy in the stray field, i.e. $H \to M_0$. Therefore, the magnetic flux B inside is zero.

2.7 Continuum fluid dynamics

A simple fluid is a substance that hardly resists deformation (or more precisely shear forces) and is continuously deformed under its influence. The molecules of a fluid are only loosely coupled resulting in a very flexible molecular structure. A fluid can be a liquid, but the term can generalize to gases and plasmas as well. By comparison, the molecules of a solid are tightly coupled and tend to oscillate around a fixed position. Hence, a solid body resists (small) deformation and restores its original shape after the influence has ceased.

Although an explicit treatment of these complex dynamics of all fluid molecules is in principle feasible for small systems, on larger scales it is very difficult and costly. Luckily, for length and time scales larger than the molecular scale a continuum approach, similar to the magnetization discussed in Section 2.6.3, is very successful. Conservation laws for mass, momentum obeyed by the fluid molecules, still must hold for a continuous field and can be used to describe the dynamics of an infinitesimal fluid element, the so-called fluid parcel.

2.7.1 Navier-Stokes equation

The Navier-Stokes equation is derived from the conservation of momentum for the fluid elements, an infinitesimal parcel of a continuous flow field. The momentum conservation can be formulated as [97]

$$\rho \frac{D}{Dt}\mathbf{u} = \nabla \cdot \boldsymbol{\sigma} + \mathbf{f}, \tag{2.64}$$

with the flow velocity $\mathbf{u}$, the density of the fluid ρ, the stress in the fluid [8], and a body force density $\mathbf{f}$. The *substantial* or *material derivative* is given by

$$\frac{D}{Dt}g \equiv \partial_t g + \mathbf{u} \cdot \nabla g$$

and describes the rate of change of a physical quantity g of a fluid element in a comoving frame.

The tensor $\boldsymbol{\sigma}$ denotes the Cauchy stress tensor. Its isotropic part describes the pressure in the fluid and the anisotropic part includes the shear stresses. For a Newtonian fluid it is linear with respect of the rate of strain tensor $\mathbf{E}$

$$\boldsymbol{\sigma} \equiv -P\mathbb{1} + 2\eta\mathbf{E} + \left(\zeta - \frac{2}{3}\eta\right)\mathbb{1}\nabla \cdot \mathbf{u}, \tag{2.65}$$

with the pressure P and the (dynamic) viscosity η, the bulk viscosity ζ, and the unit matrix $\mathbb{1}$. The rate of strain tensor is given by

$$\mathbf{E} = \frac{1}{2}\left(\nabla\mathbf{u} + (\nabla\mathbf{u})^\top\right),$$

where the vector gradient and its transpose is defined as $(\nabla\mathbf{u})_{ij} = \partial_{x_i} u_j$ and $(\nabla\mathbf{u})^\top{}_{ij} = \partial_{x_j} u_i$.

The density ρ of the fluid is unknown as well. Therefore, another equation is needed and can be given by the mass conservation equation of the fluid:

$$\frac{D}{Dt}\rho = -\rho\nabla \cdot \mathbf{u}.$$

In case of an incompressible fluid the left side is zero and it follows that the flow is divergence free, i.e. $\nabla \cdot \mathbf{u} = 0$.

By substituting the Newtonian stress tensor in equation (2.65) back into the momentum conservation equation (2.64) and assuming $\nabla \cdot \mathbf{u} = 0$, the Navier-Stokes equation for an incompressible Newtonian fluid is derived:

$$\rho\frac{D}{Dt}\mathbf{u} = \nabla \cdot \boldsymbol{\sigma} + \mathbf{f} = \eta\,\Delta\,\mathbf{u} - \nabla P + \mathbf{f}. \tag{2.66}$$

At time and length scales of an active colloidal suspension, where inertia only plays a negligible role, the Navier-Stokes equation can be further simplified, leading to the Stokes equation.

[8] Concerning the used sign convention: Upon any (imaginary) surface that divides a body, the force that one part exerts on the other is given by $\mathrm{d}\mathbf{A}\,\boldsymbol{\sigma}$, where $\mathrm{d}\mathbf{A}$ an infinitesimal surface element vector, pointing outwards, the force acts on.

2.7.2 Stokes equation

By scaling the length, velocity, and time in the Navier-Stokes equation by characteristic values L, u_0 and t_0, equation (2.66) yields [9]

$$\mathrm{Re}_T\, \partial_t' \mathbf{u}' + \mathrm{Re}\, \mathbf{u}' \cdot \nabla' \mathbf{u}' = \Delta' \mathbf{u}' - \nabla P' + \mathbf{f}',$$

where the primed quantities are dimensionless. The Reynolds number $\mathrm{Re} = \frac{\rho u_0 L}{\eta}$ is a measure comparing inertial and viscous forces. The oscillatory Reynolds number $\mathrm{Re}_T = \frac{\rho L^2}{\eta t_0}$, also referred to as Stokes number, indicates the relevance of the explicit time dependency and is the ratio between the viscous and the characteristic time scale [9, 70]. Both numbers are small ($\ll 1$) for microswimmers and consequently, the material derivative can be neglected and the left side of equation (2.66) vanishes in good approximation. The equations

$$\eta\, \Delta\, \mathbf{u} - \nabla P = \nabla \cdot \boldsymbol{\sigma} = -\mathbf{f} \tag{2.67}$$

$$\nabla \cdot \mathbf{u} = 0, \tag{2.68}$$

are called the incompressible Stokes equations.

The Stokes equation is linear and time-independent. Because of the time separation between typical time scales of the dynamics of a microswimmer and the fluid-dynamics, the fluid reacts virtually instantaneously to external perturbations. This leads to a quasi-static approximation.

After having derived the Stokes equations to describe the fluid dynamics, the interaction between the flow and the immersed microswimmer can be studied.

2.8 Interactions with the flow field

Microswimmers moving through a solvent exert forces on the surrounding fluid. The Stokes equation (2.67) describes how the solvent reacts to the resulting stresses given by $\nabla \cdot \boldsymbol{\sigma} = -\mathbf{f}$, for a force density $\mathbf{f}$ exerted on the fluid. Other particles exposed to the resulting flow field are influenced in their dynamics. These fluid-mediated interactions between particles are called hydrodynamic interactions.

In reality, every movement of a particle A influences a particle B which in turn influences A, and back and forth[9]. These higher order interactions can be of importance

[9] Taking one reflection into account, leads to the Rotne-Prager approximation. The Rotne-Prager tensor is the next order correction of the Oseen tensor [70] introduced below.

in the case of passive particles [98] and in the case of near-field interactions, but are usually negligible for (dilute) suspensions of active particles [62]. In the following, only active and fairly dilute colloidal suspensions are considered. Therefore, higher order interactions are neglected and the interactions are restricted to far-field hydrodynamics.

For the hydrodynamic interaction, two stress contributions are considered: an active stress $\boldsymbol{\sigma}_a$ as a result of the self-propulsion of the particle and an alignment stress $\boldsymbol{\sigma}_m$ created by particles that are rotated in the direction of a magnetic field.

2.8.1 Force dipole approximation

A biological microswimmer typically propels itself by converting internal energy into a periodic deformation of its body. Because of the Scallop Theorem, stated in the introduction in Section 1.2, this deformation has to be non-reciprocal in time in order to induce a net thrust in one direction. Some artificial swimmers, for example Janus particles using self-phoresis, employ different, chemical-reactive based, self-propulsion mechanisms [14, 49, 99]. However, the results of this section hold for all force-free self-propelled particles, including phoretic swimmers. The aim of this section is to derive the flow field $\mathbf{u}$ that is the result of the self-propulsion of a microswimmer and eventually to obtain the mean flow field for an ensemble of swimmers. As a first step, the stress $\boldsymbol{\sigma}_\mathbf{p}$ generated by a single microswimmer is sought.

As discussed in the previous Section, the flow field $\mathbf{u}$ is described by the incompressible Stokes equations (2.7.2) and (2.68). The solution to these equations can be constructed using its Green's function, the so called Oseen tensor [100]. The Oseen tensor is the solution of the Stokes equation for a point force $\mathbf{F}$ acting on the fluid, for example through a point-like forced particle,

$$\eta\Delta\mathbf{u}(\mathbf{x}) - \nabla P(\mathbf{x}) = -\mathbf{F}\delta(\mathbf{x}) \Rightarrow \mathbf{u} = \mathbb{O}\cdot\mathbf{F}.$$

The Oseen tensor is given by [100]

$$\mathbb{O}(\mathbf{x}) \equiv \frac{1}{8\pi\eta x}\left(\mathbb{1} + \frac{\mathbf{xx}}{x^2}\right). \tag{2.69}$$

The pressure P is of no consequence for the dynamics and is therefore irrelevant in the discussion[10].

More generally, given a force density $\mathbf{f} = -\nabla \cdot \boldsymbol{\sigma}$, the solution is

$$\begin{aligned}\mathbf{u}(\mathbf{x}) &= -(\mathbb{O} * (\nabla \cdot \boldsymbol{\sigma}))(\mathbf{x}) \\ &= (\mathbb{O} * \mathbf{f})(\mathbf{x}) \\ &= \int \mathrm{d}\mathbf{x}'\, \mathbb{O}(\mathbf{x} - \mathbf{x}') \cdot \mathbf{f}(\mathbf{x}'). \end{aligned} \tag{2.70}$$

In order to find an approximate expression for the stress caused by a microswimmer, the Oseen tensor can be expanded into its multipole contributions. Similar to electrostatics, $\mathbb{O}(\mathbf{x} - \mathbf{x}')$ can be written as a Taylor series in $\mathbf{x}'$ around $\mathbf{x}_0 = 0$,

$$\begin{aligned}\mathbb{O}(\mathbf{x} - \mathbf{x}') &= \sum_n \frac{(-1)^n}{n!} (\mathbf{x}' \cdot \nabla)^n \mathcal{O}(\mathbf{x}) \\ &= \mathbb{O}(\mathbf{x}) - \mathbf{x}' \cdot \nabla \mathbb{O}(\mathbf{x}) + \mathcal{O}(\mathbf{x}'\mathbf{x}'). \end{aligned} \tag{2.71}$$

Substituting equation (2.71) into equation (2.70) results in a multipole expansion of the flow field,

$$\begin{aligned}\mathbf{u}(\mathbf{x}) &= \mathbb{O}(\mathbf{x}) \cdot \int \mathrm{d}\mathbf{x}'\, \mathbf{f}(\mathbf{x}') - \left(\int \mathrm{d}\mathbf{x}'\, \mathbf{x}' \otimes \mathbf{f}(\mathbf{x}') \right) : \nabla \mathbb{O}(\mathbf{x}) + \dots \\ &= \mathbb{O}(\mathbf{x}) \cdot \mathbf{F} - \mathbf{D} : \nabla \mathbb{O}(\mathbf{x}) + \dots, \end{aligned} \tag{2.72}$$

with $\mathbf{A} : \mathbf{B} = A_{ij} B_{ij}$, $\nabla \mathbb{O}(\mathbf{x}) = \partial_{x_i} O_{jk}(\mathbf{x})\ \mathbf{e}_i \otimes \mathbf{e}_j \otimes \mathbf{e}_k$, the monopole contribution $\mathbf{F}$, and the dipole moment tensor

$$\mathbf{D} = \int \mathrm{d}\mathbf{x}'\, \mathbf{x}' \otimes \mathbf{f}(\mathbf{x}'). \tag{2.73}$$

Here, the explicit operator $\otimes$ denoting a dyadic product is used to clarify the notation.

The fundamental force dipole solution $\nabla \mathbb{O}(\mathbf{x})$, consisting of the *stresslet* (symmetric part) and the *rotlet* (anti-symmetric part), is element of $\mathcal{O}(x^{-2})$, the next higher contribution goes with $\mathcal{O}(x^{-3})$ and so on. As a consequence, the far field created by a forced particle immersed in a fluid is often well described by a point force (monopole or *stokeslet*) and a force dipole contribution [101]. An illustration of the first two multipole contributions can be seen in Figure 2.5. The monopole term vanishes for a

[10] It corresponds to the isotropic part $\propto P\mathbb{1}$ of the stress tensor $\boldsymbol{\sigma}$. Therefore, the Stokes equation can also be written as $\eta \Delta \mathbf{u} = \nabla \cdot \boldsymbol{\sigma}'$, where $\boldsymbol{\sigma}'$ includes the isotropic pressure. Moreover, there also exists a simple Green's function for the pressure, if the need to handle it arises [100].

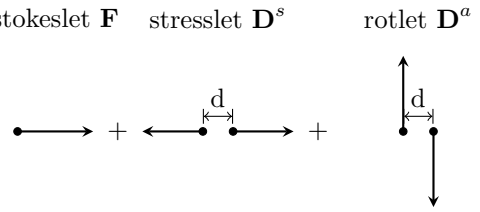

Fig. 2.5.: Illustration of the first two multipole contributions to a Stokes flow. The *stokeslet* is the monopole contribution, the *stresslet* $\mathbf{D}^a$ and *rotlet* $\mathbf{D}^s$ the symmetric and asymmetric part of the dipole moment. The stresslet corresponds to a force-dipole, the rotlet to a point torque. The correct multipole expansion is obtained in the limit of $d \to 0$.

force-free microswimmer, as will be shown in the following.

A microswimmer, by definition, self-propels due to *internal* forces only. A mechanical swimmers for example ingeniously relies on modulating the friction in the fluid across its surface (drag-based thrust [62]) in order to propel itself[11]. It does not transfer any net-momentum to the fluid. Thus, a self-propelled particle, in the absence of an external body force, is as a whole force- and torque-free [62], i.e.

$$\mathbf{F}_p(t) = 0 \tag{2.74}$$

$$\mathbf{M}_p(t) = 0. \tag{2.75}$$

Given the stress $\boldsymbol{\sigma}$ in the fluid, the net force on the swimmer is given by the integral over the particle's surface ∂V_p of the stress

$$\mathbf{F}_p(t) = \oint_{\partial V_p} \mathrm{d}\mathbf{A} \cdot \boldsymbol{\sigma}(\mathbf{x}, t), \tag{2.76}$$

with the surface normal element $\mathrm{d}\mathbf{A}$ pointing outwards. Similarly, the torque on a swimmer in a fluid is given by

$$\mathbf{M}_p(t) = -\int_{V_p} \mathrm{d}\mathbf{x}\, \mathbf{x} \times \mathbf{f}(\mathbf{x}, t). \tag{2.77}$$

[11] For illustration, imagine a two bead-swimmer that can change the size of the beads and their relative distance (also known as Vic's swimmer, see Ref. [102]). The velocity of a forced ($\mathbf{F}$) bead depends on its friction $\xi_{1,2}(R)$, $\dot{\mathbf{x}} = \xi^{-1}(R_{1,2})\mathbf{F}_{1,2}$, which it can modulate over the bead-size. Because of Newton's third law, the forces on the beads match in magnitude, $\mathbf{F}_1 = -\mathbf{F}_2$, so that is in total force-free and a fixed sized swimmer would not move. However, by changing the friction coefficient as well, i.e. by introducing a drag anisotropy, propulsion can be achieved [62, 102].

Because of Gauß' divergence theorem, the surface force in equation (2.76) can be identified with a body force density $\mathbf{f} = -\nabla \cdot \boldsymbol{\sigma}$ acting on the fluid, yielding the monopole contribution of the multipole expansion in equation (2.72)

$$\mathbf{F}_p(t) = \int_{V_p} \mathrm{d}\mathbf{x}\, \nabla \cdot \boldsymbol{\sigma}(\mathbf{x}, t) = -\int_{V_p} \mathrm{d}\mathbf{x}\, \mathbf{f}(\mathbf{x}, t) = \mathbf{F}.$$

For a force-free microswimmer, as established above, the total force $\mathbf{F}_p$ is zero, i.e. $\mathbf{F}_p$. Thus, the monopole contribution equal to $\mathbf{F}_p$ vanishes as well and in the far field only the force dipole solution remains.

In summary, by only taking contributions up to the dipolar order into account, the stress in the fluid due to a swimming particle at the position $\mathbf{y}$ with an orientation unit vector $\mathbf{n}$ can be approximated by

$$\boldsymbol{\sigma}_p(\mathbf{x}, \mathbf{y}, \mathbf{n}) = -\mathbf{D}(\mathbf{n})\delta(\mathbf{x} - \mathbf{y}). \tag{2.78}$$

This can be directly seen from the multipole expansion in equation (2.72) and the definition of the dipole moment (2.73) by substitution. Note that the dipole moment of a particle $\mathbf{D}$ depends on the particle's orientation.

Under the assumption of a first order interaction, as discussed in the introduction of this section, the stress field of N point-like particles is given by a linear superposition of the single particle stresses. Therefore, the total stress in the fluid at the location $\mathbf{x}$ caused by particles at positions $\mathbf{y}_j$ and orientations $\mathbf{n}_j$ is given by

$$\boldsymbol{\sigma}(\mathbf{x}, \{\mathbf{y}\}, \{\mathbf{n}\}) = \sum_{j=1}^{N} \boldsymbol{\sigma}_p(\mathbf{x}, \mathbf{y}_j, \mathbf{n}_j) = -\sum_{j=1}^{N} \mathbf{D}(\mathbf{n}_j)\delta(\mathbf{x} - \mathbf{y}_j). \tag{2.79}$$

In a probabilistic description of Brownian particles their configuration is encoded in the PDF Ψ, as discussed in Section 2.3. Hence, similar to the mean magnetization in equation (2.48), the mean stress $\overline{\boldsymbol{\sigma}}[\Psi]$ is given by the expectation value,

$$\begin{aligned}
\overline{\boldsymbol{\sigma}}(\mathbf{x}, t) &= \langle \boldsymbol{\sigma}(\mathbf{x}, \{\mathbf{y}\}, \{\mathbf{n}\}) \rangle \\
&= \left(\prod_{i=1}^{N} \int \mathrm{d}\mathbf{y}_i \mathrm{d}\mathbf{n}_i \right) \Psi(\{\mathbf{y}\}, \{\mathbf{n}\}, t)\, \boldsymbol{\sigma}(\mathbf{x}, \{\mathbf{y}\}, \{\mathbf{n}\}) \\
&= -\left(\prod_{i=1}^{N} \int \mathrm{d}\mathbf{y}_i \mathrm{d}\mathbf{n}_i \right) \Psi(\{\mathbf{y}\}, \{\mathbf{n}\}, t) \sum_{j=1}^{N} \mathbf{D}(\mathbf{n}_j)\, \delta(\mathbf{x} - \mathbf{y}_j) \\
&= -\sum_{j=1}^{N} \int \mathrm{d}\mathbf{n}_j \mathbf{D}(\mathbf{n}_j) \left(\prod_{i \neq j} \int \mathrm{d}\mathbf{y}_i \mathrm{d}\mathbf{n}_i \right) \int \mathrm{d}\mathbf{y}_j \Psi(\{\mathbf{y}\}, \{\mathbf{n}\}, t)\, \delta(\mathbf{x} - \mathbf{y}_j)
\end{aligned}$$

$$
\begin{aligned}
&= -\sum_{j=1}^{N} \int \mathrm{d}\mathbf{n}_j \mathbf{D}(\mathbf{n}_j) \left(\prod_{i \neq j} \int \mathrm{d}\mathbf{y}_i \mathrm{d}\mathbf{n}_i \right) \Psi(\{\mathbf{y}\}|_{\mathbf{y}_j = \mathbf{x}}, \{\mathbf{n}\}, t) \\
&= -\sum_{j=1}^{N} \int \mathrm{d}\mathbf{n}_j \, \frac{1}{N} \Psi_1(\mathbf{x}, \mathbf{n}_j, t) \, \mathbf{D}(\mathbf{n}_j) \\
&= -\int \mathrm{d}\mathbf{n} \, \Psi_1(\mathbf{x}, \mathbf{n}, t) \, \mathbf{D}(\mathbf{n}) \\
&= -\langle \mathbf{D}(\mathbf{n}) \rangle_{\mathbf{n}},
\end{aligned} \tag{2.80}
$$

where $\langle \bullet \rangle_{\mathbf{n}} \equiv \int_{\mathbb{S}^2} \mathrm{d}\mathbf{n} \; \Psi_1 \bullet$ denotes the orientational expectation value. In the second to last step the interchangeability of the particles, equation (2.24), was implicitly used. The sum is over identical terms, so that the sum can replaced by the number of particles N, i.e. $\sum_i \mapsto N$. Furthermore, the definition of the single particle distribution Ψ_1 in equation (2.25) was substituted and the particle index has been dropped, without loss of generality. In the following, the mean stress is just denoted by $\boldsymbol{\sigma}$, dropping the overline. Eventually, the mean flow field $\mathbf{u}$ of a dipolar suspension is given by,

$$
\mathbf{u}(\mathbf{x}) = \int \mathrm{d}\mathbf{x}' \mathbb{O}(\mathbf{x} - \mathbf{x}') \cdot \left(\nabla \cdot \int \mathrm{d}\mathbf{n} \, \Psi_1(\mathbf{x}, \mathbf{n}, t) \, \mathbf{D}(\mathbf{n}) \right).
$$

On a side note, a force-dipole is momentum conserving, thus the resulting total flow surrounding force-free dipolar swimmers is given by

$$
\int_{\mathbb{R}^3} \mathrm{d}\mathbf{x} \, \mathbf{u}(\mathbf{x}) = -\int_{\mathbb{R}^3} \mathrm{d}\mathbf{x} \, \mathbf{D} : \nabla \mathbb{O}(\mathbf{x}) = 0, \tag{2.81}
$$

and vanishes — which remains true for a superposition of force-dipoles. This property becomes relevant in Chapter 3, when the flow field is solved numerically.

In the following, closed expressions for the active dipole moment $\mathbf{D}_a$, modelling the leading order effect of self-propulsion on the fluid, and for the dipole moment of magnetic alignment $\mathbf{D}_m$ due to an external torque, are derived.

2.8.2 Active stress

In order to acquire an expression for the active dipole moment $\mathbf{D}_a(\mathbf{n})$, further properties of the dipole moment can be used.

Because the divergence of the Oseen tensor $\nabla \cdot \mathbb{O} = 0$ vanishes (a consequence of the incompressibility assumption of the fluid), the isotropic part of a dipole moment $\mathbf{D}$ is irrelevant for the dynamics [97]:

$$\begin{aligned}\mathbf{D} : \nabla\mathbb{O} &= \sum_{k,i,j} \mathbf{e}_k D_{ij} \partial_{x_i} O_{jk} \\ &= \sum_{k,i} \mathbf{e}_k D_{ii}\, \partial_{x_i} O_{ik} + \sum_{k,i\neq j} \mathbf{e}_k D_{ij} \partial_{x_i} O_{jk} \\ &= \sum_{k,i} \mathbf{e}_k (D_{ii} - \delta_{ii}\frac{1}{3}\operatorname{Tr}\mathbf{D})\, \partial_{x_i} O_{ik} + \frac{1}{3}\operatorname{Tr}\mathbf{D} \underbrace{\nabla \cdot \mathbb{O}}_{=0} + \mathbf{e}_k \sum_{k,i\neq j} D_{ij} \partial_{x_i} O_{jk}.\end{aligned}$$

In the second line, the dipole moment tensor $\mathbf{D}$ is split into its diagonal and off-diagonal part. In the last line, the diagonal part is further split into a traceless and its isotropic part, given by the second term which in total vanishes. Hence, two dipole moment tensors only differing in their isotropic part are isomorphic in terms of the dynamics, $\mathbf{D} + \alpha\mathbb{1} \cong \mathbf{D}, \alpha \in \mathbb{R}$.

In the absence of an external torque, the total torque $\mathbf{M}_p = 0$ is zero, which implies that the active dipole moment tensor $\mathbf{D}_a$ must be symmetric, as can be seen from the definition of $\mathbf{M}_p$:

$$\begin{aligned}\mathbf{M}_p = \int \mathrm{d}\mathbf{x}'\, \mathbf{x}' \times \mathbf{f}(\mathbf{x}') &= \mathbf{e}_i \int \mathrm{d}\mathbf{x}'\, \varepsilon_{ijk}\, x'_j f_k(\mathbf{x}') \\ &= \mathbf{e}_i \varepsilon_{ijk} D_{a,jk} \\ &\overset{!}{=} 0.\end{aligned}$$

From $\varepsilon : \mathbf{D}^a = 0$, it follows that $\mathbf{D}_a = \mathbf{D}_a^\top$, using the Levi-Civita symbol $\boldsymbol{\varepsilon}$ (a total antisymmetric pseudo tensor). Therefore, $\mathbf{D}^a$ is symmetric.

If the force density $\mathbf{f}$ is additionally axially symmetrical, the dipole moment tensor of a self-propelled particle can be written in terms of a traceless dyadic product of the orientation vector $\mathbf{n}$, pointing along the principal direction[12],

$$\mathbf{D}_a \equiv D_a \left(\mathbf{nn} - \frac{1}{3}\mathbb{1} \right). \tag{2.82}$$

Equation (2.82) finally defines the active dipole moment $\mathbf{D}_a$ with a strength D_a. The tensor $\mathbb{Q} = \left\langle \mathbf{nn} - \frac{1}{3}\mathbb{1} \right\rangle_{\mathbf{n}}$ is called the nematic tensor[13]. Note that it is invariant under point mirroring, $\mathbf{n} \mapsto -\mathbf{n}$, reflecting the symmetry of the force dipole.

[12] Equation (2.82) can be derived, assuming $\check{\mathbf{z}}$ is the symmetry axis, by recognizing that $\mathbf{f} = \mathbf{f}(\vartheta) \Rightarrow \mathbf{D} \propto \check{\mathbf{z}}\check{\mathbf{z}}$. That is, up to an irrelevant isotropic part, which is isomorphic to $\mathbf{nn}$ under $\mathrm{SO}(3)$, i.e. there exists a rotational transformation between both expressions.

[13] In the literature about liquid crystals, a prefactor of $\frac{3}{2}$ is often added [103].

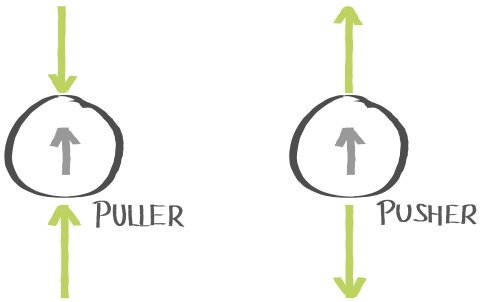

Fig. 2.6.: Depiction of a force dipole in *puller* and *pusher* configuration.

In summary, according to equation 2.80, the mean active stress generated collectively by a suspension of microswimmers is given by

$$\boldsymbol{\sigma}_a(\mathbf{x},t) \equiv -D_a \int_{\mathbb{S}^2} \mathrm{d}\mathbf{n}\ \Psi_1(\mathbf{x},\mathbf{n},t)\ \left(\mathbf{nn} - \frac{1}{3}\mathbb{1}\right) = -D_a \left\langle \mathbf{nn} - \frac{1}{3}\mathbb{1} \right\rangle_{\mathbf{n}} (\mathbf{x},t). \quad (2.83)$$

Depending on the details of the swimming mechanism, dipolar microswimmers fall into two categories: pushers ($D_a < 0$) and pullers ($D_a > 0$). A pusher generates forces pointing away from his centre, whereas the forces of pullers points towards it. Figure 2.6 illustrates the concept. The flow field of a pusher is depicted in Figure 2.7 revealing its dipolar nature. A puller of the same strength has the same flow field but all the signs are reversed.

The prefactor of the active stress can be roughly estimated with the help of Stokes' law. The internal forces of the swimming actuation should be comparable to the local friction force in magnitude and proportional to the swimming speed U_0 of the swimmer. Given a characteristic length scale of the swimmer ℓ (for example $\ell \approx R$, with the radius R of a spherical swimmer), the friction force, and therefore the internal force, is approximated using Stokes' law, given by

$$F_f \approx \xi_{\mathrm{t}} U_0 = 6\pi\eta\ell U_0,$$

with the dynamic viscosity η. Under this assumption the active dipole moment can be estimated by

$$D_a \approx F_f\, \ell,$$

according to the virial stress derived in the Kirkwood-theory of suspensions [21, 62, 104]. It should be noted, that the actual dipole moment strength depends on the precise swimming mechanism, so that the above estimate should be only be used cautiously as an order of magnitude estimate.

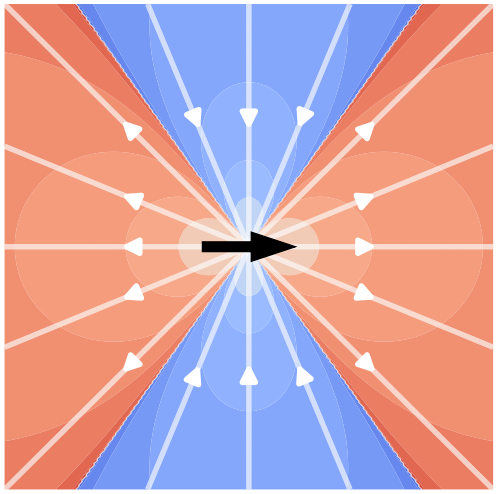

Fig. 2.7.: Flow field of a single force dipole (pusher) in the centre of the image. The white lines are stream lines, in the background contour lines of the velocity magnitude are shown. Blue corresponds to velocities going towards the swimmer, red going away from it. For a puller all signs (and arrow directions) are inverted. The field for a swimmer going into the opposite direction is exactly the same because of the symmetry of the force-dipole.

By plugging a single particle stress of the form $\boldsymbol{\sigma}_p(\mathbf{x}, \mathbf{n}) = -D_a(\mathbf{nn} - 1/3\mathbb{1})\delta(\mathbf{x})$ into equation (2.70), the far-field of the flow of a force-dipole with a dipole strength D_a can also be given in a closed form,

$$\mathbf{u}(\mathbf{x}) = \frac{D_a}{8\pi\eta x^3}\left[-1 + 3\frac{(\mathbf{x}\cdot\mathbf{n})^2}{x^2}\right]\mathbf{x}.$$

The stress a rotating particle exerts on the fluid due to an external torque can also be described in terms of a dipole moment. However, unlike a force-dipole (stresslet), which is captured by the symmetric part of the dipole moment tensor, an external torque is expressed by its anti-symmetric part (rotlet).

2.8.3 Alignment stress in an external field

Particles rotating due to an external torque exert an alignment stress $\boldsymbol{\sigma}_m$ on the fluid as they drag the surface fluid layer with them. In case of a magnetic field the external torque is given by

$$\mathbf{M}_B = \mu\mathbf{n} \times \mathbf{B}.$$

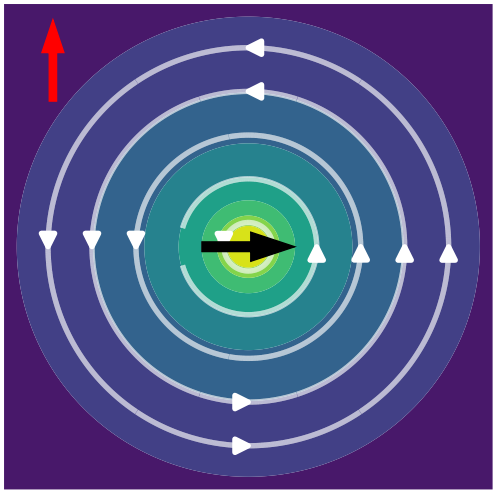

Fig. 2.8.: Flow around a single particle rotating towards the direction of an external magnetic field pointing in y-direction (red arrow).

Hence, the torque on a particle $\mathbf{M}_p$ can be expressed with the help of the dipole moment tensor, defined in equation (2.73), by

$$\begin{aligned}
\mathbf{M}_B = \mathbf{M}_p &= \int \mathrm{d}\mathbf{x}\, \mathbf{x} \times f(\mathbf{x}) \\
&= \check{\mathbf{e}}_i \int \mathrm{d}\mathbf{x}\, \varepsilon_{ijk} x_j f_k(\mathbf{x}) \\
&= \boldsymbol{\varepsilon} : \mathbf{D} \\
&= \check{\mathbf{e}}_i \frac{1}{2} \left(\varepsilon_{ijk} D_{ij} + \varepsilon_{ijk} D_{ij} \right) \\
&= \check{\mathbf{e}}_i \frac{1}{2} \left(\varepsilon_{ijk} D_{ij} - \varepsilon_{ikj} D_{ij} \right) \\
&= \check{\mathbf{e}}_i \varepsilon_{ijk} \frac{1}{2} \left(D_{ij} - D_{ji} \right) \\
&= \boldsymbol{\varepsilon} : \mathbf{D}^a,
\end{aligned} \tag{2.84}$$

with the Levi-Civita symbol $\boldsymbol{\varepsilon}$, an orthonormal basis $\check{\mathbf{e}}$, and the antisymmetric part of the dipole moment tensor $\mathbf{D}^a = \frac{1}{2}\left(\mathbf{D} - \mathbf{D}^\top\right)$. Note that $\boldsymbol{\varepsilon} : \mathbf{D} = \boldsymbol{\varepsilon} : \mathbf{D}^a$ for any matrix $\mathbf{D}$. The same result was obtained in Ref. [97]. By multiplying equation (2.84) with $\boldsymbol{\varepsilon}$ and using $\varepsilon_{ijk}\varepsilon_{ilm} = \delta_{jl}\delta_{km} - \delta_{lj}\delta_{mk}$, it follows that given an external torque $\mathbf{M}_B = \mu \mathbf{n} \times \mathbf{B}$, the alignment dipole moment is given by

$$\begin{aligned}
\mathbf{D}_m &= \frac{1}{2} \boldsymbol{\varepsilon} \cdot \mathbf{M}_B(\mathbf{n}) \\
&= \frac{\mu B}{2} \left(\mathbf{n}\check{\mathbf{B}} - \check{\mathbf{B}}\mathbf{n} \right),
\end{aligned} \tag{2.85}$$

with $\mathbf{B} = B\check{\mathbf{B}}$.

The mean alignment stress contribution is found analogously to equation (2.80) by

$$\begin{aligned}\boldsymbol{\sigma}_m(\mathbf{x},t) &\equiv -\frac{D_m}{2}\int_{\mathbb{S}^2} \mathrm{d}\mathbf{n}\ \Psi_1(\mathbf{x},\mathbf{n},t)\ \left(\mathbf{n}\check{\mathbf{B}} - \check{\mathbf{B}}\mathbf{n}\right)\\ &= -\frac{D_m}{2}\left(\langle\mathbf{n}\rangle_{\mathbf{n}}\check{\mathbf{B}} - \check{\mathbf{B}}\langle\mathbf{n}\rangle_{\mathbf{n}}\right)(\mathbf{x},t),\\ &= -\frac{D_m}{2}\left(\mathbf{p}\check{\mathbf{B}} - \check{\mathbf{B}}\mathbf{p}\right)(\mathbf{x},t),\end{aligned} \tag{2.86}$$

with $D_m = \mu B$.

For magnetic suspensions of passive particles, the same hydrodynamic stress contribution was found [105]. Figure 2.8 shows the flow field resulting from the alignment stress for a particle orientated along the x-axis and an external magnetic field along the y-axis.

In summary, magnetic microswimmers in an external torque field cause active and alignment stresses in the fluid. The mean total stress $\boldsymbol{\sigma}$ is therefore generated by the combined dipole moments, given in equation (2.83) and equation (2.86), of every particle, so that

$$\boldsymbol{\sigma} = -\langle\mathbf{D}_a + \mathbf{D}_m\rangle_{\mathbf{n}}.$$

Naturally, the relationship between the flow field and the particle dynamics is not one-sided. The influence of the flow field on the particles dynamics is discussed in the following.

2.8.4 Particles in a flow field

The translational motion of a small, rigid colloid due to the fluid flow is in very good approximation equal to the local undisturbed flow $\mathbf{u}$ (in absence of the particle) of the fluid. The advection velocity $\mathbf{v}$ of an immersed particle is given by Faxén's first law [70],

$$\mathbf{v} = -\frac{1}{\xi_{\mathrm{t}}}\mathbf{F}_p + \mathbf{u} + \frac{R^2}{6}\Delta\,\mathbf{u}.$$

This implicitly assumes *no-slip* boundary conditions, i.e. the velocity of the fluid at the surface of the particle is equal to the velocity of the corresponding surface element of the particle. Or to put it differently, the fluid layer closest to the particle's surface sticks to the surface. In case of a point-like particle, the radius $R \to 0$ goes to zero and the last term in the equation above vanishes. Furthermore, the force the fluid exerts on the particle $\mathbf{F}_p$ vanishes as well for a microswimmer, as established in

Section 2.8.1, equation (2.76). Hence, the advection velocity of the particle is just given by

$$\mathbf{v} = \mathbf{u}. \tag{2.87}$$

This means that a particle follows the streamlines of the local flow. A microswimmer swims in the moving fluid, i.e. the advection and self-propulsion velocities add up.

In addition, the surrounding flow can rotate the particle. Again, the angular velocity $\boldsymbol{\omega}$ of an immersed particle is given by Faxén's 2nd law [70], given by

$$\boldsymbol{\omega} = -\frac{1}{\xi_\mathrm{r}}\mathbf{M}_p + \frac{1}{2}\nabla \times \mathbf{u}.$$

Again, as established in Section 2.8.1, for a microswimmer the torque the fluid exerts on the particle $\mathbf{M}_p$ vanishes and the advective angular velocity is given by

$$\boldsymbol{\omega} = \frac{1}{2}\nabla \times \mathbf{u}. \tag{2.88}$$

Using $\dot{\mathbf{n}} = \boldsymbol{\omega} \times \mathbf{n}$, the change of the orientation $\mathbf{n}$ of a particle, due to a hydrodynamic torque can be written as

$$\dot{\mathbf{n}} = \frac{1}{2}(\nabla \times \mathbf{u}) \times \mathbf{n} \equiv -\mathbf{W} \cdot \mathbf{n}, \tag{2.89}$$

where the vorticity tensor $\mathbf{W}$ has been introduced. It is defined by

$$\mathbf{W} \equiv \frac{1}{2}\left[\nabla\mathbf{u} - (\nabla\mathbf{u})^\top\right]. \tag{2.90}$$

2.9 Units of a model: Nondimensionalization

In order to focus on the essence of the equations, it makes sense to use characteristic units for the system and render the equations dimensionless. Not only does this simplify the equations, it also allows parameters to be introduced that already reflect dependencies between different quantities. The non-dimensional units are used throughout Chapters 4 and 5 for all equations, parameters, and results.

In the presented kinetic model, two out of three dimensions have to be set. These dimensions are: time, length, and speed. It turns out that the rotational diffusion, parametrizing the rotational noise in the model, plays an important role and lends itself to define a characteristic time $t_c = \frac{1}{D_\mathrm{r}}$. In the same spirit, the self-propulsion

speed of the active colloids is a decisive quantity for their dynamics, defining the characteristic speed $u_c = U_0$. The length is derived from both dimensions by $x_c = \frac{t_c}{u_c}$ and can be interpreted as a mean persistent path length before change of orientation happens due to rotational diffusion. Temporal and spatial derivatives and integrals have to be transformed accordingly. Given the original dimensional position $\mathbf{X} = \mathbf{x}x_c$ and time $T = t\,t_c$, the operators transform like

$$\begin{aligned}\partial_T &\mapsto \frac{1}{t_c}\partial_t \\ \nabla_{\mathbf{X}} &\mapsto \frac{1}{x_c}\nabla_{\mathbf{x}} \\ \int_V \mathrm{d}\mathbf{X} &\mapsto x_c^3 \int_{V/x_c^3} \mathrm{d}\mathbf{x},\end{aligned}$$

so that for example for a function $F(\mathbf{X}, T) = F(\mathbf{x}x_c, t\,t_c) \equiv f(\mathbf{x}, t)$ the time derivative is given by

$$\partial_T F(\mathbf{X}, T) = \frac{1}{t_c}\partial_t f(\mathbf{x}, t).$$

See Appendix A.1 for a derivation. As a shorthand, in the dimensionless equations the subscript of the spatial derivative is dropped, $\nabla = \nabla_{\mathbf{x}}$, while the semantics should remain clear from the context.

In order to find a dimensionless equivalent of the single particle distribution Ψ_1, defined in equation (2.25), the distribution is considered on a sufficiently large[14] volume V on which the normalization in equation (2.22) still holds. It follows that

$$\frac{1}{V}\int_V \mathrm{d}\mathbf{X} \int_{\mathbb{S}^2} \mathrm{d}\mathbf{n}\ \Psi_1(\mathbf{X}, \mathbf{n}, T) = N/V = \varrho.$$

Therefore, the single particle distribution is scaled by the inverse number density $1/\varrho$ to make it dimensionless. This defines the dimensionless particle distribution ψ,

$$\psi(\mathbf{x}, \mathbf{n}, t) = \frac{1}{\varrho}\Psi_1(\mathbf{X}/x_c, \mathbf{n}, t/t_c). \tag{2.91}$$

The dimensionless probability density ψ/v is normalized to one,

$$\begin{aligned}\int_v \mathrm{d}\mathbf{x} \int_{\mathbb{S}^2} \mathrm{d}\mathbf{n}\ \psi(\mathbf{x}, \mathbf{n}, t) &= \int_v \mathrm{d}\mathbf{x} \int_{\mathbb{S}^2} \mathrm{d}\mathbf{n}\ \frac{1}{\varrho}\Psi_1(\mathbf{x}x_c, \mathbf{n}, tt_c) \\ &= \frac{1}{x_c^3}\int_V \mathrm{d}\mathbf{X} \int_{\mathbb{S}^2} \mathrm{d}\mathbf{n}\ \frac{1}{\varrho}\Psi_1(\mathbf{X}, \mathbf{n}, T) \\ &= \frac{V}{x_c^3 N}N\end{aligned}$$

[14] By assuming the PDF has finite support because of a finite information propagation, the volume has to be larger than the support over the time interval of interest.

$$
\begin{aligned}
&= v \\
\Leftrightarrow \qquad \frac{1}{v}\int_v \mathrm{d}\mathbf{x}\int_{\mathbb{S}^2}\mathrm{d}\mathbf{n}\ \psi(\mathbf{x},\mathbf{n},t) &= 1,
\end{aligned}
$$

with $V = x_c^3 v$.

In summary, given the original dimensional quantities in capital letters they transform into the dimensionless quantities in lower case as

$$
\begin{aligned}
u_c &= U_0 \\
t_c &= \frac{1}{D_\mathrm{r}} \\
x_c &= \frac{t_c}{u_c} \\
\Psi_1(\mathbf{x}x_c,\mathbf{n},tt_c) &= \varrho\psi(\mathbf{x},\mathbf{n},t) \\
\partial_T &\mapsto \frac{1}{t_c}\partial_t \\
\nabla_\mathbf{X} &\mapsto \frac{1}{x_c}\nabla_\mathbf{x} \\
\nabla_\mathbf{X}^2 = \Delta_\mathbf{X} &\mapsto \frac{1}{x_c^2}\Delta_\mathbf{x} \\
\int_V \mathrm{d}\mathbf{X} &\mapsto x_c^3\int_{V/x_c^3}\mathrm{d}\mathbf{x}.
\end{aligned}
\tag{2.92}
$$

To transform a dimensional Fokker-Planck/Smoluchowski equation of the form

$$
\begin{aligned}
\partial_T\Psi_1(\mathbf{X},\mathbf{n},T) = &-\nabla_\mathbf{X}\cdot\left[\Psi_1(\mathbf{X},\mathbf{n},T)\mathbf{v}_t\right] \\
&-\nabla_\mathbf{n}^\circ\cdot\left[\Psi_1(\mathbf{X},\mathbf{n},T)\mathbf{v}_r\right] \\
&+(D_\mathrm{t}\Delta_\mathbf{X} + D_\mathrm{r}\,\Delta_\mathbf{n}^\circ)\Psi_1(\mathbf{X},\mathbf{n},T)
\end{aligned}
$$

into a non-dimensional form, the rules in (2.92) are applied.

$$
\begin{aligned}
\frac{1}{t_c}\partial_t\Psi_1(\mathbf{x}x_c,\mathbf{n},t\,t_c) = &-\frac{1}{x_c}\nabla_\mathbf{x}\cdot\left[\Psi_1(\mathbf{x}x_c,\mathbf{n},t\,t_c)\mathbf{v}_t\right] \\
&-\nabla_\mathbf{n}^\circ\cdot\left[\Psi_1(\mathbf{x}x_c,\mathbf{n},t\,t_c)\mathbf{v}_r\right] \\
&+(D_\mathrm{t}\frac{1}{x_c^2}\Delta_\mathbf{x} + D_\mathrm{r}\,\Delta_\mathbf{n}^\circ)\Psi_1(\mathbf{x}x_c,\mathbf{n},t\,t_c) \\
\Leftrightarrow \qquad \partial_t\psi(\mathbf{x},\mathbf{n},t) = &-\frac{t_c}{x_c}\nabla_\mathbf{x}\cdot\left[\psi(\mathbf{x},\mathbf{n},t)\mathbf{v}_t\right] \\
&-t_c\,\nabla_\mathbf{n}^\circ\cdot\left[\psi(\mathbf{x},\mathbf{n},t)\mathbf{v}_r\right] \\
&+(D_\mathrm{t}\frac{t_c}{x_c^2}\Delta_\mathbf{x} + t_c D_\mathrm{r}\,\Delta_\mathbf{n}^\circ)\psi(\mathbf{x},\mathbf{n},t).
\end{aligned}
$$

The number density ϱ cancels out. In the chosen units, this equation becomes

$$\begin{aligned}\partial_t \psi(\mathbf{x},\mathbf{n},t) = &-\frac{1}{U_0}\nabla_{\mathbf{x}}\cdot\psi(\mathbf{x},\mathbf{n},t)\mathbf{v}_t \\ &-\frac{1}{D_{\mathrm{r}}}\nabla^{\circ}_{\mathbf{n}}\cdot\psi(\mathbf{x},\mathbf{n},t)\mathbf{v}_r \\ &+(d_t\Delta_{\mathbf{x}}+\Delta^{\circ}_{\mathbf{n}})\psi(\mathbf{x},\mathbf{n},t),\end{aligned}$$

with $d_t \equiv D_{\mathrm{t}}\frac{D_{\mathrm{r}}}{U_0^2}$.

This concludes the introduction to the theoretical background required for the following chapters. In the next chapter, the methodology used for the analysis and solution of the kinetic models developed in this thesis is discussed. First, a method to solve Smoluchowski equation numerically is developed. Second, the linear stability analysis is introduced that allows to approximate the Smoluchowski equation by a linearization around a steady state and gives information about the stability of a steady state.

3 Numerical treatment of Kinetic model equations

The main focus of this thesis is to develop a mean-field kinetic model to study the collective dynamics of interacting active-particles. The particles' dynamics is described in form of a non-linear Smoluchowski coupled to differential interaction-field equations that cannot easily be solved analytically. However, it is possible to find solutions of the linearized equations and there exist numerical methods to solve the full non-linear equations. In this chapter, methods for the analysis and numerical solution (simulation) of a Smoluchowski equation with mean-field long-ranged interactions are introduced and discussed that are extensively used in Chapters 4 and 5. First, a numerical scheme to simulate the Smoluchowski equation is presented in detail. It is based on the correspondence of the stochastic differential equations of Brownian particles, the Langevin equations, and the Smoluchowski equation, describing the evolution of the probability density function (PDF) of the whole particle ensemble. A Langevin integrator is used to numerically evolve a large sample of particles of the ensemble for a small time step. Based on the sample the value of the PDF is estimated at discrete points of a simulation grid. The PDF is needed to calculate the mean interaction fields. The latter are calculated by means of a spectral method [106]. By iterating the whole procedure in a loop, the time evolution of the PDF can be calculated. Second, the method of linear stability analysis is introduced. By linearizing the Smoluchowski equation around a known steady-state, the dynamics near a steady state can be approximated. Specifically, it can be assessed, if a small perturbation of the steady state is growing or decaying and the steady state is stable or unstable, respectively.

A Smoluchowski equation is a second order partial differential equation. Traditionally such an equation can be solved directly by numerical schemes such as the finite-difference, the finite-volume, or by spectral methods[1]. However, for a N-particle Smoluchowski equation that depends on the position and the orientation of the particles this would involve solving the equation on a $5N$-dimensional grid. In case of a mean-field approximation, as discussed in the previous Chapter, the single par-

[1]The finite-volume method has the advantage that the conservative property of the Fokker-Planck equation holds true for the numerical approximation.

ticle distribution still requires a five dimensional grid. That poses a considerable challenge to implement a scheme with good scaling and performance characteristics. In the experience of the author, existing, highly optimized CFD (computational fluid dynamics) software packages (such as OpenFoam) cannot be extended straightforwardly to include an orientational dependence. Instead, in this work a different method, dubbed »Stochastic Sampling«, is explored, which can be implemented with parallelizable algorithms, and was developed as part of the presented work.

In order to avoid surface effects, ideally a simulation has to be set up with an infinite large box size — which is impossible. Instead, an infinite system is approximated by demanding periodic boundary conditions, which is, topologically speaking a compactification of a d-dimensional simulation box volume into the surface of a $d+1$-dimensional torus. Only a cubic unit cell of the system is simulated and virtually copied and shifted to cover the whole space. Particles in the unit cell interact with mirrors of themselves, introducing artificial correlations. These artefacts, also called »finite size effects«, can be noticeable especially if the correlation and interactions length in the system are larger than the simulated box size. In practice, the dependency of relevant properties of the system on the simulation box size has to be monitored and a sufficiently large box size has to be chosen.

As discussed in Chapter 2, a Smoluchowski equation describes the temporal evolution of a statistical ensemble of particles following stochastic Langevin dynamics. Instead of considering only one possible realization of the stochastic process, all possible realizations are captured in a probability density $\Psi(\{\mathbf{x}\},\{\mathbf{n}\},t)$, depending on the current N-particle configuration. The probability density assigns probability to each outcome. In general, because of inter-particle interactions the dynamics of one particle depends on all the other particles.

By approximating the interactions in a mean-field manner, the particles formally do interact directly with each other, but their interactions are rather mediated by a mean-field. As shown in Sections 2.6 and 2.8, the mean interaction field only depends on the single probability density $\frac{1}{N}\Psi_1(\mathbf{x},\mathbf{n},t)$, defined in equation (2.3.2), that assigns a probability to the outcome of *any* particle being in a certain state.

As derived in Section 2.3.2, the time evolution of Ψ_1 is given by the Smoluchowski equation

$$\partial_t \Psi_1 = -\nabla\cdot[\mathbf{v}_\mathrm{t}\Psi_1] - \nabla^\circ_\mathbf{n}\cdot[\mathbf{v}_\mathrm{r}\Psi_1] + (\Delta\, D_\mathrm{t} + \Delta^\circ_\mathbf{n}\, D_\mathrm{r})\Psi_1, \tag{3.1}$$

with the translational and rotational drifts $\mathbf{v}_t$ and $\mathbf{v}_r$

$$\mathbf{v}_t = \mathbf{v}(\Psi_1(\mathbf{x}, \mathbf{n}, t), \mathbf{x}, \mathbf{n}, t)$$
$$\mathbf{v}_r = \boldsymbol{\omega}(\Psi_1(\mathbf{x}, \mathbf{n}, t), \mathbf{x}, \mathbf{n}, t) \times \mathbf{n}.$$

According to Sections 2.1 and 2.3, the corresponding Langevin-equations for position and orientation of such a particle are given by

$$\dot{\mathbf{x}} = \mathbf{v}(\Psi_1(\mathbf{x}, \mathbf{n}, t), \mathbf{x}, \mathbf{n}, t) + \sqrt{2D_\mathrm{t}}\boldsymbol{\Gamma}(t) \tag{3.2}$$
$$\dot{\mathbf{n}} = \boldsymbol{\omega}(\Psi_1(\mathbf{x}, \mathbf{n}, t), \mathbf{x}, \mathbf{n}, t) \times \mathbf{n} + \sqrt{2D_\mathrm{r}}\boldsymbol{\Lambda}(t) \times \mathbf{n}, \tag{3.3}$$

with the stochastic force $\boldsymbol{\Gamma}$ and the stochastic torque $\boldsymbol{\Lambda}$. This assumes that the diffusion coefficients D_t and D_r are constant. In the case that they depend on the position or orientation of a particle, in the Stratonovich interpretation a spurious drift has to be considered (see Section 2.3). However, because the integration scheme described in the following is based on Euler forward integration, it implicitly assumes the Itô interpretation.

Because direct inter-particle dependencies are replaced by a mean-field interaction, equations (3.1), (3.2), and (3.3) effectively describe the dynamics of a *single* particle in a mean-field. Consequently, once the mean-field is derived from the distribution function, different initial value problems for a given particle can be simulated independently of each other. This realization is the basis of the method that is dubbed »Stochastic Sampling« method.

3.1 Stochastic sampling method

Equations (3.1) and the set of equations (3.2) and (3.3) are equivalent in the sense that the Fokker-Planck equation describes the statistical ensemble of the (stochastic) Langevin equations. So instead of solving the Fokker-Planck equation directly, the probability density $\frac{1}{N}\Psi_1(\mathbf{x}, \mathbf{n}, t_n)$ can first be sampled to obtain $M \in \mathbb{N}$ representatives of the ensemble for a given time t_n. Each of these representatives, in the following also referred to as *sample particles*, can be evolved numerically by a time-discrete mean-field Langevin integrator independently of each other, resulting in a random subset of the whole ensemble, a sample, at the time t_{n+1}. From the time evolved samples the distribution $\Psi_1(t_{n+1})$ for the time t_{n+1} can be estimated and the mean interaction fields are updated. By iterating the process, the probability density can be integrated in time solving the Smoluchowski equation. An illustration of the

correspondence between both representations can be seen in Figure 2.3. On the left of the graphic the path traces of multiple sample particles are shown. On the right, the corresponding PDF Ψ is displayed that, in the context of the simulation, would be a result of an estimation process using the sample particle distribution.

The algorithm can be summarized by the following steps:

1. calculate mean interaction fields given $\Psi_1(t_n)$ at time t_n
2. sample probability distribution $\frac{1}{N}\Psi_1(t_n)$
3. integrate every sample using a discrete Langevin integrator and the mean interaction fields
4. estimate new distribution $\Psi_1(t_{n+1})$ at time t_{n+1} from the time-evolved sample
5. set $n = n + 1$ and start from 1.

The algorithm is also visualized in Figure 3.1 as a flow diagram.

In theory, $M \to \infty$ samples are required to represent the ensemble exhaustively, but this is infeasible. Instead, a finite sample is used to estimate the probability density approximatively. Therefore, a sufficiently large sample size is needed for a faithful estimation. Additionally, the sampling inevitably introduces quantization noise or *Shot*-noise. The effect is mitigated by a larger sample size as well. Furthermore, it can be counteracted by using an appropriate kernel in the density estimation process, described in Section 3.1.3[2]. In practice, the required sample size in the simulation mostly depends on the number of grid cells (discretization points). Every cell should (initially) contain a sufficient number of particles to obtain a reliable statistic of the estimates.

An implementation of the algorithm described above is presented in the following step by step.

3.1.1 Sampling the probability distribution (step 2)

Getting random samples from an arbitrary distribution can be done numerically, for example, by rejection sampling or by a Markov chain Monte Carlo method [107–109]. These methods can be rather computationally expensive. Fortunately, this step can be optimized by only sampling once from an initial distribution (for example the steady

[2]It should be noted that fluctuations must be present in the simulations in order to allow for instabilities to occur. In that sense, the Shot-noise aids to speed up the process by breaking the symmetry slightly.

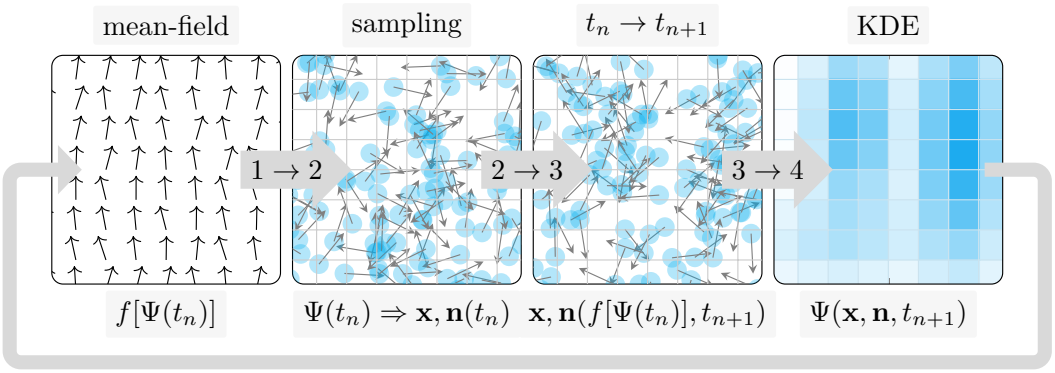

Fig. 3.1.: Flow diagram illustrating the *Stochastic Sampling*-algorithm presented in this chapter. Given a probability density function (PDF) Ψ the mean interaction fields can be calculated. Then, the PDF can be sampled to obtain particles which are integrated using the interaction field. With the updated sample the PDF can be estimated by a Kernel Density Estimation (KDE). By iterating the process, the Smoluchowski equation describing the dynamics of the PDF can be integrated in time.

state distribution) and then reusing and continuously evolving the initial samples. Physically this approach is justified by interpreting it as a particle-based simulation with mean-field interactions.

The isotropic and homogeneous steady state

$$\psi_{0,\text{iso}} = 1/4\pi$$
$$\psi_{0,\text{hom}}(\alpha, \vartheta) = \frac{\alpha}{4\pi \sinh \alpha} \exp(\alpha \cos \vartheta)$$

used in Sections 4.2 and 5.4 can be sampled by the well-known inverse transform sampling or inversion sampling method [110]. By inverting the cumulative distribution function[3] (CDF) $\mathrm{CDF}[\psi]$ of the distribution, a uniformly distributed random variable $U \sim \mathrm{unif}(0, 1)$ can be transformed into a random variable following the given distribution, that is $X = \mathrm{CDF}[\psi]^{-1}(U)$. In this section, a capital letter denotes the random variable and the same letter in lower case stands for a concrete value, i.e. a realization, of the random variable.

Because both initial states are rotationally symmetric, in spherical coordinates only the polar angle ϑ, parametrizing the orientation vector $\mathbf{n}(\vartheta, \varphi)$, has to be sampled non-uniformly. The spatial coordinates and the azimuthal angle φ can be drawn from a uniform distribution.

[3] The CDF of a distribution $P(x)$ is defined by $\mathrm{CDF}[P](\xi) = \int_{\infty}^{\xi} \mathrm{d}x\, P(x)$.

In case of the isotropic distribution, the CDF in spherical coordinates with respect to the polar angle ϑ is given by

$$\mathrm{CDF}[\psi_{0,\mathrm{iso}}](\tau) = \int_0^{2\pi} \mathrm{d}\varphi \int_0^{\tau} \mathrm{d}\vartheta \, \sin\vartheta \frac{1}{4\pi} = \sin^2\left(\frac{\tau}{2}\right),$$

and its inverse is given by

$$\vartheta = \mathrm{CDF}[\psi_{0,\mathrm{iso}}]^{-1}(u) = \arccos(1-2u).$$

Therefore, given a uniformly distributed random variable $U \sim \mathrm{unif}(0,1)$, the random variable of the polar angle $\Theta_B = \mathrm{CDF}[\psi_{0,\mathrm{iso}}]^{-1}(U)$ is distributed according to $\psi_{0,iso}$.

Similarly, the CDF of the homogeneous distribution $\psi_{0,\mathrm{hom}}$ is given by

$$\begin{aligned}\mathrm{CDF}[\psi_{0,\mathrm{hom}}](\alpha,\tau) &= \int_0^{2\pi} \mathrm{d}\varphi \int_0^{\tau} \mathrm{d}\vartheta \, \sin\vartheta \quad \frac{\alpha}{4\pi\sinh\alpha} e^{\alpha\cos\vartheta} \\ &= \frac{1}{2\sinh\alpha}\left(e^{\alpha} - e^{\alpha\cos\tau}\right)\end{aligned}$$

with an inverse given by

$$\vartheta = \mathrm{CDF}[\psi_{0,\mathrm{hom}}]^{-1}(\alpha,u) = \arccos\frac{1}{\alpha}\log\left(e^{\alpha} - 2u\sinh\alpha\right).$$

3.1.2 Langevin integrators (step 3)

In order to evolve the sample particles in time, their Langevin equations have to be integrated numerically. The deterministic velocity part of the Langevin equations (3.2) and (3.3) is integrated by means of an Euler forward scheme, whereas the stochastic noise part has to be handled differently. The noise part in a Langevin equation can be described by a *Wiener process* that can be approximated by a (Gaussian) random walk. For the translation of a particle, this amounts to a random displacement of the particle. The rotational noise can be approximated by a random walk on the surface of a sphere, tracing the tip of the orientation vector $\mathbf{n}$ of a particle. Because the surface is curved, the process differs from the translational random walk, as described in the following.

Translational integrator

Let a Langevin equation be of the form given in equation (3.2), with a stochastic force $\mathbf{\Gamma}$ that has zero mean $\langle \mathbf{\Gamma(t)} \rangle = 0$, temporally uncorrelated, $\langle \mathbf{\Gamma}(t)\mathbf{\Gamma}(t') \rangle = \delta(t - t')$, and a drift velocity $\mathbf{v}$. By integrating the Langevin equation over an infinitesimal time interval $\mathrm{d}t$ a *Wiener process* for the diffusive part is obtained [111],

$$\mathrm{d}\mathbf{x} = \mathbf{v}(\mathbf{x}, \mathbf{n}, t)\mathrm{d}t + \sqrt{2D_\mathrm{t}}\,\mathrm{d}\mathbf{W}(t). \tag{3.4}$$

A (one-dimensional) Wiener process $W(t)$ in t, with $W(0) = 0$, is a continuous stochastic process, with stationary (identically distributed), independent increments $W(t + s) - W(t)$ that are normally distributed with zero mean and variance s. For an n-dimensional process, every component is a Wiener process. The process is historically also called *Brownian motion*.

For a numerical simulation, the Wiener process has to be discretely approximated. Fortunately, it is well known that a Wiener process can also be defined as the limit of a discrete random walk. Given a simulation time step of length Δt, the result of a random walk with m steps at a time $t = m\Delta t$ is given by

$$\mathbf{W}_{1/\Delta t}(t = m\Delta t) \equiv \sqrt{\Delta t} \sum_{j=1}^{m} \boldsymbol{\gamma}_j, \tag{3.5}$$

in which the random variables $\boldsymbol{\gamma}_j$ are independent and assumed to be normally distributed with zero mean and unit variance (in every component). The random variables approximate the increments of the Wiener process, i.e. $\mathbf{W}((j + 1)\Delta t) - \mathbf{W}(j\Delta t) \approx \sqrt{\Delta t}\boldsymbol{\gamma}_j$. In the limit of small time steps, i.e. $\Delta t \to 0$, a Wiener process is obtained. Hence, a stochastic translational diffusion process with diffusion constant D_t can be approximated numerically by constructing a random force vector $\boldsymbol{\gamma}_m$ at every time step t_m, scaling it by $\sqrt{2D_\mathrm{t}\Delta t}$, and translating the particle by the resulting vector.

The drift $\mathbf{v}$ in equation (3.4) can be solved by an integration scheme such as Euler integration. In this work, an Euler-forward scheme is applied, i.e. the next time step only depends on the current one. Eventually, the position update after one time step can be approximated by

$$\mathbf{x}_{m+1} = \mathbf{x}_m + \mathbf{v}(\mathbf{x}_m, \mathbf{n}_m, t_m)\Delta t + \sqrt{2D_\mathrm{t}\Delta t}\boldsymbol{\gamma}_{m+1}, \tag{3.6}$$

where $\bullet_m$ denotes a quantity at time t_m. The integration scheme is illustrated schematically in Figure 3.2.

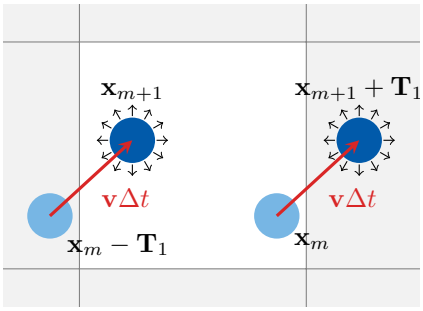

Fig. 3.2.: Illustration of translational Langevin-integrator with periodic boundary conditions with a periodicity $\mathbf{T}$. A particle at time step t_m located at $\mathbf{x}_m$. After on integration step, i.e. $t_m \rightarrow t_{m+1}$, involving a translation along the drift velocity $\mathbf{v}(t_m)$ and applying a normally distributed random translation with variance $\sqrt{2D_\mathrm{t}\Delta t}$, the particle is situated at $\mathbf{x}_{m+1}$. The image of the particle, as a result of the periodic boundary conditions, is shown as well.

It is important to note that choosing an Euler-forward integrator restricts the scheme to the Itô interpretation of stochastic integrals, as discussed in Section 2.3. This fact can be clearly seen from the definition of the Riemann-Stieltje integral in equation (2.15) that in essence is equivalent to Euler-integration. The choice of the sampling point t_k^* in equation (2.15) between the Itô and Stratonovich interpretations is equivalent to a forward or a midpoint scheme respectively. However, the distinction between both interpretations is only relevant for spatially or orientationally dependent diffusion parameter (also referred to as *multiplicative noise* versus *additive noise* for constant diffusion parameters). Thus, it is only relevant for the discussion in Section 5.2.

Lastly, to implement periodic boundary conditions, the coordinates of a particle are restricted to the box by »wrapping around« when leaving the box. After a coordinate of a particle has been updated by equation (3.6), the modulus with the respective box length is calculated,

$$\mathbf{x}_{m+1,\mathrm{pbc}} = \mathbf{x}_{m+1} \mod \mathbf{T},$$

with the simulation box size vector $\mathbf{T}$ (its components are equal to the dimensions of the simulation box in the corresponding direction).

Rotational integrator

To update the orientation $\mathbf{n}$, an analogous scheme can be employed. The stochastic process is described by the Langevin equation given in (3.3). The rotational diffusion can be modelled as a Wiener process as well and approximated by a two-dimensional

Gaussian random walk on the surface of the unit sphere, tracing the tip of the orientation vector. Unlike in the case of a random walk in flat space, the curvature of the sphere's surface has to be taken into account[4]. A visualization of such a random walk is shown in Figure 2.2.

The equivalence can derived by considering a normally distributed (with zero mean and unit variance) Langevin torque vector $\mathbf{\Lambda}$. Then the angular velocity of the orientation vector is given by the component perpendicular[5] to the orientation vector $\mathbf{n}$ that is $\boldsymbol{\omega} = (\mathbb{1} - \mathbf{nn}) \cdot \sqrt{2D_\mathrm{r}}\mathbf{\Lambda}$. By transforming the coordinate system by a rotation, so that the orientation vector points in z-direction and the torque in x-direction, it follows for the transformed, primed vector components: $\omega'_1 = \sqrt{2D_\mathrm{r}}\sqrt{\Lambda'^2_1 + \Lambda'^2_2}$, in which the components of $\mathbf{\Lambda}'$ are still normally distributed. These steps are equivalent to introducing two new random variables: a polar angle Φ representing the direction of a step and an arc or step size R, given by the compound random variable $R = \sqrt{2D_\mathrm{r}}\sqrt{\Lambda'^2_1 + \Lambda'^2_2}$. The direction $\Phi \sim \mathrm{unif}(0, 2\pi)$ can be drawn from a uniform distribution. The step size $R \sim \mathcal{R}(\sigma^2)$ on the other hand is Rayleigh-distributed[6], where $\mathcal{R}(r \geq 0|\sigma^2 = 2D_\mathrm{r}\Delta t) = \frac{r}{\sigma^2}\exp(-r^2/2\sigma^2)$ is the Rayleigh distribution.

On the surface of the unit sphere a curved walking distance of R corresponds to a circular arc covering an angle of R. Or to put it differently, it corresponds to a rotation with an angle equal to R with respect to a rotation axis $\mathbf{b} \perp \mathbf{n}$ perpendicular to the current orientation vector. Given an orientation vector $\mathbf{n}(\vartheta, \varphi) = \check{\mathbf{e}}_r(\vartheta, \varphi)$ parametrized by the polar and azimuthal angles ϑ and φ and given a random variable Φ, the rotation vector $\mathbf{b}(\mathbf{n}, \Phi)$ can be constructed

$$\mathbf{b}(\mathbf{n}, \Phi) \equiv \cos(\Phi)\check{\mathbf{e}}_\vartheta + \sin(\Phi)\check{\mathbf{e}}_\varphi, \tag{3.7}$$

where $\{\check{\mathbf{e}}_r, \check{\mathbf{e}}_\vartheta, \check{\mathbf{e}}_\varphi\}$ is the local basis in spherical coordinates (with $\check{\mathbf{e}}_\vartheta = \partial_\vartheta\check{\mathbf{e}}_r$ and $\check{\mathbf{e}}_\varphi = \sin^{-1}(\vartheta)\,\partial_\vartheta\check{\mathbf{e}}_r$). The scheme is illustrated in Figure 3.3.

A rotation in three dimensions around a given axis can be implemented using (unit) quaternions[7]. A detailed introduction to quaternions is out of scope of this work, but it is sufficient to state that the imaginary part of quaternions are a representation

[4] In a 2D system in flat space, it would be sufficient to draw the polar angle from a normal distribution. Unfortunately, spherical polar coordinates are not suitable for an equivalent manipulation.

[5] A rotation around the orientation vector does not change the vector and can therefore be neglected.

[6] This fact can be derived by considering the radius as a compound random variable given by $R = \sqrt{X^2 + Y^2}$ with the normally distributed coordinate random variables $X, Y = \sqrt{2D_\mathrm{r}}\Lambda'_1, \sqrt{2D_\mathrm{r}}\Lambda'_2 \sim \mathcal{N}(\mu = 0, \sigma^2)$. Therefore, the probability density for a radius of r is given by $\mathcal{R}(r, \sigma^2) = \int_0^r \mathrm{d}\rho \int_0^{2\pi} \mathrm{d}\varphi \quad \mathcal{N}(\rho\cos\varphi|0, \sigma^2)\mathcal{N}(\rho\sin\varphi|0, \sigma^2)$.

[7] The representation of the 3D rotation group as quaternions is popular among the game development, computer graphics, and simulation community, as quaternion based schemes avoid the use of more expensive rotation matrices (see for example References [112, 113]).

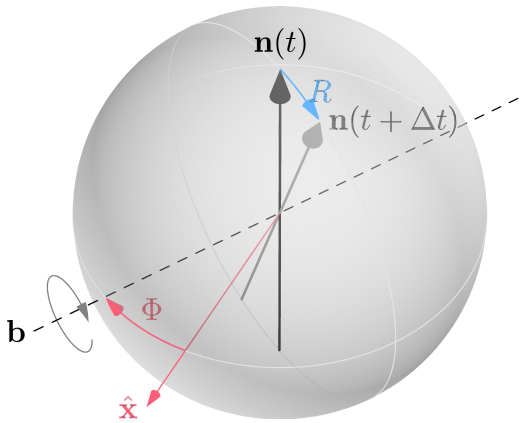

Fig. 3.3.: Illustration of the rotational diffusion algorithm. Given the original orientation vector $\mathbf{n}(t)$, a randomly chosen rotation axis (dashed line) in the perpendicular plane is chosen by drawing the azimuthal angle φ from a uniform distribution. Then the orientation vector is rotated around that axis by an angle ϑ, drawn from a Rayleigh-distribution, resulting in the updated orientation $\mathbf{n}(t+\Delta t)$.

of the $SO(3)$ group. Quaternions are an extension A quaternion is given by four numbers $b_0 + b_x\mathrm{i} + b_y\mathrm{j} + b_z\mathrm{k}$ and a basis fulfilling $\mathrm{i}^2 = \mathrm{j}^2 = \mathrm{k}^2 = \mathrm{ijk} = -1$. Analogous to complex numbers, b_0 denotes the real part and $b_x\mathrm{i}+b_x\mathrm{j}+b_z\mathrm{k}$ denotes the imaginary part (or vector part). For the following discussion, the real part of any quaternion is irrelevant and set to zero, i.e. $b_0 = 0$. In that case, a Cartesian vector, $\mathbf{b} = (b_x, b_y, b_z)$, can be identified with the imaginary part of the quaternion. This is especially true for the rotation axis $\mathbf{b}$ and the orientation vector $\mathbf{n}$.

The rotation of the orientation vector $\mathbf{n}$ around the axis defined by the unit vector $\mathbf{b}$ by an angle R can be calculated by the *conjugation* of $\mathbf{n}$ with an imaginary quaternion $\mathbf{q}$ defined by

$$\mathbf{n}' = \mathbf{q}\mathbf{n}\mathbf{q}^{-1}.$$

The product of two quaternions is similarly defined as for complex numbers and follows from the distributive law and the products of the basis elements given above.

The unit quaternion $\mathbf{q}$, representing a rotation around the axis $\mathbf{b}$ by an angle of R is given by an extension of Euler's formula,

$$\mathbf{q}(\mathbf{b}, R) = e^{\frac{R}{2}(b_x\mathrm{i}+b_y\mathrm{j}+b_z\mathrm{k})} = \cos\frac{R}{2} + (b_x\mathrm{i} + b_y\mathrm{j} + b_z\mathrm{k})\sin\frac{R}{2}, \tag{3.8}$$

and the quaternion of the inverse rotation $\mathbf{q}^{-1}(\mathbf{b}, R) = \mathbf{q}(\mathbf{b}, -R)$ is given by equation (3.8) while replacing $R \mapsto -R$. The inverse quaternion $\mathbf{q}^{-1}$ is equal the conjugate of $\mathbf{q}$ (similar to complex numbers, the conjugate of a quaternion is obtained by replacing its imaginary part with its negative).

In summary, the protocol to implement rotational diffusion starts with drawing at the time step t_{m+1} an angle ϕ_{m+1}, a realization of the uniformly distributed random variable Φ, in order to construct a rotation axis $\mathbf{b}_{m+1} = \mathbf{b}(\mathbf{n}_m, \phi_{m+1})$ perpendicular to the current orientation $\mathbf{n}_m$. Secondly, a realization r_{m+1} of the Rayleigh-distributed walking distance R is drawn, with $\sigma^2 = 2D_\mathrm{r}\Delta t$. Finally, the current orientation vector $\mathbf{n}_m$ is rotated around $\mathbf{b}_{m+1}$ by an angle of r_{m+1} with help of the unit quaternion $\mathbf{q}(\mathbf{b}_{m+1}, r_{m+1})$. The drift velocity is updated using an Euler forward scheme. These steps can be expressed by

$$\begin{aligned}
\mathbf{n}' &= \mathbf{n}_m + \boldsymbol{\omega}(\mathbf{x}_m, \mathbf{n}_m, t_m) \times \mathbf{n}_m \Delta_t \\
\mathbf{q}_{m+1} &= \mathbf{q}(\mathbf{b}(\mathbf{n}', \phi_{m+1}), r_{m+1}) \\
\mathbf{n}_{m+1} &= \mathbf{q}_{m+1} \mathbf{n}' \mathbf{q}_{m+1}^{-1}.
\end{aligned}$$

In the first line, the Euler integration step is applied, resulting in an intermediate result $\mathbf{n}'$. In the second line, the transformation quaternion $\mathbf{q}_{m+1}$ is constructed. And finally, the intermediate orientation after Euler integration is rotated to execute the rotational diffusion step, resulting in the new orientation $\mathbf{n}_{m+1}$ at a time step t_{m+1}.

A sample from a Rayleigh-distribution again can be drawn by making use of the inverse transform sampling method. The CDF of the Rayleigh-distribution is given by $\mathrm{CDF}[\mathcal{R}(r|\sigma^2)] = 1 - \exp(-r^2/2\sigma^2)$ and its inverse by $r = \mathrm{CDF}^{-1}[\mathcal{R}(u|\sigma^2)] = \sigma\sqrt{-2\ln(1-u)}$, with a uniformly distributed random variable $U \sim \mathrm{unif}(0,1)$.

3.1.3 Probability density estimation (step 4)

After evolving all sample particles in time by means of the Langevin integrator described in the previous Subsection 3.1.2, the single particle distribution Ψ_1, representing the whole ensemble, has to be estimated. A widely used technique is the so called kernel density estimation (KDE) [114, 115].

Given the generalized coordinates (including their orientation) $\mathbf{y}_m, m = 1, \ldots, M$ of M sample particles [8] the distribution function Ψ_1 can be estimated by

$$\Psi_1^{\mathrm{app}}(\mathbf{x}) = \frac{N}{M} \sum_{m=1}^{M} K(\mathbf{x} - \mathbf{y}_m; \mathbf{H}). \tag{3.9}$$

The number of particles in the original ensemble, described by Ψ (see equation (2.25)), is denoted by N. The kernel K is a normalized, positive function, sometimes also

[8] For three spatial and two orientational degrees of freedom $\mathbf{x} \in \mathbb{R}^3 \times [0, \pi) \times [0, 2\pi)$.

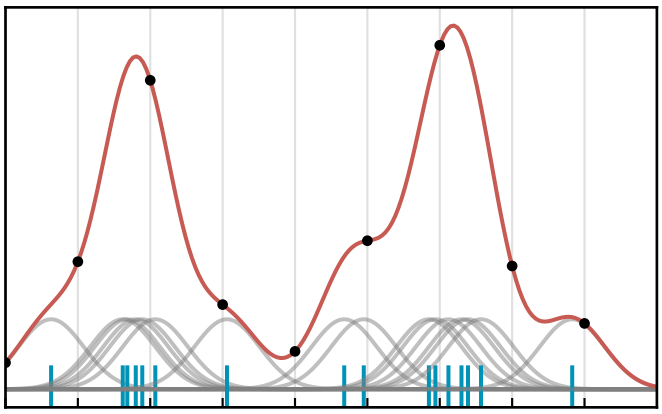

Fig. 3.4.: Illustration of the Kernel Density Estimation method. In this example, a Gaussian kernel is used. In order to estimate the probability density, a scaled Gaussian kernel (grey line) is placed at every sample position (blue lines). The resulting estimate is the sum of all scaled kernels displayed as a red line. To obtain a discretized estimate, the estimate can be evaluated at discrete grid points (black dots).

referred to as a »window function« and parametrized by a symmetric and positive definite matrix $\mathbf{H}$. This matrix is called the »bandwidth« and has the same dimensions squared as the degree of freedoms. Without prior knowledge, it is usually chosen to be diagonal, which is equal to assuming no correlations between the degrees of freedom. The kernel must be normalized to one, i.e. $\int \mathrm{d}\mathbf{x}\, K(\mathbf{x};\mathbf{H}) = 1$. A standard kernel $K(\mathbf{x})$ with unit bandwidth $\mathbb{1}$ can be transformed into having a bandwidth $\mathbf{H}$ by

$$K(\mathbf{x};\mathbf{H}) = \frac{1}{\sqrt{\det \mathbf{H}}} K\left(\mathbf{H}^{-\frac{1}{2}} \cdot \mathbf{x}\right). = \frac{1}{\sqrt{\det \mathbf{H}}} K\left(\sqrt{\mathbf{x} \cdot \mathbf{H}^{-1} \cdot \mathbf{x}}\right).$$

The KDE formula above can be understood as a linear superposition or summation of »smeared out« particles with a weight given by the kernel function and a smoothing factor given by the bandwidth matrix. The concept is illustrated in Figure 3.4 for a Gaussian kernel. In general, the optimal bandwidth matrix depends on the unknown density distribution and often has to be treated as a free parameter (hyperparameter) of the method. Commonly used standard kernels are the Triangular $((1-\|\mathbf{x}\|), \|\mathbf{x}\| \leq 1)$, Epanechnikov $(\frac{3}{4}(1-\mathbf{x}^2), \|\mathbf{x}\| \leq 1)$, Gaussian $((2\pi)^{-d/2} \exp(-\mathbf{x}^2/2))$ or Uniform kernel $(1/2, \|\mathbf{x}\| \leq 1)$ [116]. Choosing a Triangular kernel with a bandwidth equal to the grid widths results into a linear binning algorithm, closely related to linear interpolation. Another choice would be the Epanechnikov kernel. It has the desirable property that is optimal in the sense that it minimizes the Asymptotic Mean Integrated Squared Error (AMISE) [117]. However, as a rule of thumb the bandwidth of any

kernel has a greater impact on the accuracy of the estimator[9]. A local kernel with finite support (zero for $\|\mathbf{x}\| > 1$) is much more performant in an implementation. This rules out the Gaussian kernel. For reasons of simplicity and performance characteristics, in this work a rectangular Uniform kernel

$$K_{\text{rect}}(\mathbf{x}) = \begin{cases} \frac{1}{2}, & \|\mathbf{x}\| \leq 1 \\ 0, & \text{else} \end{cases} \tag{3.10}$$

with a bandwidth of half a grid width in every dimension was used, which is equivalent to a binning algorithm resulting in a histogram. Given the grid width vector $\mathbf{w}$ of dimension d (number of degrees of freedom), the bandwidth matrix would be given by the diagonal matrix $\mathbf{H} = \text{diag}((w_1/2)^2, \ldots, (w_d/2)^2)$.

A discrete estimate of the distribution function $\Psi_1^{\text{app}}(\mathbf{x_j})$ can be found by evaluating equation (3.9) at the points of the simulation grid. Let the grid points be indexed by the index set $\mathbb{G} = \{(g_1, g_2, \ldots, g_d) \in \mathbb{N}_0^d \,|\, g_l < G_l \in \mathbb{N}, \forall l = 1, \ldots, d\}$, in which G_l denote the number of grid points in the lth dimension. Then, the discretized estimate $\left(\Psi_1^{\text{app}}\right)_{\mathbf{j}}$ is found by

$$\left(\Psi_1^{\text{app}}\right)_{\mathbf{j}} \equiv \Psi_1^{\text{app}}(\mathbf{x_j}) = \frac{N}{M} \sum_{m=1}^{M} K_{\mathbf{H}}\left(\mathbf{x_j} - \mathbf{y}_m\right), \quad \forall \mathbf{j} \in \mathbb{G}. \tag{3.11}$$

3.1.4 Numerical integration and normalization

In the simulations, expectation values are calculated from the discrete estimate of the distribution function Ψ_1^{app} by means of numerical integration. A continuous integral is approximated by a weighted sum,

$$\int_{\mathbb{V}} \mathrm{d}\mathbf{x}\, \Psi_1^{\text{app}}(\mathbf{x}) \approx \sum_{\mathbf{j} \in \mathbb{G}} w_{\mathbf{j}} \Psi_1^{\text{app}}{}_{\mathbf{j}}, \tag{3.12}$$

with integration weights $w_{\mathbf{j}}$. The weights have to be chosen in such a way that the approximation Ψ_1^{app} under the numerical integration scheme is still normalized. This requirement is generally not fulfilled because of discretization errors in

[9] Most kernels of the ones listed here actually have a comparable *efficiency* [118].

equation (3.11)[10]. For this reason in the simulation the discrete estimate has to be normalized by

$$\Phi_{\mathbf{j}}(t) = \frac{1}{M}\sum_{m=1}^{M} K_{\mathbf{H}}\left(\mathbf{x}_{\mathbf{j}} - \mathbf{y}_m(t)\right)$$
$$\left(\Psi_1^{\text{app}}\right)_{\mathbf{j}}(t) = \frac{N\Phi_{\mathbf{j}}(t)}{\sum_{\mathbf{j}\in\mathbb{G}} w_{\mathbf{j}}\Phi_{\mathbf{j}}(t)} \tag{3.13}$$

in every time step.

The grid/interpolation points $\mathbf{x}_{\mathbf{j}}$ and the weights $w_{\mathbf{j}}$ have to be chosen carefully in order to obtain the most accurate result. It turns out that under periodic boundary conditions an equally spaced grid with constant weights $w_j = \Delta x = T/G$, with the box length T and the number of grid points G, is optimal in the sense that the relation (in 1D)

$$\int_0^T \mathrm{d}x\, f(x) = \sum_{j=1}^{G} w_j f(x_j) = \sum_{j=1}^{G} \Delta x f(j\Delta x)$$

is exact for trigonometric polynomials of degree $2G-2$. This remains true in higher dimensions and includes polynomials in the Fourier basis [106]. Therefore, an approximation of a function in terms of a Fourier expansion, as used for the spectral method described in the next Subsection (see equation (3.15)), can be integrated exactly by the above scheme as well.

This concludes the detailed description of steps 2 to 4 of the Stochastic Sampling algorithm outlined the listing in the beginning of Section 3.1. Step 1, the calculation of the mean interaction fields, is discussed in the next section. First, a spectral method, to numerically calculate an arbitrary field described by a linear partial differential equation, is introduced. Then, the technique is applied, to obtain numerical solutions of the solvent's flow field of an active suspension and the magnetic field generated by a magnetic suspension.

3.2 Solving the mean-fields with a spectral method (step 1)

Let $\mathbf{h}[\Psi_1](\mathbf{x})$ be a mean-field that can be derived from a configuration described by the single particle distribution Ψ_1. Examples for such fields are the mean stress field given

[10] It is automatically fulfilled for a rectangular kernel defined in equation (3.10), though.

in equation (2.80), driving the solvent's flow field of an active suspension and the mean magnetization of a magnetic suspension defined in equation (2.48), creating the internal magnetic field. The aim of this section is to derive the corresponding mean interaction fields, the flow field and the internal magnetic field, relevant for the dynamics of the kinetic models presented in this work. The flow field is defined by partial differential equations, the incompressible Stokes equations (2.67) and (2.68). Its solution can be formulated in terms of a convolution operation on the mean stress field given in equation (2.70). Similarly, given a mean magnetization field, the internal magnetic field can be derived from Maxwell's equations and can be obtained by the convolution applied to the mean magnetization defined in equation (2.62) as well.

To discretize and solve the differential equations giving rise to the mean interaction fields, in this work a (pseudo)spectral method is used [106, 119–121]. In this method, the functions in a partial differential equation are approximated by a linear combination of a suitable discrete basis. As a consequence, the differential equation decomposes into several equations for the coefficients of the expansion which are solvable more easily. Optimal coefficients have to be chosen, defined more formally in the following, to retain as many properties as possible of the original, continuous equations.

In the simulations, periodic boundary conditions are used. Therefore, a suitable basis is given by the discrete Fourier basis, because it naturally fulfils the periodic boundary conditions.

3.2.1 Spectral Fourier method of solving linear PDEs

Let a time-independent and linear[11] equation in $\mathbf{h}$ be given as,

$$\mathbf{f}(\mathbf{x}) = (\mathbf{A} * \mathbf{h})(\mathbf{x}) \tag{3.14}$$

with periodic boundary conditions with periodicity $\mathbf{T}$ (simulation box size vector), $\mathbf{h}(\mathbf{x} + \mathbf{T}) = \mathbf{h}(\mathbf{x})$, and a convolution kernel $\mathbf{A}$[12]. The field $\mathbf{h}$ in equation (3.14) is also called the inhomogeneity. In the context of this thesis, the aim is to find an approximation of $\mathbf{f}$ given the field $\mathbf{h}$.

[11] Spectral methods are not limited to linear or time-independent problems. However, in this work this restriction is sufficient and simplifies the presentation.

[12] Typically, in spectral methods this ansatz is given for a differential operator of the form of $\mathbf{f} = \mathbb{D}\mathbf{h}$. The formalism using a convolution is a generalization of this ansatz, because every linear differential operator can be expressed as a convolution kernel with the help of the delta distribution. It is equivalent to $\mathbf{f} = (\mathbb{D}\delta) * \mathbf{h}$.

The function $\mathbf{h}$ is approximated by a discrete Fourier expansion,

$$\mathbf{h}^{\text{app}}(\mathbf{x}) = \sum_{\mathbf{k}\in\mathbb{G}} \widehat{\mathbf{h}}_{\mathbf{k}} \phi_{\mathbf{k}}(\mathbf{x}), = \sum_{\mathbf{k}\in\mathbb{G}} \widehat{\mathbf{h}}_{\mathbf{k}} e^{\mathrm{i}2\pi(\mathbf{T}^{-1}\odot\mathbf{k})\cdot\mathbf{x}}, \tag{3.15}$$

with the Fourier basis $\phi_{\mathbf{k}}(\mathbf{x}) \equiv e^{\mathrm{i}2\pi(\mathbf{T}^{-1}\odot\mathbf{k})\cdot\mathbf{x}}$, intrinsically satisfying the periodic boundary conditions for a box of dimensions given by $\mathbf{T}$, and the expansion coefficients $\widehat{\mathbf{h}}_{\mathbf{k}}$. The set $\mathbb{G} = \{(g_1, g_2, \ldots, g_d) \in \mathbb{N}_0^d \,|\, g_l < G_l \in \mathbb{N}, \forall l = 1, \ldots, d\}$ is the grid index set, in which G_l denote the number of grid points in the lth dimension, the point-wise inverse of a vector is denoted by $\mathbf{T}^{-1} \equiv (1/T_1, 1/T_2, \ldots, 1/T_d)$, and the Hadamard-product (point-wise multiplication) of two vectors is given by $\mathbf{a} \odot \mathbf{b} = (a_1 b_1, a_2 b_2, \ldots, a_d b_d)$. For the use of the method in the present thesis, the number of degrees of freedom $d = 3$ is given by three spatial dimension, however, generally the method works for an arbitrary number of dimensions.

Substituting the approximation back into the original equation (3.14) yields an approximation of the function $\mathbf{f}$, denoted by $\mathbf{f}^{\text{app}}$,

$$\begin{aligned}
\mathbf{f}^{\text{app}}(\mathbf{x}) = \mathbf{A} * \mathbf{h}^{\text{app}}(\mathbf{x}) &= \int \mathrm{d}\mathbf{y}\, \mathbf{A}(\mathbf{x}-\mathbf{y}) \cdot \mathbf{h}^{\text{app}}(\mathbf{y}) \\
&= \sum_{\mathbf{k}\in\mathbb{G}} \widehat{\mathbf{h}}_{\mathbf{k}} \cdot \int \mathrm{d}\mathbf{y}\, \mathbf{A}(\mathbf{y})\, e^{\mathrm{i}2\pi(\mathbf{T}^{-1}\odot\mathbf{k})\cdot(\mathbf{x}-\mathbf{y})} \\
&= \sum_{\mathbf{k}\in\mathbb{G}} e^{\mathrm{i}2\pi(\mathbf{T}^{-1}\odot\mathbf{k})\cdot\mathbf{x}} \widehat{\mathbf{h}}_{\mathbf{k}} \cdot \int \mathrm{d}\mathbf{y}\, \mathbf{A}(\mathbf{y})\, e^{-\mathrm{i}2\pi(\mathbf{T}^{-1}\odot\mathbf{k})\cdot\mathbf{y}} \\
&= \sum_{\mathbf{k}\in\mathbb{G}} e^{\mathrm{i}2\pi(\mathbf{T}^{-1}\odot\mathbf{k})\cdot\mathbf{x}}\, \widehat{\mathbf{A}}(\mathbf{k}) \cdot \widehat{\mathbf{h}}_{\mathbf{k}},
\end{aligned} \tag{3.16}$$

in which $\widehat{\mathbf{A}}(\mathbf{k}) = \int \mathrm{d}\mathbf{y}\, \mathbf{A}(\mathbf{y})\, e^{-\mathrm{i}2\pi(\mathbf{T}^{-1}\odot\mathbf{k})\cdot\mathbf{y}}$ is the Fourier transform of the kernel $\mathbf{A}(\mathbf{x})$. Equation (3.16) is actually the discrete convolution theorem.

The residual function $\mathbf{r}$, the error of the approximation, can be defined by

$$\mathbf{r}(\mathbf{x}, \{\widehat{\mathbf{h}}\}) \equiv \mathbf{A} * \mathbf{h}^{\text{app}}(\mathbf{x}) - \mathbf{f}(\mathbf{x}).$$

For the exact function $\mathbf{h}$, the residual function would be zero. Therefore, the challenge is to find the coefficients that minimize the residual.

Most minimization methods can be cast into the form

$$\int_{\mathbb{T}} \mathrm{d}\mathbf{x}\, \tau_{\mathbf{j}}(\mathbf{x})\, \mathbf{r}(\mathbf{x}, \{\widehat{\mathbf{h}}\}) \stackrel{!}{=} 0, \quad \forall \mathbf{j} \in \mathbb{G},$$

for test functions $\tau_{\mathbf{j}}$. Common choices are setting the test functions equal to the basis functions $w_{\mathbf{j}} = \phi_{\mathbf{j}}$ (Galerkin method) or demanding the minimization requirement

to be satisfied at discrete points $\tau_{\mathbf{j}}(\mathbf{x}) = \delta(\mathbf{x} - \mathbf{x}_{\mathbf{j}})$ (collocation or pseudo-spectral method). In this work, the collocation method is used, because the function $\mathbf{h}$ in the simulation is known, or rather approximated, only at certain points[13]. Hence, the goal is to find expansion coefficients so that the residual is zero at given points $\mathbf{x}_{\mathbf{j}}$, i.e.

$$\mathbf{r}(\mathbf{x}_{\mathbf{j}}, \{\widehat{\mathbf{h}}\}) = (\mathbf{A} * \mathbf{h}^{\text{app}} - \mathbf{f})|_{\mathbf{x}=\mathbf{x}_{\mathbf{j}}} = 0. \tag{3.17}$$

If the points $\mathbf{x}_{\mathbf{j}}$ are chosen to lie on a regular grid, so that

$$\mathbf{x}_{\mathbf{j}} = \mathbf{j} \odot \boldsymbol{\Delta}\mathbf{x} = (j_1 \Delta x_1, j_2 \Delta x_2, \ldots, j_d \Delta x_d),$$

with the grid width vector $\boldsymbol{\Delta}\mathbf{x} = \mathbf{T} \odot \mathbf{G}^{-1}$, then the function $\mathbf{f}(\mathbf{x}_{\mathbf{j}})$ evaluated at the grid points is exactly the inverse discrete Fourier transformation (IDFT) of $\widehat{\mathbf{A}} \cdot \widehat{\mathbf{h}}$ given by equation (3.16),

$$\begin{aligned} \mathbf{f}_{\mathbf{j}}^{\text{app}} = \mathbf{f}^{\text{app}}(\mathbf{x}_{\mathbf{j}}) &= \sum_{\mathbf{k} \in \mathbb{G}} \widehat{\mathbf{A}}(\mathbf{k}) \cdot \widehat{\mathbf{h}}_{\mathbf{k}} \, e^{\mathrm{i}2\pi \mathbf{k} \cdot (\mathbf{j} \odot \mathbf{G}^{-1})} \\ &= \mathrm{IDFT}_{\mathbf{G}} \left[\widehat{\mathbf{A}} \cdot \widehat{\mathbf{h}}, \mathbf{j} \right], \end{aligned} \tag{3.18}$$

given that

$$\begin{aligned} \left(\mathbf{T}^{-1} \odot \mathbf{k} \right) \cdot (\mathbf{j} \odot \boldsymbol{\Delta}\mathbf{x}) &= \mathbf{k} \cdot \left(\mathbf{j} \odot \mathbf{T}^{-1} \odot \mathbf{T} \odot \mathbf{G}^{-1} \right) \\ &= \mathbf{k} \cdot \left(\mathbf{j} \odot \mathbf{G}^{-1} \right). \end{aligned}$$

By the same argument, the approximation $\mathbf{h}^{\text{app}}$ of the function $\mathbf{h}$, which is only known at the discrete points $\mathbf{x}_{\mathbf{j}}$ and derived from the discrete estimate of the single particle distribution function Ψ_1^{app} (see Section 3.1.3), is given by the IDFT of $\widehat{\mathbf{h}}$,

$$\mathbf{h}_{\mathbf{j}}^{\text{app}} = \mathrm{IDFT}_{\mathbf{G}} \left[\widehat{\mathbf{h}}, \mathbf{j} \right].$$

Hence, the coefficients $\widehat{\mathbf{h}}$ can be found by calculating the DFT, with a normalization constant of $\prod_j 1/G_j$, of the interpolation points of the inhomogeneity $\mathbf{h}^{\text{app}}[\Psi_1^{\text{app}}](\mathbf{x}_{\mathbf{j}})$,

$$\widehat{\mathbf{h}}_{\mathbf{k}} = \mathrm{DFT}_{\mathbf{G}} \left[\mathbf{h}^{\text{app}}[\Psi_1^{\text{app}}], \mathbf{k} \right] = \frac{1}{\prod_l G_l} \sum_{\mathbf{k} \in \mathbb{G}} \mathbf{h}_{\mathbf{j}}^{\text{app}} \, e^{-\mathrm{i}2\pi \mathbf{k} \cdot (\mathbf{j} \odot \mathbf{G}^{-1})}$$

The DFT and IDFT can be efficiently computed using the Fast Fourier Transformation algorithm [122] available in several software libraries.

[13] It can be shown that for a regular grid with periodic boundary conditions both methods are actually equivalent [106].

In summary, given a convolution kernel $\mathbf{A}$ and a function $\mathbf{h}[\Psi_1]$ that derives from the single particle distribution Ψ_1, the estimate of the field $\mathbf{f}$ can be calculated by means of the inverse discrete Fourier transform of the Fourier transformed convolution kernel applied to the Fourier transformed inhomogeneity, $\widehat{\mathbf{A}}(\mathbf{k}) \cdot \widehat{\mathbf{h}}_\mathbf{k}$. The discrete Fourier coefficients of the inhomogeneity, $\widehat{\mathbf{h}}$ are obtained via a DFT, while the inhomogeneity itself is derived from the discrete estimate of the single particle distribution $\left(\Psi_1^{\text{app}}\right)_\mathbf{j}$.

Once the coefficients $\widehat{\mathbf{h}}$ are known, the approximation in equation 3.16 provides an excellent off-grid interpolation of the mean-field $\mathbf{f}$ that could be used in simulations to improve the accuracy. However, this requires an evaluation of $|\mathbb{G}| = \prod_l G_l$ exponentials for *every* sample particle in the Langevin integrator, described in 3.1.2, and is therefore very expensive. A more efficient but less accurate approach is approximating the function $\mathbf{f}$ by either assuming it to be constant inside a grid-cell $\mathbf{j}$ with a value of $\mathbf{f}_\mathbf{j}$, or use a lower order local interpolation scheme like (tri)-linear interpolation.

The method described above can now be applied to solve for the flow field and internal magnetic field of an active, magnetic colloidal suspension.

3.2.2 Solving the flow field

The flow field $\mathbf{u}$ is defined by the incompressible Stokes equations (2.67) and 2.68. Given a stress $\boldsymbol{\sigma}$, their solution in terms of a Green's function, the Oseen tensor, is given by

$$\mathbf{u} = -\mathbb{O} * (\nabla \cdot \boldsymbol{\sigma}),$$

according to equation (2.70), and in which the Oseen tensor identifies with the convolution operator $\mathbf{A}$ introduced in the last section (compare with equation (3.14)). The discrete Fourier coefficients of the inhomogeneity $\mathbf{h} = -\nabla \cdot \boldsymbol{\sigma}$ are given by

$$\widehat{\mathbf{h}}_\mathbf{k} = -\mathrm{i}2\pi \left(\mathbf{T}^{-1} \odot \mathbf{k}\right) \cdot \widehat{\boldsymbol{\sigma}}[\Psi_1],$$

where the Fourier transform of the stress tensor can be calculated from the mean active and alignment stress contributions using

$$\widehat{\boldsymbol{\sigma}}_\mathbf{k}[\Psi_1](t) = \mathrm{DFT}_\mathbf{G}\left[-\int_{\mathbb{S}^2} \mathrm{d}\mathbf{n}\ \Psi_1^{\text{app}}(\mathbf{x}_\mathbf{j}, \mathbf{n}, t)\ \left(\mathbf{D}_a(\mathbf{n}) + \mathbf{D}_m(\mathbf{n})\right), \mathbf{k}\right].$$

The active and magnetic flow dipole moments are defined by $\mathbf{D}_a(\mathbf{n}) = D_a\left(\mathbf{nn} - \frac{1}{3}\mathbb{1}\right)$ and $\mathbf{D}_m(\mathbf{n}) = \frac{D_m}{2B}\left(\mathbf{nB} - \mathbf{Bn}\right)$ according to equations (2.83) and (2.86). The integration in the brackets has to be done numerically as described by equation (3.12).

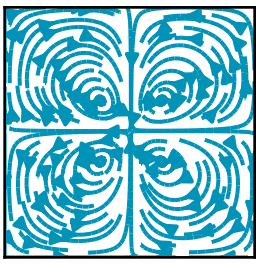

Fig. 3.5.: Flow field generated by a narrow polarized Gaussian distributed density Ψ_1 in the centre with periodic boundary condition.

By making use of the Fourier transform of the Oseen tensor [100],

$$\widehat{\mathbb{O}}(q) = \frac{1}{q^2}(\mathbb{1} - q^{-2}\mathbf{q}\mathbf{q}),$$

and the coefficients $\widehat{\mathbf{h}}$ derived above, the discrete Fourier coefficients of the flow field $\mathbf{u}$ are given by

$$\widehat{\mathbf{u}}_{\mathbf{k}}[\Psi_1] = -\frac{\mathrm{i}}{q^2}(\mathbb{1} - q^{-2}\mathbf{q}\mathbf{q}) \cdot \widehat{\boldsymbol{\sigma}}[\Psi_1] \cdot \mathbf{q}\Big|_{\mathbf{q}=2\pi\,\mathbf{T}^{-1}\odot\mathbf{k}}, \quad \forall \mathbf{k} \in \mathbb{G}.$$

The expression is undefined in the case of $\mathbf{k} = 0$. However, the total flow must be zero, because of momentum conservation, as stated in equation (2.81), which is equivalent to setting the constant mode, $\mathbf{k} = (0,0,0)$ to zero, i.e.

$$\widehat{\mathbf{u}}[\Psi_1]_{(0,0,0)} \stackrel{!}{=} 0.$$

Eventually, the discrete flow field approximation $\mathbf{u}_{\mathbf{j}}^{\mathrm{app}}$ at the grid points $\mathbf{x}_{\mathbf{j}}$ can be calculated by the IDFT of $\widehat{\mathbf{u}}$.

A similar procedure can be applied to find the internal magnetic field of a magnetic suspension.

3.2.3 Solving the magnetic field

The internal magnetic field can be approximated analogous to the flow field in the previous Subsection 3.2.2. According to equation (2.62), the internal magnetic field is given by

$$\mathbf{B}_{\mathrm{int}} = \mu_0 \mathcal{B}^{\mathrm{dip}} * \mathbf{M},$$

Fig. 3.6.: Magnetic flux density generated by a narrow, polarized Gaussian distributed density Ψ_1 in the centre with periodic boundary condition.

where the operator $\mu_0 \mathcal{B}^{\text{dip}}$, defined in equation (2.41), can be identified with $\mathbf{A}$ in equation (3.14), and the corresponding inhomogeneity $\mathbf{h} = \mathbf{M}$ is given by the mean magnetization.

The discrete Fourier coefficients of $\mathbf{h}$, respectively $\mathbf{M}$, can again be found in terms of a DFT given by

$$\widehat{\mathbf{h}}_{\mathbf{k}}(t)\widehat{\mathbf{M}}_{\mathbf{k}}(t) = \mathrm{DFT}_{\mathbf{G}}\left[\mu \int_{\mathbb{S}^2} \mathrm{d}\mathbf{n}\ \mathbf{n}\, \Psi_1^{\text{app}}(\mathbf{x_j}, \mathbf{n}, t), \mathbf{k}\right],$$

using equation (2.48) to calculate the mean magnetization from the single particle distribution estimate Ψ_1^{app}. The integral must be calculated numerically as well (see equation (3.12)).

Hence, the discrete Fourier coefficients of the internal magnetic flux density $\widehat{B}_{\mathbf{k}}^{\text{int}}$ can be obtained by

$$\check{\mathbf{B}}_{\mathbf{k}}^{\text{int}} = \mu_0 \check{\mathcal{B}}^{\text{dip}}(\mathbf{q}) \cdot \check{\mathbf{M}}(\mathbf{k})\Big|_{\mathbf{q}=2\pi\, \mathbf{T}^{-1}\odot\mathbf{k}}, \quad \forall \mathbf{k} \in \mathbb{G},$$

in which $\check{\mathcal{B}}^{\text{dip}}$ is the Fourier transform of the dipolar operator $\mathcal{B}^{\text{dip}}$ given by equation (2.61). Finally, the approximation of the internal magnetic field $\mathbf{B}_{\text{int}}^{\text{app}}$ can be calculated by applying an IDFT to $\widehat{\mathbf{B}}^{\text{int}}$. An exemplary magnetic flux density, generated by a narrow, polarized Gaussian density distribution in the centre is shown in Figure 3.6.

This concludes the complete description of the Stochastic Sampling method, given here and the previous section. The algorithm consists of a number of complex steps, hence, an optimized implementation of the algorithm is required. The following section gives an overview of the concrete implementation developed during and used in the present work.

3.3 Implementation and performance

The method described in this chapter was implemented from scratch in the memory safe programming language Rust [123] due to its excellent performance characteristics, first-class support of parallelism, and its expressiveness. The type system is used to introduce constraints preventing many careless mistakes already at compile time [124]. Unit tests are performed to check invariants and other properties in the algorithm. The implementation heavily relies on the libraries `ndarray` [125] for an n-dimensional array type and `rayon` [126] for parallelization of homogeneous data. To perform calculations of the Discrete Fourier Transformation the library [124] is used. To produce (pseudo) random values a Pseudo Random Number Generator of the PCG-family [127] provided by the `rand_pcg` library [128] [128]. It has excellent statistical properties and features high performance. Normally distributed random variables are produced by the ZIGNOR [129] variant of the Ziggurat method implemented in [130].

The program is optimized and highly parallelized using a shared memory model and has minimal external dependencies. The modular software design allows for an easy adaptation and extension of the framework for similar models. For example, the Langevin integrator exposed its API (Application Programming Interface) in form of a *builder pattern* [131], showcased in the Listing 3.1. The results of the simulation can be stored in a standardized serialization format (for example *CBOR* [132]) for easy access and analysis.

```
new_particle = LangevinBuilder::new(&old_particle)
   .with(self_propulsion)
   .with_param(convection, flow_field)
   .with_param(external_field_alignment, param.magnetic_reorientation)
   .with_param(jeffery_vorticity, flow_vorticity.view())
   .step(&TimeStep(simulation.timestep))
   .with_param(rotational_diffusion, &dr)
   .integrate(&simulation.box_size);
```

Listing 3.1: Showcase of the Langevin integrator API. Given the previous particle coordinates, the updated coordinates can be found by building a Langevin integrator with the components needed.

The *Stochastic Sampling*-algorithm described in this chapter and used in this work is fully parallelizable and has a complexity of $\mathcal{O}(M)$ with regard to the number of sample particles which, in turn depends on the number of grid cells (including the orientational degree of freedom) G, $M \propto G$ (if one wants to assure sufficient statistics for the density estimation). For comparison, a spectral solver (including a non-linear ODE integrator) of the non-linear Fokker-Planck equation has a complexity

of $\mathcal{O}(G \log G)$ with regard to the number of interpolation points. Solving the mean-field, as described in Section 3.2, is the same for both approaches and has a complexity of $\mathcal{O}(G \log G_s)$, with the number G_s of spatial grid cells. Asymptotically, *Stochastic Sampling*-algorithm should have a better runtime than a spectral method. However, the actual runtime depends on the needed precision and accuracy and time prefactors of concrete implementations of both algorithms. A final assessment of the algorithm's performance in comparison with traditional approaches needs further studies.

An interesting property of the *Stochastic Sampling*-algorithm is that the number of sample particles intrinsically and dynamically adapts to the local density of the distribution function Ψ_1. In volumes of high density that have the highest impact on the dynamics, more sample particles are used, improving the statistics and lowering the numerical error in these volumes. Because of this property, it was observed that a relative low number of sample particles is sufficient to obtain (at least qualitatively) good results similar to more exhaustive simulations. This property is closely related to the importance sampling method used, for instance, in Monte-Carlo simulations [133].

3.4 Linear stability analysis

The linear stability analysis is a powerful tool to evaluate the stability of a known steady state depending on various system parameters. The basic idea of this method is to perturb the steady state only by a small amount so that is sufficient to only consider the more tractable, linearized dynamics of the system. What makes this technique so useful, is the fact that the assessment of the stability of the linearized system carries over to the non-linear system (except for degenerate cases, see footnote) [134]. Furthermore, the linearized dynamics near the steady state is qualitatively equivalent to the non-linear dynamics[14].

The method starts by considering a steady state ψ_0 of the dynamical equation[15] given by

$$\partial_t \psi = \mathbb{S}\psi, \tag{3.19}$$

[14]The Hartman-Grobman theorem assures qualitatively equivalent dynamics of the linearized system in the neighbourhood of a non-degenerate, hyperbolic steady state ($\mathrm{Re}\,\lambda_i \neq 0$) [135, 136].

[15]in the present work, usually a Smoluchowski equation

in which $\mathbb{S}$ is a non-linear, differentio-integro operator that evolves the state ψ in time. Hence, the steady state fulfils $\partial_t \psi_0 = \mathbb{S}\psi_0 = 0$ by definition. A small perturbation of this state can be written as

$$\psi = \psi_0 + \varepsilon \psi_p, \tag{3.20}$$

where $0 < \varepsilon \ll 1$ and ψ_p denotes an arbitrary perturbation. The perturbed state ψ is substituted back into the dynamical equation (3.19). By disregarding terms of the order $\mathcal{O}(\varepsilon^2)$, the linearized dynamics of the perturbation ψ_p is obtained and can be expressed by

$$\partial_t \psi_p = \mathbb{L}\psi_p, \tag{3.21}$$

in which $\mathbb{L}$ is the linearization of the time-evolution operator $\mathbb{S}$. In case the (linear) perturbation decays and the system returns to the steady state, it is called stable. On the other hand, if the small perturbation grows even further and the system continues to depart from the steady state, the steady state is called unstable. Therefore, the aim of this section is to find a solution to the dynamical equation of the perturbation, given in equation (3.21) that allows the perturbation to be classified as growing (unstable) or decaying (stable).

For an eigenfunction ϕ of the operator $\mathbb{L}$, for which $\mathbb{L}\phi = \lambda\phi$ with the corresponding eigenvalue λ, equation (3.21) reduces to

$$\partial_t \phi = \lambda \phi,$$

and can be solved by an exponential ansatz,

$$\phi(\mathbf{x}, \mathbf{n}, t) = e^{\lambda t} \phi(\mathbf{x}, \mathbf{n}, t = 0).$$

Hence, the real part of the eigenvalue $\mathrm{Re}\,\lambda$, called the growth rate, decides if the eigenmode grows or decays exponentially in time and if a perturbation of this form renders the steady state unstable or not. Every perturbation ψ_p can be expressed as linear combination of the eigenbasis ϕ_j of the operator $\mathbb{L}$. In this eigenmode decomposition, every eigenmode contributes with a factor of $e^{\lambda_j t}$ to the dynamics of the perturbation. The eigenmode with the largest growth rate $\mathrm{Re}\,\lambda_{\max}$ dominates the dynamics. Therefore, and because of the linearity of equation (3.21), it is sufficient to only consider the dominant eigenmode with the largest growth rate.

3.4.1 Eigenmodes of the time-evolution operator

In order to obtain the eigenmodes ϕ_j and -values λ_j of the operator $\mathbb{L}$, it is useful to express the problem in a known basis. For the present work it is sufficient to limit oneself to operators whose spatial-integro part is given by convolutional operators and that are not explicitly dependent on space and time, i.e. $\mathbb{L} = \mathbb{L}(\mathbf{n})$. In this case, the basis of Fourier modes $e^{\mathrm{i}\mathbf{k}\cdot\mathbf{x}}$ is an eigenbasis of the operator, due to the fact that spatial derivatives and convolutions algebraize[16], resulting in an algebraized operator $\widehat{\mathbb{L}}$. Therefore, the spatial degree of freedom is expanded into Fourier modes $\widehat{\psi}_p(\mathbf{k}, \mathbf{n}, t)$ by an inverse Fourier transform

$$\psi_p(\mathbf{x}, \mathbf{n}, t) = \frac{1}{(2\pi)^{\frac{3}{2}}} \int_{\mathbb{R}^3} \mathrm{d}\mathbf{x}\, e^{\mathrm{i}\mathbf{k}\cdot\mathbf{x}}\, \widehat{\psi}_p(\mathbf{k}, \mathbf{n}, t), \tag{3.22}$$

in which the Fourier modes are given by the Fourier transform

$$\widehat{\psi}_p(\mathbf{k}, \mathbf{n}, t) = \frac{1}{(2\pi)^{\frac{3}{2}}} \int_{\mathbb{R}^3} \mathrm{d}\mathbf{x}\, e^{-\mathrm{i}\mathbf{k}\cdot\mathbf{x}}\, \psi_p(\mathbf{x}, \mathbf{n}, t). \tag{3.23}$$

Substituting the Fourier expansion in equation (3.22) back into in equation (3.21) yields

$$\begin{aligned} \frac{1}{(2\pi)^{\frac{3}{2}}} \int_{\mathbb{R}^3} \mathrm{d}\mathbf{x}\, e^{\mathrm{i}\mathbf{k}\cdot\mathbf{x}}\, \partial_t \widehat{\psi}_p(\mathbf{k}, \mathbf{n}, t) &= \frac{1}{(2\pi)^{\frac{3}{2}}} \int_{\mathbb{R}^3} \mathrm{d}\mathbf{x}\, \mathbb{L} e^{\mathrm{i}\mathbf{k}\cdot\mathbf{x}}\, \widehat{\psi}_p(\mathbf{k}, \mathbf{n}, t) \\ &= \frac{1}{(2\pi)^{\frac{3}{2}}} \int_{\mathbb{R}^3} \mathrm{d}\mathbf{x}\, e^{\mathrm{i}\mathbf{k}\cdot\mathbf{x}}\, \widehat{\mathbb{L}} \widehat{\psi}_p(\mathbf{k}, \mathbf{n}, t), \end{aligned} \tag{3.24}$$

in which the operator $\widehat{\mathbb{L}}$ denotes the algebraized operator after applying it to the Fourier basis. This can be recast into the coefficient equation given by

$$\partial_t \widehat{\psi}_p(\mathbf{k}, \mathbf{n}, t) = \widehat{\mathbb{L}}(\mathbf{k}, \mathbf{n}) \widehat{\psi}_p(\mathbf{k}, \mathbf{n}, t), \tag{3.25}$$

shifting the focus on the orientational part of the perturbation. The aim is now to find an eigenbasis and eigenvalues of the algebraized operator $\widehat{\mathbb{L}}$.

In the following, the Dirac notation [137] is used to make the change of basis transformations easier to follow. In this notation, $|\widehat{\psi}_p\rangle$ denotes an abstract vector

[16] Derivatives expressed by the nabla operator algebraize like $\nabla \mapsto \mathrm{i}\mathbf{k}$, whereas the algebraization of a convolution is given by the convolution theorem, i.e. $\mathcal{F}(\mathbf{A} * \mathbf{b}) = \mathcal{F}\mathbf{A} \cdot \mathcal{F}\mathbf{b}$.

whose coefficient/coordinate with respect to a basis vector $|\tilde{\psi}_j\rangle$ is given by a projection, using the scalar product in $\mathbf{n}$

$$\langle\tilde{\psi}_j|\widehat{\psi}_p\rangle\,(\mathbf{k},t) = \int_{\mathbb{S}^2} \mathrm{d}\mathbf{n}\;\tilde{\psi}_j^*(\mathbf{k},\mathbf{n})\,\widehat{\psi}_p(\mathbf{k},\mathbf{n},t),$$

in which $\bullet^*$ denotes the complex conjugation. Now, the Fourier coefficient equation (3.25) is expressed by

$$\partial_t\,|\widehat{\psi}_p\rangle\,(\mathbf{k},\mathbf{n},t) = \widehat{\mathbb{L}}(\mathbf{k},\mathbf{n})\,|\widehat{\psi}_p\rangle\,(\mathbf{k},\mathbf{n},t). \tag{3.26}$$

Let $|\tilde{\psi}_j\rangle\,, j \in \mathbb{N}_0$ be an eigenbasis of $\widehat{\mathbb{L}}$ with eigenvalues λ_j. By inserting the unit operator $\sum_j |\tilde{\psi}_j\rangle\,\langle\tilde{\psi}_j| = \mathbb{1}$ into equation (3.26), it follows

$$\begin{aligned}
\partial_t \sum_j |\tilde{\psi}_j\rangle\,\langle\tilde{\psi}_j|\widehat{\psi}_p\rangle &= \sum_j |\tilde{\psi}_j\rangle\,\partial_t\,\langle\tilde{\psi}_j|\widehat{\psi}_p\rangle \\
&= \sum_j \widehat{\mathbb{L}}\,|\tilde{\psi}_j\rangle\,\langle\tilde{\psi}_j|\widehat{\psi}_p\rangle \\
&= \sum_j \lambda_j\,|\tilde{\psi}_j\rangle\,\langle\tilde{\psi}_j|\widehat{\psi}_p\rangle \qquad (3.27)\\
\Leftrightarrow \qquad \partial_t\,\langle\tilde{\psi}_j|\widehat{\psi}_p\rangle &= \lambda_j\,\langle\tilde{\psi}_j|\widehat{\psi}_p\rangle\,, \qquad (3.28)
\end{aligned}$$

for the coordinates $\langle\tilde{\psi}_j|\widehat{\psi}_p\rangle\,(\mathbf{k},t)$. The partial differential equation for the coordinates (3.28) follows by projecting equation (3.27) onto an eigenvector by applying $\langle\tilde{\psi}_j|$ from the left side. The coordinate equation has the solution given by the exponential ansatz

$$\langle\tilde{\psi}_j|\widehat{\psi}_p\rangle\,(\mathbf{k},t) = e^{\lambda_j\,t}\,\langle\tilde{\psi}_j|\widehat{\psi}_p\rangle\,(\mathbf{k},t=0).$$

Hence, the solution to equation (3.26) is given by a superposition of all eigenmodes,

$$|\widehat{\psi}_p\rangle\,(\mathbf{k},\mathbf{n},t) = \sum_j |\tilde{\psi}_j\rangle\,(\mathbf{k},\mathbf{n})\;e^{\lambda_j\,t}\,\langle\tilde{\psi}_j|\widehat{\psi}_p\rangle\,(\mathbf{k},0). \tag{3.29}$$

As a result, the solution to the original equation can be expressed by a continuous superposition of the Fourier modes given by equation (3.22), which is identical to the inverse Fourier transform of the form

$$\begin{aligned}
|\psi_p\rangle\,(\mathbf{x},\mathbf{n},t) &= \frac{1}{(2\pi)^{3/2}} \int_{\mathbb{R}^3} \mathrm{d}\mathbf{k}\;e^{\mathrm{i}\mathbf{k}\cdot\mathbf{x}} \sum_j |\tilde{\psi}_j\rangle\,(\mathbf{k},\mathbf{n})\;e^{\lambda_j\,t}\,\langle\tilde{\psi}_j|\widehat{\psi}_p\rangle\,(\mathbf{k},0) \\
&= \frac{1}{(2\pi)^{3/2}} \int_{\mathbb{R}^3} \mathrm{d}\mathbf{k}\;\sum_j e^{\mathrm{i}\mathbf{k}\cdot\mathbf{x}+\lambda_j\,t}\;|\tilde{\psi}_j\rangle\,(\mathbf{k},\mathbf{n})\,\langle\tilde{\psi}_j|\widehat{\psi}_p\rangle\,(\mathbf{k},0). \qquad (3.30)
\end{aligned}$$

As discussed in the introduction of this section, equation (3.30) represents the perturbation $|\psi_p\rangle$ as a superposition of exponentially growing or decaying eigenmodes

$$|\phi_j\rangle\,(\mathbf{k},\mathbf{n},t) = e^{\mathrm{i}\mathbf{k}\cdot\mathbf{x}+\lambda_j\,t}\;|\tilde{\psi}_j\rangle\,(\mathbf{k},\mathbf{n})\,\langle\tilde{\psi}_j|\widehat{\psi}_p\rangle\,(\mathbf{k},0). \tag{3.31}$$

Therefore, a general perturbation ansatz of the form

$$|\psi_p\rangle\,(\mathbf{k};\mathbf{x},\mathbf{n},t) = |\tilde{\psi}\rangle\,(\mathbf{k},\mathbf{n})\,e^{\mathrm{i}\mathbf{k}\cdot\mathbf{x}+\lambda\,t}, \tag{3.32}$$

can be made, in which $|\tilde{\psi}\rangle\,(\mathbf{k},\mathbf{n})$, is an eigenfunction of the algebraized time-evolution operator $\widehat{\mathbb{L}}$. The ansatz allows to formulate an eigenvalue problem that in the end yields the eigenmode $|\phi_{\max}\rangle$ with the largest growth rate $\lambda \equiv \lambda_{\max}$ that dominates the dynamics.

The amplitude $|\tilde{\psi}\rangle\,(\mathbf{k},\mathbf{n})$ of the plane wave $e^{\mathrm{i}\mathbf{k}\cdot\mathbf{x}}$ with wavevector $\mathbf{k}$ additionally encodes the orientational mode structure of the perturbation. The real part of the eigenvalue $\mathrm{Re}\,\lambda$, the growth rate, determines if the mode is growing or decaying, its imaginary part corresponds to a time-oscillation with frequency of $\omega = \mathrm{Im}\,\lambda$. Therefore, the perturbation corresponds to a plane wave travelling with a speed of $c = \omega/k$, whose amplitude evolves according to $\exp(\mathrm{Re}\,\lambda(\mathbf{k})t)$.

It remains to determine a concrete representation of the eigensystem of the operator $\widehat{\mathbb{L}}$. An eigenvalue problem is best solved in a known basis, leading to coefficient matrix of the operator. This way, conventional methods for the calculation of the spectrum of a matrix can be used.

3.4.2 Calculation of the operator eigensystem

In order to calculate the spectrum λ_j and the eigenbasis $|\tilde{\psi}\rangle$ of the algebraized time-evolution operator $\widehat{\mathbb{L}}(\mathbf{k},\mathbf{n})$, it is represented as a coefficient matrix of a known basis. The operator explicitly depends on the orientation vector $\mathbf{n}$, parametrizing the unit sphere. Therefore, a natural choice for a basis on the unit sphere are spherical harmonics Y_l^m, with degree l and order m [138]. To allow for a compact notation, the index pair (l,m) can be flattened by remapping it onto one index $\pi(l,m)$ by the bijection,

$$\pi(l,m) = l^2 + l + m, \tag{3.33}$$

which produces the maps

$$0 \mapsto (0,0), 1 \mapsto (1,-1), 2 \mapsto (1,0), 3 \mapsto (1,1), 4 \mapsto (2,-2), 4 \mapsto (2,-1), \ldots,$$

so that $Y_{\pi(l,m)} = Y_l^m$ (for example $Y_3 = Y_1^1, Y_5 = Y_2^0$). The inverse mapping can be defined as

$$\pi^{-1}(j) = (l, j - l^2 - l), l = \left\lfloor \sqrt{j} \right\rfloor, \tag{3.34}$$

with the floor braces $\lfloor \bullet \rfloor$ rounding to the next smallest integer.

Starting from the perturbation ansatz in equation (3.32), its time evolution can be written as

$$\begin{aligned} & \widehat{\mathbb{L}} \left| \tilde{\psi} \right\rangle = \lambda \left| \tilde{\psi} \right\rangle \\ \Leftrightarrow \quad & \sum_{i,j} \left| Y_i \right\rangle \left\langle Y_i | \widehat{\mathbb{L}} | Y_j \right\rangle \left\langle Y_j | \tilde{\psi} \right\rangle = \lambda \sum_j \left| Y_j \right\rangle \left\langle Y_j | \tilde{\psi} \right\rangle \\ \Leftrightarrow \quad & \sum_{i,j} \left\langle Y_i | \widehat{\mathbb{L}} | Y_j \right\rangle \left\langle Y_j | \tilde{\psi} \right\rangle = \lambda \sum_j \left\langle Y_j | \tilde{\psi} \right\rangle . \end{aligned} \tag{3.35}$$

The last equation is equivalent to the matrix notation

$$\mathbf{L} \cdot \tilde{\boldsymbol{\psi}} = \lambda \tilde{\boldsymbol{\psi}}, \tag{3.36}$$

in which the coefficient matrix of the operator $\widehat{\mathbb{L}}$ is given by $L_{ij} = \langle Y_i | \widehat{\mathbb{L}} | Y_j \rangle$ and the coefficient vector of the eigenvector by $\tilde{\psi}_j = \langle Y_j | \tilde{\psi} \rangle$. Equation (3.36) takes the form of a classical eigenvalue problem that can be solved numerically with commonly known algorithms provided by a number of software packages. However, the matrix $\mathbf{L}$ has infinite dimension. Therefore, its spectrum has to be approximated by truncating highly oscillating modes, i.e. large indices. A more detailed discussion on the numerical solution of the truncated eigenvalue problem can be found in in Section 4.3, when the method is applied to a kinetic model for an active suspension in an external field.

When truncating the expansion in spherical harmonics given by equation (3.35), the linear stability analysis is closely related to a spectral method using a Galerkin method for discretization, as described in Section 3.2, of the linearized time evolution of the state ψ_p near the steady state ψ_0.

The linear stability analysis is an invaluable tool in the studies of pattern formation. It provides a way to determine under which circumstances a departure from a steady is to be expected and patterns can form. Furthermore, it can reproduce the dynamics near the steady state qualitatively, delivering more insight in the early pattern formation dynamics. Both methods described in this chapter, the Stochastic Sampling method and the linear stability analysis, are extensively used in

the following two chapters, discussing two related kinetic models of active colloids with long-ranged interactions.

4 A kinetic theory of active suspensions in an alignment field

Based on the theoretical background established in Chapters 2 and 3, in this chapter a 3D kinetic theory of hydrodynamically interacting, active particles in an external alignment field is developed and studied. A special focus lies on the description and explanation of their collective dynamics and emerging patterns. For example, magnetotactic bacteria (MTB) have been observed to form intriguing patterns like travelling bands [22, 23] and pearling instability under flow [24].

To this end, a Smoluchowski equation is formulated that is coupled to the Stokes equation describing the dynamics of the flow field. As a result of the self-propulsion of the microswimmers, a flow in the solvent is created that in turn influences the other swimmers' dynamics. This long ranged[1] fluid mediated interaction is described in a mean-field approximation. The proposed model in this chapter incorporates hydrodynamic interactions and the effect of an external alignment field is included in form of an external magnetic field coupling to the magnetic dipole moments of the swimmers. The interplay between the anisotropic hydrodynamic interactions and the polarization effects due to the external alignment field gives rise to a rich dynamics that is presented in this chapter.

The magnetic dipole-dipole interactions between particles are neglected in this chapter, considering the weak magnetic dipole moment of magnetotactic bacteria in the order of $\mu \approx 1 \times 10^{-16}\,\mathrm{Am}^2$ (see Table 4.1). At the mean inter-particle distance $\bar{l}$, the magnetic dipole-dipole interaction energy is given by $\mu_0\mu^2/4\pi\bar{l}^3$, where $\mu_0 \approx 4\pi \times 10^{-16}\,\mathrm{N/A}^2$ is the magnetic constant. For a fairly dilute suspensions, i.e. at a volume fraction $\phi \lesssim 0.1$, it is at least one order of magnitude smaller than the thermal energy scale given by k_BT. Hence, in good approximation it can be neglected. However, artificial swimmers can carry stronger magnetic dipole moments. In this case, the magnetic interactions are not negligible any more and need to be considered as discussed in Chapter 5.

[1] A force dipole has a ρr^{-2} scaling with the distance r, while the density ρ in a spherical angle scales with r^2.

Quantity	Symbol	Typical value	Source
particle radius	R	$1\,\mu\mathrm{m}$-$10\,\mu\mathrm{m}$	[14, 24]
swimming speed	U_0	$10\,\mu\mathrm{m\,s^{-1}}$-$100\,\mu\mathrm{m\,s^{-1}}$	[14, 24]
magnetic dipole moment	μ	$10^{-16}\,\mathrm{Am^2}$-$10^{-15}\,\mathrm{Am^2}$	[89, 91, 139, 140]

Tab. 4.1.: Typical values for magnetic swimmers

In the following, first the model and its ingredients are presented. Then, a homogenous steady state of the Smoluchowski is identified and the dynamics close to the steady state and its stability as a function of the system's parameter are explored using a linear stability analysis, as introduced in Section 3.4. To gain a deeper insight into the mechanism of the pattern formation, a linear stability analysis of orientational moments of the particle distribution is performed, isolating the contributions of the particle density and their polarization to the dynamics near the steady state. Numerical solutions of the Smoluchowski equation reveal the formation of distinct patterns for pushers and pullers, in form of hydrodynamically induced travelling bands and pillar like patterns. The mechanism behind these phenomena is explained with the help of the results from the linear stability analysis and leads to a description in terms of bend and splay deformations for pushers and pullers, respectively. Eventually, the pattern formation has an effect on the transport velocities — how fast the particles travel in the external field direction, which is studied in the last section of this chapter. It turns out that especially for pullers, the transport velocity is significantly reduced.

To get started, the Smoluchowski equation for the system is formulated.

4.1 Kinetic model

According to Section 2.4, the Smoluchowski equation of the single particle distribution Ψ_1 for active particles at the position $\mathbf{X}$ and orientation $\mathbf{n}$ carrying a magnetic dipole moment in an external field, including hydrodynamic interactions, is given by

$$\partial_T \Psi_1 + \nabla_{\mathbf{X}} \cdot [\mathbf{V}_{\mathbf{x}} \Psi_1] + \nabla^\circ_{\mathbf{n}} \cdot [\mathbf{V}_{\mathbf{n}} \Psi_1] - \mathbb{D}\Psi_1 = 0,$$

in which the surface gradient for the orientation $\mathbf{n}$ is given by $\nabla^\circ_{\mathbf{n}} = (\mathbb{1} - \mathbf{nn}) \cdot \nabla_{\mathbf{n}}$ and $(\nabla_{\mathbf{n}})_j = \partial_{n_j}$. To distinguish between the dimensional and dimensionless equations, in this section the dimensional quantities are written in upper case.

The spatial flux velocity (drift coefficient) is given by

$$\mathbf{V}_{\mathbf{x}} = U_0\mathbf{n} + \mathbf{U},$$

which includes the self-propulsion along a particle's orientation $\mathbf{n}$, see Section 2.2, and a convection in the local flow $\mathbf{U}$, see Section 2.8.4. The rotational flux velocity is given by

$$\mathbf{V}_{\mathbf{n}} = (\mathbb{1} - \mathbf{nn}) \cdot \left(\frac{\mu}{\xi_{\mathrm{r}}} \mathbf{B}_{\mathrm{ext}} - \mathbf{W} \cdot \mathbf{n} \right),$$

including the realignment in an external field $\mathbf{B}_{\mathrm{ext}}$, see Section 2.6.2, and a rotation in the local flow due to flow vorticities represented by the vorticity tensor $\mathbf{W} = \frac{1}{2}(\nabla\mathbf{U} + \nabla\mathbf{U}^{\top})$, see 2.8.4. Additionally, the model includes both translational and rotational diffusion introduced by the diffusion operator

$$\mathbb{D} = D_{\mathrm{t}}\,\Delta + D_{\mathrm{r}}\,\Delta^{\circ}_{\mathbf{n}},$$

as defined in Section 2.4.

According to Section 2.7.2, the flow field is determined by the incompressible Stokes equation

$$\eta\,\Delta\,\mathbf{U} - \nabla P = -\nabla \cdot \mathbf{\Sigma}[\Psi_1]$$
$$\nabla \cdot \mathbf{U} = 0$$

determined by the mean stress profile $\mathbf{\Sigma} = \mathbf{\Sigma}_a + \mathbf{\Sigma}_m$ that depends on the mean particle configuration. The mean stress consists of the active stress generated by the self-propulsion of the swimmers and an alignment stress generated by particles aligning with an external magnetic field and is given by equations (2.83) and (2.86)

To facilitate the analysis of the model, the equation are rendered dimensionless, using characteristic units of the system. The characteristic speed is chosen to be the self-propulsion speed, $u_c = U_0$, and the characteristic time is equal to the inverse of the rotational diffusion coefficient $t_c = 1/D_{\mathrm{r}}$. The characteristic length derives from these units, by $x_c = u_c t_c$, and can be interpreted as a mean free path between random reorientation events. With this choice, the equations above can be transformed into a dimensionless form, according to Section 2.92. The dimensionless equations are used throughout the next two Chapters, if not declared differently.

4.1.1 Nondimensionalization

Nondimensionalization refers to rendering the governing equations dimensionless, as presented in Section 2.92. The Smoluchowski equation for the single particle distribution $\psi(\mathbf{x}, \mathbf{n}, t)$, transforms into

$$\partial_t \psi + \nabla \cdot [\mathbf{v}_\mathrm{t} \psi] + \nabla^\circ_\mathbf{n} \cdot [\mathbf{v}_\mathrm{r} \psi] - \mathbb{D}\psi = 0, \tag{4.1}$$

in which $\mathbf{v}_\mathrm{t}$ and $\mathbf{v}_\mathrm{r}$ represent the dimensionless spatial and rotational flux-velocities, given by

$$\mathbf{v}_\mathrm{t} = \mathbf{n} + \mathbf{u} \tag{4.2}$$

$$\mathbf{v}_\mathrm{r} = (\mathbb{1} - \mathbf{nn}) \cdot \left(\alpha_\mathrm{ext} \check{\mathbf{B}}_\mathrm{ext} - \mathbf{W} \cdot \mathbf{n} \right). \tag{4.3}$$

The vector $\check{\mathbf{B}}_\mathrm{ext} = B_\mathrm{ext}^{-1} \mathbf{B}_\mathrm{ext}$ is a unit vector pointing along the external field axis $\mathbf{B}_\mathrm{ext}$. In general, the check symbol annotation indicates a normalized vector $\check{\mathbf{v}} \equiv \|\mathbf{v}\|^{-1} \mathbf{v}$. In the reduced units, the dimensionless flow is given by $\mathbf{u} = \mathbf{U}/U_0$, the dimensionless diffusion operator by

$$\mathbb{D} = d_t \, \Delta + \Delta^\circ_\mathbf{n}, \tag{4.4}$$

with the dimensionless diffusion constant $d_t = \frac{t_c}{x_c^2} D_\mathrm{t} = \frac{D_\mathrm{r}}{U_0^2} D_\mathrm{t}$, and the alignment parameter is defined as $\alpha_\mathrm{ext} = \frac{\mu B_\mathrm{ext}}{\xi_\mathrm{r} D_\mathrm{r}}$.

The equations for the flow field transform accordingly into

$$\begin{aligned} \Delta \, \mathbf{u} - \nabla p &= -\nabla \cdot \boldsymbol{\sigma}[\psi] \\ \nabla \cdot \mathbf{u} &= 0, \end{aligned} \tag{4.5}$$

where the reduced pressure is given by $p = P t_c / \eta$ and the Stokes equation additionally has been divided by the viscosity η that is absorbed into the dimensionless mean stress

$$\boldsymbol{\sigma} = \frac{\varrho t_c}{\eta} \boldsymbol{\Sigma} = \frac{\varrho}{\eta D_\mathrm{r}} \left(\boldsymbol{\Sigma}_a + \boldsymbol{\Sigma}_m \right),$$

including both the active stress $\boldsymbol{\sigma}_a = \frac{\varrho}{\eta D_\mathrm{r}} \boldsymbol{\Sigma}_a$ and the alignment stress $\boldsymbol{\sigma}_a = \frac{\varrho}{\eta D_\mathrm{r}} \boldsymbol{\Sigma}_m$. Therefore, according to equations (2.83) and (2.86), the dimensionless stresses can be defined as

$$\begin{aligned} \boldsymbol{\sigma}_a &= \sigma_a \int_{\mathbb{S}^2} \mathrm{d}\mathbf{n} \; \psi \left(\mathbf{nn} - \frac{1}{3} \mathbb{1} \right) \\ \boldsymbol{\sigma}_m &= \sigma_m \int_{\mathbb{S}^2} \mathrm{d}\mathbf{n} \; \psi \left(\mathbf{n} \check{\mathbf{B}}_\mathrm{ext} - \check{\mathbf{B}}_\mathrm{ext} \mathbf{n} \right), \end{aligned}$$

where the prefactors σ_a and σ_m define the dimensionless active and alignment stress strengths given by $\sigma_a = \varrho D_a / D_\mathrm{r} \eta$ and $\sigma_m = \varrho D_m / D_\mathrm{r} \eta$. The active dipole moment strength D_a depends on the swimming mechanism of the microswimmer, whereas the alignment dipole moment $D_m = \mu B_\mathrm{ext}$ is given by the magnetic dipole moment μ and the external magnetic field strength B_ext. The average number density is given by $\varrho = N/V$, i.e. on average N particle share a volume V.

It is infeasible to solve the equations (4.1) and (4.5) analytically under general conditions. To still gain some predictive insight into the dynamics of the equations a suitable steady state ψ_0, with $\partial_t \psi_0 = 0$, is identified and linearly perturbed in order to assess its stability. The stability of the steady state parametrized in terms of the alignment parameter α_ext and the active stress magnitude σ_a is analysed for a wide range of these parameters. As a result, the parameter space can be divided into a stable region described by the steady state and an unstable region with yet unknown dynamics departing from the steady state. Furthermore, the linear stability analysis offers a limited but powerful insight into the dynamics at the onset if instability.

4.2 Steady state

The external magnetic field breaks the rotational symmetry of the system. However, it is still translational invariant and has an axial symmetry around the magnetic field direction. Therefore, an ansatz of a homogeneous[2] axially symmetric steady state is made, reflecting the symmetry of the system. This implies $\psi(\mathbf{x}, \mathbf{n}, t) = \psi_0(\vartheta)$ with $\nabla \psi_0 = 0$, where ϑ denotes the polar angle in spherical coordinates for the orientation $\mathbf{n}(\vartheta, \varphi)$. Without loss of generality, the magnetic field vector is assumed to be parallel to the z-axis, i.e. $\mathbf{B}_\mathrm{ext} = B_\mathrm{ext} \check{\mathbf{z}}$. After substituting the ansatz ψ_0 back into the Smoluchowski equation (4.1), all spatial derivatives vanish, as well as the flow field $\nabla \cdot \boldsymbol{\sigma} = 0 \Rightarrow \mathbf{u}_0 = 0$. Only the rotational flux velocity remains, which includes both diffusive and drift contributions,

$$\partial_t \psi_0 = 0 = -\nabla^\circ_\mathbf{n} \cdot \psi_0 \left(\mathbf{v}_\mathrm{r} - \nabla^\circ_\mathbf{n} \ln \psi_0 \right). \tag{4.6}$$

A solution to this equation can be found by setting the bracket to zero. It remains to solve

$$\psi_0 \nabla^\circ_\mathbf{n} \ln \psi_0 = \check{\mathbf{e}}_\vartheta \partial_\vartheta \psi_0 = (\mathbb{1} - \mathbf{nn}) \cdot \alpha_\mathrm{ext} \psi_0 \check{\mathbf{z}}$$

[2] Strictly speaking, it is assumed that the PDF is a uniform distribution unif(V) in the position $\mathbf{x}$ over the volume V, which is large enough that boundary effects can be neglected and the uniform distribution is in good approximation a steady state for the time interval of interest.

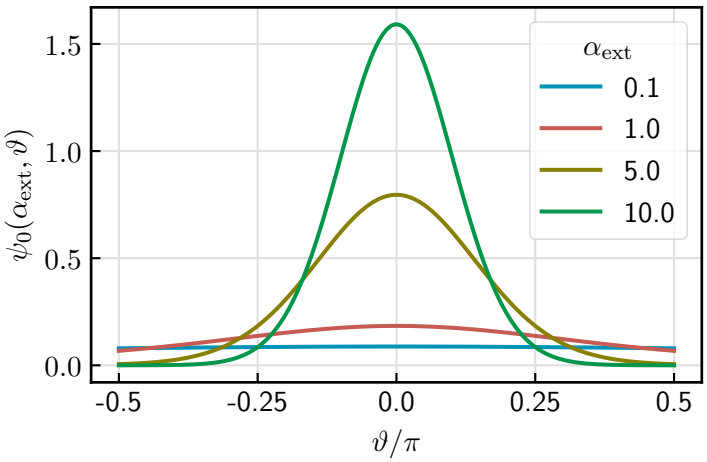

Fig. 4.1.: Angular distribution of the homogeneous steady state $\psi_0(\vartheta)$ for different values of the external alignment parameter $\alpha_{\text{ext}} \propto B$ proportional to the external magnetic field strength B.

$$
\begin{aligned}
&= \alpha_{\text{ext}} \psi_0(\check{\mathbf{z}} - \cos\vartheta\, \mathbf{n}) \\
&= -\alpha_{\text{ext}} \sin\vartheta\, \psi_0\, \check{\mathbf{e}}_\vartheta \\
\Leftrightarrow \qquad & \partial_\vartheta \psi_0(\vartheta) = -\alpha_{\text{ext}} \psi_0(\vartheta) \sin\vartheta.
\end{aligned}
$$

The solution to the last line is

$$
\begin{aligned}
\psi_0(\vartheta) &= \frac{\alpha_{\text{ext}}}{4\pi \sinh \alpha_{\text{ext}}} e^{\alpha_{\text{ext}} \cos\vartheta} \\
&= \frac{\alpha_{\text{ext}}}{4\pi \sinh \alpha_{\text{ext}}} e^{\alpha_{\text{ext}} \mathbf{n}\cdot\check{\mathbf{B}}_{\text{ext}}},
\end{aligned}
\tag{4.7}
$$

where the normalization condition

$$
\int_{\mathbb{S}^2} \mathrm{d}\mathbf{n}\ \psi_0(\vartheta) = \int_0^{2\pi} \mathrm{d}\varphi \int_0^{\pi} \mathrm{d}\vartheta \sin(\vartheta)\psi_0(\vartheta) = 1
$$

has been used. In the last line of equation (4.7), the general solution without the assumption that the magnetic flux density $\mathbf{B}_{\text{ext}}$ points along the z-axis is given. The angular dependency of the solution is shown in Figure 4.1.

The (external) alignment parameter $\alpha_{\text{ext}} = \frac{\mu B_{\text{ext}}}{\xi_{\text{r}} D_{\text{r}}}$ represents the ratio between the characteristic alignment time in an external field $\tau_{\text{e}} = \frac{\xi_{\text{r}}}{\mu B_{\text{ext}}}$ and the time scale given by the rotational diffusion $\tau_{\text{r}} = \frac{1}{D_{\text{r}}}$. The higher the external magnetic field, the stronger the particles tend to align with the magnetic field. This results in a focused angular distribution around the magnetic field axis at $\vartheta = 0$. In the extreme case of a very strong field, all particles are completely aligned, i.e. $\lim_{\alpha_{\text{ext}}\to\infty} \psi_0 = \delta(\mathbf{n} - \check{\mathbf{B}}_{\text{ext}})$. On the other hand, for weak magnetic fields, fluctuations will increasingly decorrelate

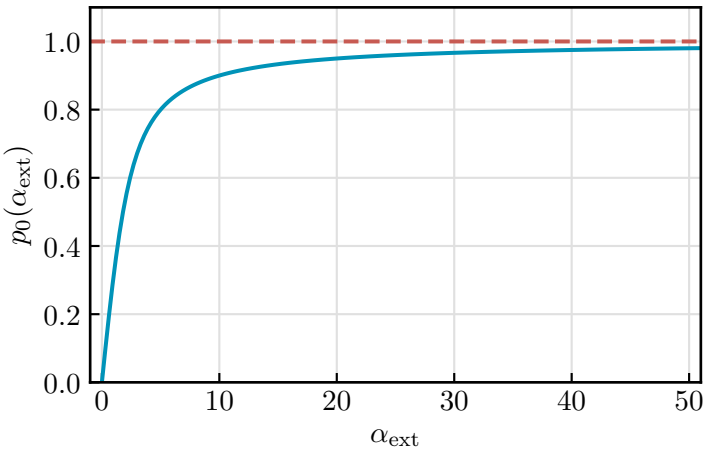

Fig. 4.2.: The total polarization p_0 of the steady state ψ_0 in dependency of the alignment parameter $\alpha_{\text{ext}} \propto B$. The stronger the external torque (the higher α_{ext}), the more particles are polarized.

the orientations of the particle ensemble, leading to a uniform profile in the angular distribution, i.e. $\lim_{\alpha_{\text{ext}} \to 0} \psi_0 = 1/4\pi$.

The competition between »order« (alignment) and »disorder« (fluctuations) is reflected in the polarization order parameter p_0. It is equal to the magnitude of the first orientational moment of ψ_0, see equation (2.28),

$$\mathbf{p}_0 = \int_{\mathbb{S}^2} \mathrm{d}\mathbf{n}\ \mathbf{n}\, \psi_0(\mathbf{n}) = p_0 \check{\mathbf{B}}_{\text{ext}}$$
$$p_0(\alpha_{\text{ext}}) = \coth \alpha_{\text{ext}} - \frac{1}{\alpha_{\text{ext}}}, \tag{4.8}$$

which is equal to the Langevin function known in the context of paramagnetism. The functional dependency on the alignment parameter α_{ext} is plotted in Figure 4.2. The stronger the external alignment torque competes with the rotational fluctuations, i.e. the higher α_{ext}, the higher the polarization becomes, asymptotically approaching a perfectly aligned state with $p_0 = 1$ for an infinitely strong external field.

4.3 Linear stability analysis

A linear stability analysis provides information about the dynamics close to a steady state of a system. By only looking at small perturbations of the steady state, it is sufficient to consider the linearized dynamical equations. The concept is described in the methology chapter in Section 3.4.

4.3.1 Linear perturbation of the steady state

In order to assess the stability of the steady state solution ψ_0, given by equation (4.7), in dependency of the system's parameters a linear stability analysis is conducted. The steady state is disturbed by a small perturbation ψ_p,

$$\psi = \psi_0 + \varepsilon\psi_p.$$

The flow field of the solvent has to be perturbed accordingly, $\mathbf{u} = \mathbf{u}_0 + \varepsilon\mathbf{u}_p$. The corresponding steady state is $\mathbf{u}_0 = 0$, because the spatial derivatives on the right-hand side of Stokes equation (4.5) vanish for the homogeneous steady state ψ_0.

By substituting the perturbed distribution into the Smoluchowski equation (4.1), the equation governing the dynamics of the perturbation reads

$$\begin{aligned}\partial_t(\psi_0 + \varepsilon\psi_p) = &- \nabla \cdot [(\mathbf{n} + \varepsilon\mathbf{u}_p)(\psi_0 + \varepsilon\psi_p)] \\ &- \nabla^\circ_{\mathbf{n}} \cdot \left[(\psi_0 + \varepsilon\psi_p)(\mathbb{1} - \mathbf{nn}) \cdot \left(\alpha_{\text{ext}}\check{\mathbf{B}}_{\text{ext}} - \varepsilon\mathbf{W}[\mathbf{u}_p] \cdot \mathbf{n}\right)\right] \\ &+ \mathbb{D}(\psi_0 + \varepsilon\psi_p).\end{aligned}$$

It can be expanded into

$$\begin{aligned}\cancel{\partial_t\psi_0} + \varepsilon\partial_t\psi_p = &- \nabla \cdot \left[\cancel{\mathbf{n}\psi_0} + \varepsilon\mathbf{u}_p\psi_0 + \mathbf{n}\varepsilon\psi_p + \varepsilon^2\mathbf{u}_p\psi_p\right] \\ &- \nabla^\circ_{\mathbf{n}} \cdot \Bigg[\cancel{\psi_0(\mathbb{1} - \mathbf{nn}) \cdot \alpha_{\text{ext}}\check{\mathbf{B}}_{\text{ext}}} + \varepsilon\psi_p(\mathbb{1} - \mathbf{nn}) \cdot \alpha_{\text{ext}}\check{\mathbf{B}}_{\text{ext}} \\ &\qquad - \varepsilon\psi_0(\mathbb{1} - \mathbf{nn}) \cdot (\mathbf{W}[\mathbf{u}_p] \cdot \mathbf{n}) \\ &\qquad - \varepsilon^2\psi_p(\mathbb{1} - \mathbf{nn}) \cdot (\mathbf{W}[\mathbf{u}_p] \cdot \mathbf{n})\Bigg] \\ &+ \cancel{\mathbb{D}\psi_0} + \varepsilon\mathbb{D}\psi_p.\end{aligned}$$

The terms corresponding to the steady state sum up to zero and can be discarded. The divergence of the incompressible flow field is zero, i.e. $\nabla \cdot \mathbf{u}_p = 0$.

By neglecting terms of $\mathcal{O}(\varepsilon^2)$, the resulting linearized equation becomes

$$\begin{aligned}\partial_t\psi_p = &- \mathbf{n} \cdot \nabla\psi_p \\ &+ 2\mathbf{n} \cdot \check{\mathbf{B}}_{\text{ext}}\psi_p - ((\mathbb{1} - \mathbf{nn}) \cdot \check{\mathbf{B}}_{\text{ext}}) \cdot \nabla^\circ_{\mathbf{n}}\,\psi_p \\ &+ ((\mathbb{1} - \mathbf{nn}) \cdot \mathbf{W}[\mathbf{u}_p[\psi_p]] \cdot \mathbf{n}) \cdot \nabla^\circ_{\mathbf{n}}\,\psi_0 - 3\psi_0\,\mathbf{nn} : \mathbf{W}[\mathbf{u}_p[\psi_p]] \\ &+ \mathbb{D}\psi_p.\end{aligned} \tag{4.9}$$

In this derivation the following two identities for a tensor $\mathbf{W}$ and a vector $\mathbf{a}$ are used,

$$(\mathbb{1} - \mathbf{nn}) \cdot (\mathbf{W} \cdot \mathbf{n}) = \operatorname{Tr} \mathbf{W} - 3\mathbf{nn} : \mathbf{W}$$
$$\nabla^{\circ}_{\mathbf{n}} \cdot ((\mathbb{1} - \mathbf{nn}) \cdot \mathbf{a}) = -2\mathbf{n} \cdot \mathbf{a}.$$

The trace of the vorticity tensor is zero, $\operatorname{Tr} \mathbf{W} = 0$. According to Section 2.8, the flow field of the perturbation $\mathbf{u}_p$ is given by a spatial convolution of the Oseen tensor and the divergence of the mean stress, which in turn depends on the ψ_p:

$$\mathbf{u}_p[\psi_p] = -\mathbb{O} * \nabla \cdot \boldsymbol{\sigma}[\psi_p] \tag{4.10}$$

in which $\mathbb{O}$ is the Oseen tensor and $\boldsymbol{\sigma}$ is the mean stress is defined by

$$\boldsymbol{\sigma}[\psi_p] = \sigma_a \mathbf{Q}[\psi_p] + \sigma_m \left(\mathbf{p}[\psi_p] \check{\mathbf{B}}_{\text{ext}} + \check{\mathbf{B}}_{\text{ext}} \mathbf{p}[\psi_p] \right),$$

where the polarization vector and the nematic tensor of the perturbation are respectively given by

$$\mathbf{p}[\psi_p](\mathbf{k}) = \int_{\mathbb{S}^2} \mathrm{d}\mathbf{n}\ \mathbf{n}\, \psi_p(\mathbf{k}, \mathbf{n})$$
$$\mathbf{Q}[\psi_p](\mathbf{k}) = \int_{\mathbb{S}^2} \mathrm{d}\mathbf{n}\ \left(\mathbf{nn} - \frac{1}{3}\mathbb{1} \right) \psi_p(\mathbf{k}, \mathbf{n}).$$

Equation (4.9) can be cast into an operator equation of the form

$$\partial_t \psi_p = \mathbb{L} \psi_p, \tag{4.11}$$

in which the operator applied to a perturbation $\mathbb{L}\psi_p$ is given by the right hand-side of equation (4.9). As derived in Section 3.4, the equation is easily solvable once the eigenmodes and corresponding eigenvalues of the operator $\mathbb{L}$ are found. As further discussed in Section 3.4, a single eigenmode can be expressed by a plane wave ansatz for the spatial dependency, an orientational dependent amplitude $\tilde{\psi}(\mathbf{k}, \mathbf{n})$, and an exponential time dependency of the form

$$\psi_p(\mathbf{x}, \mathbf{n}, t) = \tilde{\psi}(\mathbf{k}, \mathbf{n})\, e^{\mathrm{i}\mathbf{k}\cdot\mathbf{x} + \lambda t}. \tag{4.12}$$

Hereby, the amplitude $\tilde{\psi}$ is an eigenfunction of the algebraized operator $\widehat{\mathbb{L}}$ with an eigenvalue given by λ that is obtained after the partial application (in $\mathbf{x}$) of $\mathbb{L}$ to the plane wave part of the ansatz above, i.e.

$$\mathbb{L}\psi_p(\mathbf{x}, \mathbf{n}, t) = \mathbb{L} e^{\mathrm{i}\mathbf{k}\cdot\mathbf{x} + \lambda t}\, \tilde{\psi}(\mathbf{k}, \mathbf{n})$$

$$
\begin{aligned}
&= e^{\mathrm{i}\mathbf{k}\cdot\mathbf{x}+\lambda t}\,\widehat{\mathbb{L}}\tilde{\psi}(\mathbf{k},\mathbf{n}) \\
&= e^{\mathrm{i}\mathbf{k}\cdot\mathbf{x}+\lambda t}\,\lambda\tilde{\psi}(\mathbf{k},\mathbf{n}) \\
\Leftrightarrow \qquad & \widehat{\mathbb{L}}\tilde{\psi} = \lambda\tilde{\psi}
\end{aligned} \tag{4.13}
$$

The real part of the eigenvalue $\mathrm{Re}\,\lambda$ is called the growth rate of the corresponding mode, the imaginary part $\mathrm{Im}\,\lambda$ is its frequency. This ansatz (4.12) is a solution to equation (4.11) and represents one of many eigenmodes. In the end, the eigenmode with the largest growth rate is of interest, as it dominates the dynamics. Therefore, the ansatz (4.12) serves as a general proxy to formulate an eigenvalue problem. When applying the operator $\mathbb{L}$ to the eigenmode ansatz in equation (4.12), the spatial derivatives and convolutions algebraize, i.e. $\nabla \mapsto \mathrm{i}\mathbf{k}$ and $\mathbb{O} * (\nabla \cdot \boldsymbol{\sigma}[\psi_p]) \mapsto e^{\mathrm{i}\mathbf{k}\cdot\mathbf{x}+\lambda t}\widehat{\mathbb{O}} \cdot (\mathrm{i}\mathbf{k} \cdot \boldsymbol{\sigma}[\tilde{\psi}])$, respectively. Equation (4.13) formulates an eigenvalue problem for the amplitude $\tilde{\psi}(\mathbf{k},\mathbf{n})$ of the plane wave perturbation with an eigenvalue λ. The algebraized operator $\widehat{\mathbb{L}}$ is given by

$$
\begin{aligned}
\widehat{\mathbb{L}}[\tilde{\psi}] = & -\mathrm{i}\mathbf{n}\cdot\mathbf{k}\tilde{\psi} \\
& + 2\mathbf{n}\cdot\check{\mathbf{B}}_{\text{ext}}\tilde{\psi} - ((\mathbb{1}-\mathbf{nn})\cdot\check{\mathbf{B}}_{\text{ext}})\cdot\nabla^{\circ}_{\mathbf{n}}\tilde{\psi} \\
& + ((\mathbb{1}-\mathbf{nn})\cdot\widehat{\mathbf{W}}[\hat{\mathbf{u}}_p[\tilde{\psi}]]\cdot\mathbf{n})\cdot\nabla^{\circ}_{\mathbf{n}}\psi_0 - 3\psi_0\,\mathbf{nn} : \widehat{\mathbf{W}}[\hat{\mathbf{u}}_p[\tilde{\psi}]] \\
& + \Delta^{\circ}_{\mathbf{n}}\tilde{\psi} - d_t k^2\tilde{\psi},
\end{aligned} \tag{4.14}
$$

in which the vorticity tensor becomes $\widehat{\mathbf{W}}[\hat{\mathbf{u}}_p] = \frac{\mathrm{i}}{2}(\mathbf{k}\hat{\mathbf{u}}_p - \hat{\mathbf{u}}_p\mathbf{k})$ and the flow field can be expressed by applying equation (4.10) to the ansatz ψ_p, yielding

$$
\hat{\mathbf{u}}_p[\tilde{\psi}](\mathbf{k}) = \frac{\mathrm{i}}{k}(\mathbb{1}-\check{\mathbf{k}}\check{\mathbf{k}})\cdot\boldsymbol{\sigma}[\tilde{\psi}]\cdot\check{\mathbf{k}}, \tag{4.15}
$$

with the normalized wave vector $\check{\mathbf{k}} = k^{-1}\mathbf{k}$ and the Fourier transform of the Oseen tensor $\widehat{\mathbb{O}} = \frac{1}{k^2}(\mathbb{1}-\check{\mathbf{k}}\check{\mathbf{k}})$.

In order to determine the growth rate $\mathrm{Re}\,\lambda$ for a certain perturbation, equation (4.13) needs to be solved. The methodology for solving the eigenvalue problem is discussed in the following section.

4.3.2 Solving the eigenvalue problem

According to the derivation in Section 3.4, the linear differentio-integro operator $\widehat{\mathbb{L}}$, defined in (4.14), is best expressed in the basis of spherical harmonics $Y_j^m(\vartheta,\varphi) = Y_{\pi(l,m)}$. The notation uses the index remapping $\pi(l,m) = l^2 + l + m$, defined in

equation (3.33) to simplify the index notation. The operator's coefficient matrix $\mathbf{L}$ can be found by

$$L_{lj} = \langle Y_l | \widehat{\mathbb{L}} | Y_j \rangle = \langle Y_l | \widehat{\mathbb{L}}[Y_j] \rangle$$

where the scalar product is defined by

$$\langle f | g \rangle = \int_{\mathbb{S}^2} \mathrm{d}\mathbf{n}\ f^*(\mathbf{n})\, g(\mathbf{n}),$$

with the complex conjugate $\bullet^*$. In this representation the eigenvalue problem in equation (4.13) can be expressed by the matrix equation

$$\mathbf{L} \cdot \tilde{\boldsymbol{\psi}} = \lambda \tilde{\boldsymbol{\psi}}, \tag{4.16}$$

with the coefficient vector $(\tilde{\boldsymbol{\psi}})_j = \langle Y_j | \tilde{\psi} \rangle$, see equation (3.36).

When calculating the expansion of equation (4.14) in spherical harmonics, products of spherical harmonics appear. They in turn can be further expanded into spherical harmonics using the Clebsch-Gordan coefficients, $\langle j_1, m_1, j_2, m_2 | j_3, m_3 \rangle$,

$$Y_{j_1}^{m_1} Y_{j_2}^{m_2} = \sum_{j_3, m_3} \sqrt{\frac{(2j_1+1)(2j_2+1)}{4\pi\ (2j_3+1)}}\, \langle j_1, 0, j_2, 0 | j_3, 0 \rangle\, \langle j_1, m_1, j_2, m_2 | j_3, m_3 \rangle\, Y_{j_3}^{m_3}.$$

Or equivalently,

$$\langle Y_{j_3}^{m_3} | Y_{j_1}^{m_1} Y_{j_2}^{m_2} \rangle = \sqrt{\frac{(2j_1+1)(2j_2+1)}{4\pi(2j_3+1)}}\, \langle j_1, 0, j_2, 0 | j_3, 0 \rangle\, \langle j_1, m_1, j_2, m_2 | j_3, m_3 \rangle\,,$$

which implicitly makes use of the orthogonality property

$$\langle Y_l^h | Y_j^m \rangle = \delta_{l,j}\, \delta_{h,m}.$$

Values for the Clebsch-Gordan coefficients can be calculated and are tabulated in various software packages [141, 142].

The matrix $\mathbf{L}$ is of infinite size. To calculate its spectrum approximately, high frequency angular modes are neglected by truncating the matrix at coefficients of Y_j^m, with $j > j_{\max}$. Figure 4.3 shows a representation of the truncated (here $j_{\max} = 8$) coefficient matrix. Non-zero entries are shown as dark blue. The blocks corresponding to different j-orders are highlighted in the background.

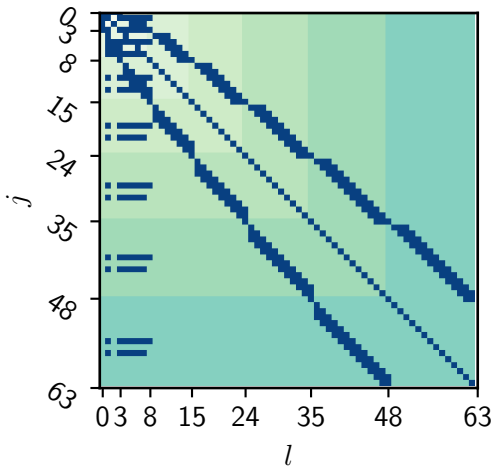

Fig. 4.3.: Representation of the truncated coefficient matrix of $(\mathbf{L})_{\mu\nu} = \langle Y_\mu | \widehat{\mathbb{L}} | Y_\nu \rangle$, defined in equation (4.3.2). The indices of the matrix are connected to the order and modes of spherical harmonics by $\mu, \nu = \pi(j_1, m_1), \pi(j_2, m_2)$, with the bijection $\pi(l, m) = l^2 + l + m$ given in equation (3.33). Dark blue pixels denote a non-vanishing of otherwise zero entries in the matrix. The highlighted blocks correspond to the same polynomial degree/order j of the spherical harmonic basis Y_j^m, thus the matrix is shown up to the seventh order.

Truncation error

Truncating the coefficient matrix $\mathbf{L}$ introduces an error in the calculation of the eigensystem. However, the error gets progressively smaller and has super-exponential convergence when adding further modes. The change of the eigenvalue with the largest real part and its corresponding eigenvector when varying the truncation order is plotted in Figure 4.4.

Depending on the system's parameter the convergence rate varies. There is an especially strong dependence on α_{ext}, partly due to the growing order needed to represent the steady state for high magnetic fields with sufficient precision. Its dependency is shown in Figure 4.4 (b), where coefficients smaller than 10^{-6} are neglected and truncated[3]. As an example the spectrum of the steady state for a fixed α_{ext} is shown in Figure 4.5 (a).

To summarize, the fast convergence behaviour justifies a truncation of the coefficient matrix while retaining sufficient precision. Additionally, higher modes of the eigen-

[3] An important technical detail worth mentioning is the exact expansion coefficients of the steady state involve fractions with very large (de)nominators. Therefore, a numerical evaluation has to be done with care. Numerical stability can be improved by introducing a cut-off value, for example 10^{-6}, and only consider coefficients larger than the cut-off. By fitting a square root to the resulting highest non-zero mode, a functional dependency can be established, compare with Figure 4.4.

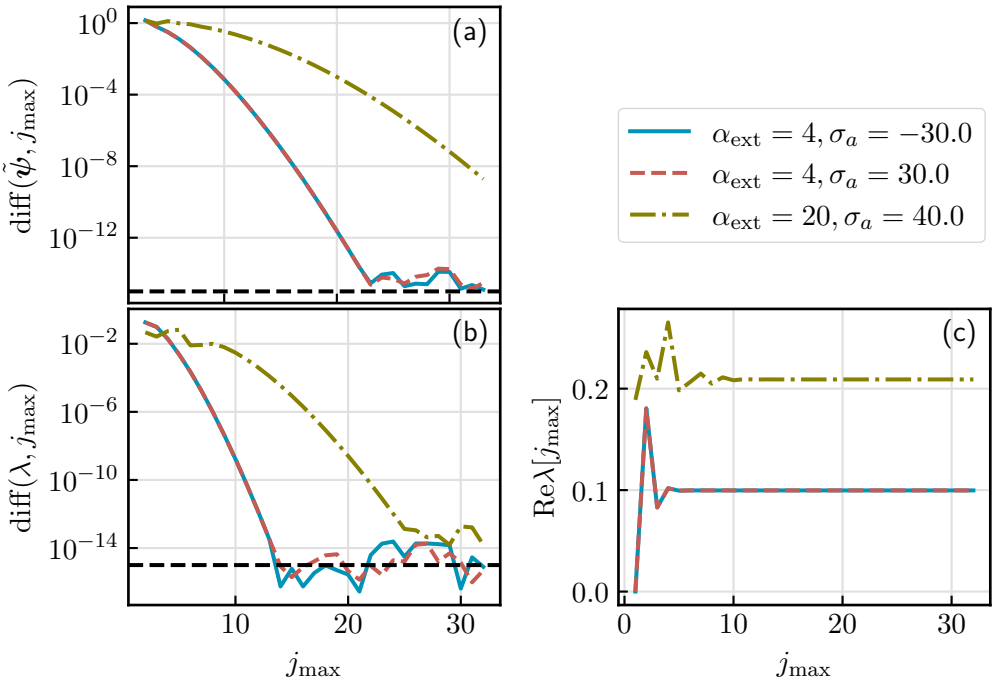

Fig. 4.4.: (a) Magnitude of change of the corresponding eigenvectors (in the basis of spherical harmonics) with respect to a truncation order $j_{\max}$, $\text{diff}(\tilde{\boldsymbol{\psi}}, j_{\max}) = \|\tilde{\boldsymbol{\psi}}[j_{\max}] - \tilde{\boldsymbol{\psi}}[j_{\max} - 1]\|$. The coefficient vector is given by $(\tilde{\boldsymbol{\psi}})_j^m = \langle Y_l^m | \tilde{\psi} \rangle$. The remaining parameters are fixed to $\sigma_m = 0.4\alpha_{\text{ext}}, d_t = 3 \times 10^{-6}$. (b) Change of the largest eigenvalues $\text{diff}(\lambda, j_{\max}) = |\lambda[j_{\max}] - \lambda[j_{\max} - 1]|$ in dependence of the number of included modes $j_{\max}$ on a logarithmic scale. After a certain number of modes, the changes are marginal, drop below numerical precision (black dashed line) and can be safely neglected. (c) The largest growth rate $\text{Re}\,\lambda_{\max}[j_{\max}]$ for different truncations.

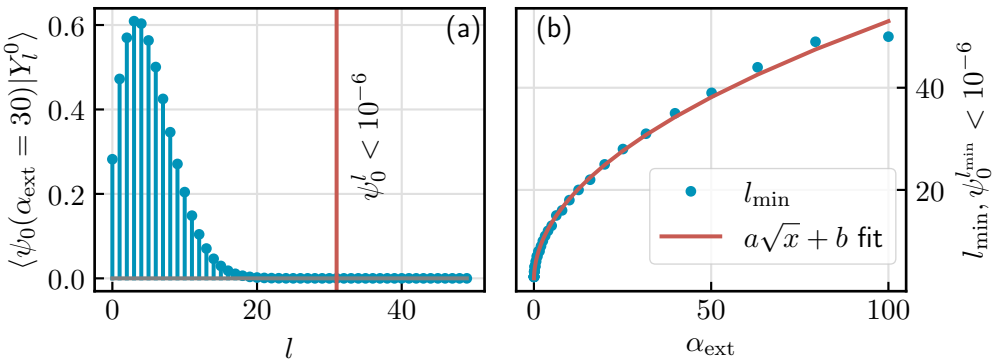

Fig. 4.5.: (a) Expansion coefficients of the homogeneous steady state $\psi_0(\alpha_{\text{ext}} = 30; \vartheta)$ in terms of spherical harmonics $Y_l^0(\vartheta)$. The higher the alignment parameter $\alpha_{\text{ext}} \propto B$, the more spherical modes, of polynomial degree l, have to be considered. (b) The smallest l, for which the coefficient drops below the chosen threshold of 10^{-6}.

vectors, shown in Figure 4.9, vanish quickly as well. After determining the growth rates $\mathrm{Re}\,\lambda$ of the modes of perturbation with high precision, the conditions under which the steady state ψ_0 is stable or unstable can be ascertained as discussed in the subsequent section.

4.3.3 Linear stability of the homogeneous steady state

The (linear) stability of the homogeneous steady state ψ_0 in equation (4.7) depends on the system's parameters: the strength of the active stress σ_a, the alignment parameter $\alpha_{\text{ext}} \propto mB$, the alignment stress strength $\sigma_m \propto B$, and the translational diffusion d_t. The active stress strength and the alignment parameter are usually experimentally adjustable quantities. The translational diffusion is assumed to be constant, whereas the alignment stress is covaried with the external magnetic field by a fixed linear law.

The parameter space spanned by $(\sigma_a, \alpha_{\text{ext}})$ can be divided into a stable and unstable regime with respect to the steady state $\psi_0(\alpha_{\text{ext}})$. In the stable regime, the system evolves towards the steady state $\psi_0(\alpha_{\text{ext}})$ and becomes stationary. In the unstable, regime even small fluctuations make the system depart from ψ_0 towards possibly non-trivial and non-linear dynamics. A line of neutral stability, defined by $\mathrm{Re}\,\lambda = 0$, divides both regimes. Figure 4.6 shows such a stability diagram. Alongside of it the polarization $p_0(\alpha_{\text{ext}})$ is plotted, highlighting the dependency of the polarization p_0 on α_{ext} of the steady state. This diagram represents an experimentally accessible range. The creation of a stability diagram presents several challenges. How some of these challenges are overcome is described in more detail in Section A.2 of the appendix.

From the stability diagram in Figure 4.6 it can be seen that the steady state ψ_0 is stable for a small activity $|\sigma_a| \lesssim 20$ and for low external magnetic fields, i.e. $\alpha_{\text{ext}} \lesssim 0.5$. In both cases, the hydrodynamic interactions are too weak to destabilize the steady state. In the first case, the hydrodynamic interactions cannot overcome the external torque. In the second case, the system is dominated by the rotational diffusion and thus orientationally disordered. Therefore, the mean active stress that is proportional to the nematic order parameter is very small or vanishes altogether.

For a sufficiently large active stress and a moderate external magnetic field strength, the homogeneous polar steady state is unstable. In this regime, the externally induced alignment of the force dipoles amplifies the strength of the anisotropic active stress, which would vanish otherwise in an isotropic distribution. That means, the

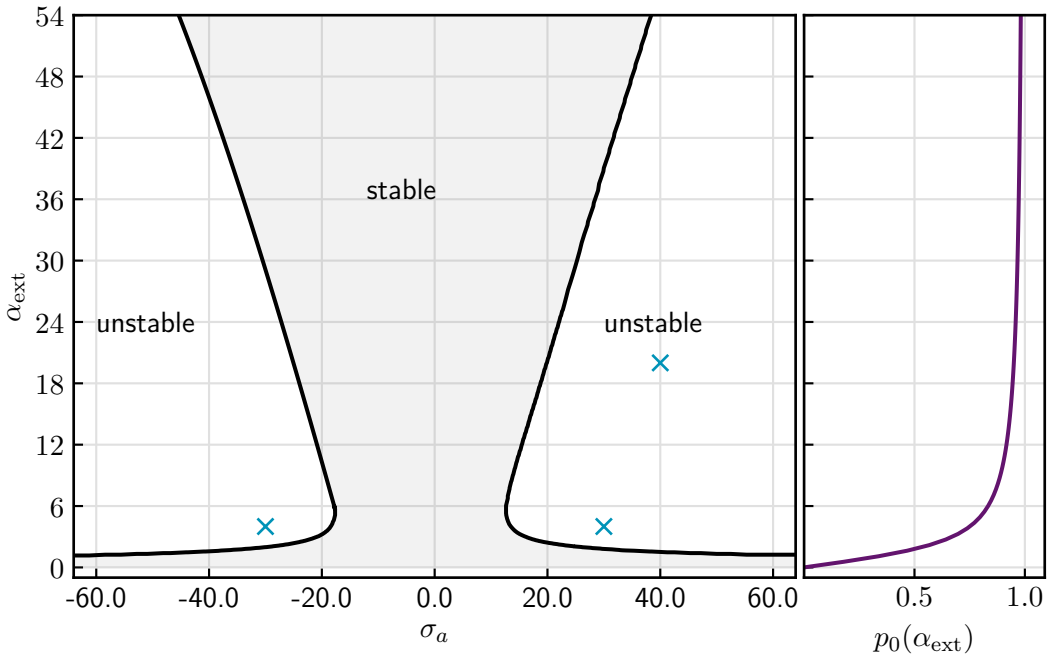

Fig. 4.6.: Stability diagram of the steady state $\psi_0(\alpha_{\text{ext}})$ in (4.1). The border of neutral stability (black line, $\operatorname{Re}\lambda = 0$) is calculated by the linear stability analysis. The remaining parameters are fixed to $\sigma_m = 0.4\alpha_{\text{ext}}, d_t = 3 \times 10^{-6}$. On the right panel the corresponding polarization $p_0(\alpha_{\text{ext}})$ of the steady state $\psi_0(\alpha_{\text{ext}})$ is plotted. Some points that are discussed in more detail in text are marked by cross symbol for reference.

hydrodynamic interactions (or more specifically the resulting hydrodynamic torques on the particles) become strong enough to resists the external alignment torque and destabilize the homogeneous polar state. Surprisingly, by further increasing the external magnetic field strength the steady state becomes stable again. This is due to the fact that the active stress magnitude is bounded, because it is proportional to the nematic order tensor $\mathbf{Q}$, as stated above. Assuming only small gradients near the steady state, the divergence of the active stress magnitude in equation (4.10) is primarily determined by the norm of $\mathbf{Q}(\alpha_{\text{ext}})$, which has a finite upper bound given in the limit of a perfectly aligned swimmers. In contrast, the external magnetic field strength and the resulting external torque is virtually unbounded and can eventually overcome all destabilizing hydrodynamic torques.

In the unstable regime, where the steady state becomes unstable, three distinct instability patterns are observed. To get a better idea of the nature of the instabilities, three exemplary representative points from the parameter space are presented for further analysis. These points are marked in the stability diagram in Figure 4.6 by crosses as well. As a reminder, a single perturbation mode has the form

$$\psi_p(\mathbf{k};\mathbf{x},\mathbf{n},t) = \tilde{\psi}(\mathbf{k},\mathbf{n})\, e^{\mathrm{i}\mathbf{k}\cdot\mathbf{x}+\lambda t}, \tag{4.17}$$

as defined by equation (4.12). The wavevector $\mathbf{k}$ defines the direction and wavelength of the perturbation. Eventually, the full perturbation is given by a superposition of all perturbation modes as given in equation (3.30), however, because of the linearity of the problem, it is sufficient to focus on just the dominant mode. The eigenfunction $\tilde{\psi}$ of the time-evolution operator $\widehat{\mathbb{L}}$, as defined in equation (4.14), associated with the eigenvalue λ encodes the amplitude of the spatial plane wave perturbation and the structure of the orientational part of the perturbation. The mode structure $\tilde{\psi}$ and the corresponding growth rate $\mathrm{Re}\,\lambda$ is obtained from the linear stability analysis as described in the previous section. The largest growth rate $\mathrm{Re}\,\lambda_{\max}(\mathbf{k})$ in dependence of the wavevector $\mathbf{k}$ of the perturbation is shown in Figures 4.7 and 4.8 for the three exemplary representatives. Figure 4.8 shows slices through the plots in Figure 4.7 at distinct angles. Additionally, it shows the imaginary part of the largest eigenvalue $\mathrm{Im}\,\lambda_{\max}$.

For both pushers and pullers at $\sigma_a = \pm 30$ and $\alpha_{\text{ext}} = 4$, the dominant perturbation, i.e. the one with the largest growth rate, can be found at $k = 0$. For pushers at $\sigma_a = -30$ and $\alpha_{\text{ext}} = 4$ the dominant perturbation mode is parallel to the external field, whereas for pullers at $\sigma_a = 30$ and $\alpha_{\text{ext}} = 4$ Figure 4.8 (b.1) shows two dominant modes both parallel and perpendicular to the external field. Additionally, the eigenvalues of the dominant modes at $k = 0$, for both pullers and pushers, have

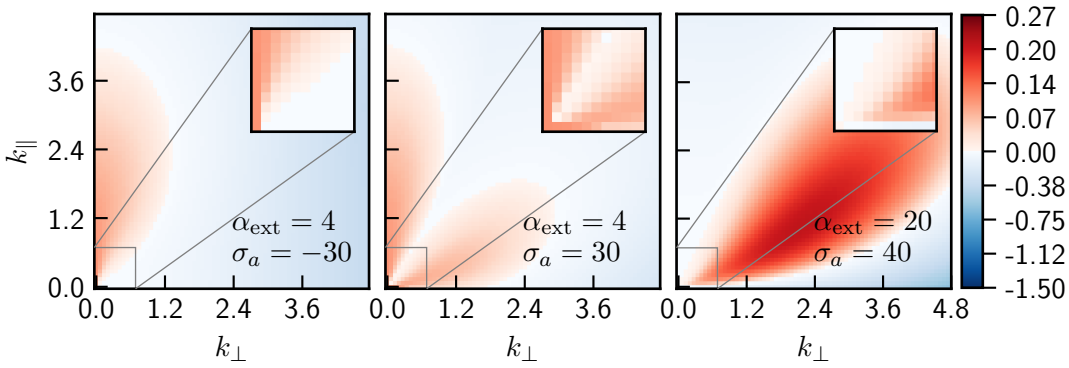

Fig. 4.7.: Growth rate ($\operatorname{Re}\lambda_{\max}$) for different wave vectors with components parallel, $k_\parallel$, and perpendicular to the external field, $k_\perp$. A positive growth rate (red) indicates a linearly unstable perturbation of the steady state ψ_0. The inset shows the values around $k = 0$ at a higher resolution. Note that the growth rate for $k = 0$ is not faithfully representable in this plot because it does not have unique value and still depends on the direction of the perturbation given by the angle with the magnetic flux density Θ_B. Instead, $\max_{\Theta_B} \operatorname{Re}\lambda_{\max}(k = 0, \Theta_B)$ is plotted.

a vanishing imaginary part, indicating a non-travelling perturbation (the amplitude of the perturbation still varies).

Perturbation modes at $k = 0$ cannot correspond to density perturbations, because they represent uniform perturbations. A uniform density perturbation is forbidden due to the conservation of probability. This observation can be proven formally and illustrated by having a closer look into the mode structure of the perturbation given by $\tilde{\psi}$. Its components in the basis of spherical harmonics are given by the inner product $(\tilde{\boldsymbol{\psi}})_l^m = \langle Y_l^m | \tilde{\psi} \rangle$ (compare with equation (4.16)). The components with a certain degree l correspond to the lth orientational moment, as is discussed in the following Section 4.4. As derived in equation (2.28), the density perturbation for a certain wavevector $\mathbf{k}$ is given by

$$\begin{aligned}
\rho_p(\mathbf{k}; \mathbf{x}, t) &= \int_{\mathbb{S}^2} \mathrm{d}\mathbf{n}\ \psi_p(\mathbf{k}; \mathbf{x}, \mathbf{n}, t) \\
&= \int_{\mathbb{S}^2} \mathrm{d}\mathbf{n}\ \tilde{\psi}(\mathbf{k}, \mathbf{n})\, e^{\mathrm{i}\mathbf{k}\cdot\mathbf{x}+\lambda t} \\
&= e^{\mathrm{i}\mathbf{k}\cdot\mathbf{x}+\lambda t}\, \langle \sqrt{4\pi} Y_0^0 | \tilde{\psi} \rangle\, (\mathbf{k}) \\
&= e^{\mathrm{i}\mathbf{k}\cdot\mathbf{x}+\lambda t} \sum_{j=0}^{\infty} \sum_{m=-j}^{j} \sqrt{4\pi}\, \langle Y_0^0 | Y_j^m \rangle\, \langle Y_j^m | \tilde{\psi} \rangle\, (\mathbf{k}) \\
&= e^{\mathrm{i}\mathbf{k}\cdot\mathbf{x}+\lambda t} \sqrt{4\pi} (\tilde{\boldsymbol{\psi}})_0^0(\mathbf{k}),
\end{aligned}$$

where the orthogonality of the spherical harmonics and $1 = \sqrt{4\pi} Y_0^0$ was used. Hence, the zeroth component $(\tilde{\boldsymbol{\psi}})_0^0$ of the eigenvector encodes the amplitude of a density

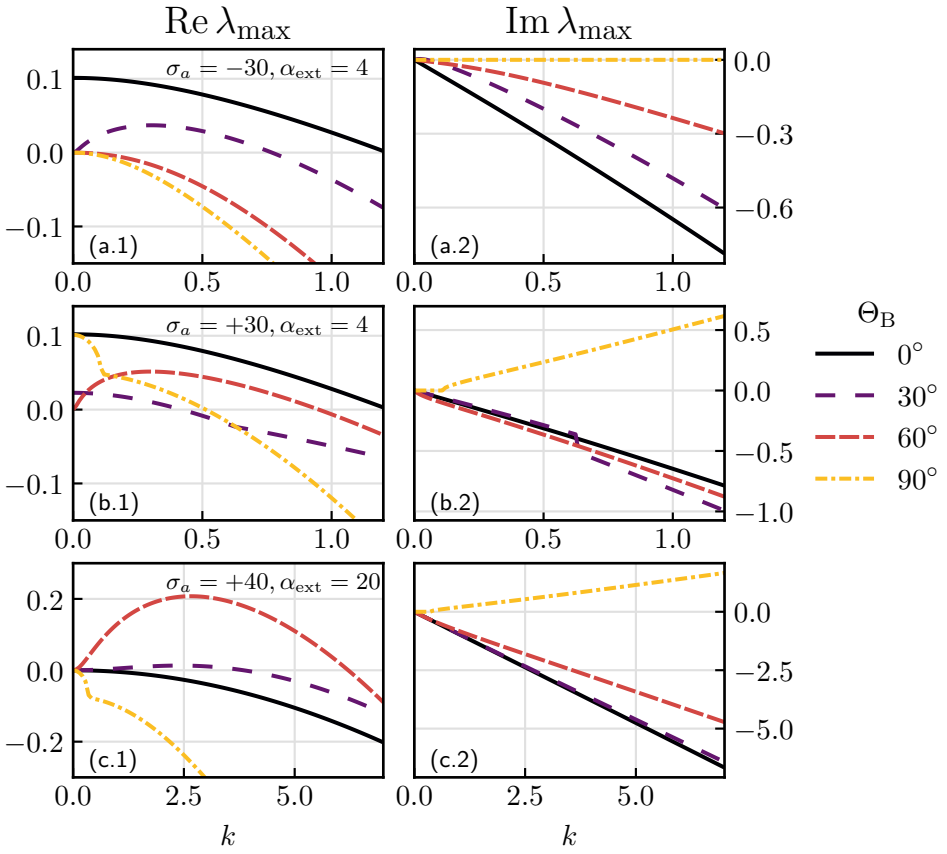

Fig. 4.8.: Growth rate $\mathrm{Re}\,\lambda_{\max}$ and oscillation frequency $\mathrm{Im}\,\lambda_{\max}$ for different perturbation angle Θ_B with respect to the external magnetic field and parameter pairs corresponding to the points marked by a cross symbol in the stability diagram in Figure 4.6. (a) Pushers at $\alpha_{\text{ext}} = 4, \sigma_a = -30$. (a.1) The dominant mode is obtained for a perturbation parallel to the external field at long wavelengths, i.e. wavenbumber $k \to 0$. (a.2) For $k \to 0$ the perturbation's frequency vanishes indicating a uniformly growing perturbation; for a finite wavenumber, the perturbation is a travelling wave with finite frequency and growing amplitude. (b) Puller at $\alpha_{\text{ext}} = 4, \sigma_a = 30$. (b.1) Two dominant modes at $k \to 0$ for directions $\Theta_B = 0, \pi/2$. (b.2) A similar situation as in (a.2), however, for finite wavenumbers the dominant modes have frequencies with opposite sign. (c) Puller at $\alpha_{\text{ext}} = 20, \sigma_a = 40$. (c.1) Dominant mode has a characteristic wavenumber $k \approx 2.5$ at a direction $\Theta_B \approx 60°$ and a finite frequency (see (c.2)). The dynamics represented in subfigures (c) is fundamentally different from those observed in (a) and (b).

perturbation ρ_p. Because probability must be conserved, the density perturbation has to fulfil the normalization condition

$$\begin{aligned}
& \frac{1}{v}\int_v \mathrm{d}\mathbf{x}\int_{\mathbb{S}^2}\mathrm{d}\mathbf{n}\ \psi(\mathbf{x},\mathbf{n},t) = 1 \\
\Leftrightarrow \quad & \frac{1}{v}\int_v \mathrm{d}\mathbf{x}\int_{\mathbb{S}^2}\mathrm{d}\mathbf{n}\ \left(\psi_0(\mathbf{n}) + \varepsilon\psi_p(\mathbf{k};\mathbf{x},\mathbf{n},t)\right) = 1 \\
\Leftrightarrow \quad & 1 + \frac{1}{v}\int_v \mathrm{d}\mathbf{x}\int_{\mathbb{S}^2}\mathrm{d}\mathbf{n}\ \varepsilon\psi_p(\mathbf{k};\mathbf{x},\mathbf{n},t) = 1 \\
\Leftrightarrow \quad & \frac{1}{v}\int_v \mathrm{d}\mathbf{x}\int_{\mathbb{S}^2}\mathrm{d}\mathbf{n}\ \psi_p(\mathbf{k};\mathbf{x},\mathbf{n},t) = 0 \\
\Leftrightarrow \quad & \int \mathrm{d}\mathbf{x}\,\rho_p(\mathbf{k};\mathbf{x},t) = 0, \quad \forall\mathbf{k}\in\mathbb{R}^3,
\end{aligned}$$

which is clearly not the case for a non-zero growth rate at $k = 0$, if $(\tilde{\boldsymbol{\psi}})_0^0(\mathbf{k} = \mathbf{0}) \neq 0$. It follows that a perturbation with $k = 0$ can only affect the orientation of the distribution function $\psi(\mathbf{x},\mathbf{n},t)$ and $(\tilde{\boldsymbol{\psi}})_0^0(k = 0)$ must vanish.

This observation is confirmed exemplarily by the first two eigenmodes shown in Figure 4.9. In this graph, the components, with respect to the basis of spherical harmonics, of the dominant eigenmode[4] for each the three exemplary points in the parameter space are shown. As can be seen in the magnified inset, the component $(\tilde{\boldsymbol{\psi}})_0^0$ is zero for the first two examples, where $k = 0$. In both of these cases, the perturbations correspond to a globally simultaneous change of polarization and is a reflection the symmetry of the system and the steady state. Similar to phononic excitations with $k = 0$, corresponding to a translation of the whole crystal, the $k = 0$ perturbations are of limited dynamical relevance. However, the perturbations near $k = 0$ have virtually the same eigenvector structure, so the $k = 0$ modes remain to be a useful limiting case for the discussion.

Pullers at $\sigma_a = 40$ and $\alpha_{\text{ext}} = 20$ show a completely different instability pattern. Neither parallel nor perpendicular perturbations are unstable, but rather perturbations of a finite angle $0 < \Theta_B < \pi/2$ dominate the system's dynamics. The largest growth rate is now associated with a characteristic finite wavelength, as depicted in Figure 4.8. The non-zero zeroth component of the eigenvector $(\tilde{\psi}_p)_0^0 \neq 0$ confirms the presence of an unstable density mode. Additionally, the imaginary part of the eigenvector $\mathrm{Im}\,\lambda$ is non-zero at the characteristic wavenumber, indicating a travelling wave perturbation with a finite phase velocity and a exponentially growing amplitude.

[4] Although, a puller at $\sigma_a = 30$ and $\alpha_{\text{ext}} = 4$ has two dominant modes at $k \to 0$, non-linear simulations show that the perpendicular one has a stronger influence on the dynamics than the parallel. Therefore, only the perpendicular mode is shown.

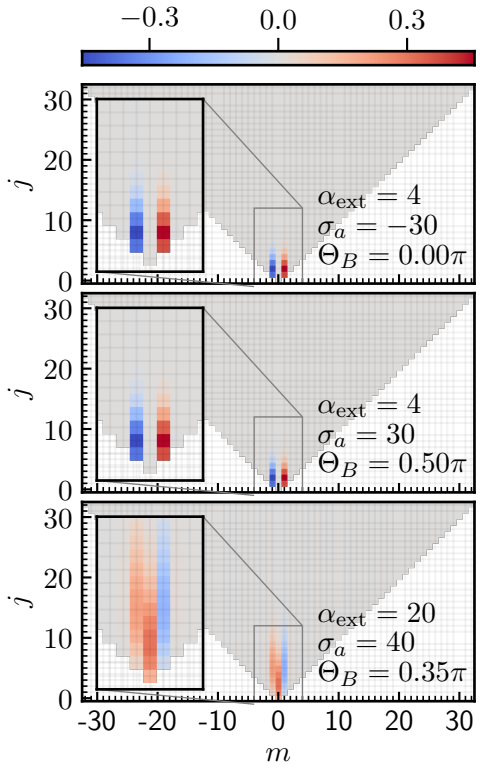

Fig. 4.9.: Exemplary coefficients $(\tilde{\boldsymbol{\psi}})_j^m = \langle Y_l^m | \tilde{\psi} \rangle$ — compare with equation (4.16) — of the eigenfunctions $\tilde{\psi}$ belonging to the largest growth rate (real part of eigenvalue) at the corresponding wavenumber $k_{\max}$ ($k_{\max} = 0$ in the first two cases and $k_{\max} \approx 2.5$ in the last) at a perturbation in the direction of the angle Θ_B with respect to the external magnetic field. To obtain the eigenfunction's coefficients, a coefficient matrix $\mathbf{L}$ truncated at the degree $j_{\max} = 32$ is used. The cone represents valid (j, m)-pairs. The eigenfunction encodes the orientational mode structure of the perturbation, as well as the amplitude ($(\tilde{\boldsymbol{\psi}})_0^0$) of a density perturbation. The parameter values correspond to the points marked with a cross symbol in Figure 4.6.

These three examples represent the three different types of instabilities observed: Parallel orientational perturbations for pushers, mixed parallel and perpendicular orientational instabilities for pullers at moderate external field strengths, and a more complex perturbation structure at higher field strengths and moderate magnitudes of the active stress for both pullers and pushers (here only an example for pullers is shown). Non-linear simulations show that for the second instability type (for pullers with moderate active stress and external magnetic field strength) the perpendicular perturbation mode has a stronger influence on the system's dynamics than the parallel one. It is therefore a good approximation to classify the second type as a perpendicular type, as confirmed in the subsequent section and in Section 4.4. The last type of instability features a finite characteristic wavelength for a perturbation at an angle between parallel and perpendicular. Furthermore, in contrast to the first two types, the last type perturbs the density of system directly, i.e. $(\tilde{\boldsymbol{\psi}})_0^0 \neq 0$.

From this analysis, different dynamics for pullers and pushers in the different unstable regimes (especially the first two types) are expected. For pushers patterns with axiall symmetry are expected, because the perturbations are in the direction of the symmetry axis. On the other hand, pullers should show a more complex behaviour once entering the unstable regime, as reflected by their richer mode structure. To develop a better understanding of the dynamics near the steady state, the complex mode structure, encoded in the eigenvector, is decomposed into orientational moments. The resulting linearized dynamics of the density and polarization field are the focus of the next section.

4.4 Linear stability of orientational moments

Instead of expanding the orientational part of the single particle distribution ψ in terms of spherical harmonics, as done in equation (3.35), it equivalently[5] can be expanded in terms of dyadic products of the orientation vector $\mathbf{n}$ [143, 144],

$$\psi(\mathbf{x}, \mathbf{n}, t) = \sum_j \mathbf{M}(j, \mathbf{x}, \mathbf{n}) \odot^j \mathbf{n}^{\otimes j}, \tag{4.18}$$

where the l-fold dyadic product is denoted by

$$\mathbf{n}^{\otimes l} = \underbrace{\mathbf{n} \otimes \ldots \otimes \mathbf{n}}_{l \,\text{times}}, \tag{4.19}$$

[5] $\mathbf{M}(j, \mathbf{x}, \mathbf{n}) \odot^j \mathbf{n}^{\otimes j}$ can be expressed as a linear combination of spherical harmonics Y_j^l, $l \in \{l || l| \leq j\}$ of rank j, see [143]

and $\odot^l$ denotes the l-fold contraction of two tensors,

$$(\mathbf{A} \odot^l \mathbf{B})^{i_1,\ldots,i_{n-l}}{}_{k_{l+1},\ldots k_m} = A^{i_1,\ldots,i_{n-l},j_1,\ldots j_l} B_{j_1,\ldots,j_l,k_{l+1},\ldots k_m},$$

for tensors $\mathbf{A} \in T_0^n(\mathbb{R}^3), \mathbf{B} \in T_m^0(\mathbb{R}^3)$ using Einstein summation convention. The coefficients[6] $\mathbf{M}(j, \mathbf{x}, \mathbf{n}) \propto \left\langle \mathrm{ST}(\mathbf{n}^{\otimes j}) \right\rangle_{\mathbf{n}}$ are proportional to the symmetric and traceless (irreducible) part of $\mathbf{n}^{\otimes j}$, as shown in [143], which are called orientational moments of ψ. The orientational expectation value is denoted by $\langle \bullet \rangle_{\mathbf{n}} = \int_{\mathbb{S}^2} \mathrm{d}\mathbf{n}\ \psi \bullet = \langle \psi | \bullet \rangle$. The operator $\mathrm{ST}(\mathbf{T}^n) = \mathbb{I}^{(n)} \odot^n \mathbf{T}^n$ projects a tensor onto its symmetric and traceless part. An explicit form of the rank $2n$ projection tensor $\mathbb{I}^{(n)}$, referred to as the *isotropic tensor*, can be found in [145].

The first three moments are the density, the polarization, and the nematic field, given by

$$\rho \equiv \left\langle \mathrm{ST}(\mathbf{n}^{\otimes 0}) \right\rangle_{\mathbf{n}} = \langle 1 \rangle_{\mathbf{n}} = \int_{\mathbb{S}^2} \mathrm{d}\mathbf{n}\ \ \psi\ 1 \tag{4.20}$$

$$\mathbf{p} \equiv \left\langle \mathrm{ST}(\mathbf{n}^{\otimes 1}) \right\rangle_{\mathbf{n}} = \langle \mathbf{n} \rangle_{\mathbf{n}} = \int_{\mathbb{S}^2} \mathrm{d}\mathbf{n}\ \ \psi\ \mathbf{n} \tag{4.21}$$

$$\mathbf{Q} \equiv \left\langle \mathrm{ST}(\mathbf{n}^{\otimes 2}) \right\rangle_{\mathbf{n}} = \langle \mathbf{nn} - \mathbb{1}/3 \rangle_{\mathbf{n}} = \int_{\mathbb{S}^2} \mathrm{d}\mathbf{n}\ \ \psi\ \left(\mathbf{nn} - \frac{1}{3}\mathbb{1} \right) \tag{4.22}$$

Higher moments are defined accordingly. Hence, the distribution ψ expanded in the orientational moments reads

$$\psi(\mathbf{x}, \mathbf{n}, t) = \frac{1}{4\pi} \left[\rho(\mathbf{x}, t) + 3\mathbf{n} \cdot \mathbf{p}(\mathbf{x}, t) + \frac{15}{2} \mathbf{nn} : \mathbf{Q}(\mathbf{x}, t) + \cdots \right].$$

The moment expansion has the advantage that it is easier to manipulate the resulting terms algebraically and gives a chance to find approximate analytical expressions for the linear stability analysis. The orientational moments each obey dynamical equations that can be derived directly form the Smoluchowski equation (4.1) by integration. The equation of moments is derived for the first three moments in the subsequent section.

[6] $\mathbf{M}(j, \mathbf{x}, \mathbf{n})_{i_1, i_2, \ldots, i_j} = \frac{2j+1}{4\pi} \int_{\mathbb{S}^2} \mathrm{d}\mathbf{n}\ \psi(\mathbf{x}, \mathbf{n}, t) \left[\frac{\partial^j}{\partial y_{i_1} \partial y_{i_2} \cdots \partial y_{i_j}} P(\mathbf{y}, \mathbf{n}) \right]_{y=0}$, with the Poisson kernel for the unit ball $P(\mathbf{y}, \mathbf{n}) = \frac{1 - |\mathbf{y}|^2}{|\mathbf{y} - \mathbf{n}|^3}$ in three dimensions

4.4.1 Equation of moments

The time evolution of the density field $\rho(\mathbf{x}, t)$ can be derived by tracing out the angular dependency in equation (4.1), i.e. integrating over all possible orientations. Using the identity $\int_{\mathbb{S}^2} \mathrm{d}\mathbf{n}\ \Delta^\circ_{\mathbf{n}}\, \psi = 0$, its time evolution is given by

$$\partial_t \rho = -\nabla \cdot (\rho \mathbf{u} + \mathbf{p}) + d_t\, \Delta\, \rho. \tag{4.23}$$

The time evolution of the polarization field $\mathbf{p}(\mathbf{x}, t)$ can be obtained likewise by integrating equation (4.1) by $\int_{\mathbb{S}^2} \mathrm{d}\mathbf{n}\ \mathbf{n}\bullet$. By using the identities, proven in the Propositions A.3.1 and A.3.2,

$$\int_{\mathbb{S}^2} \mathrm{d}\mathbf{n}\ \mathbf{n}\, \Delta^\circ_{\mathbf{n}}\, \psi = -2\mathbf{p} \tag{4.24}$$

and

$$\int_{\mathbb{S}^2} \mathrm{d}\mathbf{n}\ \mathbf{n}\, \nabla^\circ_{\mathbf{n}} \cdot (\mathbf{v}_\mathrm{r} \psi) = -\int_{\mathbb{S}^2} \mathrm{d}\mathbf{n}\ \mathbf{v}_\mathrm{r} \psi \tag{4.25}$$

for a tangential vector field $\mathbf{v}_\mathrm{r}$ on a sphere with $\mathbf{v}_r \cdot \mathbf{n} = 0$, here given by the rotational drift velocity (see equation (4.3)), the equation for the polarization field is given by

$$\partial_t \mathbf{p} = -\mathbf{u}\cdot\nabla\mathbf{p} - \nabla\cdot\mathbf{Q} - \frac{1}{3}\nabla\rho - \left(\mathbf{Q} - \frac{2}{3}\rho\mathbb{1}\right)\cdot\alpha_{\text{ext}}\check{\mathbf{B}}_{\text{ext}} + \mathbf{W}\cdot\mathbf{p} - \mathbf{W}:\langle\mathbf{nnn}\rangle_{\mathbf{n}} + d_t\,\Delta\,\mathbf{p} - 2\mathbf{p}, \tag{4.26}$$

in which the normalized magnetic flux density is denoted by $\check{\mathbf{B}}_{\text{ext}} = \|\mathbf{B}_{\text{ext}}\|^{-1}\mathbf{B}_{\text{ext}}$, and $\mathbf{W} = \frac{1}{2}\left(\nabla\mathbf{u} - (\nabla\mathbf{u})^\top\right)$ is the vorticity tensor (see equation (2.90)).

Lastly, by integrating equation (4.1) with $\int_{\mathbb{S}^2} \mathrm{d}\mathbf{n}\ \mathbf{nn}\bullet$ and using the following identities proven in the appendix in Propositions A.3.3 and A.3.4,

$$\begin{aligned} \nabla^\circ_{\mathbf{n}}\, \mathbf{n} &= \mathbf{e}_\vartheta \mathbf{e}_\vartheta + \mathbf{e}_\varphi \mathbf{e}_\varphi = \mathbb{1} - \mathbf{nn} \\ \mathbf{v}\cdot\mathbf{n} = 0 \Rightarrow \int_{\mathbb{S}^2} \mathrm{d}\mathbf{n}\ \mathbf{nn}\, \nabla^\circ_{\mathbf{n}} \cdot \mathbf{v} &= -\int_{\mathbb{S}^2} \mathrm{d}\mathbf{n}\, [\mathbf{nv} + \mathbf{vn}] \qquad (4.27) \\ \int_{\mathbb{S}^2} \mathrm{d}\mathbf{n}\ \mathbf{nn}\, \Delta^\circ_{\mathbf{n}}\, \psi &= -2\int_{\mathbb{S}^2} \mathrm{d}\mathbf{n}\ \mathbf{n}\psi\, \Delta^\circ_{\mathbf{n}}\, \mathbf{n} + 2\int_{\mathbb{S}^2} \mathrm{d}\mathbf{n}\ \psi\, \nabla^\circ_{\mathbf{n}}\, \mathbf{n} \\ &= -6\mathbf{Q}, \qquad (4.28) \end{aligned}$$

the time evolution of the nematic tensor field can be obtained:

$$\begin{aligned} &\partial_t \mathbf{Q} + \frac{1}{3}\mathbb{1}\partial_t\rho + \mathbf{u}\cdot\nabla\mathbf{Q} + \frac{1}{3}\mathbb{1}\mathbf{u}\cdot\nabla\rho + \nabla\cdot\langle\mathbf{nnn}\rangle_{\mathbf{n}} - \alpha_{\text{ext}}(\mathbf{p}\check{\mathbf{B}}_{\text{ext}} + \check{\mathbf{B}}_{\text{ext}}\mathbf{p}) \\ &\quad - \mathbf{W}\cdot\mathbf{Q} - \underbrace{\mathbf{Q}^\top\cdot\mathbf{W}^\top}_{=-\mathbf{Q}\cdot\mathbf{W}} - \frac{1}{3}\mathbf{W}\rho - \frac{1}{3}\underbrace{\mathbf{W}^\top}_{=-\mathbf{W}}\rho + 2\alpha_{\text{ext}}\check{\mathbf{B}}_{\text{ext}}\cdot\langle\mathbf{nnn}\rangle_{\mathbf{n}} + 2\mathbf{W}:\langle\mathbf{nnnn}\rangle_{\mathbf{n}} \end{aligned}$$

$$+ 6\mathbf{Q} - d_t \Delta \mathbf{Q} + \frac{1}{3} d_t \mathbb{1} \Delta \rho = 0.$$

For an asymmetric matrix $\mathbf{W}$ the term $\mathbf{W} : \langle \mathbf{nnnn} \rangle_{\mathbf{n}} = 0$ vanishes. By subtracting $\frac{1}{3}\mathbb{1}$ times equation (4.23) from the equation above, the time evolution of the nematic field finally yields:

$$\begin{aligned} \partial_t \mathbf{Q} = &-\mathbf{u} \cdot \nabla \mathbf{Q} + \frac{1}{3}\mathbb{1} \nabla \cdot \mathbf{p} + \alpha_{\text{ext}} (\mathbf{p}\check{\mathbf{B}}_{\text{ext}} + \check{\mathbf{B}}_{\text{ext}}\mathbf{p}) - \mathbf{W} \cdot \mathbf{Q} + \mathbf{Q} \cdot \mathbf{W} - 6\mathbf{Q} \\ &+ d_t \Delta \mathbf{Q} - \nabla \cdot \langle \mathbf{nnn} \rangle_{\mathbf{n}} - 2\alpha_{\text{ext}} \check{\mathbf{B}}_{\text{ext}} \cdot \langle \mathbf{nnn} \rangle_{\mathbf{n}}. \end{aligned} \tag{4.29}$$

Closure

As can be seen from the equation of moments (4.23), (4.26), and (4.29), they build a hierarchy of equations: Each moment equation depends on higher moments. In order to make progress, this hierarchy is broken by introducing closure relations. Because the steady state is polarized, a suitable closure is given by,

$$\begin{aligned} \bar{\mathbf{Q}} &= \mathbf{pp} - \frac{1}{3}\mathbb{1} \\ \langle \mathbf{nnn} \rangle_{\mathbf{n}} &= 0 \end{aligned} \tag{4.30}$$

sometimes referred to the *Hand*-closure [146]. In the next section, it can be seen that this closure generates perturbations that are structurally consistent with the result of the previous linear stability analysis in Section 4.3. Near the homogeneous steady state, the dynamics is assumed to be slowly changing. Therefore, higher moments are set to zero and neglected. This is equivalent to the assumption that the dynamics are dominated by low frequency components. In this closure, the nematic tensor near the polarized steady state is directly derived from the polarization field and its own independent dynamics is neglected.

4.4.2 Stability of moments

After establishing the moment equations of the system, reduced to the density and polarization field, their respective linear stability can be studied by using the closure relation above. The homogeneous steady state ψ_0, in equation (4.7), in terms of moments is given by

$$\rho_0 = \langle 1 \rangle_{\mathbf{n}}^{\psi_0} = 1$$

$$\mathbf{p}_0 = \langle \mathbf{n} \rangle_{\mathbf{n}}^{\psi_0} = \frac{\sqrt{4\alpha_{\text{ext}}^2 + 9} - 3}{2\alpha_{\text{ext}}}.$$

However, p_0 can be substituted by the more exact $\mathbf{p}_0 = p_0(\alpha_{\text{ext}})\mathbf{e}_z = \frac{\alpha_{\text{ext}} \coth \alpha_{\text{ext}} - 1}{\alpha_{\text{ext}}}$ obtained in Section 4.7 in equation (4.8). As before, the steady state is linearly disturbed by small perturbations.

By considering small perturbations of the form

$$\begin{aligned}
\rho &= \rho_0 + \varepsilon \rho_p \\
\mathbf{p} &= \mathbf{p}_0 + \varepsilon \mathbf{p}_p \\
\bar{\mathbf{Q}} &= \bar{\mathbf{Q}}_0 + \varepsilon \bar{\mathbf{Q}}_p = \left(\mathbf{p}_0 \mathbf{p}_0 - \frac{1}{3} \mathbb{1} \right) + \varepsilon (\mathbf{p}_0 \mathbf{p}_p + \mathbf{p}_p \mathbf{p}_0) \\
\mathbf{u} &= \mathbf{u}_0 + \varepsilon \mathbf{u}_p,
\end{aligned}$$

in which $0 < \varepsilon \ll 1$ and $\mathbf{u}_0 = 0$, and substituting them into equations (4.23) and (4.29), the dynamics of the linearized perturbations in $\mathcal{O}(\varepsilon)$ can be formulated as

$$\partial_t \rho_p = -\nabla \cdot \mathbf{p}_p + d_t \, \Delta \, \rho_p \tag{4.31}$$

$$\begin{aligned}
\partial_t \mathbf{p}_p = &\frac{2}{3} \rho_p \alpha_{\text{ext}} \check{\mathbf{B}}_{\text{ext}} - \frac{1}{3} \nabla \rho_p + \tilde{\mathbf{W}} \cdot \mathbf{p}_0 + \mathbf{W}_p \cdot \mathbf{p}_0 + d_t \, \Delta \, \mathbf{p}_p - 2\mathbf{p}_p \\
&- \nabla \cdot \bar{\mathbf{Q}}_p - \bar{\mathbf{Q}}_p \cdot \alpha_{\text{ext}} \check{\mathbf{B}}_{\text{ext}}.
\end{aligned} \tag{4.32}$$

Analogous to equation (3.32), an eigenmode ansatz for the perturbations of the moments can be made, as

$$\begin{aligned}
\rho_p(\mathbf{k}; \mathbf{x}, t) &= \tilde{\rho}(\mathbf{k}) \, e^{\mathrm{i}\mathbf{k}\cdot\mathbf{x} + \lambda t} \\
\mathbf{p}_p(\mathbf{k}; \mathbf{x}, t) &= \tilde{\mathbf{p}}(\mathbf{k}) \, e^{\mathrm{i}\mathbf{k}\cdot\mathbf{x} + \lambda t} \\
\mathbf{Q}_p(\mathbf{k}; \mathbf{x}, t) &= \tilde{\mathbf{Q}}(\mathbf{k}) \, e^{\mathrm{i}\mathbf{k}\cdot\mathbf{x} + \lambda t} \equiv (\mathbf{p}_0 \tilde{\mathbf{p}} + \tilde{\mathbf{p}} \mathbf{p}_0)(\mathbf{k}) \, e^{\mathrm{i}\mathbf{k}\cdot\mathbf{x} + \lambda t} \\
\mathbf{u}_p(\mathbf{k}; \mathbf{x}, t) &= \tilde{\mathbf{u}}(\mathbf{k}) \, e^{\mathrm{i}\mathbf{k}\cdot\mathbf{x} + \lambda t},
\end{aligned}$$

where the flow field perturbation $\tilde{\mathbf{u}}$ is derived from $\tilde{\mathbf{Q}}$ by

$$\tilde{\mathbf{u}} = \frac{\mathrm{i}}{k^2} \left(\mathbb{1} - \check{\mathbf{k}} \check{\mathbf{k}} \right) \cdot \sigma_a \tilde{\mathbf{Q}} \cdot \mathbf{k}, \tag{4.33}$$

in which $\check{\mathbf{k}} = k^{-1}\mathbf{k}$ and $\tilde{\mathbf{Q}} \equiv \mathbf{p}_0 \tilde{\mathbf{p}} + \tilde{\mathbf{p}} \mathbf{p}_0$. By substituting the ansatzes back into the equations they transform into

$$\lambda \tilde{\rho} = -\mathrm{i}\mathbf{k} \cdot \tilde{\mathbf{p}} - d_t k^2 \tilde{\rho} \tag{4.34}$$

$$\lambda\tilde{\mathbf{p}}=\frac{2}{3}\tilde{\rho}\,\alpha_{\text{ext}}\check{\mathbf{B}}_{\text{ext}}-\frac{\mathrm{i}}{3}\mathbf{k}\tilde{\rho}+\tilde{\mathbf{W}}\cdot\mathbf{p}_0-d_tk^2\,\tilde{\mathbf{p}}-2\tilde{\mathbf{p}}$$
$$-\mathrm{i}\mathbf{k}\cdot(\mathbf{p}_0\tilde{\mathbf{p}}+\tilde{\mathbf{p}}\mathbf{p}_0)-(\mathbf{p}_0\tilde{\mathbf{p}}+\tilde{\mathbf{p}}\mathbf{p}_0)\cdot\alpha_{\text{ext}}\check{\mathbf{B}}_{\text{ext}}, \tag{4.35}$$

in which the vorticity tensor in terms of the eigenmodes is defined by

$$\tilde{\mathbf{W}}=\frac{\mathrm{i}}{2}\left(\tilde{\mathbf{u}}\mathbf{k}-\mathbf{k}\tilde{\mathbf{u}}\right).$$

At this point, a comparison of the intermediate result of the perturbation of moments with the results of the previous linear stability analysis of the full single particle distribution $\psi(\mathbf{x},\mathbf{n},t)$ in Section 4.3 is instructive. Because of the equivalence of the approaches, the components of the eigenfunctions $(\tilde{\boldsymbol{\psi}})_j^m=\langle Y_l^m|\tilde{\psi}\rangle$ of the perturbation ansatz $\psi_p(\mathbf{k};\mathbf{x},\mathbf{n},t)=\tilde{\psi}(\mathbf{k},\mathbf{n})\,e^{\mathrm{i}\mathbf{k}\cdot\mathbf{x}+\lambda t}$, calculated in the previous sections and plotted in Figure 4.9, already contain the information on how the different orientational moments of the PDF are perturbed. Their specific perturbation amplitudes $\tilde{\rho},\tilde{\mathbf{p}},\ldots$ can be projected out by the inner product, $\langle f|g\rangle=\int_{\mathbb{S}^2}\mathrm{d}\mathbf{n}\;f^*(\mathbf{n})\,g(\mathbf{n})$, or equivalently, directly calculated from the coefficient vector of the eigenfunction $\tilde{\boldsymbol{\psi}}$ in the basis of spherical harmonics:

$$\begin{aligned}\left\langle \mathrm{ST}(\mathbf{n}^{\otimes l})\right\rangle_{\mathbf{n}}^{\tilde{\psi}}&\equiv\int_{\mathbb{S}^2}\mathrm{d}\mathbf{n}\;\mathrm{ST}(\mathbf{n}^{\otimes l})\,\tilde{\psi}(\mathbf{k},\mathbf{n})\\&=\langle\mathrm{ST}(\mathbf{n}^{\otimes l})|\tilde{\psi}\rangle\\&=\sum_{j=0}^{\infty}\sum_{m=-j}^{j}\langle\mathrm{ST}(\mathbf{n}^{\otimes l})|Y_j^m\rangle\underbrace{\langle Y_j^m|\tilde{\psi}\rangle}_{=(\tilde{\boldsymbol{\psi}})_l^m}\\&=\sum_{j=0}^{\infty}\sum_{m=-j}^{j}\langle\mathrm{ST}(\mathbf{n}^{\otimes l})|Y_j^m\rangle\,(\tilde{\boldsymbol{\psi}})_l^m,\end{aligned}$$

in which $\sum_{j=0}^{\infty}\sum_{m=-j}^{j}|Y_j^m\rangle\langle Y_j^m|=\mathbb{1}$ was used, in the second line $\mathbf{n}\in\mathbb{R}^3\Rightarrow\mathbf{n}^*=\mathbf{n}$, and $\mathrm{ST}(\mathbf{n}^{\otimes l})$ can be expressed solely in terms of spherical harmonics of rank l, so that $\langle\mathrm{ST}(\mathbf{n}^{\otimes l})|Y_j^m\rangle=0$ for $l\neq j$ [143]. Finally, projecting the concrete eigenfunctions $\tilde{\psi}$ that are calculated in the previous section and plotted in Figure 4.9, of the parallel perturbation ($\mathbf{k}\parallel\mathbf{B}_{\text{ext}}$) for pushers and perpendicular perturbation ($\mathbf{k}\perp\mathbf{B}_{\text{ext}}$) for pullers (for example at $|\sigma_a|=30,\alpha_{\text{ext}}=4$) onto the first three moments, as described above, results in amplitudes of the form

$$\tilde{\rho}=\langle 1\rangle_{\mathbf{n}}^{\tilde{\psi}}=0 \tag{4.36}$$

$$\tilde{\mathbf{p}}=\langle\mathbf{n}\rangle_{\mathbf{n}}^{\tilde{\psi}}\propto(1,0,0) \tag{4.37}$$

$$\tilde{\mathbf{Q}} = \langle \mathbf{nn} - \mathbb{1}/3 \rangle_{\mathbf{n}}^{\tilde{\psi}} \propto \begin{pmatrix} 0 & 0 & 1 \\ 0 & 0 & 0 \\ 1 & 0 & 0 \end{pmatrix} \propto \tilde{\mathbf{p}}\mathbf{p}_0 + \mathbf{p}_0\tilde{\mathbf{p}} \tag{4.38}$$

for both the parallel and perpendicular perturbations. The projections onto these fields show that the perturbations have no density component, equation (4.36), and the polarization is perturbed in x-direction (without loss of generality) perpendicular to the external field in $\mathbf{p}_0$-direction, equation (4.37). So it is safe to assume that $\tilde{\mathbf{p}} \cdot \mathbf{p}_0 = 0$, which effectively means that small linear perturbations influence the direction but not the magnitude of the polarization. To this end, considering only the first component $\tilde{p}_\perp$ of $\tilde{\mathbf{p}}$ is sufficient, focusing on the hydrodynamically induced orientational instability. Additionally, the closure in equation (4.30) naturally generates a nematic perturbation of the form $\tilde{\mathbf{p}}\mathbf{p}_0 + \mathbf{p}_0\tilde{\mathbf{p}}$ also found in equation (4.38), retroactively confirming the validity of the choice of closure. Physically, a polarization perturbation of this form corresponds to bend (for pushers) and splay (for pullers) deformations of the polarization field, to be discussed in the upcoming Section 4.6.

Setting $\tilde{\mathbf{p}} \cdot \mathbf{p}_0 = 0$ and thus focusing on $\tilde{\rho}$ and $\tilde{p}_\perp$, the equations (4.34) and (4.35) can be written in the reduced form of

$$\lambda \begin{pmatrix} \tilde{\rho} \\ \tilde{p}_\perp \end{pmatrix} = \mathbf{T} \cdot \begin{pmatrix} \tilde{\rho} \\ \tilde{p}_\perp \end{pmatrix}, \tag{4.39}$$

with the operator

$$\mathbf{T} \equiv \begin{pmatrix} -d_t k^2 & -ik \sin\Theta_B \\ -\frac{1}{3}\mathrm{i} \sin\Theta_B & -2 - d_t k^2 + \mathrm{i}p_0\, k\, \cos\Theta_B - \alpha_{\text{ext}} p_0 - \frac{1}{2} p_0^2 \sigma_a \cos 2\Theta_B \end{pmatrix}.$$

Here, $\mathbf{k} = k\sin(\Theta_B)\check{\mathbf{e}}_x + k\cos(\Theta_B)\check{\mathbf{e}}_z$ was used, where Θ_B denotes the angle of the direction of the perturbation with respect to the external field axis pointing in z-direction, $\Theta_B = \angle(\mathbf{k}, \mathbf{B}_{\text{ext}})$. The eigenvalues can be found analytically[7].

It comes as no surprise that the largest eigenvalue can be found at $k \to 0$, as previously determined in Section 4.3.3 as well. Therefore, it is sufficient to restrict the analysis to these modes in order assess the stability of the steady state. In this case the eigenvalues read

$$\lambda_{1,2} = \frac{1}{4}(a \pm |a|) \tag{4.40}$$

[7] If in doubt regarding dropping the parallel component of $\tilde{\mathbf{p}}$ in the calculation, it should be noted the same result is obtained at $k = 0$ when including it.

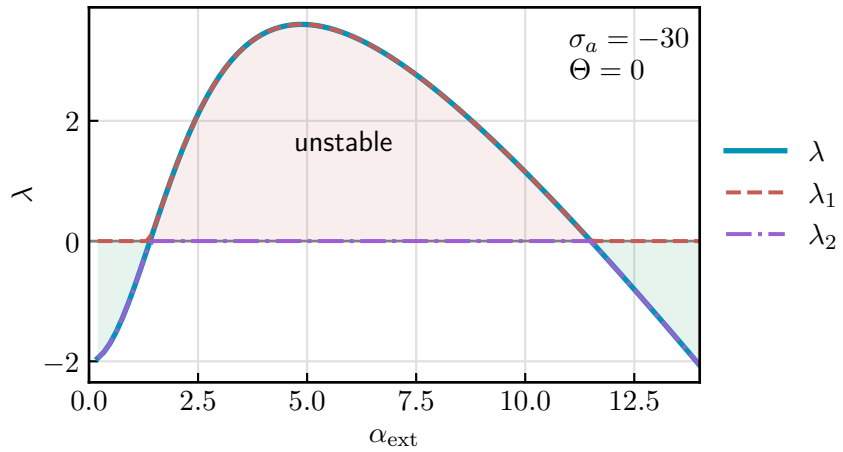

Fig. 4.10.: The growth rates $\mathrm{Re}\,\lambda$ against the alignment parameter α_{ext} of a linear perturbation of the polarization field, equation (4.41). This illustrates the re-entrant stability for a growing magnetic field. The blue line is the eigenvalue of a mode crossing over from negative to positive and back to negative growth rate. It is constructed from the eigenvalues $\lambda_{1,2}$ defined in equation (4.40).

with $a = -4 - 2\alpha_{\text{ext}}p_0 - p_0^2\sigma_a \cos 2\Theta_B$. The largest eigenvalue is given by $\lambda_{\text{max}} = \max(0, a/2)$ (and the smallest by $\min(0, a/2)$). However, simulations show that the perturbation associated with the $\lambda = 0$ can be considered stable. On the other hand, the eigenvalue corresponding to the mode that becomes unstable, i.e. has a change of sign in its growth rate, can be constructed by combining the non-zero parts of eigenvalues into one, yielding

$$\lambda = \frac{a}{2} = -2 - \alpha_{\text{ext}}p_0 - \frac{1}{2}p_0^2\sigma_a \cos 2\Theta_B. \tag{4.41}$$

The dependence of the non-zero eigenvalue λ on the external aligning parameter α_{ext} is plotted in Figure 4.10. This result demonstrates that the simplified approach is sufficient to obtain the re-entrant stability, observed earlier in both the full linear stability analysis and the simulations.

The line of neutral stability can be found by solving $\lambda = 0$ for σ_a:

$$\sigma_a^0(\alpha_{\text{ext}}) = -\frac{2p_0(\alpha_{\text{ext}})\,\alpha_{\text{ext}} + 4}{p_0(\alpha_{\text{ext}})^2 \cos 2\Theta_B}. \tag{4.42}$$

It is shown in Figure 4.11 in direct comparison to the result of the full linear stability analysis. The result of the linear analysis using the first two moments (blue solid line) nearly coincides with the results of the parallel and perpendicular perturbations

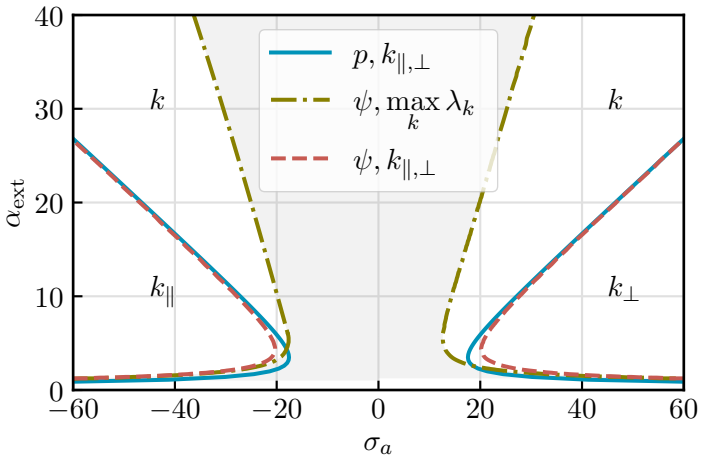

Fig. 4.11.: The line of neutral stability found by the linear stability analysis of the first two moments compared to the full perturbation in all moments.

obtained from the linear stability analysis of the distribution function ψ discussed in Section 4.3.3 (red dashed line).

For larger external field strengths, the full analysis reveals additional unstable modes that do not fall into the same scheme (amber dash-dotted line). This fact becomes clear when comparing the eigenfunctions $\tilde{\psi}_j^m$ in Figure 4.9 of the different regions. The first two plots in the figure are taken in the region that is well described by the moment analysis. Compared to the last plot, which shows an eigenfunction in the extended unstable region, a wider spectrum of orientational modes contribute to the instability that are not covered by the used closure in equation 4.30. Additional moments would be required to obtain a complete description.

However, it turns out that there is an elegant physical interpretation for the perturbations described by moments equations. Similar to the hydrodynamic instabilities appearing in liquid crystals, the so called *bend* and *splay* deformations (see for example Ref. [147]), these instabilities and their consequences on pattern formation are discussed in more detail in Section 4.6. But first, results of non-linear dynamics are shown and compared to those of the linear stability analysis.

4.5 Non-linear dynamics

The *linear* stability analysis predicts the stability of a given steady state and gives qualitative insight into the dynamics near the steady state. However, as the system departs from the initial steady state, non-linearities become predominant and the

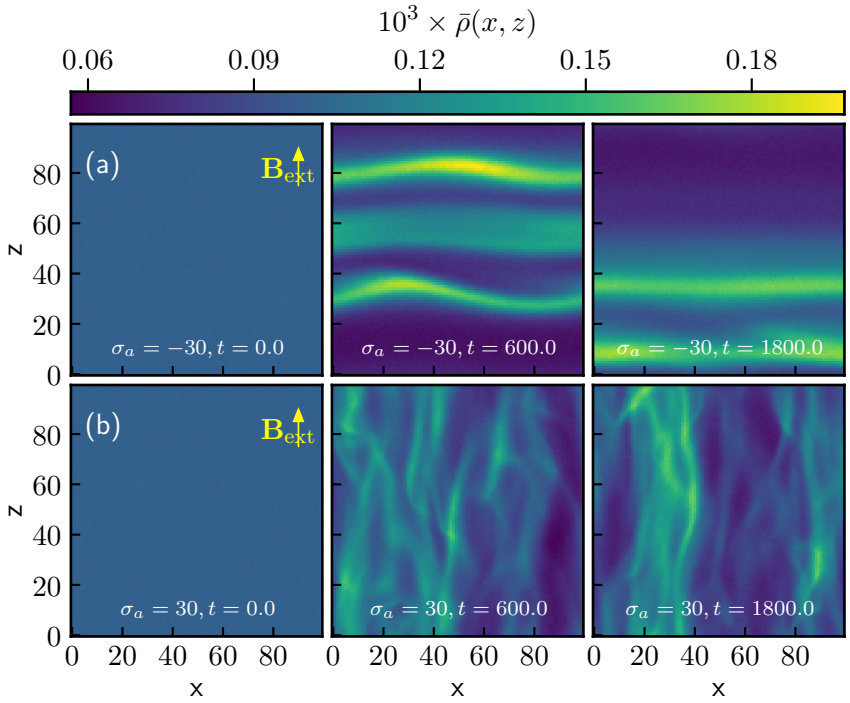

Fig. 4.12.: Snapshots of density projections averaged along the y-axis from 3D non-linear simulations at different time steps for pusher (row a) and puller swimmers (row b) in the unstable regime with dimensionless active stress $|\sigma_a| = 30$ and alignment parameter $\alpha_{\text{ext}} = 4$. The colours encode the probability density integrated in the y-direction $\bar{\rho}(x, z) = \Delta y \sum_y \rho(x, y, z)$. The translational diffusion is fixed to $d_t = 3 \times 10^{-6}$ and the alignment stress is covaried with the external field by $\sigma_m = 0.4\alpha_{\text{ext}}$.

linearized equation start to fail to describe the dynamics correctly. The solution of the full non-linear equation (4.1) is therefore required. Using the technique described in Chapter 3, the time evolution of an arbitrary initial state can be simulated with good accuracy.

The simulations, conducted in a box size of $V_{\text{sim}} = (5\, x_c)^3$, are initialized with the homogeneous steady state ψ_0, given in equation (4.7) for different system parameters. As in the previous sections, the translational diffusion is fixed to $d_t = 3 \times 10^{-6}$, the alignment stress magnitude is set to $\sigma_m = 0.4\alpha_{\text{ext}}$, while the external magnetic field and the active stress magnitude are varied through the alignment parameter α_{ext} and σ_a. Results from simulations of the first two previously discussed exemplary representatives of pushers and pullers are shown in Figure 4.12. Here, projections of density field snapshots are plotted at different times. The last snapshots are also rendered in 3D in Figure 4.13 to allow for a better interpretation. The representatives correspond to the first two panels in Figures 4.7, 4.8, and 4.9, and lie in the regime of parallel and perpendicular type of perturbations, classified in Section 4.3.3 and 4.4.

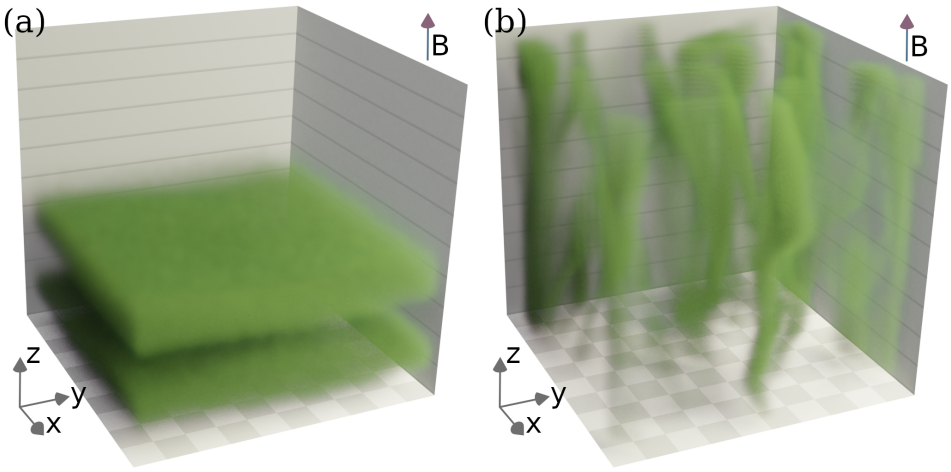

Fig. 4.13.: 3D volumetric rendering of the density field of a pusher (c) and puller (d) at $t = 1800$ corresponding to the last time-step presented in panels (a) and (b) in Figure 4.12, respectively.

In both cases, distinct patterns emerge after some time. For pushers at $\alpha_{\text{ext}} = 4$ and $\sigma_a = -30$, Figure 4.12 (a), a travelling band formation of higher density appears that extends perpendicular to the external magnetic field pointing upwards in the plots. This pattern looks remarkable close to the findings in [22]. Preliminary experiments conducted in the lab of Eric Clement by Benoît Vincenti also show a very promising agreement. A snapshot of the experiments is shown in Figure 4.14. This might indicate that the strand of MTB used in the experiment are indeed pushers. Pullers at the same alignment parameters, i.e. $\alpha_{\text{ext}} = 4$ and $\sigma_a = 30$, form a more complex density profile, see Figure 4.12 (b). Its structure becomes more obvious in the 3D rendering in Figure 4.13 (b). Pullers tend to form dynamic pillar-like structures parallel to the external field axis. The more complex patterns compared to pullers are also reflected in the linear stability analysis. Pullers display a more complex mode structure of destabilizing perturbation, as can be seen for example in Figure 4.8. As discussed previously, perturbations of the steady state for pullers show two dominant perturbation modes, both in parallel and in perpendicular direction. However, as argued in the following Section 4.6, their non-linear dynamics is primarily determined by the perpendicular perturbations.

With the results from the non-linear simulations, the predicted linear stability of the steady state given in Section 4.3 can be assessed quantitatively. An overview of the density snapshots, projected into the x-z-plane, at a time after the instability has already established itself, is plotted in Figure 4.15 for different values of the active stress σ_a and the alignment parameter α_{ext}. For comparison, the line of neutral stability, for which the largest growth rate is zero, i.e. $\operatorname{Re}\lambda_{\max} = 0$ is

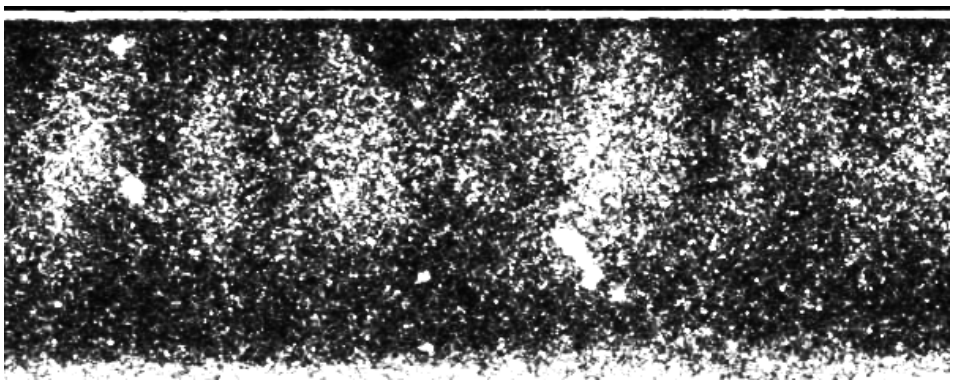

Fig. 4.14.: Preliminary result of an experiment conducted by Benoît Vincenti in the group of Eric Clement. It shows magnetotactic bacteria (MTB) swimming in an external magnetic field pointing to the right in a flat channel from the top in a light microscopy. Brighter areas correspond to higher densities. Although, the displayed strand of MTB has an ellipsoid shape and the wall impose different boundary conditions, the experimental results and the theoretical predictions are strikingly similar. The channel has dimensions of $2\,\mathrm{cm} \times 600\,\mu\mathrm{m} \times 100\,\mu\mathrm{m}$ in length, width, and thickness.

superimposed as a red line. Additionally, the borders of the purely parallel (for negative σ_a) and perpendicular perturbations (for positive σ_a) respectively are shown as a dashed amber line (compare with Figure 4.11). For moderate external magnetic field strengths, proportional to the alignment parameter α_{ext}, and moderate activity, patterns with the most distinct characteristics appear. The higher the external field, the patterns display finer structures (of higher frequency) in the density profile. However, the basic characteristics seem to be conserved, with a band like structure for pushers and a pillar like structure for pullers. In the intermediate regions between the red and amber lines, the perturbative mode structure of the instabilities differs from the region with the ambient line, as discussed previously. Nonetheless, pullers in the intermediate region produce a similar density profile as in the amber region. However, the density structures appear to be finer. For pushers in this region, the evolved density profile is not as pronounced as in the other regions and hardly visible in this plot. In general, as expected, the instabilities near the line of neutral stability are rather weak and the resulting dynamics only depart very slowly from the steady state.

The plot in Figure 4.15 serves well to give an overview of the different density profiles at different system parameters. However, the representation is not precise enough to permit a quantitative comparison with the predictions of the linear stability analysis concerning the stability of the steady state. A more quantitative approach shows the excellent agreement between simulations and linear stability analysis, as discussed in the subsequent subsection.

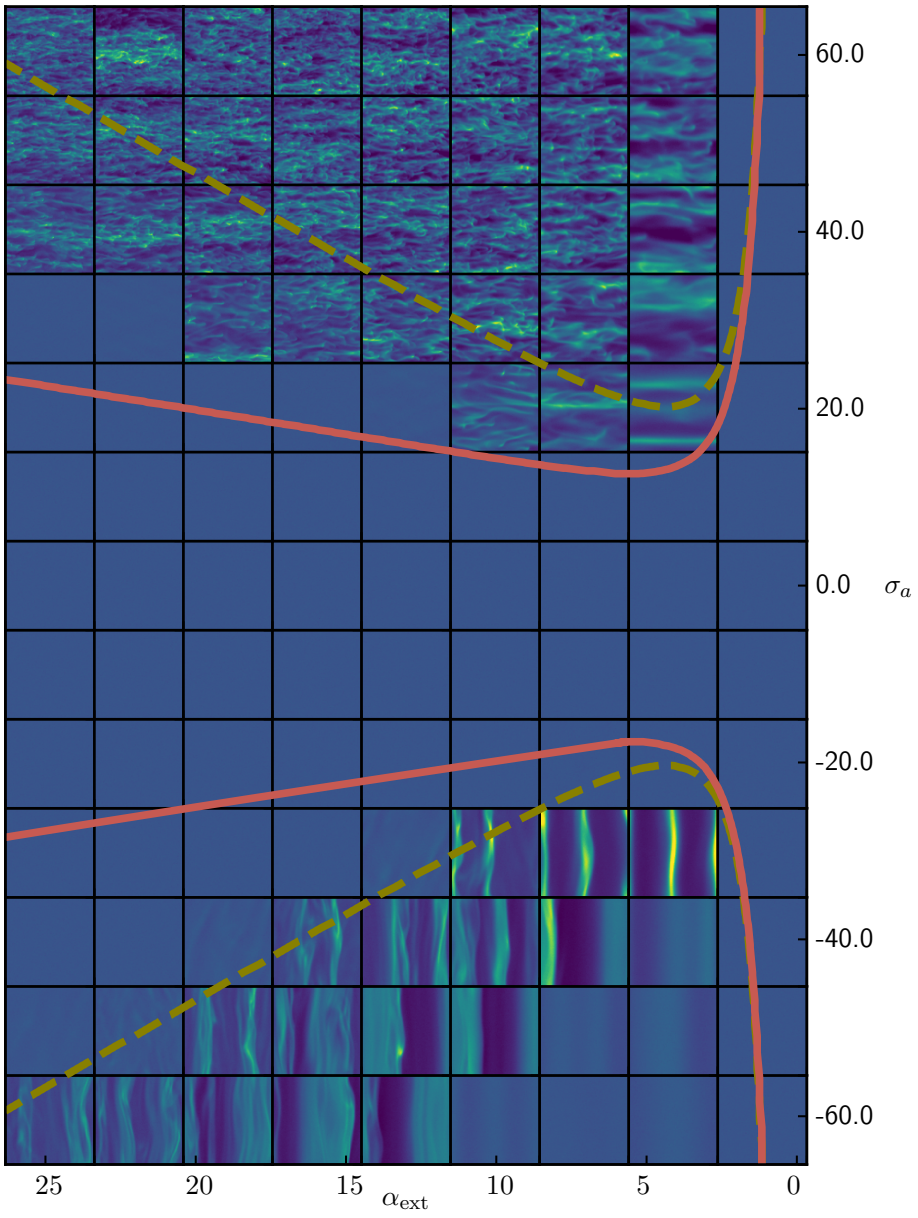

Fig. 4.15.: Density projections for different parameters superposed by the line of neutral stability from linear stability analysis. The red line marks the line of neutral stability calculated by the linear stability analysis. The amber dashed line is the line of neutral stability only including parallel and perpendicular perturbations, with respect to the external field. The translational diffusion is fixed to $d_t = 3 \times 10^{-6}$ and the alignment stress is covaried with the external field as $\sigma_m = 0.4\,\alpha_{\text{ext}}$.

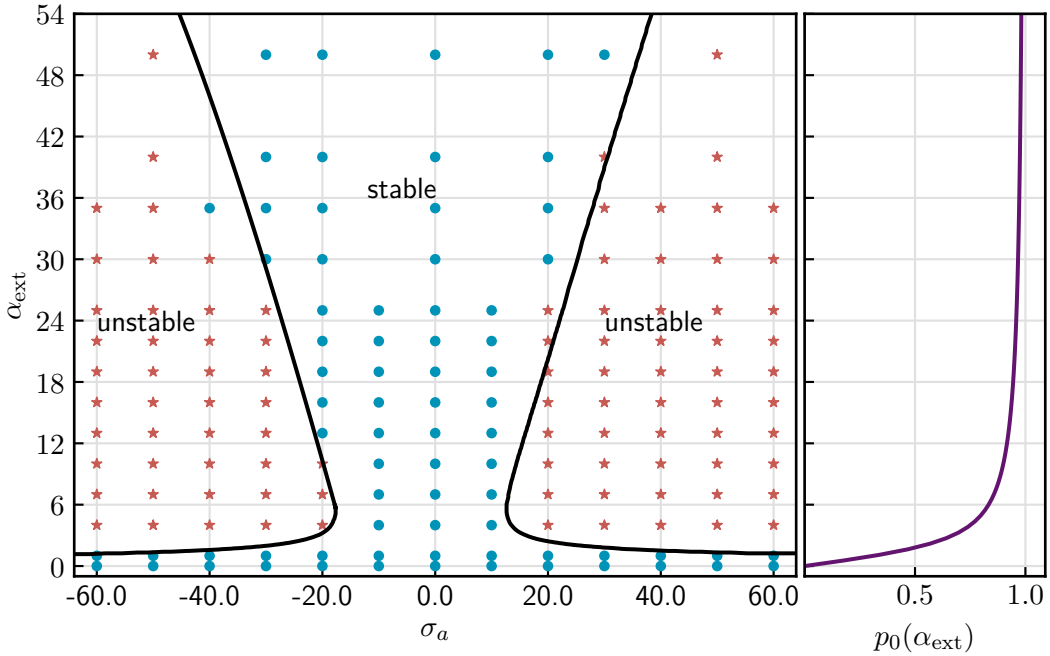

Fig. 4.16.: Stability diagram of the steady state $\psi_0(\alpha_{\text{ext}})$ in (4.1). The border of neutral stability (black line) is calculated by the linear stability analysis. The symbol denote non-linear numerical solutions under periodic boundary conditions of the full equations that are stable (blue bullets) or unstable (red stars). On the right the corresponding polarization of the steady state $\psi_0(\alpha_{\text{ext}})$ is plotted.

Quantitative measure of stability

The superimposed red line in Figure 4.15 corresponds to the line of neutral stability taken from the linear stability analysis. The agreement between the predictions concerning the stability of the homogeneous steady state and simulations is hard to judge on the plot alone, especially at the border of stability. However, a quantitative analysis, presented in Figure 4.16, of the stability of the steady state in the simulations shows a very good agreement with the theoretical predictions. The symbols show simulations run at the given parameter pair. Blue circles denote stable simulations, whereas red stars denote simulations that depart from the steady state.

In order to decide whether a simulation departs from the steady state, deviations of the probability density function from ψ_0 are measured. In order to get a more robust, noise insensitive measure, spatial and orientational deviations are separated by tracing out (summing over) $\mathbf{n}$ and $\mathbf{x}$, respectively

$$\rho_{\text{sim}}(\mathbf{x}) = \Delta\vartheta\Delta\varphi \sum_{i,j} \psi(\mathbf{x}, \vartheta_i, \varphi_j)$$

$$\Omega_{\text{sim}}(\vartheta, \varphi) = \Delta x \Delta y \Delta z \sum_{i,j,k} \psi((x_i, y_j, z_k), \vartheta, \varphi).$$

The spatial and orientational deviations are defined to be the variance (mean square displacement)

$$\Delta\rho = \left\langle |\rho_0 - \rho_{\text{sim}}|^2 \right\rangle = \Delta x \Delta y \Delta z \sum_{i,j,k} |\rho_0 - \rho_{\text{sim}}(x_i, y_j, z_k)|^2$$
$$\Delta\Omega = \left\langle |\Omega_0 - \Omega_{\text{sim}}|^2 \right\rangle = \Delta\vartheta \Delta\varphi \sum_{i,j} |\Omega_0(\vartheta_i, \varphi_j) - \Omega_{\text{sim}}(\vartheta_i, \varphi_j)|^2.$$

The theoretical steady state density and orientational distribution are given by

$$\rho_0 \equiv \int_{\mathbb{S}^2} \mathrm{d}\mathbf{n}\ \psi_0(\mathbf{n}) = 1$$
$$\Omega_0(\mathbf{n}) \equiv \frac{1}{v} \int_v \mathrm{d}\mathbf{x} \psi_0(\mathbf{n}) = \psi_0(\mathbf{n}).$$

In order to classify the stability of a simulation, two methods come to mind. First, a threshold for the values of $\Delta\rho$ and $\Delta\Omega$ is defined. Simulations with values above the threshold are classified as unstable[8]. For example, a suitable threshold would be a five percent deviation from the steady state to take numerical noise into account.

A second approach is to standardize[9] the features given by $\Delta\rho$ and $\Delta\Omega$ and represent all simulations as points in the spanned feature space. A clustering algorithm[10] can help to identify points that are not in the stable cluster. In this work, the second approach is chosen and a Gaussian Mixture is used as the clustering algorithm. Because of noise present in the simulations, there is a chance of misclassification that is most likely to happen at the onset of instability. Near the line of neutral stability, the deviations from the steady state are not as pronounced and become comparable to the noise. Nevertheless, this approach gives reasonable results that are in very good agreement with the linear stability analysis.

In order to understand the mechanism behind the pattern formation presented in this section, the linearized dynamics given in Sections 4.3 and 4.4 can be studied on the onset of instability. Their simpler structure enables a closer examination of the dynamics that lead to pattern formation.

[8] Because of quantization/Shot-noise (a consequence of the particle based simulation method) the value of $\Delta\rho$ has to be compared with the variance of the Poisson-distribution with mean of the mean particle number per cell.

[9] $x' = \frac{x - \overline{x}}{\sigma}$, with the mean $\overline{x}$ and the standard deviation σ

[10] Cluster analysis refers to classical machine learning algorithms to group points in a feature space that are similar with respect to a previously defined metric [148].

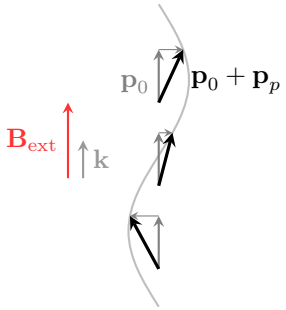

Fig. 4.17.: Illustration of an exaggerated bend perturbation of the polarization $\mathbf{p} = \mathbf{p}_0 + \tilde{p}_\perp \check{\mathbf{e}}_1 e^{i\mathbf{k}\cdot\mathbf{x}}$.

4.6 Bend and splay: pattern formation

Although linear unstable modes in general do not capture the full non-linear dynamics, in this case they lay the foundation on which the patterns to develop. As shown in Section 4.3.3, for a large region in the parameter space the most unstable mode for pushers is parallel to the external field, whereas pullers show both parallel and perpendicular unstable modes with a comparable growth rate. However, simulations suggest that for pullers the perpendicular perturbation is more prominent. This allows to restrict the following discussions to a specific mode of instability which comes in two variants: *bend* and *splay* deformations.

In the parameter region framed by the blue line in Figure 4.11, the prevalent instability has the form

$$\mathbf{p}_p = \begin{pmatrix} \tilde{p}_\perp \\ 0 \\ 0 \end{pmatrix} e^{i\mathbf{k}\cdot\mathbf{x}}$$

with $\mathbf{k} \parallel \mathbf{B}_{\text{ext}}$ for pushers and $\mathbf{k} \perp \mathbf{B}_{\text{ext}}$ for pullers. That means, for pushers the polarized steady state $\mathbf{p}_0 \parallel \mathbf{B}_{\text{ext}}$ is deflected in a spatial sinusoidal manner forming a *bend*-deformation, illustrated in Figure 4.17. In other words, the polarization perturbation is perpendicular to $\mathbf{p}_0$, but its magnitude is modulated in the direction parallel to $\mathbf{p}_0$.

A *bend*-deformed line of pushers (blue) creates a force density (grey arrows) in the fluid that is perpendicular to the direction of the perturbation. As can be seen in Figure 4.18, the forces of the force dipoles one side of the line of swimmers converge towards a focus point, creating a high force density at this point. At the same time, the corresponding force partners of the dipoles must spread out on the other side of the line, diluting their impact on the fluid. This left-right imbalance sums to a net force in one direction perpendicular to the line with a maximum at the nodes of the

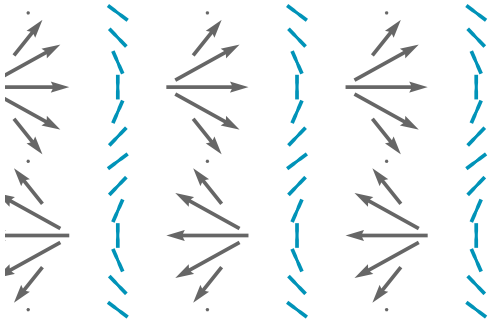

Fig. 4.18.: Illustration of the force distribution (grey arrows) resulting from a flow-induced bend instability of an array of force dipoles (blue lines). A converging configuration of the forces on one side of a line of force dipoles produces a higher force density in the fluid than the diverging partner forces on the other side of the dipoles. Thus, a net force density is created that in turn generates the flow of the fluid.

bend perturbation. The same perturbation but perpendicular to the external field, i.e. $\mathbf{k} \perp \mathbf{B}_{\text{ext}}$, arises with pullers and is called a *splay* deformation.

In Figure 4.19, the whole scheme is summarized in one illustration for pushers (a) and pullers (b). The deformed polarization is shown in the form of stream lines in the background. Their stream profile making the nomenclature of *bend* and *splay* evident: The streamlines of a *bend*-deformed polarization field are bent like a spline whereas the streamlines of a *splay*-deformed field spread out. These kinds of perturbations are unstable because the resulting vorticities in the flow further rotate the polarization vectors/the particles out of their steady state orientation and as a result the perturbations amplify themselves. Eventually, the flow induced and destabilizing rotation is counterbalanced by the torque of the external aligning field and the described feedback loop is broken. The competition between both effects allows for (rather) stable patterns to develop.

This scheme accurately illustrates the nature of the instability. But it goes even one step further by giving an intuition for the non-linear patterns forming much later. The key to this intuition is the divergence of the polarization field, $\nabla \cdot \mathbf{p}$. In Figure 4.19, it is depicted by green and purple boxes; the colour depends on the sign of the divergence. The mean contribution to the self-propulsion velocity of the swimmers, in reduced units, is given by

$$\overline{\mathbf{u}}_{\text{sp}}(\mathbf{x}, t) = \mathbf{p}(\mathbf{x}, t). \tag{4.43}$$

Therefore, the divergence of the mean self-propulsion velocity, which is proportional to the divergence of the polarization field, is a measure of how many swimmers enter

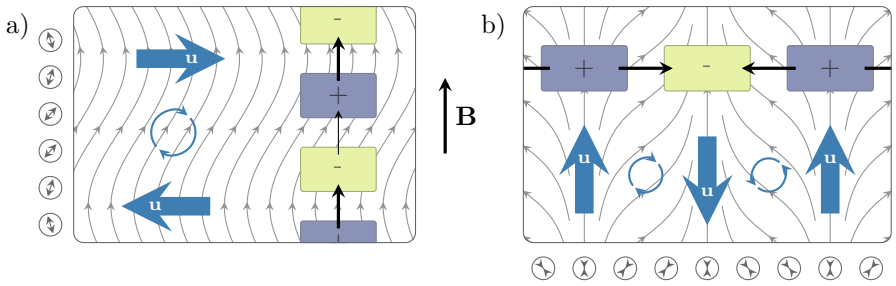

Fig. 4.19.: Schematics of (a) *bend* and (b) *splay* deformation of the polarizations field (grey lines) of pushers and pullers respectively. Bend deformation create an alternating flow field perpendicular to the magnetic field axis, generating a vorticity in the flow that influence on the particles' orientation opposes the alignment due to the magnetic torque. The mean particle speed $\propto \mathbf{p}$ varies along the magnetic field axis. Particles accumulate in volumes of negative divergence of $\mathbf{p}$. Splay deformations for pullers have an analogous effect. They deflect the polarization field in perpendicular direction creating a force-dipole configuration that results in an alternating flow parallel to the external field axis. The flow enhances the deflection until balanced by the external torque. As a result, the particles accumulate in a volume with a flow field that points in the opposite direction of their orientation.

a given volume compared to how many leave. Mathematically this is expressed as a conservation equation for the density, given by

$$\partial_t \rho = -\nabla \cdot \mathbf{p},$$

which follows directly from equation 4.23 by neglecting the advection and diffusion terms. Therefore, in volumes of negative divergence more particles enter than leave: they accumulate. For volumes of positive divergence, it is the other way round, they get depleted. The volumes of negative divergence are exactly the volumes where the bands and pillars in the non-linear simulations form, presented in Section 4.5.

To make the mechanism more tangible, an idealized *bend*- and *splay*-deformation can be studied in 2D, restricting the discussion to a plane with components parallel and perpendicular to the external field, $x_\parallel$ and $x_\perp$, respectively. The polarization field with a *bend*-deformation is approximated by

$$\mathbf{p}_{\text{bend}}(x_\parallel) = \left(\tilde{p}_\perp \cos(k x_\parallel), \sqrt{1 - \tilde{p}_\perp^2 \cos^2(k x_\parallel)}\right),$$

assuming the norm of the vector is unchanged[11] and given an amplitude $\tilde{p}_\perp$, a wavenumber k of the perturbation, and a steady state $\mathbf{p}_0 = p_0 \check{\mathbf{z}}$. A splay deformation is analogously given by

$$\mathbf{p}_{\text{splay}}(x_\perp) = \left(\tilde{p}_\perp \cos(k x_\perp), \sqrt{1 - \tilde{p}_\perp^2 \cos^2(k x_\perp)} \right).$$

The force field of the dipoles can then be approximated by

$$\mathbf{f} \approx -\sigma_a \nabla \cdot \left(\mathbf{pp} - \frac{1}{3} \mathbb{1} \right)$$

for a given polarization field $\mathbf{p}$. For simplicity, $\sigma_a = \pm 1$ is assumed. Given the force field, the Stokes equation

$$\Delta \mathbf{u} - \nabla p + \mathbf{f} = 0$$

can be solved using the Oseen tensor and a spectral method. The flow for pushers is perpendicular to the external field $\mathbf{u} = u_\perp(x_\parallel) \check{\mathbf{x}}_\perp$ and parallel for pullers $\mathbf{u} = u_\parallel(x_\perp) \check{\mathbf{x}}_\parallel$. It is in very good approximation given by

$$u_{\{\perp,\parallel\}}(\{x_\parallel, x_\perp\}) \approx c_1 \sin\{x_\parallel, x_\perp\} + c_2 \sin 3\{x_\parallel, x_\perp\},$$

in which the braces $\{\}$ evaluate to the first entry for pushers, the second for pullers, and some numerical values $c_1, c_2 \in \mathbb{R}$. The result is shown in Figure 4.20 for pushers and in Figure 4.21 for pullers. The subplot (a) shows the stream lines of the polarization field $\mathbf{p}$ and its divergence colour encoded in the background. In the red areas, the divergence is negative and concentrated bands will form. In the subplot (b), the flow field as a result of the deformation of the polarization field is shown as a vector plot. In (c) the flow field's vorticity $\nabla \times \mathbf{u}$ is shown, where red encodes a counter clockwise rotation and blue a clockwise rotation. The flow vorticity rotates the particle according to Faxen's law, given by

$$\boldsymbol{\omega} = \frac{1}{2} \nabla \times \mathbf{u} \propto \mathbf{M}_{\text{HD}}.$$

in equation (2.88) that can be thought of as being proportional to a (virtual) hydrodynamic torque $\mathbf{M}_{\text{HD}}$ (although a microswimmer on its own is in total torque free).

These idealized patterns can be observed in the non-linear solutions of the Smoluchowski equation (4.1) as well! By restricting the perpendicular (parallel) dimensions

[11] Actually, this is required to make the divergence argument work. A pure perturbation of the form $\check{\mathbf{e}}_z \varepsilon \cos kz$ results in a zero divergence, which is not in line with the observations. It has to be understood as a liner approximation of a rotation for arbitrary small $\varepsilon > 0$. The exact normalization procedure is irrelevant for the qualitative discussion.

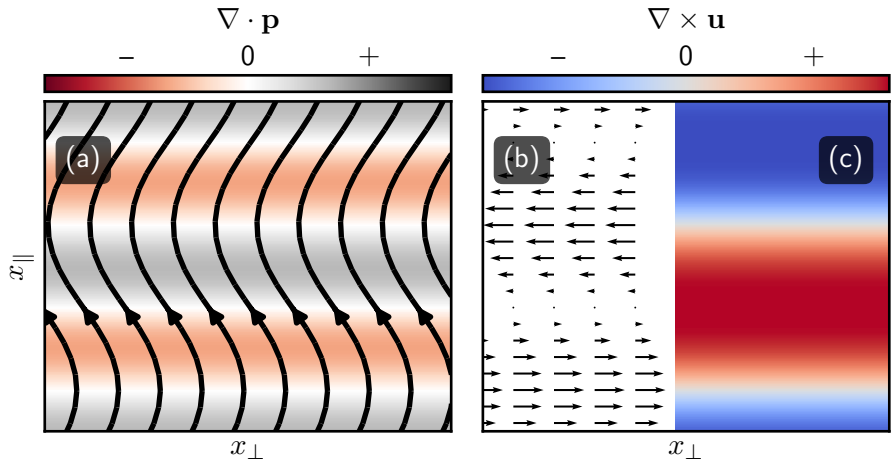

Fig. 4.20.: An idealized (static) *bend* deformation for polarized pushers (in $x_\parallel$-direction). (a) shows the stream lines of the polarization field $\mathbf{p}$ with its divergence $\nabla \cdot \mathbf{p}$ colour coded in the background. Swimmers accumulate eventually in volumes of negative divergence (red). (b) Created flow field perpendicular to polarization axis. (c) The resulting vorticities in the flow enhance the *bend* perturbation further (red CCW rotation, blue CW).

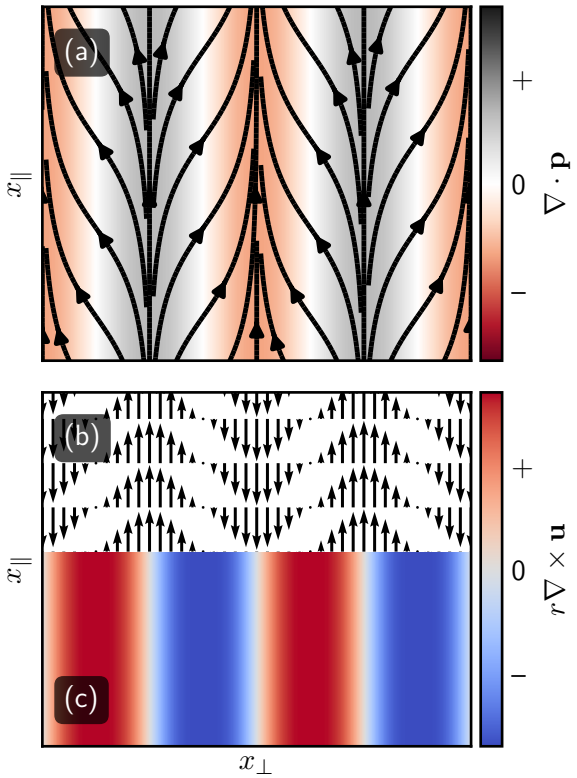

Fig. 4.21.: An idealized (static) *splay* deformation for polarized pullers (in $x_\parallel$-direction) analogous to Figure 4.20.

of the box with periodic boundaries modes with long wave-length in that direction are suppressed. This way *bend*- and *splay*-modes can be selectively recovered. For pushers Figure 4.22 shows a snapshot of such a simulation. The left plot shows the density field in colour overlaid by the streamlines of the polarization field. As predicted, pushers form bands in volumes of negative divergence. In the right plot, the flow field is shown as a vector plot and the corresponding vorticity is plotted in the background. The similarity to the idealized picture in Figure 4.20 is striking. The same plots are shown for pullers in a wide box in Figure 4.22.

The vorticity plot of the flow field illustrates that the hydrodynamics further rotate the particles out of the polarization axis. As stated previously, this would lead to a highly unstable feedback loop if the external torque would not eventually compensate the rotatory motion. In the idealized case, both torques are easy to calculate and are plotted in arbitrary units in Figure 4.24 for a *bend*-deformation (it is qualitatively the same for *splay*-deformations). The mean, dimensionless external torque, given by $\mathbf{M}_\mathrm{B} \propto \alpha_\mathrm{ext}\mathbf{p} \times \check{\mathbf{B}}_\mathrm{ext}$ nearly fully balances the HD torque stopping the deformation from growing further. This way a more stable pattern can establish itself. The competition becomes apparent in the rotational drift velocity,

$$\dot{\mathbf{n}} = \left(\alpha_\mathrm{ext}\mathbf{n} \times \check{\mathbf{B}}_\mathrm{ext} + \frac{1}{2}(\nabla \times \mathbf{u})\right) \times \mathbf{n},$$

which is equal to equation (4.3). In the case both terms compensate each other, the bracket vanishes and the orientation $\mathbf{n}$ does not change any more.

The patterns resulting from the bend and splay deformations have an impact on the dynamics of the microswimmers. The significant influence on the speed of the swimmers along the direction of the external field in the reference frame of the laboratory, called the transport speed, is presented in the following section.

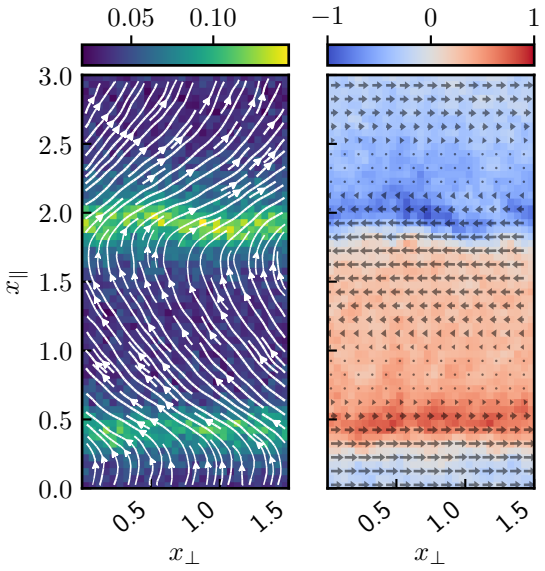

Fig. 4.22.: Exemplary pattern in a quasi-2D (thin third dimension) formed after a *bend*-instability occurred (compare with Figure 4.19). On the left, the colour encoded local density is superimposed by streamlines of the polarization field. The streamline width is weighted by the magnitude of polarization. On the right panel, the corresponding flow field is represented as vector arrows. Its vorticity, responsible for the hydrodynamically induced particle rotation, is encoded in colour in the background. Red colours correspond to a vorticity vector pointing out of the plane (counter clockwise rotation).

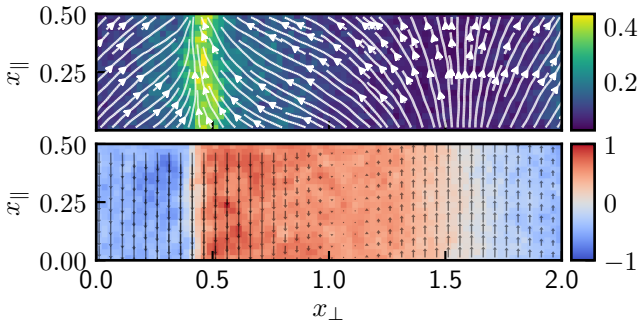

Fig. 4.23.: Analogue of Figure 4.22 for pullers developing a »splay« instability.

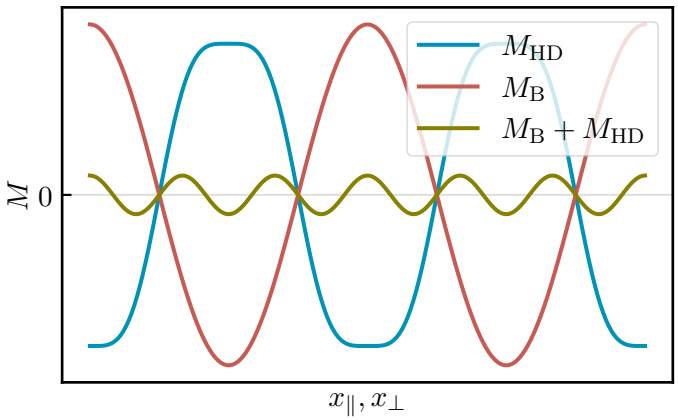

Fig. 4.24.: Illustration of the competition between a (virtual) hydrodynamic torque $M_{\mathrm{HD}} \propto \frac{1}{2}\|\nabla \times \mathbf{u}\|$ and an external magnetic torque $M_{\mathrm{B}} \propto \alpha_{\mathrm{ext}}\|\mathbf{n} \times \check{\mathbf{B}}_{\mathrm{ext}}\|$ for *bend* and *splay* instabilities in arbitrary units. The instabilities cause the flow vorticity to grow while rotating the particles, until the rotation is compensated by the external torque (amber).

4.7 Transport speed

A potential application of microswimmers is targeted drug delivery. The idea is that the swimmers carry some cargo that is transported to some target, for example a cancerous cell or an egg to aid in fertilization [149]. In this context, an external control is desirable. Guiding magnetic swimmers with an external magnetic field towards a target could be an important component implementing such a system. A natural question arising is that of efficiency: How well and fast can such a setup direct microswimmers toward a target?

In the previous sections, the interplay between an external aligning and the resulting enhanced hydrodynamic interactions have been discussed. This leads to the question, how (much) the hydrodynamic interactions influence the mean transport speed in the direction of the external field? To answer the question, the baseline speed of a partially polarized ensemble has to be established. The mean velocity is defined as

$$\bar{v} = \check{\mathbf{B}}_{\mathrm{ext}} \cdot \langle \mathbf{n} + \mathbf{u} \rangle = (\bar{\mathbf{p}}_t + \bar{\mathbf{u}}_t) \cdot \check{\mathbf{B}}_{\mathrm{ext}}, \tag{4.44}$$

and consists of the mean self-propulsion speed and the convecting local flow. The homogeneous steady state presents ideal conditions for an optimal mean velocity $\bar{v}_0 = \mathbf{p}_0(\alpha_{\mathrm{ext}})$, in reduced units.

In the simulations, the time-averaged global polarization is measured, defined as $\bar{\mathbf{p}}_t = \frac{1}{N_t}\sum_{j=0}^{N_t} \| \langle \mathbf{n} \rangle (t_0 + j\Delta t)\|$, where $\Delta t = 40\,\delta t$ (with the simulation time step

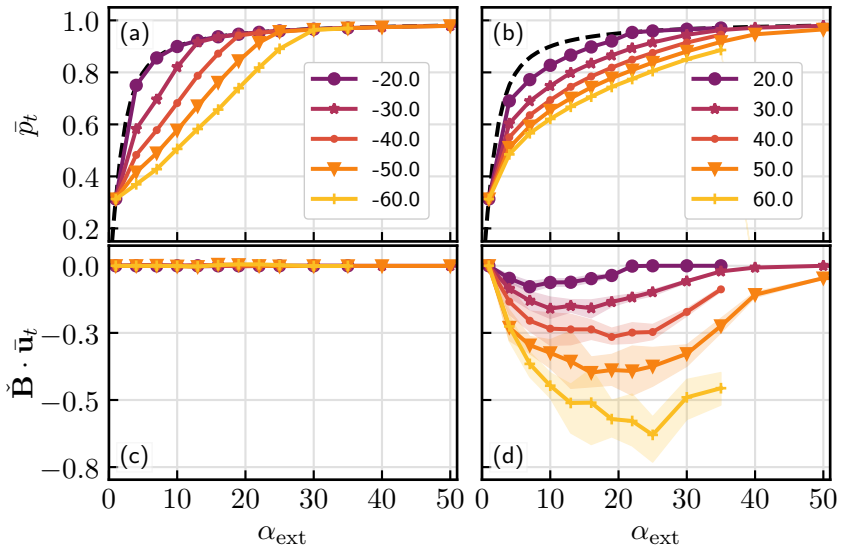

Fig. 4.25.: (a), (b) The time-averaged polarization magnitude $\bar{p}_t$ versus $\alpha_{\text{ext}} \propto B_{\text{ext}}$ at different activity strengths $\propto \sigma_a$ for pushers and pullers. The dashed line shows the polarization of the steady state given in equation (4.8). (c), (d) The time-averaged advection transport speed in the magnetic field direction versus α_{ext} at different σ_a for pushers and pullers. The box size in all simulations is $V_{\text{sim}} = 5^3 x_c^3$, the translational diffusion is fixed to $d_t = 3 \times 10^{-6}$, and the alignment stress $\sigma_a = 0.02\alpha_{\text{ext}}$ is covaried with the external field strength. In panels (a) to (c), the confidence intervals are comparable to the symbol size.

$\delta_t = 0.2$ in units of t_c) is about an order of magnitude larger than the alignment time $\tau_e = \frac{\xi_r}{\mu B_{\text{ext}}}$. The braces $\langle \bullet \rangle \equiv \int d\mathbf{x} \int d\mathbf{n}\, \psi(\mathbf{x}, \mathbf{n}, t) \bullet$ define the expectation value. t_0 marks a relaxation time after which $\bar{p}_t$ is nearly time-independent despite exhibiting non-stationary patterns (see Figure 4.26). Choosing $N_t = 20$ gives sufficient statistics. It can be observed that $\check{\mathbf{B}}_{\text{ext}} \cdot \bar{\mathbf{p}}_t \approx \bar{p}_t$ and $\bar{p}_t$ is independent of the system size for $L \gtrsim 2.5 x_c$ (see Figure 4.27).

Figures 4.25a and 4.25d present the $\bar{p}_t$ as a function of α_{ext} for pushers and pullers at different activity strengths σ_a. For moderate σ_a and α_{ext} values falling in the unstable regime, a significant reduction in the polarization compared to the ideal case $p_0(\alpha_{\text{ext}})$ (equation (4.2)), shown by the dashed line, can be observed. The decrease in the mean polarization is stronger for larger activity strengths. Stronger magnetic fields drive the system back into the stable regime and $\bar{p}_t$ agrees with $p_0(\alpha_{\text{ext}})$ in those regions. For the efficient transport in the direction of magnetic field, a high polarization of swimmers parallel to $\mathbf{B}_{\text{ext}}$ is desirable that can be achieved by increasing the field strength.

In addition to the mean self-propulsion speed, the mean velocity depends on the net advection speed. To evaluate the contribution of $\bar{\mathbf{u}}_t \cdot \check{\mathbf{B}}_{\text{ext}}$ to the transport speed, the

average advection velocity $\bar{\mathbf{u}}_t = \frac{1}{N_t} \sum_{j=0}^{N_t} \langle \mathbf{u} \rangle (t_0 + j\Delta t)$ is measured. The component parallel to the external field is shown in Figure 4.25c for pushers and in Figure 4.25d for pullers. It has already been established that the bend instabilities generate a flow perpendicular to the external axis. This is confirmed by the measurements. On the other hand, splay instabilities for pullers result in a significant advective contribution to the mean velocity. As illustrated in Figure 4.19, pullers accumulate in the lane with a flow anti-parallel to the external axis. The result is a negative net contribution to the mean velocity. Consequently, pullers in the bulk create a flow field that reduces their speed considerably.

As discussed in the introduction of this chapter, magnetic dipole-dipole interactions were neglected in this chapter, focusing on microswimmers with a weak magnetic dipole-dipole moment in an external field. However, these interactions can become relevant for swimmers with stronger magnetic moment. The dynamics of active particles with magnetic dipole-dipole interactions are discussed in the following chapter.

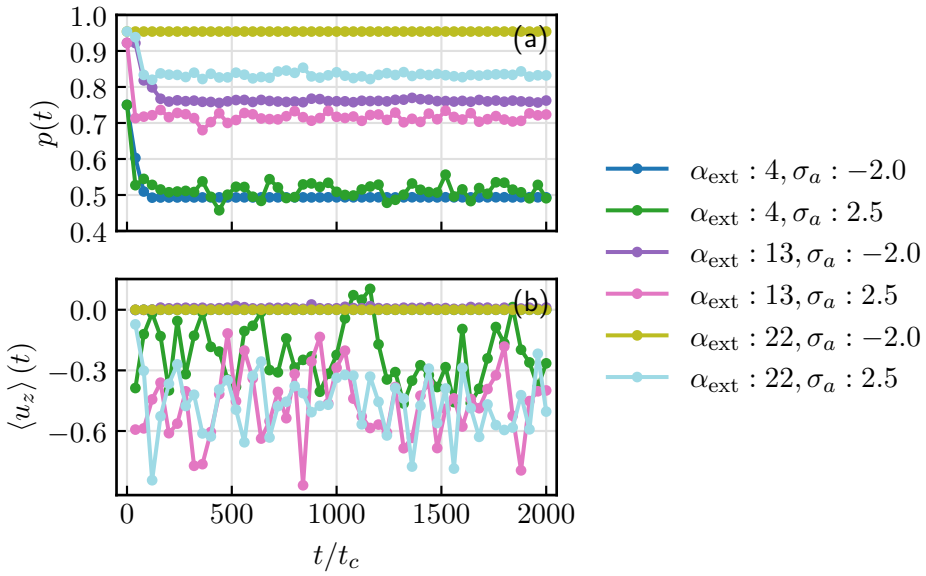

Fig. 4.26.: (a) Plot of the polarization magnitude p over time in simulations for different parameters. After a relaxation time, the polarization converges to a steady value. (b) Parallel component of the mean flow field velocity, with respect to the external field, versus time.

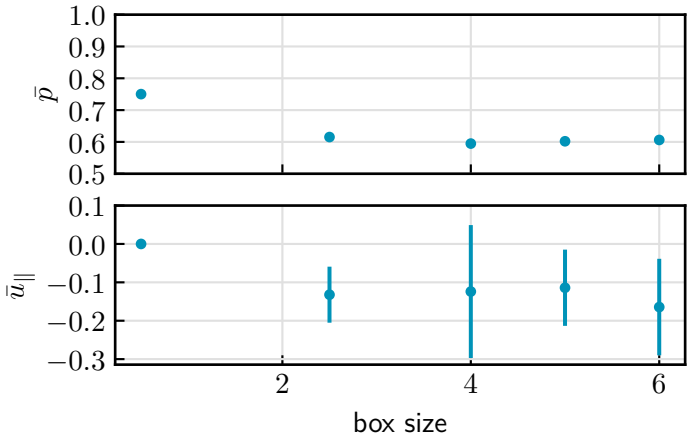

Fig. 4.27.: The polarization measured after a relaxation time in simulations of varying box size.

5 Active particles with magnetic dipole-dipole interactions

Colloids that carry a magnetic moment interact with a magnetic field. In the previous chapter, the interaction of magnetic particles with an external magnetic field has been studied. However, magnetic colloids create a magnetic field themselves and if their magnetization is strong enough, they influence each others motion. Incorporating the effect of the internal magnetic field leading to interactions between the colloids is the topic of this chapter. The interaction is studied in terms of the leading order contribution: a dipole-dipole interaction. Every localized current distribution creating a magnetic field can be expressed as a multipole expansion, its leading order is the magnetic dipole moment. It creates a characteristic magnetic flux which, unlike the external field considered in the previous chapter, is inhomogeneous. As a result, the colloids not only apply a rotating torque to each other but exert translating forces as well.

In this chapter, a kinetic theory of magnetically interacting active microswimmers in an external magnetic field is developed, based on the considerations in Chapter 2. First, an effective mean-field volume exclusion to counter attractive magnetic forces between the particles is introduced and its implementation in the simulations is discussed. Then, a steady state of the resulting Smoluchowski equation is identified and its stability with respect to the system's parameters is determined via a linear stability analysis. Finally, emerging patterns found by solving the non-linear equations are presented and their formation mechanism is discussed with the aid of the results from the linear stability analysis.

5.1 Langevin equations of magnetically interacting colloids

As a first building block, the Langevin-equation of magnetically interacting colloids have to be formulated. Every colloid is assumed to carry the same magnetic dipole

moment $\boldsymbol{\mu} = \mu\mathbf{n}$ along its orientation. Collectively these magnetic moments are described as a mean-field magnetization $\mathbf{M} = \mu\mathbf{p}$, as derived in equation (2.48).

The magnetic mean-field interaction between the colloids is mediated by the internal magnetic flux density

$$\mathbf{B}_{\text{int}}(\mathbf{x}) = \mu_0 \left(\mathcal{B}^{\text{dip}} * \mathbf{M}\right)(\mathbf{x}) = \mu_0 \int \mathrm{d}\mathbf{x}'\, \mathcal{B}^{\text{dip}}(\mathbf{x} - \mathbf{x}') \cdot \mathbf{M}(\mathbf{x}'), \tag{5.1}$$

given by a convolution of the dipolar flux density operator $\mathcal{B}^{\text{dip}}$, defined in equation (2.41), and the magnetization. The magnetic flux both causes a force and torque interaction between the colloids. The mean force on a particle at position $\mathbf{x}$ is given by

$$\overline{\mathbf{F}_m} = \mu\mathbf{n} \cdot \nabla\mathbf{B}_{\text{int}}. \tag{5.2}$$

To highlight the consistency of the mean-field approach using the mean magnetization, the same result is derived from the magnetic pair-interaction potential defined in equation 2.42,

$$U_m(\mathbf{x}, \mathbf{x}', \mathbf{n}, \mathbf{n}') = -\mu\mathbf{n} \cdot \mathbf{B}_{\text{dip}}(\mathbf{x} - \mathbf{x}', \mathbf{n}'),$$

between two particles with coordinates $(\mathbf{x}, \mathbf{n})$ and $(\mathbf{x}', \mathbf{n}')$ generating a dipolar magnetic flux density $\mathbf{B}_{\text{dip}}(\mathbf{x}, \mathbf{n}) = \mu_0\mathcal{B}^{\text{dip}}(\mathbf{x}) * \mu\mathbf{n}$ given in equation (2.41). According to equation (2.39), the mean magnetic interaction force can be written as

$$\begin{aligned}
\overline{\mathbf{F}_m}(\mathbf{x}, \mathbf{n}, t) &= -\int \mathrm{d}\mathbf{x}'\mathrm{d}\mathbf{n}'\, \Psi_1(\mathbf{x}', \mathbf{n}', t)\, \nabla_{\mathbf{x}} \left(U_m(\mathbf{x}, \mathbf{x}', \mathbf{n}, \mathbf{n}')\right) \\
&= -\int \mathrm{d}\mathbf{x}'\mathrm{d}\mathbf{n}'\, \Psi_1(\mathbf{x}', \mathbf{n}', t)\, \nabla_{\mathbf{x}} \left(-\mu\mathbf{n} \cdot \mathbf{B}_{\text{dip}}(\mathbf{x} - \mathbf{x}', \mathbf{n}')\right) \\
&= \mu\mathbf{n} \cdot \nabla_{\mathbf{x}} \int \mathrm{d}\mathbf{x}'\mathrm{d}\mathbf{n}'\, \Psi_1(\mathbf{x}', \mathbf{n}', t)\, \left(\mu_0\mathcal{B}^{\text{dip}}(\mathbf{x} - \mathbf{x}') \cdot \mu\mathbf{n}'\right) \\
&= \mu\mathbf{n} \cdot \nabla_{\mathbf{x}} \int \mathrm{d}\mathbf{x}'\, \left(\mu_0\mathcal{B}^{\text{dip}}(\mathbf{x} - \mathbf{x}') \cdot \int \mathrm{d}\mathbf{n}'\Psi_1(\mathbf{x}', \mathbf{n}', t)\, \mu\mathbf{n}'\right) \\
&= \mu\mathbf{n} \cdot \nabla_{\mathbf{x}} \int \mathrm{d}\mathbf{x}'\, \left(\mu_0\mathcal{B}^{\text{dip}}(\mathbf{x} - \mathbf{x}') \cdot \mu\mathbf{p}(\mathbf{x}', t)\right) \\
&= \mu\mathbf{n} \cdot \nabla_{\mathbf{x}} \left(\int \mathrm{d}\mathbf{x}'\, \mu_0\mathcal{B}^{\text{dip}}(\mathbf{x} - \mathbf{x}') \cdot \mathbf{M}(\mathbf{x}', t)\right) \\
&= \mu\mathbf{n} \cdot \nabla(\mu_0\mathcal{B}^{\text{dip}} * \mathbf{M})(\mathbf{x}, t) \\
&= \mu\mathbf{n} \cdot \nabla\mathbf{B}_{\text{int}}(\mathbf{x}, t),
\end{aligned}$$

where $\nabla_{\mathbf{x}} = \nabla$ denotes the gradient operator with respect to $\mathbf{x}$ as usual, and the definition of the magnetization in equation (2.48) and equation (2.63) was used.

As derived in Section 2.1.2, given the force $\overline{\overline{\mathbf{F}}}_m$ on a particle, the equation of motion for the position is given by

$$\dot{\mathbf{x}} = \frac{\overline{\overline{\mathbf{F}}}_m}{\xi_\mathrm{t}} = \frac{1}{\xi_\mathrm{t}} \mu \mathbf{n} \cdot \nabla \mathbf{B}_\mathrm{int}. \tag{5.3}$$

As before, inertia can be neglected in an overdamped, low Reynolds-regime and the colloids react nearly instantaneously to a force or torque. According to Stokes' law the translational friction coefficient ξ_t is given by $\xi_\mathrm{t} = 6\pi\eta R$, for a spherical particle with radius R and the viscosity η of the suspension.

As derived in Section 2.6.2, the equation of motion for the orientation is given by equation (2.46) and results from the magnetic torque. In this case the magnetic flux is given by the sum of the internal magnetic flux $\mathbf{B}_\mathrm{int}$ and a possible external flux $\mathbf{B}_\mathrm{ext}$, i.e. $\mathbf{B} = \mathbf{B}_\mathrm{ext} + \mathbf{B}_\mathrm{int}$.

$$\dot{\mathbf{n}} = (\mathbb{1} - \mathbf{nn}) \cdot \frac{\mu}{\xi_\mathrm{r}} \mathbf{B} = (\mathbb{1} - \mathbf{nn}) \cdot \frac{\mu}{\xi_\mathrm{r}} (\mathbf{B}_\mathrm{ext} + \mathbf{B}_\mathrm{int}). \tag{5.4}$$

The translational and orientational equations of motion (5.3) and (5.4) above, supplemented with transnational and rotational noise, translate into a Smoluchowski equation of the form

$$\begin{aligned} \partial_t \Psi_1(\mathbf{x}, \mathbf{n}, t) = &- \nabla \cdot \left[\Psi_1(\mathbf{x}, \mathbf{n}, t) \frac{\mu}{\xi_\mathrm{t}} \mathbf{n} \cdot \nabla \mathbf{B}_\mathrm{int}(\mathbf{x}, t) \right] \\ &- \nabla_\mathbf{n}^\circ \cdot \left[\Psi_1(\mathbf{x}, \mathbf{n}, t) (\mathbb{1} - \mathbf{nn}) \cdot \frac{\mu}{\xi_\mathrm{r}} (\mathbf{B}_\mathrm{ext} + \mathbf{B}_\mathrm{int}(\mathbf{x}, t)) \right] \end{aligned} \tag{5.5}$$

Attractive inter-particle forces, if not balanced, can lead to insensible dense cluster formations and other unphysical results. For extended particles, their volume exclusion naturally limits their density. However, in a mean-field model of point-like particles, including a volume exclusion is not straight forward. Nonetheless, an effective volume exclusion can be formulated that, to some extent, compensates unbounded attractive forces arising for point-like particles. The following chapter describes an effective mean-field volume exclusion and discusses a possible implementation to be used in the simulations.

5.2 Volume exclusion in a mean-field model

The magnetic interaction force $\overline{\mathbf{F}}_m$ in equation 5.2 can lead to an attraction between the particles. For point like particles without volume exclusion this can lead to arbitrary high densities, and as a result, to arbitrary strong interaction forces. Given the number density of $\varrho = \Phi_V / V_p$, with the volume fraction Φ_V and the volume of one particle V_p, the expectation value of the number density in a volume ΔV is given by

$$\overline{\varrho}(\Delta V) = \frac{1}{\Delta V} \int_{\Delta V} \mathrm{d}\mathbf{x} \int_{\mathbb{S}^2} \mathrm{d}\mathbf{n}\ \Psi_1 \overset{!}{\lesssim} \varrho^{\max}. \tag{5.6}$$

It should be smaller than the maximal number density possible inside the volume, given by $\varrho^{\max} = \Phi_V^{\max} / V_p$, to remain in the physically sensible range. Hence, to prevent unphysically high densities in the model, a volume exclusion has to be incorporated.

In molecular dynamics simulations, volume exclusion is usually modelled using a repulsive pair potential $U(\mathbf{x}_1 - \mathbf{x}_2)$. Common choices are the *WCA* (*Weeks-Chandler-Anderson* potential, shifted *Lennard-Jones* potential with only repulsive interaction) or *Yukawa* potential. In this case, a similar approach may be followed. In a probabilistic model, given a pair potential U, the resulting (repulsive) mean force on a particle can be expressed in terms of the pair probability density function Ψ_2, as has been shown in Section 2.5, equation (2.38). However, the pair-correlation is not available in a purely mean-field model, where inter-particle correlations are neglected.

Following the ansatz in equation (2.36), a simple approach is to approximate the pair distribution with the product of the single particle distributions and a pair correlation function $g^{(2)}(\mathbf{x} - \mathbf{x}') = g^{(2)}(\|\mathbf{x} - \mathbf{x}'\|)$ that is independent of the particles' orientations and only depends on the relative distance of the particles, $\|\mathbf{x} - \mathbf{x}'\|$. Under these assumptions, the pair distribution can be written as

$$\Psi_2(\mathbf{x}, \mathbf{x}', \mathbf{n}, \mathbf{n}', t) = \Psi_1(\mathbf{x}, \mathbf{n}, t)\, \Psi_1(\mathbf{x}', \mathbf{n}', t)\, g^{(2)}(\mathbf{x} - \mathbf{x}'). \tag{5.7}$$

Using equation (2.38), this defines an effective mean volume exclusion force

$$\begin{aligned}
\overline{\mathbf{F}}_{\mathrm{MF}}^{\mathrm{VE}}(\mathbf{x}, t) &= -\int \mathrm{d}\mathbf{x}' \mathrm{d}\mathbf{n}'\, \Psi_1(\mathbf{x}', \mathbf{n}', t)\, g^{(2)}(\mathbf{x} - \mathbf{x}')\, \nabla_{\mathbf{x}} U(\mathbf{x} - \mathbf{x}') \\
&= -\int \mathrm{d}\mathbf{x}'\, \rho(\mathbf{x}', t)\, g^{(2)}(\mathbf{x} - \mathbf{x}')\, \nabla_{\mathbf{x}} U(\mathbf{x} - \mathbf{x}') \\
&= -\int \mathrm{d}\mathbf{x}'\, \rho(\mathbf{x} - \mathbf{x}', t)\, g^{(2)}(\mathbf{x}')\, (\nabla U)(\mathbf{x}'),
\end{aligned} \tag{5.8}$$

where the definition of the density field in equation (4.20) has been used and the substitution $\mathbf{x}' \mapsto \mathbf{x}' - \mathbf{x}$ was executed. This expression can be further simplified when taking the short-ranged nature of U into account and expanding the density field around $\mathbf{x}_0 = 0$ to separate the particle positions $\mathbf{x}$ and $\mathbf{x}'$:

$$\rho(\mathbf{x} - \mathbf{x}') = \rho(\mathbf{x}) - \mathbf{x}' \cdot \nabla\rho(\mathbf{x}) + \mathcal{O}(\mathbf{x}'\mathbf{x}').$$

By substituting the expansion into equation (5.8) and exploiting the radial symmetry of $U$and $g^{(2)}$, the mean force can be rephrased as

$$\begin{aligned}\overline{\mathbf{F}}_{\mathrm{MF}}^{\mathrm{VE}}(\mathbf{x},t) \approx & -\rho(\mathbf{x},t) \underbrace{\int \mathrm{d}\mathbf{x}'\, g^{(2)}(\mathbf{x}')(\nabla U)(\mathbf{x}')}_{=0} \\ & + (\nabla\rho)(\mathbf{x},t) \cdot \underbrace{\int \mathrm{d}\mathbf{x}'\, g^{(2)}(\mathbf{x}')\, \mathbf{x}' \otimes (\nabla U)(\mathbf{x}')}_{\equiv \mathbf{U}_1} \\ = & \mathbf{U}_1^{\top} \cdot (\nabla\rho)(\mathbf{x},t).\end{aligned}$$

The first integral vanishes, due to the assumed symmetry. By rewriting the gradient of radial potential as $(\nabla U)(\mathbf{x}) = \frac{\mathbf{x}}{x}\partial_r U(r)$, in which $r = \|x\|$, the matrix $\mathbf{U}_1$ becomes

$$\begin{aligned}\mathbf{U}_1 &= \int \mathrm{d}\mathbf{x}'\, g^{(2)}(x')\, \mathbf{x}' \otimes \frac{\mathbf{x}'}{x'}(\partial_r U)(x') \\ &= \int \mathrm{d}r\, r^3\, g^{(2)}(r)\, \partial_r U(r) \int_0^{2\pi}\int_0^{\pi} \mathrm{d}\varphi \mathrm{d}\vartheta \sin\vartheta\, \check{\mathbf{e}}_r \otimes \check{\mathbf{e}}_r \\ &= \int \mathrm{d}r\, r^3\, g^{(2)}(r)\, \partial_r U(r)\, \frac{4\pi}{3}\mathbb{1}\end{aligned}$$

with the radial unit vector $\check{\mathbf{e}}_r$. Hence, in this approximation the mean volume exclusion force $\overline{\mathbf{F}}_{\mathrm{MF}}^{\mathrm{VE}}$ can be written as

$$\overline{\mathbf{F}}_{\mathrm{MF}}^{\mathrm{VE}} = \left(\frac{4\pi}{3}\int \mathrm{d}r\, r^3\, g^{(2)}(r)\, \partial_r U(r)\right) \nabla\rho(\mathbf{x}) = -\nu'\nabla\rho(\mathbf{x}), \tag{5.9}$$

defining the effective volume exclusion parameter

$$\nu' \equiv -\frac{4\pi}{3\xi_{\mathrm{t}}}\int \mathrm{d}r\, r^3\, g^{(2)}(r)\, \partial_r U(r) > 0. \tag{5.10}$$

Using equation (2.37), the Smoluchowski equation including the effective volume exclusion can be expressed by

$$\partial_t \Psi_1 = -\nabla \cdot \Big[-\nu'\, \Psi_1\, \nabla\rho\Big] \tag{5.11}$$

$$= \nu' \left[\Psi_1 \Delta\rho + (\nabla\Psi_1) \cdot (\nabla\rho) \right]. \tag{5.12}$$

The density gradient term in the flux velocity (2nd term) can be interpreted as an effective pressure: for a repulsive potential the whole expression creates a flow away from dense regions. It works as a local force to counterbalance the longer ranging, predominantly attractive, magnetic force $\overline{\mathbf{F}}_m$ and prevents a density collapse.

In order to calculate the effective volume exclusion parameter ν', the pair distribution function $g^{(2)}$ has to be known. If available, the radial distribution function could be treated as an external input, as discussed in Section 2.5, using experimental findings or the results from Brownian dynamics simulations. However, in a mean-field model the pair correlation function is not available intrinsically. Additionally, ν' depends on the choice of the pair-potential. Considering the limitations imposed by the mean-field assumption, in this work the effective volume exclusion ν' is treated as an external parameter. The upper bound criterion in equation (5.6) offers some guidance in the choice of the value of ν'.

Numerical treatment

In the numerical solution of the Smoluchowski equation that includes effective volume exclusion on a grid, additional issues arise. First, because of the short ranged nature of the interaction, it is impossible to faithfully represent it on a grid with a cell-size larger than the interaction range. Effectively, the strength of the interaction is reduced because the grid imposes a minimal distance onto which the interaction is evaluated. Secondly, the Langevin integrator presented in Section 3.1.2 uses the drift velocity $\mathbf{v}_{\mathrm{VE}} = -\nu'\nabla\rho$, formulated in equation (5.11), Contrary to expectations, for a peaked density distribution at the grid point with the highest density the effective volume exclusion has the lowest impact, i.e. a small drift velocity $\mathbf{v}_{\mathrm{VE}}$, because the density gradient is close to zero near the maximum. Furthermore, the radial symmetry of the short ranged interaction can no longer be realized on a discrete grid with grid width larger than the typical interaction length. On the diagonals, the interaction strength is significantly diminished compared to the off-diagonals, allowing particles to »sneak« into denser volumes. In order to mitigate the first and last issue to some extent, a trilinear-interpolation scheme can be applied in the simulations. The second issue still remains completely and the approach is unsatisfactory.

A different approach is based on the Smoluchowski equation (5.12). Under the assumption that the change of the orientational distribution is negligible on length scales of the volume exclusion interaction, the effective volume exclusion, given by

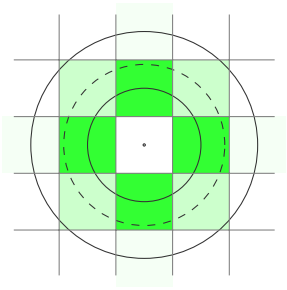

Fig. 5.1.: Illustration of the issues of calculating short-range interactions on a finite grid. A radial interaction force is sampled at the cell centres. The circle represent isolines of the force magnitude. Because the diagonals are further away from the origin, a much lower value is assigned to the grid point compared to the off-diagonal ones, misrepresenting the symmetry of the force and the underlying potential.

equation (5.12), can be modelled by a diffusive process with a density dependent diffusion coefficient. This can be seen, by considering a diffusion only Langevin equation of the form

$$\partial_t \mathbf{x} = \mathbf{g}(\mathbf{x}, t)\mathbf{\Gamma}(t),$$

in which the noise strength squared is assumed to be proportional to the local density, i.e. $\mathbf{g} = \sqrt{\zeta\rho}$. According to equations (2.17) and (2.16), such a Langevin equation corresponds to a Smoluchowski equation given by

$$\begin{aligned}\partial_t \Psi_1 &= \Delta\, D_{\text{ve}} \Psi_1 = \Delta\, \frac{\zeta}{2}\rho\Psi_1 \\ &= \frac{\zeta}{2}\Psi_1 \Delta\rho + \zeta(\nabla\Psi_1)\cdot(\nabla\rho) + \frac{\zeta}{2}\rho\Delta\Psi_1,\end{aligned} \tag{5.13}$$

in the Itô interpretation, with an effective diffusion coefficient, due to effective volume exclusion, given by $D_{\text{ve}}(\mathbf{x}, t) = \frac{1}{2}g^2(\mathbf{x}, t) = \frac{\zeta}{2}\rho(\mathbf{x}, t)$. Equation (5.13) in general deviates from equation (5.12). While equation (5.12) represents a density driven diffusion, which vanishes for a volume of constant density, in equation (5.13) the orientational distribution, as part of Ψ_1, diffuses as well even for constant density. However, when assuming that the orientation is locally constant, the distribution function may be approximated in terms of a separation ansatz,

$$\Psi_1(\mathbf{x}, \mathbf{n}, t) = \rho(\mathbf{x}, t)h(\mathbf{n}, t), \quad \forall \mathbf{x} \in \delta V, \tag{5.14}$$

for a small volume δV with a radius comparable to the interaction length of the volume exclusion. With the ansatz in equation (5.14), equation (5.13) becomes

$$\begin{aligned}\partial_t \Psi_1 &= \frac{\zeta}{2}h\rho\Delta\rho + \zeta h(\nabla\rho)\cdot(\nabla\rho) + \frac{\zeta}{2}\rho h\Delta\rho \\ &= \zeta\rho\Delta h\rho + \zeta(\nabla h\rho)\cdot(\nabla\rho)\end{aligned}$$

$$= \zeta\rho\Delta\Psi_1 + \zeta(\nabla\Psi_1)\cdot(\nabla\rho),$$

and for $\zeta = \nu'$ this equation is equal to (5.12), under the assumption given by equation (5.14). This shows that equation (5.12) can be equally approximated by an effective diffusive process with a diffusion coefficient given by $D_{\text{ve}} = \frac{1}{2}\nu'\rho$.

In the derivation, the Itô interpretation is chosen to be compatible with the Euler-forward-integration scheme, discussed in Section 3.1.2. Using the Stratonovich interpretation would just lead to a different prefactor, so that $\zeta = \frac{4}{3}\nu'$, which can be shown by applying equation (2.18) instead of (2.17).

In order to incorporate this method into the simulation framework efficiently, equation (3.6) can be modified to use a combined diffusion coefficient

$$D_{\text{eff}}(\mathbf{x},t) = D_{\text{t}} + D_{\text{ve}}(\mathbf{x},t) = D_{\text{t}} + \frac{1}{2}\nu'\rho(\mathbf{x},t),$$

fusing two Gaussian random walks of different variance into one with combined variance.

The method described above, i.e. the incorporation of the effective volume exclusion as a stochastic (collision) process on the particle level, finally addresses the second issue arising in the simulations, which has been raised in the beginning of this section. The issue, caused by a misrepresentation of the density gradient on a grid, is circumvented by instead relying on the density itself. This discussion concludes the necessary preparations in order to formulate and calculate a kinetic theory of active microswimmers with magnetic dipole-dipole interaction in the following sections.

5.3 Dimensionless Smoluchowski equation

The complete Smoluchowski equation incorporates the magnetic dipole-dipole interaction from equation (5.5), the effective volume exclusion interaction from equation (5.11) and translational and rotational diffusion. By immediately applying the nondimensionalization procedure, formalized in Section 2.9, it can be written as

$$\partial_t\psi = -\nabla\cdot\mathbf{v}_{\text{t}}\psi - \nabla^{\circ}_{\mathbf{n}}\cdot\mathbf{v}_{\text{r}}\psi + \mathbb{D}\psi. \tag{5.15}$$

The diffusion operator is defined, as before, by $\mathbb{D} = d_t\Delta + \Delta^{\circ}_{\mathbf{n}}$, in which $d_t = \frac{D_\mathrm{t}D_\mathrm{r}}{U_0^2}$. The translational flux velocity $\mathbf{v}_\mathrm{t}$ consists of the (dimensionless) self-propulsion velocity, the mean magnetic force and the effective volume exclusion,

$$\begin{aligned}\mathbf{v}_\mathrm{t}(\mathbf{x},\mathbf{n},t) &= \mathbf{n} + \frac{\mu}{\xi_\mathrm{t}u_c x_c}\nabla(\mathbf{n}\cdot\mathbf{B}_\mathrm{int}(\mathbf{x}\,x_c, t\,t_c)) - \frac{\varrho\nu'}{u_c x_c}\nabla\rho(\mathbf{x},t)\\ &= \mathbf{n} + \frac{\varrho\mu_0\mu^2}{\xi_\mathrm{t}u_c x_c}\nabla(\mathbf{n}\cdot(\mathcal{B}^\mathrm{dip} * \mathbf{p})(\mathbf{x},t)) - \nu\,\nabla\rho(\mathbf{x},t)\\ &= \mathbf{n} + \beta\nabla(\mathbf{n}\cdot(\mathcal{B}^\mathrm{dip} * \mathbf{p})(\mathbf{x},t)) - \nu\,\nabla\rho(\mathbf{x},t),\end{aligned} \tag{5.16}$$

with the dimensionless density distribution ρ and the effective volume exclusion parameter $\nu = \frac{\varrho\nu'}{u_c x_c}$. The rotational flux velocity is determined by the mean torques on a particle inside the internal and external magnetic flux densities $\mathbf{B}_\mathrm{int}$ and $\mathbf{B}_\mathrm{ext}$,

$$\begin{aligned}\mathbf{v}_\mathrm{r}(\mathbf{x},\mathbf{n},t) &= (\mathbb{1}-\mathbf{nn})\cdot\left(\frac{t_c\mu}{\xi_\mathrm{r}}\mathbf{B}_\mathrm{ext} + \frac{t_c\mu}{\xi_\mathrm{r}}\mathbf{B}_\mathrm{int}(\mathbf{x}\,x_c, t\,t_c)\right)\\ &= (\mathbb{1}-\mathbf{nn})\cdot\left(\frac{t_c\mu B_\mathrm{ext}}{\xi_\mathrm{r}}\check{\mathbf{B}}_\mathrm{ext} + \frac{t_c\varrho\mu_0\mu^2}{\xi_\mathrm{r}}(\mathcal{B}^\mathrm{dip} * \mathbf{p})(\mathbf{x},t)\right)\\ &= (\mathbb{1}-\mathbf{nn})\cdot\left(\alpha_\mathrm{ext}\check{\mathbf{B}}_\mathrm{ext} + \alpha_\mathrm{int}(\mathcal{B}^\mathrm{dip} * \mathbf{p})(\mathbf{x},t)\right).\end{aligned} \tag{5.17}$$

As derived in Section 2.6.4, the internal magnetic flux density is determined from the magnetization $\mathbf{M} = \mu\varrho\mathbf{p}$ using equation (2.63),

$$\mathbf{B}_\mathrm{int} = \mu_0\,\mathcal{B}^\mathrm{dip} * \varrho\mu\mathbf{p}.$$

The prefactor ϱ is introduced by the nondimensionalization of the single particle distribution function $\Psi_1 = \varrho\psi$. In equations (5.16) and (5.17) the prefactor $\varrho\mu\mu_0$ is absorbed into the magnetic interaction parameters, given by the magnetic drag β and the internal alignment parameter α_int, respectively, defined by

$$\alpha_\mathrm{int} = \frac{t_c\varrho\mu_0\mu^2}{\xi_\mathrm{r}} = \frac{\varrho\mu_0\mu^2}{\xi_\mathrm{r}D_\mathrm{r}} \tag{5.18}$$

$$\beta = \frac{\varrho\mu_0\mu^2}{\xi_\mathrm{t}u_c x_c} = \frac{\varrho\mu_0\mu^2 D_\mathrm{r}}{\xi_\mathrm{t}U_0^2} = \frac{\xi_\mathrm{r}D_\mathrm{r}^2}{\xi_\mathrm{t}U_0^2}\,\alpha_\mathrm{int}, \tag{5.19}$$

in which the characteristic speed $u_c = U_0$ is chosen to be the self-propulsion speed, the characteristic time $t_c = 1/D_\mathrm{r}$ is given by the inverse rotational diffusion coefficient, and the characteristic length is given by $x_c = u_c t_c$. The external magnetic alignment parameter $\alpha_\mathrm{ext} = \frac{t_c\mu B_\mathrm{ext}}{\xi_\mathrm{r}} = \frac{\mu B_\mathrm{ext}}{\xi_\mathrm{r}D_\mathrm{r}}$ is defined as previously in Chapter 4. It should be noted that in an experiment, the internal and external alignment parameters can be

tuned independently, by varying the number density ϱ and the external flux density B_{ext} accordingly.

As in the previous chapter, a steady state of the Smoluchowski equation can be found, its stability in dependence of the systems parameter assessed, and the linearized dynamics around it can be studied.

5.4 Steady state of a magnetized suspension of microswimmers

Given the non-linear Smoluchowski equation describing the time evolution of a state ψ, considerable insight can be gained by identifying a (time-independent) steady-state of the system and assess under which conditions it is stable or unstable using a linear stability analysis.

Based on the symmetry of the problem, a homogeneous, i.e. spatially independent, steady-state $\psi_0(\vartheta)$ is sought that is axially symmetric around the external magnetic field axis. Such a steady state gives rise to constant polarization $\mathbf{p}_0 = p_0\check{\mathbf{z}}$ pointing along the symmetry axis. Without loss of generality, it can be assumed it coincides with the z-axis, $\mathbf{B}_{\text{ext}} = B_{\text{ext}}\check{\mathbf{z}}$. For a homogeneous suspension with a constant polarization the magnetic field $\mathbf{H}$, given by equation (2.51), vanishes and the internal magnetic field is given directly by the constant magnetization of the system, $\mathbf{B}_{\text{int},0} = \mu_0\mathbf{M}_0 = \mu_0\mu\,\varrho\,p_0\,\check{\mathbf{z}}$. Therefore, the nondimensional rotational flux velocity in equation (5.17) in the steady state ψ_0 can be expressed by

$$\begin{aligned}\mathbf{v}_{\text{r},0}(\mathbf{x},\mathbf{n},t) &= (\mathbb{1}-\mathbf{nn})\cdot(\alpha_{\text{ext}}\check{\mathbf{z}} + \alpha_{\text{int}}p_0\check{\mathbf{z}}) \\ &\equiv (\mathbb{1}-\mathbf{nn})\cdot\alpha_{\text{eff}}\check{\mathbf{z}}\end{aligned} \tag{5.20}$$

in which the prefactors μ_0 and μ has been absorbed into the coefficients into the alignment parameters α_{ext} and α_{int} as before, and the effective alignment parameter is given by $\alpha_{\text{eff}} = \alpha_{\text{ext}} + \alpha_{\text{int}}p_0$. It follows that for a steady-state of the form $\psi_0(\vartheta)$, implying $\nabla^\circ_{\mathbf{n}}\,\psi_0 = \check{\mathbf{e}}_\vartheta\partial_\vartheta\psi_0$, the Smoluchowski equation reduces to

$$\begin{aligned}\partial_t\psi_0 = 0 &= \nabla^\circ_{\mathbf{n}}\cdot\left[\psi_0(\mathbf{v}_r - \nabla^\circ_{\mathbf{n}}\ln\psi_0)\right] \\ &= \nabla^\circ_{\mathbf{n}}\cdot\left[\psi_0(\mathbb{1}-\mathbf{nn})\cdot\alpha_{\text{eff}}\check{\mathbf{z}} - \psi_0\,\nabla^\circ_{\mathbf{n}}\ln\psi_0\right].\end{aligned}$$

A solution can be found by demanding that term in the bracket vanishes, leading to the differential equation

$$\begin{aligned}\psi_0 \nabla^\circ_{\mathbf{n}} \ln \psi_0 = \check{\mathbf{e}}_\vartheta \partial_\vartheta \psi_0 &= (\mathbb{1} - \mathbf{nn}) \cdot \alpha_{\text{eff}} \psi_0 \check{\mathbf{z}} \\ &= \alpha_{\text{eff}} \psi_0 (\check{\mathbf{z}} - \cos\vartheta\, \mathbf{n}) \\ &= -\alpha_{\text{eff}} \sin\vartheta\, \psi_0\, \check{\mathbf{e}}_\vartheta,\end{aligned}$$

in which $\mathbf{n} \cdot \check{\mathbf{z}} = \cos\vartheta$ was used. This differential equation can be solved by the ansatz

$$\psi_0(\vartheta) = \frac{\alpha_{\text{eff}}}{4\pi \sinh \alpha_{\text{eff}}} e^{\alpha_{\text{eff}} \cos\vartheta}, \tag{5.21}$$

analogous to the case of hydrodynamically interacting suspensions in an external field in Chapter 4. However, now the effective alignment parameter is only given implicitly by the equation

$$\begin{aligned}\alpha_{\text{eff}} &= \alpha_{\text{ext}} + \alpha_{\text{int}} p_0 \\ &= \alpha_{\text{ext}} + \alpha_{\text{int}} \int_0^{2\pi} \mathrm{d}\varphi \int_0^{\pi} \mathrm{d}\vartheta \sin\vartheta\, \psi_0(\vartheta)\, n_3(\vartheta) \\ &= \alpha_{\text{ext}} + \alpha_{\text{int}} 2\pi \int_0^{\pi} \mathrm{d}\vartheta \sin\vartheta \cos\vartheta\, \psi_0(\vartheta) \\ &= \alpha_{\text{ext}} + \alpha_{\text{int}} \left(\coth \alpha_{\text{eff}} - \frac{1}{\alpha_{\text{eff}}} \right),\end{aligned} \tag{5.22}$$

using $\mathbf{n} = n_3 \check{\mathbf{z}} = \cos\vartheta$ and the definition of the polarization $\mathbf{p}_0 = \int_{\mathbb{S}^2} \mathrm{d}\mathbf{n}\ \psi_0 \mathbf{n}$. This implicit equation reflects an interesting phenomenon: spontaneous magnetization induced by magnetic interactions, similar to other magnetic systems [150, 151].

5.4.1 Spontaneous magnetization

The implicitly defined effective alignment parameter α_{eff} in the steady state, given by equation (5.22), does not have a closed formal solution. But both graphical and numerical solutions offer an insight into the physics behind its definition. In the case of a vanishing external magnetic field, i.e. $\alpha_{\text{ext}} = 0$, α_{eff} is proportional to the magnetization $\mathbf{M}_0$ and the solution to equation (5.22) is the intersection of the line $\frac{\alpha_{\text{eff}}}{\alpha_{\text{int}}}$ and the curve $p_0(\alpha_{\text{eff}}) = \coth \alpha_{\text{eff}} - \frac{1}{\alpha_{\text{eff}}}$, as plotted in Figure 5.3 for various α_{int}. For an internal magnetic alignment parameter below the critical value $\alpha_{\text{int}}^{\text{crit}} = \frac{1}{\partial_{\alpha_{\text{eff}}} p_0(\alpha_{\text{eff}})|_{\alpha_{\text{eff}} \to 0}} = 3$ the effective magnetic field is zero. But once it grows beyond the critical value a second solution appears and a spontaneous magnetization

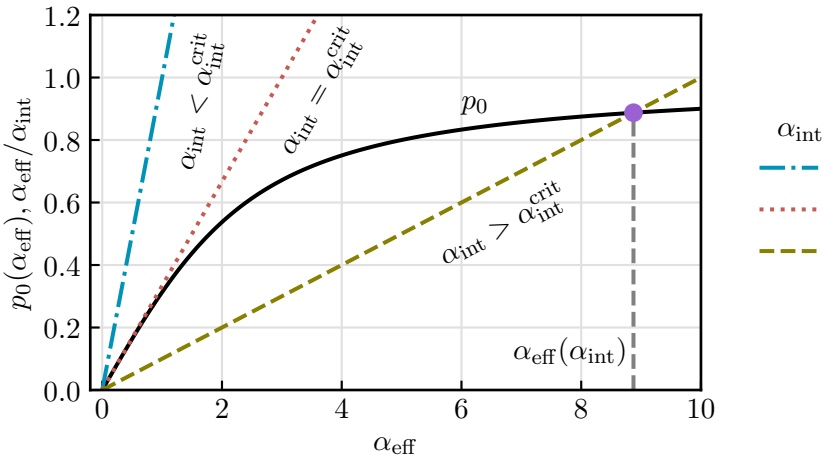

Fig. 5.2.: A graphical solution of the implicit equation (5.22) of the effective internal magnetic field in the steady state ψ_0 given in (5.21). The magnetic field is given by the intersection of the black curve $p_0(\alpha_{\text{eff}})$ and the line $\alpha_{\text{int}}/\alpha_{\text{eff}}$ (given for different interaction parameters α_{int}). For $\alpha_{\text{int}} \leq 3$ there only exists the solution $\alpha_{\text{eff}} = 0$. Above that value, an additional solution $\alpha_{\text{eff}} \neq 0$ exists.

can occur. The effective alignment parameter α_{eff} is plotted against α_{int} in Figure 5.3 illustrating the effect.

The possibility of a spontaneous magnetization is already known from passive systems and is described by an off-grid Heisenberg model [152] (the same is true for a 2D system for which the steady state is analogous to an off-grid XY-model [150]). The functional dependency between an effective temperature (here $\alpha_{\text{int}} \propto T^{-1}$ approximately) and the magnetization in the passive system is the same as the one presented here in equation (5.22). In fact, the homogeneous steady state ψ_0 is the same for the active and passive system, as the steady state is independent of the self-propulsion because of its symmetry. It is worth mentioning that the described spontaneous phase transition has a critical exponent of $1/2$ with respect to the temperature, i.e. $\mathbf{M} \propto \frac{T-T_c}{T}^{1/2}$, as expected from a mean-field theory.

If in addition an external magnetic field is present, parametrized by the aligning parameter $\alpha_{\text{ext}} \propto B_{\text{ext}}$, a unique, non-zero solution to equation (5.22) exists at all times — as illustrated in Figure 5.4. The numerical solution of $\alpha_{\text{eff}}(\alpha_{\text{int}}, \alpha_{\text{ext}})$ is shown in Figure 5.5 for different external field strengths. Eventually, for large external fields the effective alignment parameter approaches $\alpha_{\text{eff}}(\alpha_{\text{int}}, \alpha_{\text{ext}}) = \alpha_{\text{int}} + \alpha_{\text{ext}}$ asymptotically, as $p_0 \to 1$ approaches unity. This linear approximation for $\alpha_{\text{ext}} = 7$ is indicated by the grey line in Figure 5.5.

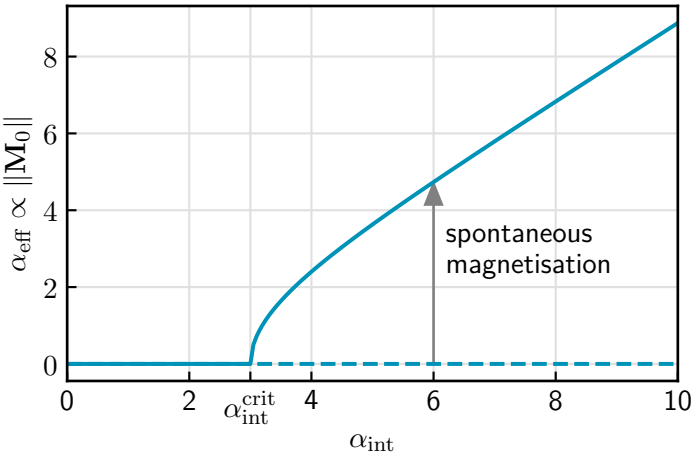

Fig. 5.3.: A numerical solution of the implicit equation (5.22) of the effective internal magnetic field in the steady state ψ_0 given in (5.21) in absence of an external field. Below $\alpha_{\text{int}}^{\text{crit}}$there only exists one solution for the effective internal field α_{eff} but above two branches of solutions appear (solid and dashed line). When considering only thermal rotational diffusion, $\alpha_{\text{int}} \propto T^{-1}$, and the plot is akin to the magnetization in the continuous (off-lattice) Heisenberg-model.

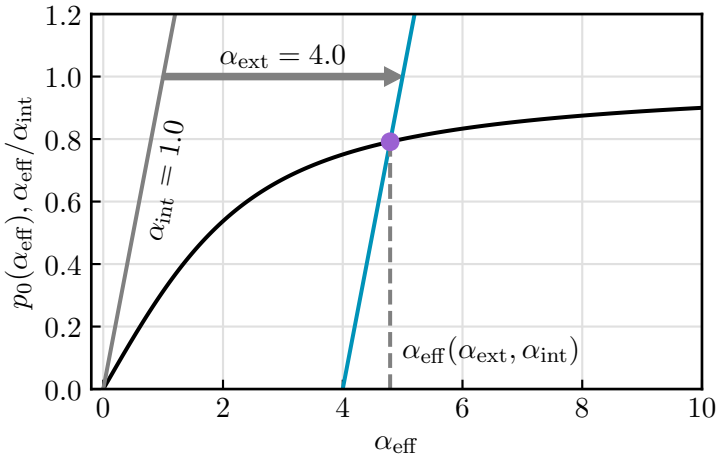

Fig. 5.4.: Graphical solution of the effective magnetic field α_{eff}, equation (5.22), in the presence of an external magnetic field, $\alpha_{\text{ext}} \neq 0$. In contrast to the case of vanishing external field, see Figure 5.2, a unique non-zero solution exists for all α_{int}.

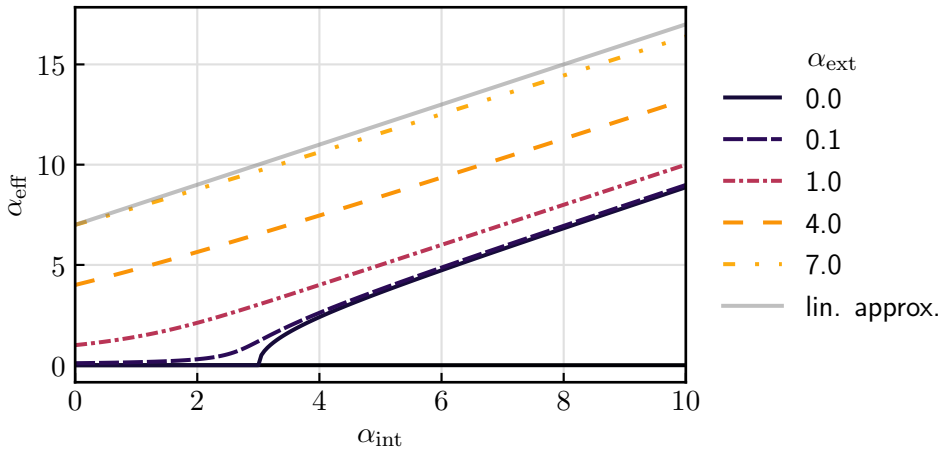

Fig. 5.5.: Numerical solution of the effective magnetic field $\alpha_{\text{eff}}(\alpha_{\text{int}}, \alpha_{\text{ext}})$, equation (5.22), in the presence of an external magnetic field. For comparison the solid black line shows $\alpha_{\text{eff}}(\alpha_{\text{int}}, 0)$ featuring two solutions. For $\alpha_{\text{ext}} \neq 0$ a unique solution exists. The grey line is given by the linearization $\alpha_{\text{eff}} \approx \alpha_{\text{ext}} + \alpha_{\text{int}}$, obtained in the limit of large external field strength. In this case, it is shown for $\alpha_{\text{ext}} = 7$.

Eventually, the dynamics of the system can be linearized around the steady state and a linear stability analysis provides information about the stability of the state.

5.5 Linear stability analysis

Just like in Chapter 4, Section 3.4, a linear stability analysis of the steady state in equation (5.21) helps to clarify for which parameter subset $(\alpha_{\text{int}}, \alpha_{\text{ext}})$ the dynamics of system depart from the homogeneous steady state ψ_0. As described in Section 3.4, the steady state of the Smoluchowski equation defined in equation (5.15) is disturbed by a small perturbation,

$$\psi = \psi_0 + \varepsilon\psi_p,$$

of the form

$$\psi_p(\mathbf{k}; \mathbf{x}, \mathbf{n}, t) = \tilde{\psi}(\mathbf{k}, \mathbf{n})\, e^{\mathrm{i}\mathbf{k}\cdot\mathbf{x}+\lambda t}.$$

By neglecting terms in $\mathcal{O}(\varepsilon^2)$, the Smoluchowski equation is linearized around the steady state, and can be reduced to an eigenvalue problem of the algebraized and linearized differentio-integro operator $\widehat{\mathbb{L}}$, yielding

$$\lambda\tilde{\psi}(\mathbf{k}, \mathbf{n}) = \widehat{\mathbb{L}}\tilde{\psi}(\mathbf{k}, \mathbf{n}).$$

The derivation of the linearized operator $\widehat{\mathbb{L}}$, for which the amplitude $\tilde{\psi}$ is an eigenfunction, is equivalent to that in Section 4.3.1, except that hydrodynamic interactions are ignored and the additional terms due to the magnetic dipole-dipole interactions have to be included. The real part of the resulting eigenvalues λ, the growth rate of the perturbation, provides information about the stability of the steady state.

5.5.1 Linearization

First, consider the perturbation of the translational flux divergence $\nabla \cdot [\mathbf{v}_t\psi]$,

$$\nabla \cdot [\psi\mathbf{v}_t] = \nabla \cdot \left[\psi(\mathbf{n} + \underbrace{\beta\nabla(\mathbf{n} \cdot \mathcal{B}^{\text{dip}} * \mathbf{p})}_{(1)} + \underbrace{\nu\,\nabla\rho}_{(2)})\right].$$

The density and polarization fields $\rho[\psi]$ and $\mathbf{p}[\psi]$ as linear functionals of the distribution function ψ, see equations (2.28) and (2.29), is perturbed according to

$$\rho[\psi] = \rho[\psi_0] + \varepsilon\rho[\psi_p] \equiv \rho_0 + \varepsilon\rho_p$$
$$\mathbf{p}[\psi] = \mathbf{p}[\psi_0] + \varepsilon\mathbf{p}[\psi_p] \equiv \mathbf{p}_0 + \varepsilon\mathbf{p}_p.$$

The magnetic force between particles, (1), is disturbed like

$$\begin{aligned}\nabla\cdot\Big[\psi\beta\nabla(\mathbf{n}\cdot\mathcal{B}^{\text{dip}}*\mathbf{p})\Big]=&\nabla\cdot\Big[(\psi_0+\varepsilon\psi_p)\beta\nabla(\mathbf{n}\cdot\mathcal{B}^{\text{dip}}*(\mathbf{p}_0+\varepsilon\mathbf{p}_p))\Big]\\ =&\nabla\cdot\Big[\varepsilon\psi_0\beta\nabla(\mathbf{n}\cdot\mathcal{B}^{\text{dip}}*\mathbf{p}_p)\Big]+\nabla\cdot\left[\varepsilon\psi_p\beta\underbrace{\nabla(\mathbf{n}\cdot\mathcal{B}^{\text{dip}}*\mathbf{p}_0)}_{(\ldots)=\text{const}\Rightarrow=0}\right]\\ &+\mathcal{O}(\varepsilon^2)\\ \approx&\varepsilon\nabla\cdot\Big[\psi_0\beta\nabla(\mathbf{n}\cdot\mathcal{B}^{\text{dip}}*\mathbf{p}_p)\Big]\\ =&\varepsilon\beta\psi_0\nabla\cdot\Big[\nabla(\mathbf{n}\cdot\mathcal{B}^{\text{dip}}*\mathbf{p}_p)\Big]\\ =&\varepsilon\beta\psi_0\mathbf{n}\cdot\Delta\mathcal{B}^{\text{dip}}*\mathbf{p}_p.\end{aligned}$$

The effective volume exclusion, (2), can be written as

$$\begin{aligned}\nabla\cdot[\psi\nu\nabla\rho]&=\nabla\cdot\left[(\psi_0+\varepsilon\psi_p)\nu\nabla(\rho_0+\varepsilon\rho_p)\right]\\ &=\varepsilon\nabla\cdot\left[\psi_0\nu\nabla\rho_p\right]+\left[\varepsilon\nabla\cdot\psi_p\nu\nabla\varepsilon\rho_0\right]+\mathcal{O}(\varepsilon^2)\\ &=\varepsilon\nabla\cdot\psi_0\nu\nabla\rho_p\\ &=\varepsilon\nu\psi_0\Delta\rho_p.\end{aligned}$$

Finally, the perturbation of the rotational flux divergence, $\nabla^\circ_{\mathbf{n}}\cdot\mathbf{v}_r\psi$ is given by

$$\begin{aligned}\nabla^\circ_{\mathbf{n}}\cdot&\Big[\psi((\mathbb{1}-\mathbf{nn})\cdot\alpha_{\text{int}}\mathcal{B}^{\text{dip}}*\mathbf{p})\Big]\\ =&\nabla^\circ_{\mathbf{n}}\cdot\Big[(\psi_0+\varepsilon\psi_p)((\mathbb{1}-\mathbf{nn})\cdot\alpha_{\text{int}}\mathcal{B}^{\text{dip}}*(\mathbf{p}_0+\varepsilon\mathbf{p}_p))\Big]\\ =&\varepsilon\,\nabla^\circ_{\mathbf{n}}\cdot\Big[\psi_0(\mathbb{1}-\mathbf{nn})\cdot\alpha_{\text{int}}\mathcal{B}^{\text{dip}}*\mathbf{p}_p\Big]\\ &+\varepsilon\,\nabla^\circ_{\mathbf{n}}\cdot\Big[\psi_p(\mathbb{1}-\mathbf{nn})\cdot\alpha_{\text{int}}\mathcal{B}^{\text{dip}}*\mathbf{p}_0\Big]\\ &+\mathcal{O}(\varepsilon^2)\\ \approx&\varepsilon\,\nabla^\circ_{\mathbf{n}}\cdot(\psi_0\alpha_{\text{int}}\mathcal{B}^{\text{dip}}*\mathbf{p}_p)-\varepsilon 2\mathbf{n}\cdot(\psi_0\alpha_{\text{int}}\mathcal{B}^{\text{dip}}*\mathbf{p}_p)\\ &+\varepsilon\,\nabla^\circ_{\mathbf{n}}\cdot(\psi_p\alpha_{\text{int}}\mathbf{p}_0)-\varepsilon 2\mathbf{n}\cdot(\psi_p\alpha_{\text{int}}\mathbf{p}_0)\\ =&\varepsilon\alpha_{\text{int}}\mathcal{B}^{\text{dip}}*\mathbf{p}_p\cdot\nabla^\circ_{\mathbf{n}}\,\psi_0-\varepsilon 2\psi_0\alpha_{\text{int}}\mathbf{n}\cdot\mathcal{B}^{\text{dip}}*\mathbf{p}_p\\ &+\varepsilon\alpha_{\text{int}}\mathbf{p}_0\cdot\nabla^\circ_{\mathbf{n}}\,\psi_p-\varepsilon 2\psi_p\alpha_{\text{int}}\mathbf{n}\cdot\mathbf{p}_0\\ =&\varepsilon\alpha_{\text{int}}\mathcal{B}^{\text{dip}}*\mathbf{p}_p\cdot(\nabla^\circ_{\mathbf{n}}\,\psi_0-2\psi_0\mathbf{n})+\varepsilon\alpha_{\text{int}}\mathbf{p}_0\cdot(\nabla^\circ_{\mathbf{n}}\,\psi_p-2\psi_p\mathbf{n})\\ =&-\varepsilon\alpha_{\text{int}}\mathcal{B}^{\text{dip}}*\mathbf{p}_p\cdot(\alpha_{\text{eff}}\sin\vartheta\,\widehat{\mathbf{e}}_\vartheta+2\mathbf{n})\psi_0\\ &-\varepsilon\alpha_{\text{int}}p_0(\sin\vartheta\,\partial_\vartheta+2\cos\vartheta)\psi_p\end{aligned}$$

From the derivations above, the linearized, algebraized time evolution operator is finally obtained.

$$\begin{aligned}\widehat{\mathbb{L}}\tilde{\psi} = &- \mathrm{i}\mathbf{n}\cdot\mathbf{k}\tilde{\psi} \\ &+ \beta\psi_0\mathbf{n}\cdot k^2(\widehat{\mathcal{B}}^{\mathrm{dip}}\cdot\tilde{\mathbf{p}}) \\ &+ \nu\psi_0 k^2\tilde{\rho} \\ &+ \alpha_{\mathrm{int}}\,(\widehat{\mathcal{B}}^{\mathrm{dip}}\cdot\tilde{\mathbf{p}})\cdot(\alpha_{\mathrm{eff}}\sin\vartheta\,\hat{\mathbf{e}}_\vartheta + 2\mathbf{n})\psi_0 \\ &+ \alpha_{\mathrm{eff}}(\sin\vartheta\,\partial_\vartheta + 2\cos\vartheta)\psi_p \\ &+ \Delta^\circ_{\mathbf{n}}\,\tilde{\psi} - d_t k^2\tilde{\psi}. \end{aligned} \tag{5.23}$$

The influence of the external magnetic field is included in the effective alignment parameter $\alpha_{\mathrm{eff}}(\alpha_{\mathrm{ext}}, \alpha_{\mathrm{int}})$, given by equation (5.22), in the second to last term.

5.5.2 Mode structure of the perturbation

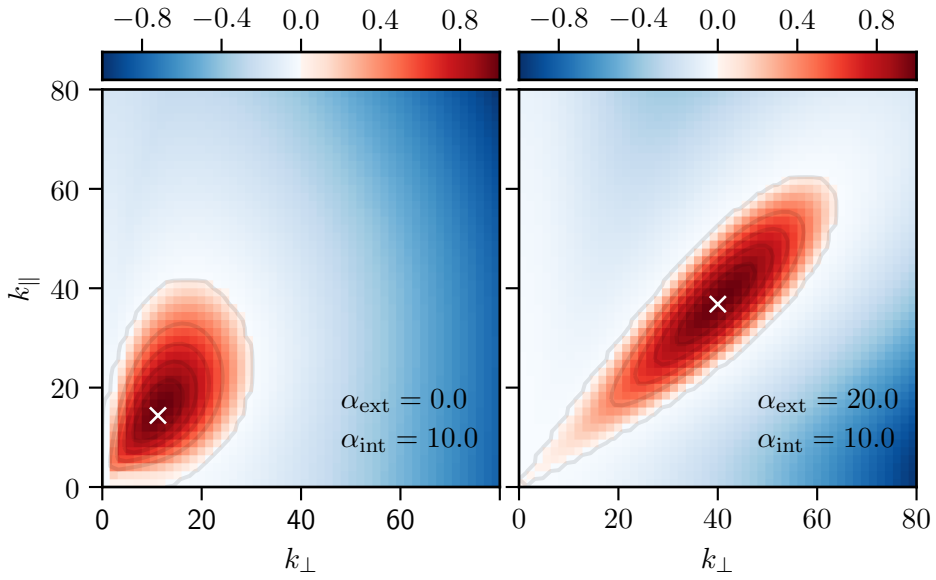

Fig. 5.6.: The maximal growth rate $\mathrm{Re}\,\lambda_{\mathrm{max}}(\mathbf{k})$ plotted against the wave vector $\mathbf{k}$ for the parameters $d_t = 3.6\times10^{-6}, \nu = 2\times10^{-5}, \beta = 3\times10^{-5}\alpha_{\mathrm{int}}$. The wavevector giving the largest growth rate is marked by a white cross. Contour lines are included to guide the eye. The three remaining quadrants (not shown) are mirror images with respect to the coordinate axes of the displayed quadrant.

By the same method as described in Section 4.3.2 the eigenvalues and -vectors of the operator $\widehat{\mathbb{L}}$ are calculated. Again, the growth rate of the dominant (eigen)mode is given by the real part of the largest eigenvalue $\mathrm{Re}\,\lambda_{\mathrm{max}}(\mathbf{k})$. In Figure 5.6, the

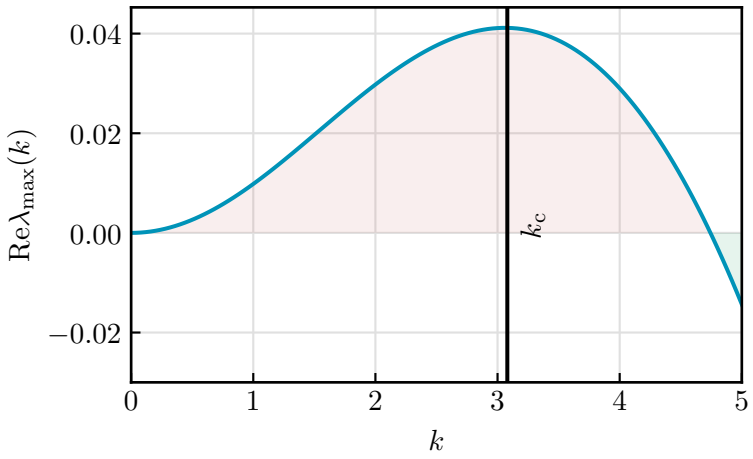

Fig. 5.7.: The maximum growth rate $\mathrm{Re}\,\lambda_{\max}(k)$ plotted against the wavenumber k of perturbations at an angle of $\Theta_B = \pi/4$ with respect to the symmetry axis and $\alpha_{\text{int}} = 5$. The remaining parameters are fixed to $d_t = 3.6 \times 10^{-6}, \nu = 2 \times 10^{-5}, \beta = 3.6 \times 10^{-6}\alpha_{\text{int}}$.

maximum growth rate is plotted against the perpendicular and parallel components of the perturbation's wave vector for a vanishing and for a non-vanishing external field, while the internal interaction strength, given by α_{int} is fixed. A clear orientational preference of the perturbation towards an angle of $\Theta_B = \pi/4$ with respect to the symmetry axis, coinciding with the external field, is visible. It becomes more pronounced the stronger the external field is. Secondly, the wavenumber of the fastest growing mode (marked with a white cross in the plot) grows with the external field strength.

A typical maximum growth rate for modes in $\Theta_B = \pi/4$ direction is shown in Figure 5.7. The fastest growing and therefore most dominant mode has a finite characteristic wavenumber, as depicted by the vertical line in the figure. This is different from the results obtained for hydrodynamically interacting active particles in Chapter 4, where in most cases the $k = 0$ mode, an orientation-only perturbation, was dominant. A look into the (typical) eigenfunctions in Figure 5.8, encoded as coordinates in the basis of spherical harmonics, reveals that not only the orientation but the density is disturbed as well, i.e. the first coordinate $(\boldsymbol{\psi})_0^0 \neq 0$ of the eigenfunction has a non-zero value. This result is true for in the absence of an external field, Figure 5.8 (a) and for a weak external field as shown in Figure 5.8 (b). The latter has a wider spectrum, i.e. the mode includes orientational perturbations of higher frequency. The presented eigenfunctions belong to the growth rates marked with a white cross in Figure 5.9.

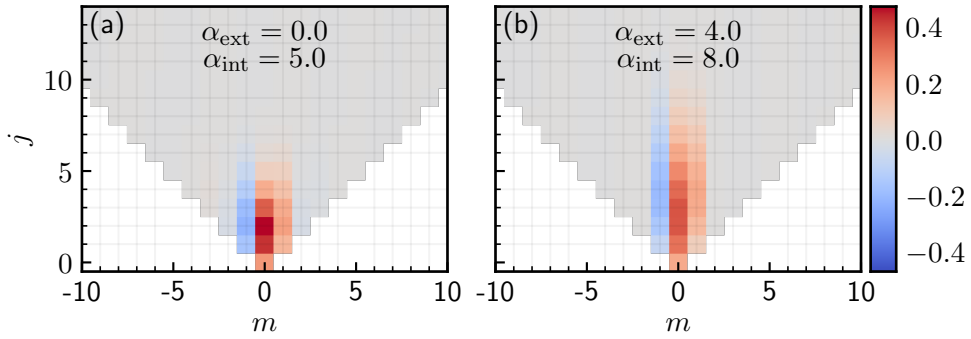

Fig. 5.8.: Colour coded coefficients of the dominant unstable eigenmode for different interaction strengths represented by α_{ext} and α_{int}. The eigenfunctions correspond to the growth rate marked by a white cross in Figure 5.6. Every row, from bottom to top, corresponds to the density, polarization, nematic order parameter, and higher orientational moments of the eigenmode, as discussed in Section 4.3.

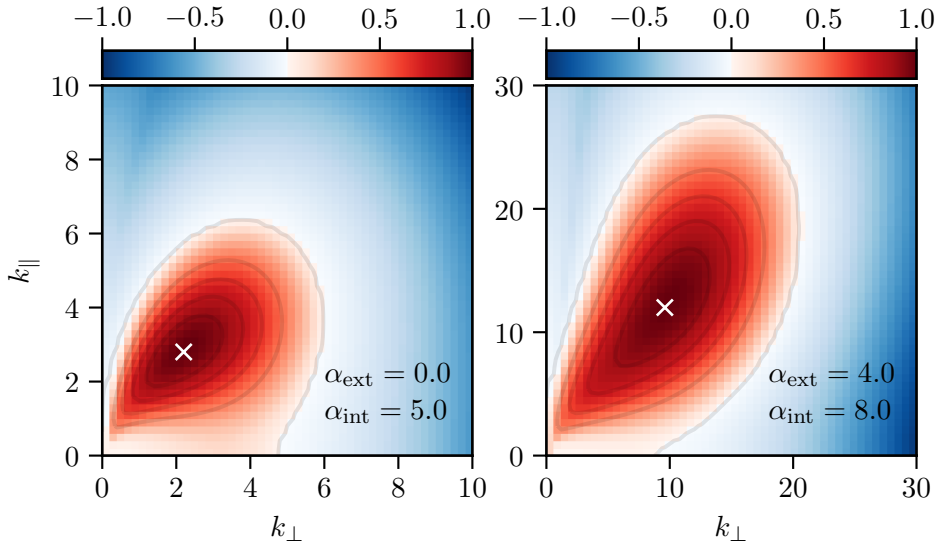

Fig. 5.9.: The maximal growth rate $\mathrm{Re}\,\lambda_{\max}(\mathbf{k})$ plotted against the wave vector $\mathbf{k}$ for the parameters $d_t = 3.6 \times 10^{-6}, \nu = 2 \times 10^{-5}, \beta = 3.6 \times 10^{-6}\alpha_{\text{int}}$. Contour lines are included to guide the eyes. The white cross marks the wavevector for which the growth rate takes the largest value.

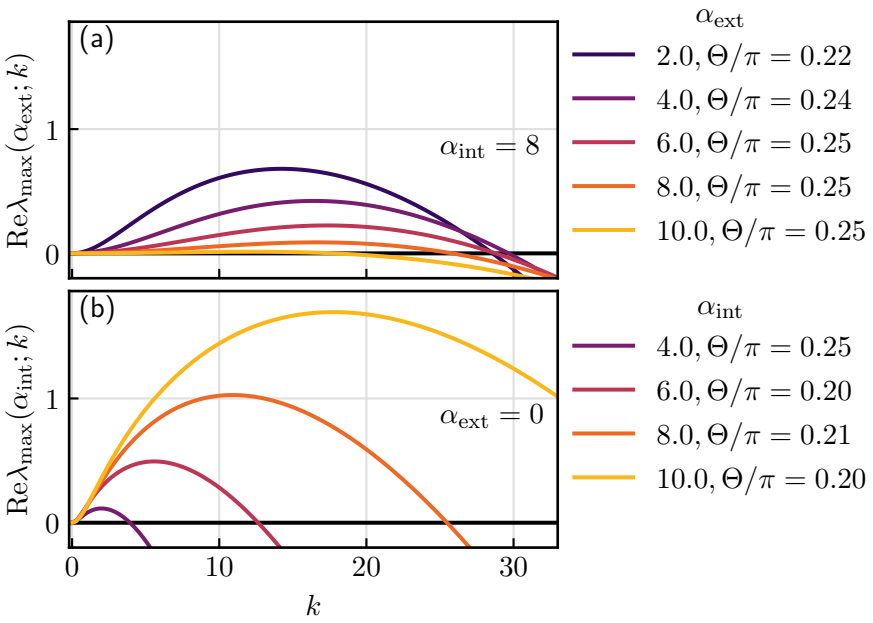

Fig. 5.10.: Growth rate $\mathrm{Re}\,\lambda_{\max}(k)$ plotted against the wavenumber k of perturbations at an angle Θ_B with respect to the external field, which includes the largest growth rate, for different internal and external magnetic interaction strength. The remaining parameters are fixed to $d_t = 3.6 \times 10^{-6}, \nu = 2 \times 10^{-5}, \beta = 3.6 \times 10^{-6}\alpha_{\mathrm{int}}$.

In Figure 5.10 (a) the maximum growth rate is plotted against the wavenumber for different external field values and a fixed internal interaction strength, while Figure 5.10 (b) shows an analogous sweep for different internal interaction strengths for a vanishing external field. The direction of the perturbation Θ_B is adapted to include the largest growth rate. Increasing the external field strength, as can be seen in Figure 5.10 (a), has only a small influence on the characteristic wavelength. On the other hand, increasing the internal interaction strength via α_{int}, as done in Figure 5.10 (b), induces instabilities at higher characteristic wavenumbers k_{c}. Thus, the higher the interaction strength, the more local interactions play a role in the instability of the steady state. Additionally, a higher external field clearly stabilizes the steady state in the chosen parameter range. This trend becomes more visible in the stability diagram in the next section, relating the stability of the steady state to both internal and external interactions.

5.5.3 Stability Diagram

In order to get an overview of the parameter range in $(\alpha_{\mathrm{ext}}, \alpha_{\mathrm{int}})$for which the homogeneous steady state ψ_0 is stable, the line of neutral stability, dividing the stable and

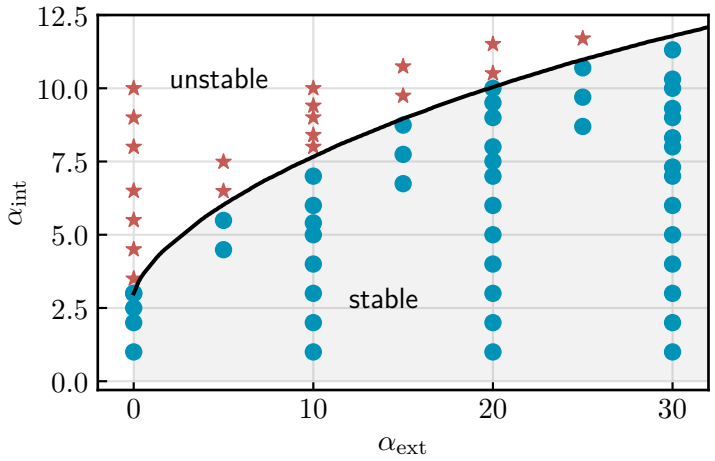

Fig. 5.11.: Stability of steady state ψ_0, given by equation (5.21), in dependency of the interaction strengths represented by $\alpha_{\text{ext}} \propto B$ and $\alpha_{\text{int}} \propto \varrho\mu^2$. The black line is the line of neutral stability. The symbols represent simulations initialized with the steady state ψ_0 and mark stable (blue bullet) and unstable (red star) points based on full numerical solutions of the Smoluchwoski equation.

unstable regime, can be calculated using the formalism of linear stability analysis (see Section 3.4). The stability diagram is shown in Figure 5.11 as a function of the internal and external alignment parameters α_{int} and α_{ext}. For a vanishing external magnetic field, i.e. $\alpha_{\text{ext}} = 0$, the steady state is unstable for $\alpha_{\text{int}} > 3$, almost immediately after the spontaneous magnetization occurs. Interestingly, a non-zero external field stabilizes the steady state for considerably larger α_{int} values. The higher the external field, the higher the internal interaction strength must be to render the steady state unstable. Figure 5.11 shows results from numerical solutions, using the method presented in Chapter 3, of the full non-linear equation for comparison as well[1]. Red stars mark simulations that depart from the steady state Ψ_0 and are therefore unstable. Blue bullets denote stable simulations. The numerical results are in excellent agreement with the findings from the linear stability analysis.

In the unstable regime, the dynamics deviates considerably from the steady state. To get an idea about the transition from the steady state to the non-linear dynamics, the linearized Smoluchowski equations can be studied for times shortly after the instability occurred.

[1]Simulations have to be set up with a large enough box size and small enough grid width in order to support the relevant unstable modes that are found by linear stability analysis. The box size controls the smallest possible supported wavenumber k_{min}, whereas the grid width controls the largest supported wavenumber k_{max}. Because of the discrete nature of the simulation, only a discrete subset of the continuous unstable spectrum is supported. This usually does not pose a problem as long as modes close to the dominant mode are included, i.e. $k_{\text{char}} \in [k_{\text{min}}, k_{\text{max}}]$.

5.6 Pattern formation

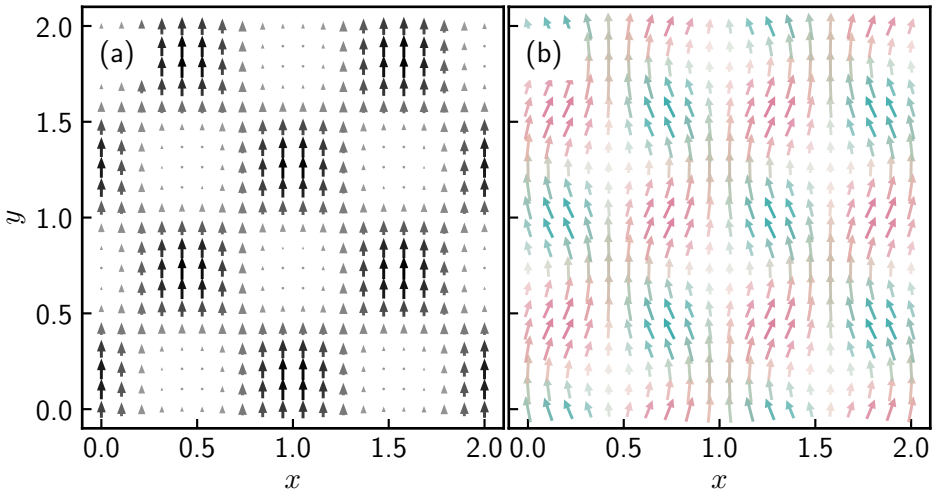

Fig. 5.12.: A cartoon of an exaggerated first order, *density only* perturbation of the polarization density $\mathbf{p}$ in diagonal direction, i.e. $\Theta_B = \pi/4$, in (a) and the resulting perturbed magnetic field in (b). The magnetic field tends to align perpendicular to the wave vector of the plane wave perturbation, forcing particles to rotate and move along the band and thus stabilizing the structure.

Although the linearized equation 5.23 does not capture the dynamics well in general, it can give qualitatively accurate predictions near a steady state. It is a useful tool to develop an understanding of the onset of pattern formation. The eigenfunction representation in Figure 5.8 reveals that a density perturbation contributes to the instability. This instability in turn has influence on the internal magnetic field, as can be seen by following consideration.

The polarization density scales by definition (see equation (2.29)) with the local particle density, reflecting that more particles in a volume also generate a stronger magnetic field than fewer particles with an equivalent orientational distribution. Hence, a density perturbation affects the magnitude of the polarization as well. Given a density perturbation of the form $\rho_p \propto A(t)e^{\mathrm{i}\mathbf{k}_c\cdot\mathbf{x}}$, with a characteristic wavevector $\mathbf{k}_c$, the resulting polarization modulation near the steady state can be approximated by the ansatz

$$\mathbf{p}_\rho(\mathbf{x},t) = \left(1 + A(t)e^{\mathrm{i}\mathbf{k}_c\cdot\mathbf{x}}\right)\mathbf{p}_0,$$

where $\mathbf{p}_0$ is the polarization of the steady state ψ_0. An exaggerated illustration of the perturbed field is shown in Figure 5.12 (a) in 2D. For symmetry reasons, there is not only a mode in Θ_B-direction but one at $-\Theta_B$ as well. Note that this

deliberately ignores higher moment perturbations and only concentrates on a density perturbation.

Such a perturbation in turn results in a magnet flux field given by

$$\begin{aligned}\mathbf{B}_\rho(\mathbf{x},t) &= A(t)\frac{1}{(2\pi)^3}\int \mathrm{d}\mathbf{k}, e^{\mathrm{i}\mathbf{k}\cdot\mathbf{x}}(\mathbb{1}-k^{-2}\mathbf{k}\mathbf{k})\cdot\mathbf{p}_0(2\pi)^3\delta(\mathbf{k}_\mathrm{c}-\mathbf{k})\\ &= \mathbf{B}_0 + A(t)e^{\mathrm{i}\mathbf{k}\cdot\mathbf{x}}(\mathbb{1}-k_c^{-2}\mathbf{k}_\mathrm{c}\mathbf{k}_\mathrm{c})\cdot p_0\check{\mathbf{z}}\\ &= \mathbf{B}_0 + A(t)e^{\mathrm{i}\mathbf{k}\cdot\mathbf{x}}p_0(-\cos\Theta_B\sin\Theta_B, 0, 1-\sin^2\Theta_B),\end{aligned}$$

using the magnetic dipole kernel $\check{\mathcal{B}}$ from equation(2.61) and $\mathbf{k}_\mathrm{c} = k_\mathrm{c}(\sin\Theta_B, 0, \cos\Theta_B)$. An illustration of the resulting field is shown in Figure 5.12 (b). It shows a cross-hatch like pattern where the magnetic field tends to point along the high density bands, i.e. nearly perpendicular to the wave vector of the perturbation, except for the crossings of both perturbations. Particles in such a band will get orientated along the magnetic flux on average, move along the band, and thus will remain there for some time. Because there is also a component perpendicular the band (parallel to the wave vector) particles move in band formation as a whole, so that the pattern travels in the direction of the external magnetic field. At the cross roads, the particles can change into a crossing band.

Although simplified, this mechanism can actually be found in non-linear simulations as well. Figure 5.13 shows a snapshot from a quasi-2D[2] simulation short after the instability has occurred. A small external field is used to break the symmetry so that on average the magnetic field points into y-direction. In Figure 5.13 (a), the local probability density ρ is colour encoded and the local mean orientation $\rho^{-1}\mathbf{p}$ is plotted on top as white vectors. In Figure 5.13 (b), the corresponding magnetic flux density field $\mathbf{B} = \mathbf{B}_\mathrm{ext} + \mathbf{B}_\mathrm{int}$ is plotted. To guide the eye, the vector arrow's colour emphasizes its orientation. The previously described cross-hatch pattern is clearly visible. The particles organize in moving bands or lanes which they follow along as they, on average, align with the self-generated magnetic field.

As a result of the cross-hatch pattern, the average polarization of the particles still points into the direction of the external field, as can be seen in Figure 5.14 depicting the orientational distribution $\psi_n = \frac{1}{v}\int \mathrm{d}\mathbf{x}\,\psi$ averaged over time. But it becomes broader the more particles point along either of the lane directions. This fact is better illustrated by the difference between the steady state distribution and the measured one plotted in Figure 5.14 (b). The difference distribution is bi-modal at angles

[2] Quasi-2D in the context means, the particle's orientation vectors is forced to stay in a 2D-plane. The dynamics are qualitatively the same as in the full 3D case.

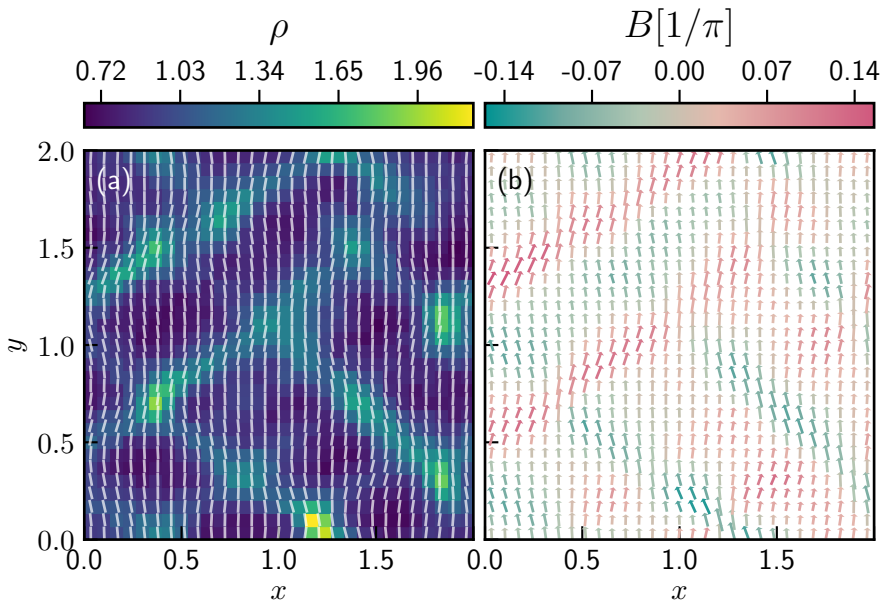

Fig. 5.13.: Exemplary snapshot from quasi 2D simulation ($\alpha_{\text{int}} = 8, \alpha_{\text{ext}} = 1$) short after the occurrence of instability ($t = 5.8t_c$), with a small external field pointing into y-direction. The characteristic wavelength of the density modulation coincides with the one from linear stability analysis, $\lambda_{\text{c}} = 2\pi/k_{\text{c}}$. (a) Colour encoded density field ρ overlaid with the polarization field $\rho^{-1}\mathbf{p}$ in white. (b) Total magnetic field $\mathbf{B}$ with an orientation dependent colour code to guide the eyes.

close the lane direction, while fewer particles point along the external magnetic field axis.

In three dimensions, the mechanism of the instability is in principle the same. But now more possible perturbation modes are supported that can occur at the same time, leading to a more complex, but equivalent pattern. In Figure 5.15, the snapshot of the three-dimensional density field is visualized. It is taken from a simulation at $\alpha_{\text{ext}} = 5$ and $\alpha_{\text{int}} = 7.5$ shortly after the instability has occurred. The front left quarter has been cut out to allow for a clearer sight. When comparing the results directly to Figure 5.13, the similarities become apparent.

However, as time progresses, non-linearities contribute to a greater extent to the dynamics and the system departs from this distinct cross-hatch pattern formation described above. A snapshot of a later time in the simulation is displayed in Figure 5.16. Because of attractive forces between the magnetic dipoles of the particles, the particles tend to form dense, polarized convoys. The higher the density the higher are the forces between them and more particles are attracted. Without an opposing force, the density cluster would collapse and become singular. In this case, an effective volume exclusion as described in Section 5.2 prevents a collapse and limits the density of a

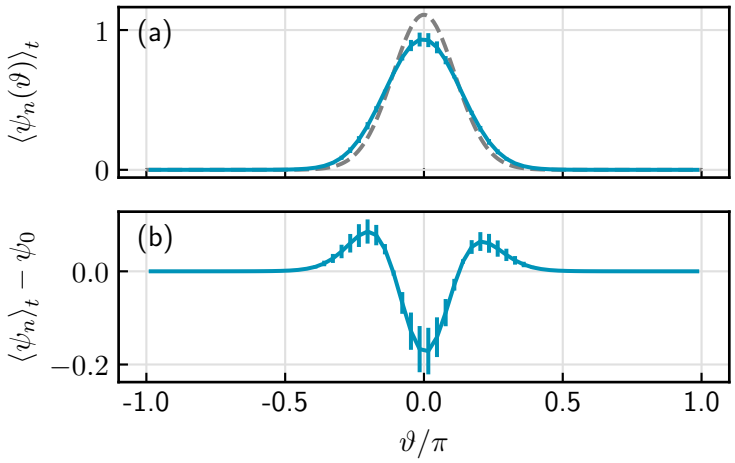

Fig. 5.14.: (a): Time-averaged orientational distribution in a quasi-2D simulation at $\alpha_{\text{ext}} = 1$ and $\alpha_{\text{int}} = 8$ shortly after the appearance of instability, with the steady state ψ_0 as a reference. (b): Difference between both curves in (a).

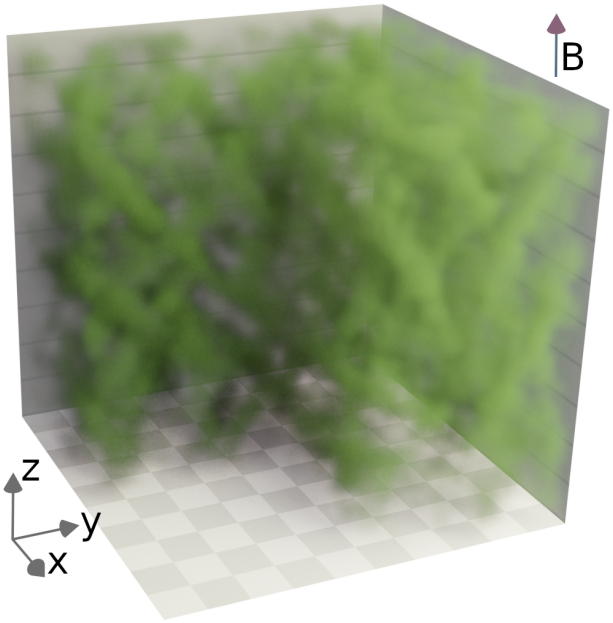

Fig. 5.15.: Three dimensional visualization of the density field of magnetic swimmer with $\alpha_{\text{ext}} = 5$ and $\alpha_{\text{int}} = 7.5$ short after the instability has occurred. A quarter of the volume has been cut out to allow a clearer sight into the volume.

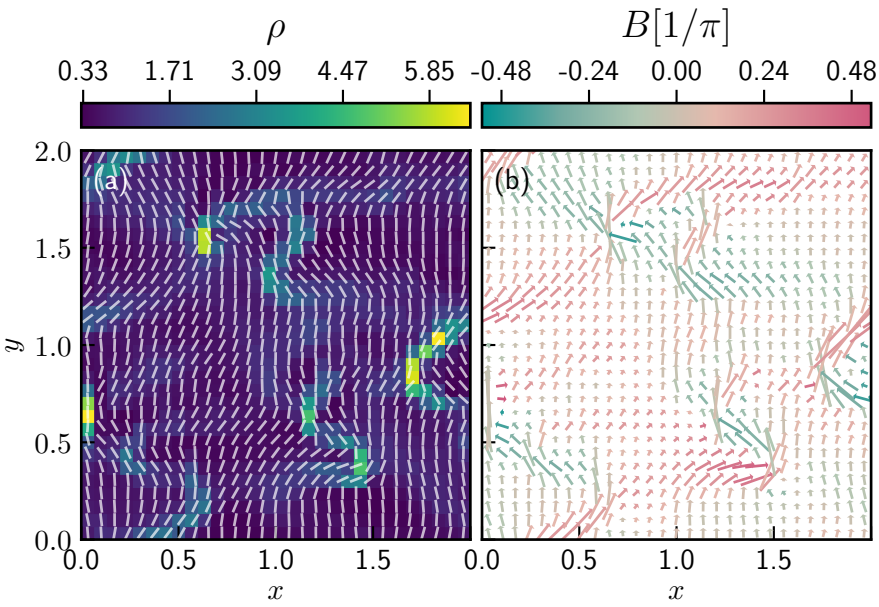

Fig. 5.16.: Exemplary snapshot from quasi 2D simulation ($\alpha_{\text{int}} = 8, \alpha_{\text{ext}} = 1$) after the instability had already occurred ($t = 9.8t_c$). It is the same simulation as in Figure 5.13 but at a later time. (b) Corresponding magnetic field $\mathbf{B}$ with an orientation dependent colouring to guide the eyes.

cluster to more sensible values. However, at high densities inter-particle correlations become more and more important, neglected in this model. Hence, the long-time predictive power and accuracy of the model and the simulation is severely limited and the results shown in Figure 5.16 should be scrutinized. Nonetheless, near the steady state the model remains useful and should give an accurate insight into the stability of the steady state and the short-term dynamics.

6 Conclusion & Outlook

6.1 Conclusion

In this work, mesoscopic kinetic theories of dilute active, magnetic particles with long-ranged interactions in an external field are presented. These models are based on a probabilistic description of a single particle distribution function and incorporate hydrodynamic and magnetic dipole-dipole interactions in a mean-field fashion. A combination of linear stability analysis and full numerical solutions of the non-linear equations is used to study the dynamics of the systems.

For colloids carrying only a weak magnetic dipole moment, the magnetic dipole-dipole interactions are negligible and the focus on hydrodynamic interactions and their interplay with an external field is justified. The competition between an external alignment torque and long-ranged anisotropic hydrodynamic interactions leads to distinct dynamical patterns for pusher and puller type microswimmers. For a moderate external field strength and activity, a suspension of pushers forms pronounced density bands perpendicular to and travelling into the external field's direction, whereas pullers display more erratic pillar like formations parallel to the external field. The observed band formation for pushers are strikingly similar to patterns observed in experiments on magnetotactic bacteria in an external field. Although the observed patterns are different for pullers and pushers, their underlying mechanisms are very similar. Based on the insights of a linear stability analysis, the origin of the pattern formation can be found in bend and splay distortions of the uniform polarization field for pushers and pullers, respectively. In both cases, instabilities cause a modulation of the polarization field. However, for pushers the polarization field is modulated in the direction parallel to the external field, whereas for pullers it is modulated in perpendicular direction. These hydrodynamic instabilities have drastic consequences for the transport velocity in the direction of the external field, especially for pullers. A splay deformation leads to an accumulation of pullers in lanes of a (self-generated) flow anti-parallel to the external field. Hence, the transport velocity is significantly reduced in comparison to the ideal case of the steady state.

In addition, the linear stability analysis provides information about the stability of a homogeneous steady state of the system. In excellent agreement with the

simulations, the linear stability analysis identifies an unstable region for moderate hydrodynamic interactions and external field strengths, where the dynamics of the system depart from the steady state and the previously described patterns emerge. On the other hand, for low interaction strengths or small external field strengths the system remains stable. Furthermore, for sufficiently high external field strengths the system is stable as well, leading to a re-entrant stability behaviour with respect to variation of the external field strength. In this regime, hydrodynamic interactions are not strong enough to overcome the alignment effect of the external field and the system remains stable.

Microswimmers that have a strong magnetic dipole moment interact with each other via non-negligible magnetic dipole-dipole interactions. As simulations show, in the absence of an external field, a transition to a spontaneous magnetization of the suspension occurs beyond a critical magnetic interaction strength, similar to passive magnetic systems (described, for example, by the Ising, XY or Heisenberg models). The swimmers align with the resulting magnetic field and, as a consequence, undergo a highly ordered clustering instability. A non-vanishing external field results in magnetization of the suspension in the field direction. In this case, the dynamics is similar to the previous case, although larger internal interaction strengths are required to render the system unstable. Again, a linear stability analysis successfully predicts quantitatively the occurrence of the instability and provides us with the qualitative understanding of the observed transient pattern formations.

The condensation into dense clusters is a consequence of attractive interaction forces between the swimmers and pushes the mean-field approach to its limits. For dense systems, inter-particle correlations become important that are neglected in a mean-field model. To mitigate the issue, an (effective) volume exclusion is introduced. To some extent, it prevents a singular density collapse in the simulations and instead results into moving dense clusters of particles that are highly polarized. However, to obtain reliable predictions of the long-time dynamics of dense systems, the model needs to be extended to include pair-correlations, which is left for future investigations.

To simulate the non-linear dynamics of these systems that are described by a Smoluchowski equation coupled to mean-interaction fields, a novel hybrid simulation method is developed in this work. The method is based on the equivalence of Langevin and Smoluchowski equations, and integrates a particle based Brownian Dynamics solver with a pseudo-spectral method applied to a continuous field description of the particle's interactions. Hence, the method places both description levels into a reciprocal relationship. A probability density function (PDF) is estimated from the particle distribution at a given time and is used to calculate long-ranged

mean-field interactions between the particles. These interactions in turn are required to evolve the particles in time, estimate the updated PDF, and thus closing the cycle. Using this method, 3D active systems with long-ranged, mean-field interactions can be simulated efficiently to study their dynamics.

6.2 Outlook

The present work still leaves room for improvement. In the following, suggestions for future directions to explore are given.

On the simulation side, Chapter 3 gives already several hints on how the current implementation of the numerical method can be improved. The accuracy of the method hinges on the quality of the single particle distribution estimation. The performance of the used kernel density estimation algorithm depends on the choice for the bandwidth of the kernel. However, an optimal choice is not straightforward. A possible approach could be to cross-verify a kernel choice with simulations of higher resolution. Another path to explore, are other interpolation techniques to obtain accurate values between grid points. For the highest possible accuracy, the field approximation from the spectral method can be used. In this approximation, a field is expanded into global basis functions. However, this approach is computationally very expensive. Instead, a local polynomial interpolation scheme of higher order than currently used in the present simulations could be applied. Furthermore, the current implementation itself leaves some room for performance improvement. First, one remaining bottleneck of the implementation is the density kernel estimation, which is the only part that is currently not parallelized. Atomic instructions offered by x86 CPUs (Central Processing Units) could lead to an efficient parallel implementation. Secondly, the code relies on auto-vectorization for SIMD (Single Instruct Multiple Data) and an explicit usage could improve the performance. Similarly, the simulation lends itself to be implemented on the GPU (Graphics Processing Unit) due to its mean-field character and independent particle integrator.

The presented simulation method, because of its stochastic nature, is potentially more efficient for high dimensional systems — at the expense of accuracy — compared to, for example, a spectral method to solve the partial differential equations. However, quantitative studies are necessary to evaluate this hypothesis. In addition, it would be very instructive to compare the presented method with the (more costly) Stokesian Dynamics simulations that include inter-particle correlations as well.

Additionally, the model itself can be extended. As suggested in the previous section, for dense active systems, inter-particle correlations cannot be neglected any more. A possible way to include pair-correlations in the present method is to treat the pair correlation function, potentially obtained from stokesian dynamics simulations, as an input to the model. Extending the kinetic theory to include the pair distribution function as well and finding a suitable closure for the three body distribution function, could be another path to explore.

Another challenge is posed by the long-ranged nature of the interactions. In simulation, the long range introduces finite-size effects (although, as demonstrated, the measured quantities in the present work become fairly independent of the simulation box size above a certain threshold). Finite size issues become less pronounced, when considering hydrodynamic screening effects — due to obstacles, other particles in denser systems, or noise — that effectively reduce the range of the hydrodynamic interactions. Reference [153] presents a screened Oseen-tensor that can be easily incorporated into the current model and leads to a finite characteristic wavelength in the linear stability analysis — as opposed to long-wavelength perturbations dominant the system in the present case. Furthermore, most experiments with microswimmers are not conducted in the bulk, but involve walls and other confined geometries that alter the flow field. Plane walls can be incorporated relatively easily into the simulations by using suitable Chebyshev polynomials in the affected dimension that automatically fulfil non-slip boundary conditions on the walls.

And last but not least, the combination of hydrodynamic and magnetic dipole-dipole interactions should be studied. There exists an intermediate regime, where both interactions can play a role. In a combined model, additional terms such as a hydrodynamic monopole contribution to the flow field due to the magnetic forces has to be considered. However, developing such a model, based on the foundation of the present work, should be rather straightforward and rewarding.

Appendix A

A.1 Transformation into non-dimensional form

Given a function $F\colon \mathbb{R} \to \mathbb{R}, T \mapsto F(T)$ and a transformation rule $\alpha(t) = t\,t_c = T$ the non-dimensional function is given by

$$f = F \circ \alpha,$$

with the function composition $(F \circ \alpha)(t) = F(\alpha(t))$. The time derivative of f in terms of the dimensionless variable t is given by

$$\begin{aligned} \partial_t f(t) &= \partial_t (F \circ \alpha)(t) \\ &= (\partial_T F)\,(\alpha(t))\;\partial_t \alpha(t) \\ &= \partial_T F(T)\, t_c \\ \Leftrightarrow \qquad \partial_T F(T) &= \frac{1}{t_c}\partial_t F(t\,t_c) = \frac{1}{t_c}\partial_t f(t). \end{aligned}$$

Analogue, for the spatial dimension with $\mathbf{h}(\mathbf{x}) = \mathbf{x}x_c = \mathbf{X}$, a function $G : \mathbb{R}^3 \to \mathbb{R}, \mathbf{X} \mapsto G(\mathbf{X})$, and its dimensionless counterpart $g = G \circ \mathbf{h}$,

$$\begin{aligned} \nabla_{\mathbf{x}} g(\mathbf{x}) &= \underbrace{\nabla_{\mathbf{x}} \mathbf{h}(\mathbf{x})}_{=x_c \mathbb{1}} \cdot (\nabla_{\mathbf{X}} G)\,(\mathbf{h}(\mathbf{x})) \\ &= x_c \nabla_{\mathbf{X}} G(\mathbf{X}) \\ \Leftrightarrow \qquad \nabla_{\mathbf{X}} G(\mathbf{X}) &= \nabla_{\mathbf{X}} G(\mathbf{x}x_c) = \nabla_{\mathbf{x}} g(\mathbf{x}). \end{aligned}$$

A spatial integral transforms as

$$\begin{aligned} \int_V \mathrm{d}\mathbf{X} G(\mathbf{X}) &= \int_V \mathrm{d}X_1 \mathrm{d}X_2 \mathrm{d}X_3\; G(\mathbf{X}) \\ &= x_c^3 \int_{V/x_c^3} \mathrm{d}x_1 \mathrm{d}x_2 \mathrm{d}x_3\; (G \circ \mathbf{h})(\mathbf{x}) \\ &= x_c^3 \int_{V/x_c^3} \mathrm{d}\mathbf{x}\; g(\mathbf{x}), \end{aligned}$$

with $\mathrm{d}X_i = x_c \mathrm{d}x_i$ and boundaries scaled accordingly.

A.2 Challenges in creating a stability diagram

In order to solve the eigenvalue problem in equation (4.13), the eigensystem of the truncated coefficient matrix $\mathbf{L}$ can be calculated numerically. The real part of the eigenvalue $\lambda_i(\mathbf{k})$ is the exponential growth rate of a plane wave perturbation with wave vector $\mathbf{k}$. If it is positive, its associated perturbation grows and renders the steady state unstable. If it is negative, the state is stable under linear perturbations. However, if it is zero, the linear stability analysis does not offer a deciding answer whether it is stable or not. In these cases, non-linear perturbations or full solutions to the Smoluchowski equation are required.

For the given system, it turns out there are two regimes: One where the eigenvalue is zero and one where its real part is positive. For the second regime, the steady state is clearly unstable, and it is called the *unstable* regime. In the first regime, the stability cannot be assessed from the linear stability analysis only, as it is a border case. However, numerical simulations confirm the stability of the steady state in this regime, and it is called the *stable* regime. Therefore, the submanifold of neutral stability $\mathcal{N}$ that divides the stable and unstable regime in the parameter space spanned by the parameters α_i is given by the closure of the volume of the parameter space where the largest eigenvalue, $\lambda_{\max} = \max_{\mathbf{k},} \lambda_i(\mathbf{k})$, is positive:

$$\mathcal{N} = \overline{\{(\alpha_i) | \lambda_{\max}(\alpha_i) > 0\}}.$$

In order to find the line of neutral stability $\mathcal{N}$ exactly, the value of the largest eigenvalue has to be known for every combination of σ_a and α_{ext}. Because an analytical expression for the largest eigenvalue is not available the eigenvalue problem has to be solved on a discrete grid $\subset \{\mathbf{k}\} \times \{(\sigma_a, \alpha_{\text{ext}})\}$ instead, consisting of the wave vector of the perturbation and the system's parameter of interest. A brute force approach on a regular four dimensional grid (two components of $\mathbf{k}$ and two parameters) is computationally expensive. Therefore, the computational budget has to be spent in a more directed manner.

Because $\mathcal{N}$ is only a 1d-manifold, a line, a lot of evaluation are wasted afar from the line. To concentrate the effort where it is needed, a self-adapting grid refinement algorithm was developed. Given a grid cell with values of $\lambda_{\max}(\sigma_a, \alpha_{\text{ext}})$ with different signs or at least a value of zero at its corners, $\mathcal{N}$ has to pass through the cell area because of continuity. Grid cells with this condition are subdivided and re-evaluated. The algorithm is given by

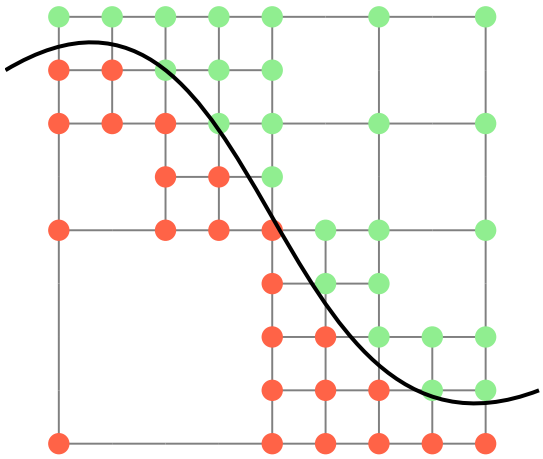

Fig. A.1.: Self-refining grid evaluation to find the 0-isoline of a function. A grid cell that has values of different signs at its grid points must contain a segment of the 0-isoline if the evaluated function is continuous. By continuously subdividing only these cells the estimate of the position of the isoline can be refined to arbitrary precision.

1. Start with a coarse grid of the area of interest that contains at least one grid point that evaluates to an eigenvalue which has a different sign than the others. Assign a negative sign to a value of zero.
2. Subdivide every grid cell with change of sign into four (in 2D) sub grid cells.
3. Stop if the subdivision depth is larger than a preset value.
4. Go back to step 2 and repeat.

and can be implemented recursively. An implementation in Mathematica/Wolfram Language is shown in the code listing A.1 and it is visualized in Figure A.1.

To restrict the evaluation space in $\mathbf{k} = k(\cos\Theta_B, 0, \sin\Theta_B)$, the type and structure of the instability has to be identified. Figures 4.8 and 4.7 suggest that the evaluation at a few points near and including $k = 0$ is sufficient, because all instabilities contain long wavelength contributions. Likewise, a small linear space in, $\Theta_B \in \{\frac{\pi}{2}\frac{i}{n} | n \in \mathbb{N}, n \geq i \in \mathbb{N}_0\}$ with for example $n = 5$, always contains at least one unstable mode, which is all what is needed for the presented scheme.

```
sameSign[cell_] := AllTrue[Map[# == 0 &, cell[[All, 2]]], TrueQ] ||
    (Abs@Total@Map[Sign, cell[[All, 2]]]) == 4

refine[depth_, f_, cell_] :=
If[depth == 0, cell,
    Module[{sub = Map[sameSign, cell]},
        FlattenAt[
            MapThread[
            If[#1,
                #2,
```

```
                refine[depth-1, f, subdivide[f, #2]]
            ]&,
            {sub, cell}],
            Position[sub, False]
        ]
    ]
]
```

Listing A.1: Simplified excerpt of the adaptive grid refinement algorithm implemented in the Wolfram Language. The function `f` is evaluated at the grid points. `subdivide` subdivides a given grid cell into four sub-cells if the corners contain a zero or have different signs.

A.3 Proof of identities

Throughout this section, the integral $\int_{\mathbb{S}^2} \mathrm{d}\mathbf{n}\ \mathbf{v}(\mathbf{n})$ is defined by the integral over the surface of the unit sphere $\mathbb{S}^2 = \{\mathbf{n} \in \mathbb{R}^3 | \|\mathbf{n}\| = 1\}$,

$$\int_{\mathbb{S}^2} \mathrm{d}\mathbf{n}\ \mathbf{v}(\mathbf{n}) = \int_{4\pi} \mathrm{d}\Omega\ \mathbf{v}(\mathbf{n}(\Omega)) = \int_0^{2\pi} \mathrm{d}\varphi \int_0^{\pi} \mathrm{d}\vartheta \sin\vartheta\ \mathbf{v}(\mathbf{n}(\vartheta, \varphi)),$$

with the solid angle differential $\mathrm{d}\Omega$.

The identities (4.24) and (4.25) both are consequences of Gauß' theorem on a surface of a sphere.

Corollary A.3.1. *Given a tangential vector field $\mathbf{v}\colon \mathbb{S}^2 \to \mathbb{R}^3$ on the surface of a sphere, i.e. $\mathbf{v}(\mathbf{x}) \in T_{\mathbf{x}}\mathbb{S}^2$, the following identity*

$$\int_{\mathbb{S}^2} \mathrm{d}\mathbf{n}\ \nabla^\circ_{\mathbf{n}} \cdot \mathbf{v}(\mathbf{n}) = 0.$$

is true.

Proof. In general for a tangent vector field $\mathbf{v}$ on a submanifold $\mathbb{A} \subset \mathbb{R}^3$ the divergence theorem

$$\int_{\mathbb{A}} \mathrm{d}\mathbf{n}\, \nabla^\circ_{\mathbf{n}} \cdot \mathbf{v}(\mathbf{n}) = \int_{\partial\mathbb{A}} \mathrm{d}s \cdot \mathbf{v},$$

holds, where $\mathrm{d}s$ is the vectorial measure normal to the boundary $\partial\mathbb{A}$ of the surface. If $\mathbb{A} = \mathbb{S}^2$, i.e. a closed manifold, then the boundary $\partial\mathbb{S}^2 = \varnothing$ is the empty set and the corollary follows directly. □

Remark. Gauß' theorem generalizes to tensor-fields as well. Given a tensor field $(\mathbf{T}) = T_{i_1,i_2,\ldots,i_n}$ of rank n,

$$\int_V \mathrm{d}V \partial_{x_{i_q}} T_{i_1,i_2,\ldots,i_q,\ldots,i_n} = \int_{\partial V} \mathrm{d}S\, a_{i_q} T_{i_1,i_2,\ldots,i_q,\ldots,i_n},$$

using Einstein summation and the surface normal vector $\mathbf{a}$.

Proposition A.3.1. *Equation 4.24 Given a scalar field $\psi\colon \mathbb{S}^2 \to \mathbb{R}, \mathbf{n} \mapsto \psi(\mathbf{n})$ on the unit sphere with $\int_{\mathbb{S}^2} \mathrm{d}\mathbf{n}\ \psi(\mathbf{n})\mathbf{n} = \mathbf{p}$,*

$$\int_{\mathbb{S}^2} \mathrm{d}\mathbf{n}\ \mathbf{n}\, \Delta^\circ_{\mathbf{n}}\, \psi(\mathbf{n}) = -2\mathbf{p}.$$

Proof. Using the identity

$$\begin{aligned} & \nabla^\circ_{\mathbf{n}} \cdot \left[(\nabla^\circ_{\mathbf{n}}\, \psi) \otimes \mathbf{n}\right] = \nabla^\circ_{\mathbf{n}}\, \psi \cdot \nabla^\circ_{\mathbf{n}}\, \mathbf{n} + \mathbf{n}\, \Delta^\circ_{\mathbf{n}}\, \psi \\ \Leftrightarrow \qquad & \mathbf{n}\, \Delta^\circ_{\mathbf{n}}\, \psi = \nabla^\circ_{\mathbf{n}} \cdot \left[(\nabla^\circ_{\mathbf{n}}\, \psi) \otimes \mathbf{n}\right] - \nabla^\circ_{\mathbf{n}}\, \psi \cdot \nabla^\circ_{\mathbf{n}}\, \mathbf{n} \\ & \qquad\qquad = \nabla^\circ_{\mathbf{n}} \cdot \left[(\nabla^\circ_{\mathbf{n}}\, \psi) \otimes \mathbf{n}\right] - \nabla^\circ_{\mathbf{n}} \cdot (\psi\, \nabla^\circ_{\mathbf{n}}\, \mathbf{n}) + \psi\, \Delta^\circ_{\mathbf{n}}\, \mathbf{n} \end{aligned}$$

the left side of equation 4.24 can be written as

$$\begin{aligned} \int_{\mathbb{S}^2} \mathrm{d}\mathbf{n}\ \mathbf{n}\, \Delta^\circ_{\mathbf{n}}\, \psi = & \underbrace{\int_{\mathbb{S}^2} \mathrm{d}\mathbf{n}\ \nabla^\circ_{\mathbf{n}} \cdot \left[(\nabla^\circ_{\mathbf{n}}\, \psi) \otimes \mathbf{n}\right]}_{=0} - \underbrace{\int_{\mathbb{S}^2} \mathrm{d}\mathbf{n}\ \nabla^\circ_{\mathbf{n}} \cdot (\psi\, \nabla^\circ_{\mathbf{n}}\, \mathbf{n})}_{=0} \\ & + \int_{\mathbb{S}^2} \mathrm{d}\mathbf{n}\ \psi\, \Delta^\circ_{\mathbf{n}}\, \mathbf{n}. \end{aligned}$$

The vanishing terms follow from the corollary A.3.1 and $\mathbf{n} \cdot (\nabla^\circ_{\mathbf{n}}\, \psi) \otimes \mathbf{n} = 0$ and $\mathbf{n} \cdot \nabla^\circ_{\mathbf{n}}\, \mathbf{n} = \mathbf{n} \cdot (\mathbb{1} - \mathbf{n}\mathbf{n}) = 0$, which follows from $\partial_\varphi \mathbf{n} = \sin\vartheta \check{\mathbf{e}}_\varphi$ and $\partial_\vartheta \mathbf{n} = \check{\mathbf{e}}_\vartheta$. With $\Delta^\circ_{\mathbf{n}}\, \mathbf{n} = -2\mathbf{n}$ equation 4.24 follows,

$$\int_{\mathbb{S}^2} \mathrm{d}\mathbf{n}\ \mathbf{n}\, \Delta^\circ_{\mathbf{n}}\, \psi = -2 \int_{\mathbb{S}^2} \mathrm{d}\mathbf{n}\ \psi\, \mathbf{n} = -2\mathbf{p}.$$

□

Proposition A.3.2. *Equation 4.25 Given a tangential vector field $\mathbf{v}\colon \mathbb{S}^2 \to \mathbb{R}^3, \mathbf{n} \mapsto \mathbf{v}(\mathbf{n})$ on the unit sphere,*

$$\int_{\mathbb{S}^2} \mathrm{d}\mathbf{n}\ \mathbf{n}\, \nabla^\circ_{\mathbf{n}} \cdot (\mathbf{v}(\mathbf{n})\psi(\mathbf{n})) = -\int_{\mathbb{S}^2} \mathrm{d}\mathbf{n}\ \ \mathbf{v}(\mathbf{n})\psi(\mathbf{n}).$$

Proof.

$$\begin{aligned}\int_{\mathbb{S}^2} \mathrm{d}\mathbf{n}\ \mathbf{n}\nabla_{\mathbf{n}}^{\circ}\cdot(\mathbf{v}\psi) &= \underbrace{\int_{\mathbb{S}^2} \mathrm{d}\mathbf{n}\ \nabla_{\mathbf{n}}^{\circ}\cdot\psi\mathbf{v}\mathbf{n}}_{=0(\Leftarrow\mathbf{n}\cdot\mathbf{v}=0)} - \int_{\mathbb{S}^2} \mathrm{d}\mathbf{n}\ \psi\mathbf{v}\cdot\nabla_{\mathbf{n}}^{\circ}\mathbf{n}\\ &= -\int_{\mathbb{S}^2} \mathrm{d}\mathbf{n}\ \psi\mathbf{v}\cdot(\mathbb{1}-\mathbf{n}\mathbf{n})\\ &= -\int_{\mathbb{S}^2} \mathrm{d}\mathbf{n}\ \psi\mathbf{v}\end{aligned}$$

□

Proposition A.3.3. *Equation 4.27 Given a tangential vector field* $\mathbf{v}\colon \mathbb{S}^2 \to \mathbb{R}^3, \mathbf{n}\mapsto \mathbf{v}(\mathbf{n})$ *on the unit sphere,*

$$\int_{\mathbb{S}^2} \mathrm{d}\mathbf{n}\ \mathbf{n}\mathbf{n}\nabla_{\mathbf{n}}^{\circ}\cdot\mathbf{v} = -\int_{\mathbb{S}^2} \mathrm{d}\mathbf{n}\,(\mathbf{n}\mathbf{v}+\mathbf{v}\mathbf{n}).$$

Proof.

$$\begin{aligned}\int_{\mathbb{S}^2} \mathrm{d}\mathbf{n}\ \mathbf{n}\mathbf{n}\nabla_{\mathbf{n}}^{\circ}\cdot\mathbf{v} &= \underbrace{\int_{\mathbb{S}^2} \mathrm{d}\mathbf{n}\ \nabla_{\mathbf{n}}^{\circ}\cdot(\mathbf{v}\mathbf{n}\mathbf{n})}_{=0} - \int_{\mathbb{S}^2} \mathrm{d}\mathbf{n}\ \mathbf{n}\mathbf{v}\cdot\nabla_{\mathbf{n}}^{\circ}\mathbf{n} - \int_{\mathbb{S}^2} \mathrm{d}\mathbf{n}\ \mathbf{v}\cdot(\nabla_{\mathbf{n}}^{\circ}\mathbf{n})\mathbf{n}\\ &= -\int_{\mathbb{S}^2} \mathrm{d}\mathbf{n}\ \mathbf{n}\mathbf{v}\cdot(\mathbb{1}-\mathbf{n}\mathbf{n}) - \int_{\mathbb{S}^2} \mathrm{d}\mathbf{n}\ \mathbf{v}\cdot(\mathbb{1}-\mathbf{n}\mathbf{n})\mathbf{n}\\ &= -\int_{\mathbb{S}^2} \mathrm{d}\mathbf{n}\,(\mathbf{n}\mathbf{v}+\mathbf{v}\mathbf{n}),\end{aligned}$$

using the product rule in the first line and $\mathbf{v}\cdot\nabla_{\mathbf{n}}^{\circ}\mathbf{n} = \mathbf{v}\cdot(\mathbb{1}-\mathbf{n}\mathbf{n}) = (\mathbb{1}-\mathbf{n}\mathbf{n})\cdot\mathbf{v} = \mathbf{v}$ for a tangential vector $\mathbf{v}$. □

Proposition A.3.4. *Equation 4.28 Given a scalar field* $\psi\colon \mathbb{S}^2 \to \mathbb{R}, \mathbf{n}\mapsto \psi(\mathbf{n})$ *on the unit sphere,*

$$\begin{aligned}\int_{\mathbb{S}^2} \mathrm{d}\mathbf{n}\ \mathbf{n}\mathbf{n}\Delta_{\mathbf{n}}^{\circ}\psi &= -2\int_{\mathbb{S}^2} \mathrm{d}\mathbf{n}\ \psi\mathbf{n}\Delta_{\mathbf{n}}^{\circ}\mathbf{n} + 2\int_{\mathbb{S}^2} \mathrm{d}\mathbf{n}\ \psi\nabla_{\mathbf{n}}^{\circ}\mathbf{n}\\ &= -6\mathbf{Q}.\end{aligned}$$

Proof.

$$\begin{aligned}\int_{\mathbb{S}^2} \mathrm{d}\mathbf{n}\ \mathbf{n}\mathbf{n}\,\Delta^\circ_{\mathbf{n}}\,\psi = &\underbrace{\int_{\mathbb{S}^2} \mathrm{d}\mathbf{n}\ \nabla^\circ_{\mathbf{n}}\cdot[(\nabla^\circ_{\mathbf{n}}\,\psi)\mathbf{n}\mathbf{n}]}_{=0\Leftarrow\mathbf{n}\cdot\nabla^\circ_{\mathbf{n}}\,\psi=0} - \int_{\mathbb{S}^2} \mathrm{d}\mathbf{n}\ \mathbf{n}(\nabla^\circ_{\mathbf{n}}\,\psi)\cdot\nabla^\circ_{\mathbf{n}}\,\mathbf{n}\\ &- \int_{\mathbb{S}^2} \mathrm{d}\mathbf{n}\,(\nabla^\circ_{\mathbf{n}}\,\psi)\cdot(\nabla^\circ_{\mathbf{n}}\,\mathbf{n})\mathbf{n}\\ = &-\int_{\mathbb{S}^2} \mathrm{d}\mathbf{n}\ \mathbf{n}(\nabla^\circ_{\mathbf{n}}\,\psi)\cdot\nabla^\circ_{\mathbf{n}}\,\mathbf{n} - \left[\int_{\mathbb{S}^2} \mathrm{d}\mathbf{n}\ \mathbf{n}(\nabla^\circ_{\mathbf{n}}\,\psi)\cdot\nabla^\circ_{\mathbf{n}}\,\mathbf{n}\right]^\top\end{aligned}$$

Furthermore,

$$-\int_{\mathbb{S}^2} \mathrm{d}\mathbf{n}\ \mathbf{n}(\nabla^\circ_{\mathbf{n}}\,\psi)\cdot\nabla^\circ_{\mathbf{n}}\,\mathbf{n} = -\int_{\mathbb{S}^2} \mathrm{d}\mathbf{n}\ \mathbf{n}[\nabla^\circ_{\mathbf{n}}\cdot(\psi\,\nabla^\circ_{\mathbf{n}}\,\mathbf{n}) - \psi\,\Delta^\circ_{\mathbf{n}}\,\mathbf{n}].$$

By using,

$$\begin{aligned}(\nabla^\circ_{\mathbf{n}}\cdot[\psi(\nabla^\circ_{\mathbf{n}}\,\mathbf{n})\mathbf{n}])^\top &= \mathbf{n}\,\nabla^\circ_{\mathbf{n}}\cdot(\psi\,\nabla^\circ_{\mathbf{n}}\,\mathbf{n}) + [\psi(\nabla^\circ_{\mathbf{n}}\,\mathbf{n})^\top\cdot\nabla^\circ_{\mathbf{n}}\,\mathbf{n}]^\top\\ &= \mathbf{n}\,\nabla^\circ_{\mathbf{n}}\cdot(\psi\,\nabla^\circ_{\mathbf{n}}\,\mathbf{n}) + \psi\,\nabla^\circ_{\mathbf{n}}\,\mathbf{n},\end{aligned}$$

it follows

$$\begin{aligned}-\int_{\mathbb{S}^2} \mathrm{d}\mathbf{n}\ \mathbf{n}(\nabla^\circ_{\mathbf{n}}\,\psi)\cdot\nabla^\circ_{\mathbf{n}}\,\mathbf{n} = &\int_{\mathbb{S}^2} \mathrm{d}\mathbf{n}\ \mathbf{n}\psi\,\underbrace{\Delta^\circ_{\mathbf{n}}\,\mathbf{n}}_{-2\mathbf{n}} - \int_{\mathbb{S}^2} \mathrm{d}\mathbf{n}\ \underbrace{[\nabla^\circ_{\mathbf{n}}\cdot[\psi(\nabla^\circ_{\mathbf{n}}\,\mathbf{n})\mathbf{n}]]^\top}_{=0\Leftarrow\mathbf{n}\cdot\nabla^\circ_{\mathbf{n}}\,\mathbf{n}=0}\\ &+\int_{\mathbb{S}^2} \mathrm{d}\mathbf{n}\ \psi\,\nabla^\circ_{\mathbf{n}}\,\mathbf{n}\\ = &-2\int_{\mathbb{S}^2} \mathrm{d}\mathbf{n}\ \psi\mathbf{n}\mathbf{n} + \int_{\mathbb{S}^2} \mathrm{d}\mathbf{n}\ \psi\,\nabla^\circ_{\mathbf{n}}\,\mathbf{n}.\end{aligned}$$

Together, the initial equation transforms to

$$\begin{aligned}\int_{\mathbb{S}^2} \mathrm{d}\mathbf{n}\ \mathbf{n}\mathbf{n}\,\Delta^\circ_{\mathbf{n}}\,\psi &= -2\int_{\mathbb{S}^2} \mathrm{d}\mathbf{n}\ \psi\mathbf{n}\mathbf{n} + \int_{\mathbb{S}^2} \mathrm{d}\mathbf{n}\ \psi\,\nabla^\circ_{\mathbf{n}}\,\mathbf{n} + [\ldots]^\top\\ &= -4\int_{\mathbb{S}^2} \mathrm{d}\mathbf{n}\ \psi\mathbf{n}\mathbf{n} + 2\int_{\mathbb{S}^2} \mathrm{d}\mathbf{n}\ \psi\,\nabla^\circ_{\mathbf{n}}\,\mathbf{n}\\ &= -4\int_{\mathbb{S}^2} \mathrm{d}\mathbf{n}\ \psi\mathbf{n}\mathbf{n} + 2\int_{\mathbb{S}^2} \mathrm{d}\mathbf{n}\ \psi(\mathbb{1}-\mathbf{n}\mathbf{n})\\ &= \int_{\mathbb{S}^2} \mathrm{d}\mathbf{n}\ \psi(-4\mathbf{n}\mathbf{n} + 2\mathbb{1} - 2\mathbf{n}\mathbf{n})\\ &= -6\int_{\mathbb{S}^2} \mathrm{d}\mathbf{n}\ \psi\mathbf{n}\mathbf{n} + 2\int_{\mathbb{S}^2} \mathrm{d}\mathbf{n}\ \psi\mathbb{1}\\ &= -6\mathbf{Q} - 2\int_{\mathbb{S}^2} \mathrm{d}\mathbf{n}\ \psi\mathbb{1} + 2\int_{\mathbb{S}^2} \mathrm{d}\mathbf{n}\ \psi\mathbb{1}\\ &= -6\mathbf{Q}\end{aligned}$$

□

Corollary A.3.2. *Given a vector field* $\mathbf{v}\colon \mathbb{S}^2 \to \mathbb{R}^3, \mathbf{n} \mapsto \mathbf{v}(\mathbf{n})$*, the director* $\mathbf{n} \in \mathbb{S}^2 \subset \mathbb{R}^3$ *with* $\|\mathbf{n}\| = 1$*, and the surface gradient* $\nabla_{\mathbf{n}}^\circ = (\mathbb{1} - \mathbf{nn}) \cdot \nabla_{\mathbf{n}} = (\mathbb{1} - \mathbf{nn}) \cdot \nabla_{\mathbf{n}}$*, where* $\nabla_{\mathbf{n}}$ *is the gradient operator with respect to* $\mathbf{n}$*, then*

$$\nabla_{\mathbf{n}}^\circ \cdot \big((\mathbb{1} - \mathbf{nn}) \cdot \mathbf{v}(\mathbf{n})\big) = \nabla_{\mathbf{n}}^\circ \cdot \mathbf{v}(\mathbf{n}) - 2\mathbf{n} \cdot \mathbf{v}(\mathbf{n}).$$

Proof.

$$\begin{aligned}
\nabla_{\mathbf{n}}^\circ \cdot \big((\mathbb{1} - \mathbf{nn}) \cdot \mathbf{v}\big) =& [(\mathbb{1} - \mathbf{nn}) \cdot \nabla_{\mathbf{n}}] \cdot [(\mathbb{1} - \mathbf{nn}) \cdot \mathbf{v}] \\
=& \nabla_{\mathbf{n}} \cdot ((\mathbb{1} - \mathbf{nn}) \cdot \mathbf{v}) + (\mathbf{nn} \cdot \nabla_{\mathbf{n}}) \cdot ((\mathbb{1} - \mathbf{nn}) \cdot \mathbf{v}) \\
=& \underbrace{(\mathbb{1} - \mathbf{nn}) \cdot \nabla_{\mathbf{n}}}_{=\nabla_{\mathbf{n}}^\circ} \mathbf{v} + \mathbf{v} \cdot \underbrace{(\nabla_{\mathbf{n}} \cdot (\mathbb{1} - \mathbf{nn}))}_{=4\mathbf{n}} \\
& - \underbrace{(\mathbf{n} \cdot (\mathbb{1} - \mathbf{nn}))}_{=0} \cdot (\mathbf{n} \cdot \nabla_{\mathbf{n}})\mathbf{v} - \mathbf{nv} : \underbrace{(\mathbf{n} \cdot \nabla_{\mathbf{n}})(\mathbb{1} - \mathbf{nn})}_{=2\mathbf{nn}} \\
=& \nabla_{\mathbf{n}}^\circ \cdot \mathbf{v} + 4\mathbf{v} \cdot \mathbf{n} - 2\underbrace{\mathbf{n} \cdot \mathbf{n}}_{=1} \mathbf{v} \cdot \mathbf{n} \\
=& \nabla_{\mathbf{n}}^\circ \cdot \mathbf{v} - 2\mathbf{v} \cdot \mathbf{n}
\end{aligned}$$

□

Bibliography

[1] Jesse L Silverberg, Matthew Bierbaum, James P Sethna, and Itai Cohen. "Collective motion of humans in mosh and circle pits at heavy metal concerts". In: *Physical review letters* 110.22 (2013), p. 228701 (cit. on p. 3).

[2] Craig W. Reynolds. "Flocks, Herds and Schools: A Distributed Behavioral Model". In: *SIGGRAPH Comput. Graph.* 21.4 (Aug. 1987), pp. 25–34 (cit. on p. 3).

[3] Tamás Vicsek, András Czirók, Eshel Ben-Jacob, Inon Cohen, and Ofer Shochet. "Novel Type of Phase Transition in a System of Self-Driven Particles". In: *Phys. Rev. Lett.* 75 (6 Aug. 1995), pp. 1226–1229 (cit. on p. 3).

[4] Alberto Colorni, Marco Dorigo, Vittorio Maniezzo, et al. "Distributed optimization by ant colonies". In: *Proceedings of the first European conference on artificial life*. Vol. 142. Cambridge, MA. 1992, pp. 134–142 (cit. on p. 3).

[5] Nurhan Cetin, Adrian Burri, and Kai Nagel. "A large-scale agent-based traffic microsimulation based on queue model". In: *IN PROCEEDINGS OF SWISS TRANSPORT RESEARCH CONFERENCE (STRC), MONTE VERITA, CH*. 2003, pp. 3–4272 (cit. on p. 3).

[6] Marco Dorigo and Luca Maria Gambardella. "Ant colonies for the travelling salesman problem". In: *Biosystems* 43.2 (1997), pp. 73–81 (cit. on p. 3).

[7] Sriram Ramaswamy. "The Mechanics and Statistics of Active Matter". In: *Annual Review of Condensed Matter Physics* 1.1 (Aug. 10, 2010), pp. 323–345 (cit. on p. 3).

[8] M. C. Marchetti, J. F. Joanny, S. Ramaswamy, et al. "Hydrodynamics of soft active matter". In: *Reviews of Modern Physics* 85.3 (July 19, 2013), pp. 1143–1189 (cit. on pp. 3, 6, 7).

[9] J Elgeti, R G Winkler, and G Gompper. "Physics of microswimmers—single particle motion and collective behavior: a review". In: *Reports on Progress in Physics* 78.5 (May 1, 2015), p. 056601 (cit. on pp. 3, 8, 17, 42).

[10] Andreas Zöttl and Holger Stark. "Emergent behavior in active colloids". In: *Journal of Physics: Condensed Matter* 28.25 (2016), p. 253001 (cit. on p. 3).

[11] Luis H. Cisneros, John O. Kessler, Sujoy Ganguly, and Raymond E. Goldstein. "Dynamics of swimming bacteria: Transition to directional order at high concentration". In: *Physical Review E* 83.6 (June 14, 2011), p. 061907 (cit. on p. 3).

[12] Thomas Speck. "Collective behavior of active Brownian particles: From microscopic clustering to macroscopic phase separation". In: *The European Physical Journal Special Topics* 225.11 (Nov. 1, 2016), pp. 2287–2299 (cit. on p. 3).

[13] Jonathan Tammo Siebert, Janina Letz, Thomas Speck, and Peter Virnau. “Phase behavior of active Brownian disks, spheres, and dimers”. In: *Soft Matter* 13.5 (2017), pp. 1020–1026 (cit. on pp. 3, 6).

[14] Clemens Bechinger, Roberto Di Leonardo, Hartmut Löwen, et al. “Active particles in complex and crowded environments”. In: *Reviews of Modern Physics* 88.4 (Nov. 23, 2016), p. 045006 (cit. on pp. 3, 8, 17, 43, 86).

[15] R. Wulfert, M. Oechsle, T. Speck, and U. Seifert. “Driven Brownian particle as a paradigm for a nonequilibrium heat bath: Effective temperature and cyclic work extraction”. In: *Phys. Rev. E* 95 (5 May 2017), p. 050103 (cit. on p. 3).

[16] Julius Adler. “Chemotaxis in Bacteria”. In: *Science* 153.3737 (Aug. 12, 1966), pp. 708–716 (cit. on p. 3).

[17] I. Theurkauff, C. Cottin-Bizonne, J. Palacci, C. Ybert, and L. Bocquet. “Dynamic Clustering in Active Colloidal Suspensions with Chemical Signaling”. In: *Physical Review Letters* 108.26 (June 26, 2012), p. 268303 (cit. on p. 3).

[18] J Gachelin, A Rousselet, A Lindner, and E Clement. “Collective motion in an active suspension of Escherichia coli bacteria”. In: *New Journal of Physics* 16.2 (2014), p. 025003 (cit. on p. 3).

[19] R. A. Simha and Sriram Ramaswamy. “Hydrodynamic Fluctuations and Instabilities in Ordered Suspensions of Self-Propelled Particles”. In: *Physical Review Letters* 89.5 (July 15, 2002), p. 058101 (cit. on p. 3).

[20] David Saintillan and Michael J. Shelley. “Instabilities, pattern formation, and mixing in active suspensions”. In: *Physics of Fluids* 20.12 (2008), p. 123304 (cit. on pp. 3, 6).

[21] Barath Ezhilan, Michael J. Shelley, and David Saintillan. “Instabilities and nonlinear dynamics of concentrated activesuspensions”. In: *Physics of Fluids (1994-present)* 25.7 (July 1, 2013), p. 070607 (cit. on pp. 3, 49).

[22] Alfred M. Spormann. “Unusual swimming behavior of a magnetotactic bacterium”. In: *FEMS Microbiology Letters* 45.1 (Feb. 1, 1987), pp. 37–45 (cit. on pp. 3, 85, 115).

[23] D. C. Guell, H. Brenner, R. B. Frankel, and H. Hartman. “Hydrodynamic forces and band formation in swimming magnetotactic bacteria”. In: *Journal of Theoretical Biology* 135.4 (Dec. 21, 1988), pp. 525–542 (cit. on pp. 3–5, 85).

[24] Nicolas Waisbord, Christopher T. Lefèvre, Lydéric Bocquet, Christophe Ybert, and Cécile Cottin-Bizonne. “Destabilization of a flow focused suspension of magnetotactic bacteria”. In: *Physical Review Fluids* 1.5 (Sept. 21, 2016), p. 053203 (cit. on pp. 3, 85, 86).

[25] Peter J. Vach, Debora Walker, Peer Fischer, Peter Fratzl, and Damien Faivre. “Pattern formation and collective effects in populations of magnetic microswimmers”. In: *Journal of Physics D-Applied Physics* 50.11 (2017) (cit. on p. 3).

[26] R. Alonso-Matilla and D. Saintillan. “Microfluidic flow actuation using magnetoactive suspensions”. In: *EPL (Europhysics Letters)* 121.2 (2018), p. 24002 (cit. on p. 3).

[27] Xabel Garcia, Salima Rafaı, and Philippe Peyla. “Light Control of the Flow of Phototactic Microswimmer Suspensions”. In: *Phys. Rev. Lett.* 110 (13 Mar. 2013), p. 138106 (cit. on p. 3).

[28] Matthieu Martin, Alexandre Barzyk, Eric Bertin, Philippe Peyla, and Salima Rafai. “Photofocusing: Light and flow of phototactic microswimmer suspension”. In: *Physical Review E* 93.5 (May 16, 2016), p. 051101 (cit. on p. 3).

[29] Christopher T Lefevre, Mathieu Bennet, Livnat Landau, et al. “Diversity of magneto-aerotactic behaviors and oxygen sensing mechanisms in cultured magnetotactic bacteria”. In: *Biophysical journal* 107.2 (2014), pp. 527–538 (cit. on p. 3).

[30] John O. Kessler. “Individual and collective fluid dynamics of swimming cells”. In: *Journal of Fluid Mechanics* 173 (1986), pp. 191–205 (cit. on p. 3).

[31] Borge ten Hagen, Felix Kümmel, Raphael Wittkowski, et al. “Gravitaxis of asymmetric self-propelled colloidal particles”. In: *Nature Communications* 5 (Sept. 19, 2014), p. 4829 (cit. on p. 3).

[32] Ottavio A. Croze, Rachel N. Bearon, and Martin A. Bees. “Gyrotactic swimmer dispersion in pipe flow: testing the theory”. In: *Journal of Fluid Mechanics* 816 (2017), pp. 481–506 (cit. on p. 3).

[33] Katrin Wolff, Aljoscha M. Hahn, and Holger Stark. “Sedimentation and polar order of active bottom-heavy particles”. In: *The European Physical Journal E* 36.4 (2013), p. 43 (cit. on p. 3).

[34] Holger Stark. “Swimming in external fields”. In: *The European Physical Journal Special Topics* 225.11 (2016), pp. 2369–2387 (cit. on p. 3).

[35] S. Ramaswamy, R. Aditi Simha, and J. Toner. “Active nematics on a substrate: Giant number fluctuations and long-time tails”. In: *EPL (Europhysics Letters)* 62.2 (Apr. 2003), p. 196 (cit. on p. 4).

[36] Knut Drescher, Jörn Dunkel, Luis H. Cisneros, Sujoy Ganguly, and Raymond E. Goldstein. “Fluid dynamics and noise in bacterial cell–cell and cell–surface scattering”. In: *Proceedings of the National Academy of Sciences* 108.27 (July 5, 2011), pp. 10940–10945 (cit. on p. 4).

[37] Tanniemola B. Liverpool. “Anomalous fluctuations of active polar filaments”. In: *Physical Review E* 67.3 (Mar. 18, 2003), p. 031909 (cit. on p. 4).

[38] Marco Leoni and Tanniemola B. Liverpool. “Swimmers in Thin Films: From Swarming to Hydrodynamic Instabilities”. In: *Physical Review Letters* 105.23 (Dec. 2, 2010) (cit. on p. 4).

[39] Volker Schaller, Christoph Weber, Erwin Frey, and Andreas R. Bausch. “Polar pattern formation: hydrodynamic coupling of driven filaments”. In: *Soft Matter* 7.7 (2011), pp. 3213–3218 (cit. on p. 4).

[40] Fanlong Meng, Daiki Matsunaga, and Ramin Golestanian. “Clustering of Magnetic Swimmers in a Poiseuille Flow”. In: *Physical Review Letters* 120.18 (May 4, 2018), p. 188101 (cit. on p. 5).

[41] Joakim Stenhammar, Davide Marenduzzo, Rosalind J Allen, and Michael E Cates. "Phase behaviour of active Brownian particles: the role of dimensionality". In: *Soft Matter* 10.10 (2014), pp. 1489–1499 (cit. on p. 5).

[42] Ivo Buttinoni, Julian Bialké, Felix Kümmel, et al. "Dynamical clustering and phase separation in suspensions of self-propelled colloidal particles". In: *Physical review letters* 110.23 (2013), p. 238301 (cit. on p. 5).

[43] Julian Bialké, Hartmut Löwen, and Thomas Speck. "Microscopic theory for the phase separation of self-propelled repulsive disks". In: *EPL (Europhysics Letters)* 103.3 (Aug. 2013), p. 30008 (cit. on pp. 5, 30, 31).

[44] Sylvain Martel, Mahmood Mohammadi, Ouajdi Felfoul, Zhao Lu, and Pierre Pouponneau. "Flagellated Magnetotactic Bacteria as Controlled MRI-trackable Propulsion and Steering Systems for Medical Nanorobots Operating in the Human Microvasculature". In: *The International Journal of Robotics Research* 28.4 (Apr. 1, 2009), pp. 571–582 (cit. on p. 5).

[45] Daniel Houle, Danuta Radzioch, Dominic de Lanauze, et al. "Magneto-aerotactic bacteria deliver drug-containing nanoliposomes to tumour hypoxic regions". In: *Nature Nanotechnology* 11.11 (Nov. 2016), p. 941 (cit. on p. 5).

[46] Famin Qiu, Satoshi Fujita, Rami Mhanna, et al. "Magnetic Helical Microswimmers Functionalized with Lipoplexes for Targeted Gene Delivery". In: *Advanced Functional Materials* 25.11 (2015), pp. 1666–1671 (cit. on p. 5).

[47] N. Beyrand, L. Couraud, A. Barbot, D. Decanini, and G. Hwang. "Multi-flagella helical microswimmers for multiscale cargo transport and reversible targeted binding". In: *2015 IEEE/RSJ International Conference on Intelligent Robots and Systems (IROS)*. 2015, pp. 1403–1408 (cit. on p. 5).

[48] John L Anderson and Dennis C Prieve. "Diffusiophoresis: migration of colloidal particles in gradients of solute concentration". In: *Separation and Purification Methods* 13.1 (1984), pp. 67–103 (cit. on pp. 5, 8).

[49] Thomas Speck. "Thermodynamic approach to the self-diffusiophoresis of colloidal Janus particles". In: *Physical Review E* 99.6 (June 13, 2019) (cit. on pp. 5, 8, 43).

[50] Tamás Vicsek, András Czirók, Eshel Ben-Jacob, Inon Cohen, and Ofer Shochet. "Novel Type of Phase Transition in a System of Self-Driven Particles". In: *Phys. Rev. Lett.* 75 (6 Aug. 1995), pp. 1226–1229 (cit. on pp. 5, 6).

[51] J. Tailleur and M. E. Cates. "Statistical Mechanics of Interacting Run-and-Tumble Bacteria". In: *Physical Review Letters* 100.21 (May 29, 2008), p. 218103 (cit. on pp. 5, 6).

[52] M. E. Cates and J. Tailleur. "When are active Brownian particles and run-and-tumble particles equivalent? Consequences for motility-induced phase separation". In: *EPL (Europhysics Letters)* 101.2 (Jan. 2013), p. 20010 (cit. on p. 6).

[53] Lutz Schimansky-Geier, Michaela Mieth, Helge Rosé, and Horst Malchow. "Structure formation by active Brownian particles". In: *Physics Letters A* 207.3 (Oct. 30, 1995), pp. 140–146 (cit. on p. 6).

[54] Gabriel S. Redner, Michael F. Hagan, and Aparna Baskaran. “Structure and Dynamics of a Phase-Separating Active Colloidal Fluid”. In: *Physical Review Letters* 110.5 (Jan. 31, 2013), p. 055701 (cit. on p. 6).

[55] Adam Wysocki, Roland G. Winkler, and Gerhard Gompper. “Cooperative motion of active Brownian spheres in three-dimensional dense suspensions”. In: *EPL (Europhysics Letters)* 105.4 (Feb. 2014), p. 48004 (cit. on p. 6).

[56] Alexandre P. Solon, Joakim Stenhammar, Raphael Wittkowski, et al. “Pressure and Phase Equilibria in Interacting Active Brownian Spheres”. In: *Physical Review Letters* 114.19 (May 11, 2015), p. 198301 (cit. on p. 6).

[57] Paul C Martin, O Parodi, and Peter S Pershan. “Unified hydrodynamic theory for crystals, liquid crystals, and normal fluids”. In: *Physical Review A* 6.6 (1972), p. 2401 (cit. on p. 6).

[58] I. E. Dzyaloshinskii and G. E. Volovick. “Poisson brackets in condensed matter physics”. In: *Annals of Physics* 125.1 (Mar. 1, 1980), pp. 67–97 (cit. on p. 6).

[59] Scott T. Milner. “Dynamical theory of concentration fluctuations in polymer solutions under shear”. In: *Physical Review E* 48.5 (Nov. 1, 1993), pp. 3674–3691 (cit. on p. 6).

[60] E. M. Purcell. “Life at low Reynolds number”. In: *American Journal of Physics* 45.1 (Jan. 1, 1977), pp. 3–11 (cit. on p. 8).

[61] Stefano Marras, Takuji Noda, John F. Steffensen, et al. “Not So Fast: Swimming Behavior of Sailfish during Predator–Prey Interactions using High-Speed Video and Accelerometry”. In: *Integrative and Comparative Biology* 55.4 (2015), pp. 719–727 (cit. on p. 8).

[62] Eric Lauga and Thomas R Powers. “The hydrodynamics of swimming microorganisms”. In: *Reports on Progress in Physics* 72.9 (Sept. 1, 2009), p. 096601 (cit. on pp. 11, 43, 45, 49).

[63] E. J. Hinch. “Application of the Langevin equation to fluid suspensions”. In: *Journal of Fluid Mechanics* 72.3 (Dec. 1975), pp. 499–511 (cit. on p. 13).

[64] W.B. Russel, W.B. Russel, D.A. Saville, and W.R. Schowalter. *Colloidal Dispersions*. Cambridge Monographs on Mechanics. Cambridge University Press, 1991 (cit. on p. 13).

[65] Laura Johanna Lukassen. “A colored-noise Fokker-Planck equation for non-Brownian particles in shear-induced diffusion”. PhD thesis. Darmstadt: Technische Universität, 2015 (cit. on p. 13).

[66] R. Kubo. “The fluctuation-dissipation theorem”. In: *Reports on Progress in Physics* 29.1 (Jan. 1966), pp. 255–284 (cit. on p. 14).

[67] H. Risken and T. Frank. *The Fokker-Planck Equation: Methods of Solution and Applications*. Springer Series in Synergetics. Springer Berlin Heidelberg, 1996 (cit. on pp. 14, 20, 21).

[68]W. Coffey, Y.P. Kalmykov, and J.T. Waldron. *The langevin equation: with applications in physics, chemistry and electrical engineering*. Series in contemporary chemical physics. World Scientific, 1996 (cit. on pp. 14, 19–21).

[69]H.C. Berg. *Random Walks in Biology: New and Expanded Edition*. Princeton University Press, 2018 (cit. on pp. 15, 17).

[70]J.K.G. Dhont. *An Introduction to Dynamics of Colloids*. Studies in Interface Science. Elsevier Science, 1996 (cit. on pp. 15, 19, 42, 52, 53).

[71]Jonathan R. Howse, Richard A. L. Jones, Anthony J. Ryan, et al. "Self-Motile Colloidal Particles: From Directed Propulsion to Random Walk". In: *Physical Review Letters* 99.4 (July 27, 2007), p. 048102 (cit. on p. 17).

[72]Hong-Ren Jiang, Natsuhiko Yoshinaga, and Masaki Sano. "Active Motion of a Janus Particle by Self-Thermophoresis in a Defocused Laser Beam". In: *Physical Review Letters* 105.26 (Dec. 20, 2010), p. 268302 (cit. on p. 17).

[73]Howard C Berg and Douglas A Brown. "Chemotaxis in Escherichia coli analysed by three-dimensional tracking". In: *Nature* 239.5374 (1972), pp. 500–504 (cit. on p. 18).

[74]B ten Hagen, S van Teeffelen, and H Löwen. "Brownian motion of a self-propelled particle". In: *Journal of Physics: Condensed Matter* 23.19 (May 18, 2011), p. 194119 (cit. on p. 18).

[75]Tobias Bäuerle, Andreas Fischer, Thomas Speck, and Clemens Bechinger. "Self-organization of active particles by quorum sensing rules". In: *Nature Communications* 9.1 (Dec. 2018) (cit. on p. 18).

[76]Edward Nelson. *Dynamical theories of Brownian motion*. Vol. 3. Princeton university press, 1967 (cit. on p. 19).

[77]Subrahmanyan Chandrasekhar. "Stochastic problems in physics and astronomy". In: *Reviews of modern physics* 15.1 (1943), p. 1 (cit. on p. 19).

[78]Joseph Leo Doob. *Stochastic processes*. Vol. 101. New York Wiley, 1953 (cit. on p. 19).

[79]Uwe Hassler. "Stochastische integration und zeitreihenmodellierung : eine einführung mit anwendungen aus finanzierung und ökonometrie". In: Statistik und ihre anwendungen (2007) (cit. on p. 20).

[80]K. Sobczyk. *Stochastic differential equations: with applications to physics and engineering*. Mathematics and its applications. Springer Netherlands, 2001 (cit. on p. 20).

[81]Edwin T Jaynes. "Prior probabilities." In: *IEEE Trans. Systems Science and Cybernetics* 4.3 (1968), pp. 227–241 (cit. on p. 21).

[82]ET Jaynes. "Statistical physics". In: *Brandeis Lectures* 316 (1963) (cit. on p. 21).

[83]Alexander Julian Marcel Bialké. "Phase separation of active fluids". PhD thesis. Heinrich-Heine-Universität Düsseldorf, Mar. 2015 (cit. on p. 30).

[84]J. Yvon. “La théorie statistique des fluides et l’équation d’état”. In: *Hermann* (1935) (cit. on p. 30).

[85]N. N. Bogoliubov. “Kinetic Equations”. In: *Journal of Physics USSR* 10 (1946), pp. 265–274 (cit. on p. 30).

[86]John G. Kirkwood. “The Statistical Mechanical Theory of Transport Processes I. General Theory”. In: *The Journal of Chemical Physics* 14.3 (Mar. 1946), pp. 180–201 (cit. on p. 30).

[87]Max Born and H. S. Green. “A general kinetic theory of liquids I. The molecular distribution functions”. In: *Proceedings of the Royal Society of London. Series A. Mathematical and Physical Sciences* 188.1012 (Dec. 31, 1946), pp. 10–18 (cit. on p. 30).

[88]R. Blakemore. “Magnetotactic bacteria”. In: *Science* 190.4212 (Oct. 24, 1975), pp. 377–379 (cit. on p. 31).

[89]Dennis A. Bazylinski and Richard B. Frankel. “Magnetosome formation in prokaryotes”. In: *Nature Reviews Microbiology* 2.3 (Mar. 2004), p. 217 (cit. on pp. 31, 86).

[90]Richard B. Frankel and Dennis A. Bazylinski. “Magnetosomes and Magneto-Aerotaxis”. In: *Bacterial Sensing and Signaling* 16 (2009), pp. 182–193 (cit. on p. 31).

[91]M. Reufer, R. Besseling, J. Schwarz-Linek, et al. “Switching of Swimming Modes in Magnetospirillium gryphiswaldense”. In: *Biophysical Journal* 106.1 (2014), pp. 37–46 (cit. on pp. 31, 86).

[92]Jean-Francois Rupprecht, Nicolas Waisbord, Christophe Ybert, Cécile Cottin-Bizonne, and Lydéric Bocquet. “Velocity Condensation for Magnetotactic Bacteria”. In: *Phys. Rev. Lett.* 116 (16 Apr. 2016), p. 168101 (cit. on p. 31).

[93]Irene Sinn, Paivo Kinnunen, Shao Ning Pei, et al. “Magnetically uniform and tunable Janus particles”. In: *Applied Physics Letters* 98.2 (2011), p. 024101 (cit. on p. 31).

[94]Nan Zhao and Mingyuan Gao. “Magnetic Janus Particles Prepared by a Flame Synthetic Approach: Synthesis, Characterizations and Properties”. In: *Advanced Materials* 21.2 (2009), pp. 184–187 (cit. on p. 31).

[95]J.D. Jackson. *Classical electrodynamics*. Wiley, 1975 (cit. on pp. 32, 34, 39).

[96]Carlo Andrea Gonano, Riccardo Enrico Zich, and Marco Mussetta. “DEFINITION FOR POLARIZATION P AND MAGNETIZATION M FULLY CONSISTENT WITH MAXWELL’S EQUATIONS”. In: *Progress In Electromagnetics Research B* 64 (2015), pp. 83–101 (cit. on p. 34).

[97]S. Kim and S.J. Karrila. *Microhydrodynamics: Principles and Selected Applications*. Dover Civil and Mechanical Engineering. Dover Publications, 2013 (cit. on pp. 40, 48, 51).

[98]C. M. Pooley, G. P. Alexander, and J. M. Yeomans. “Hydrodynamic Interaction between Two Swimmers at Low Reynolds Number”. In: *Physical Review Letters* 99.22 (Nov. 28, 2007) (cit. on p. 43).

[99]J L Anderson. “Colloid Transport by Interfacial Forces”. In: *Annual Review of Fluid Mechanics* 21.1 (Jan. 1, 1989), pp. 61–99 (cit. on p. 43).

[100]Maciej Lisicki. “Four approaches to hydrodynamic Green’s functions – the Oseen tensors”. In: *arXiv:1312.6231 [math-ph, physics:physics]* (Dec. 21, 2013). arXiv: 1312.6231 (cit. on pp. 43, 44, 75).

[101]G. K. Batchelor. “The stress system in a suspension of force-free particles”. In: *Journal of Fluid Mechanics* 41.3 (Apr. 29, 1970), pp. 545–570 (cit. on p. 44).

[102]J. M. Yeomans, D. O. Pushkin, and H. Shum. “An introduction to the hydrodynamics of swimming microorganisms”. In: *The European Physical Journal Special Topics* 223.9 (Sept. 2014), pp. 1771–1785 (cit. on p. 45).

[103]Nigel J. Mottram and Christopher J. P. Newton. “Introduction to Q-tensor theory”. In: *arXiv:1409.3542 [cond-mat]* (Sept. 11, 2014). arXiv: 1409.3542 (cit. on p. 48).

[104]Masao Doi and Samuel F. Edwards. *The theory of polymer dynamics*. International series of monographs on physics 73. Oxford: Clarendon Press, 2009. 391 pp. (cit. on p. 49).

[105]Patrick Ilg, Martin Kröger, and Siegfried Hess. “Magnetoviscosity and orientational order parameters of dilute ferrofluids”. In: *The Journal of Chemical Physics* 116.20 (May 22, 2002), pp. 9078–9088 (cit. on p. 52).

[106]J.P. Boyd. *Chebyshev and Fourier Spectral Methods: Second Revised Edition*. Dover Books on Mathematics. Dover Publications, 2013 (cit. on pp. 57, 70, 71, 73).

[107]Alan E Gelfand and Adrian FM Smith. “Sampling-based approaches to calculating marginal densities”. In: *Journal of the American statistical association* 85.410 (1990), pp. 398–409 (cit. on p. 60).

[108]Wally R Gilks, Nicky G Best, and KKC Tan. “Adaptive rejection Metropolis sampling within Gibbs sampling”. In: *Journal of the Royal Statistical Society: Series C (Applied Statistics)* 44.4 (1995), pp. 455–472 (cit. on p. 60).

[109]George Casella, Christian P Robert, Martin T Wells, et al. “Generalized accept-reject sampling schemes”. In: *A Festschrift for Herman Rubin*. Institute of Mathematical Statistics, 2004, pp. 342–347 (cit. on p. 60).

[110]M. Kolonko. *Stochastische simulation: grundlagen, algorithmen und anwendungen*. Teubner studienbücher wirtschaftsmathematik. Vieweg+teubner Verlag, 2008 (cit. on p. 61).

[111]Crispin W. Gardiner. *Handbook of stochastic methods : for physics, chemistry and the natural sciences*. 2. ed., 4. printing, study ed. Vol. 13. Springer series in synergetics. 1997 (cit. on p. 63).

[112]Ioana M Ilie, Wim J Briels, and Wouter K den Otter. “An elementary singularity-free Rotational Brownian Dynamics algorithm for anisotropic particles”. In: *The Journal of chemical physics* 142.11 (2015), 03B610_1 (cit. on p. 65).

[113]Ken Shoemake. “Animating rotation with quaternion curves”. In: *ACM SIGGRAPH computer graphics*. Vol. 19. 3. ACM. 1985, pp. 245–254 (cit. on p. 65).

[114]Murray Rosenblatt. “Remarks on Some Nonparametric Estimates of a Density Function”. In: *The Annals of Mathematical Statistics* 27.3 (Sept. 1956), pp. 832–837 (cit. on p. 67).

[115]Emanuel Parzen. “On Estimation of a Probability Density Function and Mode”. In: *The Annals of Mathematical Statistics* 33.3 (Sept. 1962), pp. 1065–1076 (cit. on p. 67).

[116]B.W. Silverman. *Density Estimation for Statistics and Data Analysis*. Chapman & Hall/CRC Monographs on Statistics & Applied Probability. Taylor & Francis, 1986 (cit. on p. 68).

[117]V. A. Epanechnikov. “Non-Parametric Estimation of a Multivariate Probability Density”. In: *Theory of Probability & Its Applications* 14.1 (Jan. 1969), pp. 153–158 (cit. on p. 68).

[118]M.P. Wand and M.C. Jones. *Kernel Smoothing*. Chapman & Hall/CRC Monographs on Statistics & Applied Probability. Taylor & Francis, 1994 (cit. on p. 69).

[119]D. Funaro. *Polynomial Approximation of Differential Equations*. Lecture Notes in Physics Monographs. Springer Berlin Heidelberg, 2008 (cit. on p. 71).

[120]D.A. Kopriva. *Implementing Spectral Methods for Partial Differential Equations: Algorithms for Scientists and Engineers*. Scientific Computation. Springer Netherlands, 2009 (cit. on p. 71).

[121]Steven A. Orszag. “Comparison of Pseudospectral and Spectral Approximation”. In: *Studies in Applied Mathematics* 51.3 (Sept. 1972), pp. 253–259 (cit. on p. 71).

[122]James W. Cooley and John W. Tukey. “An algorithm for the machine calculation of complex Fourier series”. In: *Mathematics of Computation* 19.90 (May 1, 1965), pp. 297–297 (cit. on p. 73).

[123]Rust Project Developers. *Rust*. `https://www.rust-lang.org/`. [Online; accessed 31. July 2019]. 2010 (cit. on p. 77).

[124]Matteo Frigo and Steven G. Johnson. “The Design and Implementation of FFTW3”. In: *Proceedings of the IEEE* 93.2 (2005). Special issue on “Program Generation, Optimization, and Platform Adaptation”, pp. 216–231 (cit. on p. 77).

[125]bluss et al. *rust-ndarray*. `https://crates.io/crates/ndarray`. [Online; accessed 31. July 2019]. 2015 (cit. on p. 77).

[126]Josh Stone and Niko Matsakis. *rayon*. `https://crates.io/crates/rayon`. [Online; accessed 31. July 2019]. 2015 (cit. on p. 77).

[127]Melissa E. O’Neill. *PCG: A Family of Simple Fast Space-Efficient Statistically Good Algorithms for Random Number Generation*. Tech. rep. HMC-CS-2014-0905. Claremont, CA: Harvey Mudd College, Sept. 2014 (cit. on p. 77).

[128]The Rand Project Developers. *rand_pcg*. `https://crates.io/crates/rand_pcg`. [Online; accessed 31. July 2019]. 2018 (cit. on p. 77).

[129]Jurgen A Doornik. “An improved ziggurat method to generate normal random samples”. In: *University of Oxford* (2005) (cit. on p. 77).

[130]The Rand Project Developers. *rand_distr*. `https://crates.io/crates/rand_distr`. [Online; accessed 31. July 2019]. 2019 (cit. on p. 77).

[131]unknown. *builder pattern*. `https://doc.rust-lang.org/1.0.0/style/ownership/builders.html`. [Online; accessed 31. July 2019]. 2015 (cit. on p. 77).

[132]C. Bormann and P. Hoffman. *Concise Binary Object Representation (CBOR)*. `https://tools.ietf.org/html/rfc7049`. [Online; accessed 31. July 2019]. 2013 (cit. on p. 77).

[133]R.Y. Rubinstein and D.P. Kroese. *Simulation and the Monte Carlo Method*. Wiley Series in Probability and Statistics. Wiley, 2011 (cit. on p. 78).

[134]S.H. Strogatz. *Nonlinear Dynamics And Chaos*. Studies in nonlinearity. Sarat Book House, 2007 (cit. on p. 78).

[135]F.Y.M. Wan. *Dynamical System Models in the Life Sciences and Their Underlying Scientific Issues*. World Scientific Publishing Company, 2017 (cit. on p. 78).

[136]H.G. Solari. *Nonlinear Dynamics: A Two-Way Trip from Physics to Math*. CRC Press, 2019 (cit. on p. 78).

[137]P. A. M. Dirac. “A new notation for quantum mechanics”. In: *Mathematical Proceedings of the Cambridge Philosophical Society* 35.3 (1939), pp. 416–418 (cit. on p. 80).

[138]R. Courant and D. Hilbert. *Methods of mathematical physics*. Bd. 1. Wiley, 2008 (cit. on p. 82).

[139]Fiona C. Meldrum, Stephen Mann, Brigid R. Heywood, Richard B. Frankel, and Dennis A. Bazylinski. “Electron microscopy study of magnetosomes in a cultured coccoid magnetotactic bacterium”. In: *Proc. R. Soc. Lond. B* 251.1332 (Mar. 22, 1993), pp. 231–236 (cit. on p. 86).

[140]Rohan Nadkarni, Solomon Barkley, and Cécile Fradin. “A Comparison of Methods to Measure the Magnetic Moment of Magnetotactic Bacteria through Analysis of Their Trajectories in External Magnetic Fields”. In: *Plos One* 8.12 (Dec. 2013), pp. 1–12 (cit. on p. 86).

[141]Giulio Racah. “Theory of Complex Spectra. II”. In: *Physical Review* 62.9 (Nov. 1, 1942), pp. 438–462 (cit. on p. 95).

[142]A.R. Edmonds. *Angular Momentum in Quantum Mechanics*. Investigations in Physics. Princeton University Press, 2016 (cit. on p. 95).

[143]Stefano S. Turzi. “On the Cartesian definition of orientational order parameters”. In: *Journal of Mathematical Physics* 52.5 (May 2011), p. 053517 (cit. on pp. 105, 106, 110).

[144]A. D. Buckingham. “Angular correlation in liquids”. In: *Discussions of the Faraday Society* 43 (1967), p. 205 (cit. on p. 105).

[145] M. Kröger. *Models for Polymeric and Anisotropic Liquids*. Lecture Notes in Physics. Springer Berlin Heidelberg, 2005 (cit. on p. 106).

[146] George L. Hand. "A theory of anisotropic fluids". In: *Journal of Fluid Mechanics* 13.1 (May 1962), pp. 33–46 (cit. on p. 108).

[147] Sumesh P. Thampi, Ramin Golestanian, and Julia M. Yeomans. "Instabilities and topological defects in active nematics". In: *EPL (Europhysics Letters)* 105.1 (Jan. 2014), p. 18001 (cit. on p. 113).

[148] G. Gan, C. Ma, and J. Wu. *Data Clustering: Theory, Algorithms, and Applications*. ASA-SIAM Series on Statistics and Applied Probability. Society for Industrial and Applied Mathematics (SIAM, 3600 Market Street, Floor 6, Philadelphia, PA 19104), 2007 (cit. on p. 119).

[149] Veronika Magdanz, Samuel Sanchez, and Oliver G. Schmidt. "Micro-robots: Development of a Sperm-Flagella Driven Micro-Bio-Robot (Adv. Mater. 45/2013)". In: *Advanced Materials* 25.45 (2013), pp. 6470–6470 (cit. on p. 127).

[150] Kay Kirkpatrick and Tayyab Nawaz. "Critical Behavior of Mean-Field XY and Related Models". In: *Stochastic Analysis and Related Topics*. Ed. by Fabrice Baudoin and Jonathon Peterson. Cham: Springer International Publishing, 2017, pp. 207–221 (cit. on pp. 141, 142).

[151] A. M. Polyakov. "Interaction of goldstone particles in two dimensions. Applications to ferromagnets and massive Yang-Mills fields". In: *Physics Letters B* 59.1 (Oct. 13, 1975), pp. 79–81 (cit. on p. 141).

[152] A. Oukouiss and M. Baus. "Phase diagrams of the classical Heisenberg fluid within the extended van der Waals approximation". In: *Physical Review E* 55.6 (June 1, 1997), pp. 7242–7252 (cit. on p. 142).

[153] S. A. Adelman. "Hydrodynamic screening and viscous drag at finite concentration". In: *The Journal of Chemical Physics* 68.1 (1978), p. 49 (cit. on p. 160).

List of Figures

List of Tables

Listings